ISSN en trámite

Geofísica Internacional

Revista Trimestral Publicada por el Instituto de Geofísica de la Universidad Nacional Autónoma de México

México
Volume 53 Number 2
April - June
2014

— Geofísica Internacional —

GEOFÍSICA INTERNACIONAL, Año 53, Vol. 53, Núm. 2, abril - junio de 2014 es una publicación trimestral, editada por la Universidad Nacional Autónoma de México, Ciudad Universitaria, Alcaldía Coyoacán, C.P. 04150, Ciudad de México, a través del Instituto de Geofísica, Circuito de la Investigación Científica s/n, Ciudad Universitaria, Alcaldía Coyoacán, C.P. 04150, Ciudad de México, Tel. (55)56 22 41 15. URL: http://revistagi.geofisica.unam.mx, correo electrónico: revistagi@igeofisica.unam.mx. Editora responsable: Andrea Rostan Robledo. Certificado de Reserva de Derechos al uso Exclusivo del Título: 04-2022-081610251200-102, ISSN: en trámite, otorgados por el Instituto Nacional del Derecho de Autor (INDAUTOR). Responsable de la última actualización Saúl Armendáriz Sánchez, Editor Técnico. Fecha de la última modificación: 31 de marzo 2014, Circuito de la Investigación Científica s/n, Ciudad Universitaria, Alcaldía Coyoacán, C.P. 04150, Ciudad de México.

Geofísica Internacional

Vol. 53, Núm. 2, abril-junio de 2014

Contents

Geofísica
Internacional

Geofísica Internacional (2014) 53-2: 101-115

Original paper

Daubechies wavelet coefficients: a tool to study interplanetary magnetic field fluctuations

Arian Ojeda González*, Odim Mendes Junior, Margarete Oliveira Domingues and Varlei Everton Menconi

Received: September 04, 2012; accepted: August 06, 2013; published on line: April 01, 2014

Resumen

Hemos estudiado un conjunto de 41 nubes magnéticas (MCs) detectadas por el satélite ACE, utilizamos la transformada wavelet ortogonal discreta (usando wavelet de Daubechies de orden dos) en tres regiones: vaina de plasma, nube y posterior a la nube. Trabajamos con datos de las componentes del campo magnético interplanetario (IMF) en el sistema de coordenadas GSM con resolución temporal de 16 s. Se ha elegido como herramienta matemática la media estadística de los coeficientes wavelets ($\langle Dd1 \rangle$). Los coeficientes wavelets de Daubechies se han utilizado porque ellos representan la regularidad local presente en la señal de estudio. Los resultados reprodujeron el hecho bien conocido, que la dinámica es mas compleja en la vaina de plasma que en la región de la MC. Esta técnica podría ser útil a un especialista en ayudarlo encontrar fronteras de eventos cuando se trabaja con el IMF, es decir, una mejor forma de visualizar los datos. Los coeficientes wavelets tienen la ventaja de facilitar encontrar algunos choques que serían difíciles de detectar por simple inspección visual del IMF. Podemos aprender que las fluctuaciones no son igualmente pequeñas en todas las nubes, en algunos casos las ondas pueden penetrar desde la vaina hasta la MC. Esta metodología aún no ha sido testada para identificar patrones específicos de fluctuaciones en el IMF de otros eventos interplanetarios geoefectivos, tales como, regiones de interacción corrotante (CIRs), lámina de corriente heliosférica (HCS) o para ICMEs sin características de MC. Como es la primera vez que esta técnica se aplica a los datos del IMF, opinamos que una de las contribuciones de este trabajo es la presentación de este enfoque a la Comunidad de Físicos Espaciales.

Palabras clave: electrodinámica espacial, nubes magnéticas, análisis de series temporales, transformada wavelet discreta, clima espacial.

Abstract

We have studied a set of 41 magnetic clouds (MCs) measured by the ACE spacecraft, using the discrete orthogonal wavelet transform (Daubechies wavelet of order two) in three regions: Pre-MC (plasma sheath), MC and Post-MC. We have used data from the IMF GSM-components with time resolution of 16 s. The mathematical property chosen was the statistical mean of the wavelet coefficients ($\langle Dd1 \rangle$). The Daubechies wavelet coefficients have been used because they represent the local regularity present in the signal being studied. The results reproduced the well-known fact that the dynamics of the sheath region is more than that of the MC region. This technique could be useful to help a specialist to find events boundaries when working with IMF datasets, i.e., a best form to visualize the data. The wavelet coefficients have the advantage of helping to find some shocks that are not easy to see in the IMF data by simple visual inspection. We can learn that fluctuations are not low in all MCs, in some cases waves can penetrate from the sheath to the MC. This methodology has not yet been tested to identify some specific fluctuation patterns at IMF for any other geoeffective interplanetary events, such as Co-rotating Interaction Regions (CIRs), Heliospheric Current Sheet (HCS) or ICMEs without MC signatures. In our opinion, as is the first time that this technique is applied to the IMF data with this purpose, the presentation of this approach for the Space Physics Community is one of the contributions of this work.

Key words: space electrodynamics, magnetic clouds, time series analysis, discrete wavelet transform, space weather.

A. Ojeda González*
O. Mendes Junior
V.E. Menconi
DGE/CEA
National Institute for Space Research
INPE 12227-010 São José dos Campos
SP, Brazil
*Corresponding author: ojeda.gonzalez.a@gmail.com

M. Oliveira Domingues
LAC/CTE
National Institute for Space Research
INPE 12227-010 São José dos Campos
SP, Brazil

A. Ojeda González
Department of Space Geophysics
Institute of Geophysics and Astronomy
IGA Havana City, Cuba

Introduction

One of the very important phenomena in space is the Interplanetary Coronal Mass Ejection (ICME) as a disturbance in the solar wind (SW) that presents a large importance due to its potential geoeffectivity. Physically, a subset of ICMEs has simple flux rope-like magnetic fields, in which, briefly, the magnetic field strength is higher than the average, the magnetic field direction rotates smoothly through a large angle, and the proton temperature is low (Burlaga *et al*., 1981; Klein and Burlaga, 1982; Gosling, 1990). Such events, named magnetic clouds (MCs), have received considerable attention, because they are an important source of southward interplanetary magnetic field (e.g. NS, SN and S polarity, where N ≡ north and S ≡ south).

Investigations on the relation between MCs and geomagnetic storms have been carried out by many researchers (for instance, Burlaga *et al*., 1981; Klein and Burlaga, 1982; Gonzalez and Tsurutani, 1987; Tsurutani *et al*., 1988; Tsurutani and Gonzalez, 1992; Farrugia *et al*., 1995; Lepping *et al*., 2000; Dal Lago, *et al*., 2000; Dal Lago *et al*., 2001; Wu and Lepping, 2002a,b) with many purposes. Echer *et al*. (2005) studied a total of 149 MCs from 1966 to 2001, where 51 are of the NS type, 83 of the type SN, and 15 unipolar (N or S). They did a statistical study of MC parameters and geoeffectiveness that was determined by classifying the number of MCs followed by intense, moderate and weak magnetic storms, and by calm periods. They found that around 77% of the MCs present geoeffectivity with Dst ≤ -50 nT. Taking into account weak storms (-50 nT ≤ Dst ≤ -30 nT), 97% of MCs were followed by geomagnetic activity.

Another significant example is the work of Huttunen *et al*. (2005), where they studied the geomagnetic response of MCs using the 1-h Dst index. They focused on whether the storm was caused by sheath fields or by the MC itself. They found that the geomagnetic response of a MC depends greatly on its flux-rope type.

Inside ICMEs, the measured plasma velocity typically has a linear variation along the spacecraft trajectory. A much higher velocity is present in the front than in the rear, indicating expansion (Démoulin and Dasso, 2009). Burlaga and Behannon (1982) found consistency between the expansion speed estimated from in situ observations and the increase of their typical size, obtained from measurements with different spacecraft located between 2 and 4 AUs.

The MCs closer to the Sun, i.e., the ones that are near 1 AU, had higher plasma densities than the ones surrounding SW. The density inside the flux tubes has a rapid decrease with the increasing distance from the Sun where the cloud undergoes a radial expansion. The density in MCs is generally higher than average fast SW, and the slow SW, at close distances to the Sun. Bothmer and Schwenn (1998) observed that MCs in which the densities are found to be considerably lower compared to those of the ambient slow SW should have undergone strong expansion on their way out from the Sun.

Typically, the MC magnetic field configuration may be described by a force-free model as a simple approximation useful in interpreting time series data (e.g., Lundquist, 1950; Lepping *et al*., 1990; Burlaga, 1988; Osherovich and Burlaga, 1997; Lepping *et al*., 1997; Burlaga, 1995; Bothmer and Schwenn, 1998; Dasso *et al*., 2005). Three characteristic speeds are derived from MHD theory; these are the sound speed, the Alfvén speed, and the magnetoacoustic speed. Then five kinds of MHD shocks (fast shock, slow shock and three kinds of intermediate shocks) can be found (Burlaga, 1995, p.70). In SW have been studied the fast shock and slow shock. The magnetic field strength increases across a fast shock and decreases across a slow shock (Burlaga, 1995, p.70). A shock moving away from the Sun relative to the ambient medium is called a "forward shock". A shock moving toward the Sun relative to the ambient medium is called "reverse shock" (Gosling, 1998). In MHD, the shocks are further classified on the basis of the angle between $\vec{n}$ and the ambient magnetic field observation $\vec{B}$. Therefore, shocks are classified as perpendicular, parallel and oblique. The sheath is the turbulent region between a shock and an MC (Burlaga, 1995, p.132). The SW form sheaths around solar system objects: the heliosheath around the heliosphere, cometosheaths around comets and ICME-sheaths around fast ICMEs, etc. Siscoe and Odstrcil (2008) defined two types of sheath, "propagation sheath" and "expansion sheath", but pure expansion sheaths are less common than propagation sheaths. The studies on the dynamics of those kinds of electrodynamics structures are among the current concerns of the space community.

Other studies also suggest that the Interplanetary Magnetic Field (IMF) fluctuations can be geo-effective, and then the reason for space weather studies on variability related to the interplanetary phenomena (Lyons *et al*., 2009). According to Lyons *et al*. (2009) and Kim *et al*. (2009), the interplanetary ULF

fluctuations are an important contributor to the large-scale transfer of SW energy to the magnetosphere-ionosphere system, and to the occurrence of disturbances such as substorms. In their work, the data are processed using a fast Fourier transform algorithm with 128 points (2 h) moving window to produce the power spectral density in the ULF Pc5 frequency range. Kim *et al*. (2009) show dynamic spectrograms of the IMF B_z obtained from 1-min-resolution time-shifted ACE data for the four different SW conditions that was examined. Borovsky (2012) studied the plasma fluctuations in a dataset measured by the ACE spacecraft. All of them are using Fourier transform algorithms in a skilled way.

However, some complicated fluctuations in SW plasma could be investigated by using techniques based on approaches from nonlinear dynamics (e.g. Ojeda *et al*., 2005; Ojeda *et al*., 2013). Thus, an interesting expectation is to study the ICMEs by the analyses of the time series of the IMF, because this field should preserve intrinsic aspects of the physical structures involved. Also, IMF data studies require analysis of random or non-deterministic time series, as well as analyses taking into account the non-stationary behaviour of data. The use of wavelet coefficients has proved to be a useful technique for study those kinds of data, specially of non-stationary time series (e.g. Mendes *et al*., 2005; Domingues *et al*., 2005).

The mathematical property chosen in this work is the statistical mean of the wavelet coefficients obtained by applying the discrete orthogonal wavelet transform using Daubechies wavelet of order two (i.e. Daubechies scale filters order 2, db2). The analysis is done using the components of the IMF as recorded by the instruments of the Magnetic Field Experiment (MAG) on board of the ACE S/C at the L1 point. Therefore, our interest is to study the wavelet coefficients behaviour for diagnose of disturbance level in interval of the SW data containing the MC occurrences. The tool feature explored here is the identification of regularity/no-regularity in a function that represents the physical process (see for example, Appendix A).

As used in this work, a methodology is presented to help the solar/heliospheric physics community efforts to deal with the MCs. The wavelet analysis has important advantages, adding resources to other classical mathematical tools that could be used to study SW fluctuations. The wavelet coefficients allow to find fluctuations with pseudo-frequencies corresponding to the scales given by j, the chosen wavelet function, and the sampling period. The idea is to associate a purely periodic signal of frequency Fc with a given wavelet. The frequency maximizing the Fourier transform of the wavelet function is the central frequency (Fc) of it. It enables plotting the wavelet with an associated approximation based on the center frequency. This center frequency captures the main wavelet oscillations. Thus, the center frequency is a convenient and simple characterization of the leading dominant frequency of the wavelet (Abry, 1997).

As we are interested in studying fluctuations with larger frequencies (in this case on data from 16-second time resolution), the Daubechies function db2 with one decomposition level seems an appropriate choice. A zooming in analysing the IMF fluctuations with a pseudo-period of 48 seconds could help to better locate the ICME boundaries. Thus, a statistical study has to be performed. For this reason, three regions from 41 ICMEs will be studied, i.e. plasma sheath, magnetic cloud, and region after the MC.

The aim of this work is to characterize the wavelet coefficients amplitudes of the magnetic field at the three different regions around an ICME event to relate it to features of the interplanetary medium. The primary idea is to distinguish more quiescent periods (in terms of magnetic variation) related to MC from non-quiescent periods of two other processes. For the use of magnetic field data, the motivation is that in many cases there are only those kinds of data available for investigation. The content is organized as follows. Section 2 presents dataset. Section 3 describes the implemented methodology. Section 4 discusses the results. Section 5 gives the conclusions.

IMF Dataset

The Lagrangean point L1 is a gravitational equilibrium point between the Sun and the Earth at about 1.5 million km from Earth and 148.5 million km from the Sun (Celletti and Giorgilli, 1990). The data used here are from Advance Composition Explorer (ACE) spacecraft, which has been making such measurements orbiting L1 since 1997 (Smith *et al*., 1998). From its location, ACE has a prime view of the SW, the IMF and the higher energy particles accelerated by the Sun, as well as particles accelerated in the Heliosphere and the galactic regions beyond. The plasma particles detected by ACE arrive at the magnetopause after about 30 min (Smith *et al*., 1998). The MAG on board ACE consists of twin vector fluxgate magnetometers to measure IMF (Smith *et al*., 1998). The data contains time averages of the magnetic field over time periods 1 s, 16 s, 4 min, hourly, daily and 27 days (1 Bartels rotation).

In this work we use data from the IMF GSM-components with time resolution of 16 s. We work with 41 of 80 events (73 MCs and 7 cloud candidate) identified by Huttunen *et al*. (2005). These events are shown in chronological order in Table 1. The columns from left to right give: a numeration of the events, year, shock time (UT), MC start time (UT), MC end time (UT), and the end time (UT) of the third region respectively.

A total of 17 events listed in Table 2 are not treated in this work. The reason is that the ACE data before about the end of 1997 were not qualified for research use. Huttunen *et al*. (2005) used the measurements recorded by the WIND spacecraft for this initial period. The magnetic field instrument (MFI) on board WIND is composed of dual triaxial fluxgate magnetometers. We avoid in this analysis mixing dataset from different types of spacecraft. Another problem is that the WIND data available in averages present 3 s, 1 min, and 1 h time resolution, a lower resolution than the one we used by ACE.

Table 1. Solar Wind data studied (from Huttunen *et al*., 2005).

No.	Year	Shock, UT	MC start, UT	MC stop, UT	Post-MC, UT
01	1998	06 Jan, 13:19	07 Jan,03:00	08 Jan, 09:00	10 Jan, 15:00
02		03 Feb, 13:09	04 Feb, 05:00	05 Feb, 14:00	06 Feb, 23:00
03		04 Mar, 11:03	04 Mar, 15:00	05 Mar, 21:00	07 Mar, 03:00
04		01 May, 21:11	02 May, 12:00	03 May, 17:00	04 May, 22:00
05		13 Jun, 18:25	14 Jun, 02:00	14 Jun, 24:00	15 Jun, 22:00
06		19 Aug, 05:30	20 Aug, 08:00	21 Aug, 18:00	23 Aug, 04:00
07		24 Sep, 23:15	25 Sep, 08:00	26 Sep, 12:00	27 Sep, 16:00
08		18 Oct, 19:00	19 Oct, 04:00	20 Oct, 06:00	21 Oct, 08:00
09		08 Nov, 04:20	08 Nov, 23:00	10 Nov, 01:00	12 Nov, 02:00
10		13 Nov, 00:53	13 Nov, 04:00	14 Nov, 06:00	15 Nov, 08:00
11	1999	18 Feb, 02:08	18 Feb, 14:00	19 Feb, 11:00	20 Feb, 08:00
12		16 Apr, 10:47	16 Apr, 20:00	17 Apr, 18:00	18 Apr, 16:00
13		08 Aug, 17:45	09 Aug, 10:00	10 Aug, 14:00	11 Aug, 18:00
14	2000	11 Feb, 23:23	12 Feb, 12:00	12 Feb, 24:00	13 Feb, 12:00
15		20 Feb, 20:57	21 Feb, 14:00	22 Feb, 12:00	23 Feb, 10:00
16		11 Jul, 11:22	11 Jul, 23:00	13 Jul, 02:00	14 Jul, 05:00
17		13 Jul, 09:11	13 Jul, 15:00	13 Jul, 24:00	14 Jul, 09:00
18		15 Jul, 14:18	15 Jul, 19:00	16 Jul, 12:00	17 Jul, 05:00
19		28 Jul, 05:53	28 Jul, 18:00	29 Jul, 10:00	30 Jul, 02:00
20		10 Aug, 04:07	10 Aug, 20:00	11 Aug, 08:00	11 Aug, 20:00
21		11 Aug, 18:19	12 Aug, 05:00	13 Aug, 02:00	13 Aug, 23:00
22		17 Sep, 17:00	17 Sep, 23:00	18 Sep, 14:00	19 Sep, 05:00
23		02 Oct, 23:58	03 Oct, 15:00	04 Oct, 14:00	05 Oct, 13:00
24		02 Oct, 23:58	13 Oct, 17:00	14 Oct, 13:00	15 Oct, 09:00
25		28 Oct, 09:01	28 Oct, 24:00	29 Oct, 23:00	30 Oct, 22:00
26		06 Nov, 09:08	06 Nov, 22:00	07 Nov, 15:00	08 Nov, 08:00
27	2001	19 Mar, 10:12	19 Mar, 22:00	21 Mar, 23:00	23 Mar, 24:00
28		27 Mar, 17:02	27 Mar, 22:00	28 Mar, 05:00	28 Mar, 12:00
29		11 Apr, 15:18	12 Apr, 10:00	13 Apr, 06:00	14 Apr, 02:00
30		21 Apr, 15:06	21 Apr, 23:00	22 Apr, 24:00	24 Apr, 01:00
31		28 Apr, 04:31	28 Apr, 24:00	29 Apr, 13:00	30 Apr, 02:00
32		27 May, 14:17	28 May, 11:00	29 May, 06:00	30 May, 01:00
33		31 Oct, 12:53	31 Oct, 22:00	02 Nov, 04:00	03 Nov, 10:00
34	2002	23 Mar, 10:53	24 Mar, 10:00	25 Mar, 12:00	26 Mar, 14:00
35		17 Apr, 10:20	17 Apr, 24:00	19 Apr, 01:00	20 Apr, 02:00
36		18 May, 19:44	19 May, 04:00	19 May, 22:00	20 May, 16:00
37		01 Aug, 23:10	02 Aug, 06:00	02 Aug, 22:00	03 Aug, 14:00
38		30 Sep, 07:55	30 Sep, 23:00	01 Oct, 15:00	02 Oct, 07:00
39	2003	20 Mar, 04:20	20 Mar, 13:00	20 Mar, 22:00	21 Mar, 07:00
40		17 Aug, 13:41	18 Aug, 06:00	19 Aug, 11:00	20 Aug, 16:00
41		20 Nov, 07:27	20 Nov, 11:00	21 Nov, 01:00	22 Nov, 15:00

Table 2. MC events measured by WIND (not examined). Letter "Q" denotes whether the event was an MC (l) or cloud candidate (cl).

No.	Year	Shock, UT	MC start, UT	MC stop, UT	Q
01	1997	10 Jan, 00:20	10 Jan, 05:00	11 Jan, 02:00	l
02		09 Feb, 23:43	10 Feb, 03:00	10 Feb, 19:00	cl
03		10 Apr, 12:57	11 Apr, 08:00	11 Apr, 16:00	l
04		-	21 Apr, 17:00	22 Apr, 24:00	cl
05		15 May, 00:56	15 May, 10:00	15 May, 24:00	l
06		-	15 May, 07:00	16 May, 16:00	l
07		26 May, 09:10	26 May, 16:00	27 May, 19:00	l
08		-	09 Jun, 06:00	09 Jun, 23:00	l
09		19 Jun, 00:12	19 Jun, 06:00	19 Jun, 16:00	l
10		-	15 Jul, 09:00	16 Jul, 06:00	l
11		-	03 Aug, 14:00	04 Aug, 02:00	l
12		-	18 Sep, 03:00	19 Sep, 21:00	l
13		-	22 Sep, 01:00	22 Sep, 18:00	l
14		01 Oct, 00:20	01 Oct, 15:00	02 Oct, 22:00	l
15		10 Oct, 15:48	10 Oct, 23:00	12 Oct, 01:00	l
16		06 Nov, 22:07	07 Nov, 05:00	08 Nov, 03:00	l
17		22 Nov, 08:55	22 Nov, 19:00	23 Nov, 12:00	l

The MC events that are not associated with shock waves are not tested here. They are presented in Table 3. The purpose of this selection, in this exploratory study, is to deal with the cases presenting the three periods (clear Pre-MC, MC and Post-MC). Thus, with the well-defined MC cases, the assumption is to objectively unravel the magnetically quiescent interval related to the MC period. If there are significant differences of the coefficient features among the periods, then this tool can be used to identify boundaries of ICMEs in most clear basis. Other SW disturbances different of MCs are not studied here.

Table 3. These magnetic cloud events are not preceded by shock waves. Letter "Q" denotes whether the event was an MC (l) or cloud candidate (cl).

No.	Year	Shock, UT	MC start, UT	MC stop, UT	Q
01	1998	-	17 Feb, 10:00	18 Feb, 04:00	l
02		-	02 Jun, 10:00	02 Jun, 16:00	l
03		-	24 Jun, 12:00	25 Jun, 16:00	l
04	1999	-	25 Mar, 16:00	25 Mar, 23:00	l
05		-	21 Apr, 12:00	22 Apr, 13:00	l
06		-	22 Aug, 12:00	23 Aug, 06:00	l
07		-	21 Sep, 20:00	23 Sep, 05:00	l
08		-	14 Nov, 01:00	14 Nov, 09:00	cl
09		-	16 Nov, 09:00	16 Nov, 23:00	l
10	2000	-	15 Jul, 05:00	15 Jul, 14:00	cl
11		-	31 Jul, 22:00	01 Aug, 12:00	l
12	2001	-	04 Mar, 16:00	05 Mar, 01:00	l
13		-	18 Jun, 23:00	19 Jun, 14:00	l
14		-	10 Jul, 17:00	11 Jul, 23:00	l
15		03 Oct, 08:??	03 Oct, 01:00	03 Oct, 16:00	l
16		-	24 Nov, 17:00	25 Nov, 13:00	cl
17	2002	-	28 Feb, 18:00	01 Mar, 10:00	l
18		-	19 Mar, 22:00	20 Mar, 10:00	l
19		-	20 Apr, 13:00	21 Apr, 15:00	l
20		23 May, 10:15	23 May, 22:00	24 May, ??:??	cl
21	2003	-	27 Jan, 01:00	24 May, ??:??	l
22		-	29 Oct, 12:00	30 Oct, 01:00	l

Methodology

The Discrete Wavelet Transform (DWT) is a linear multilevel efficient transform that is very popular in data compression (Mallat, 1989; Daubechies, 1992; Hubbard, 1997). Mathematically, this transform is built based on a multiscale tool called Multiresolution analysis $\{V^j, \Phi\} \in L^2$ proposed by S. Mallat (see details in Mallat (1989)), where Φ is a scale function, $V^j = span\{\Phi_k^j\}$, and L^2 is the functional space of the square-integrable functions. The DWT uses discrete values of scale (j) and position (k).

The great contribution of wavelet theory is the characterization of complementary spaces between two embedded spaces $V^{j+1} \subset V^j$, through direct sums $V^j = V^{j+1} + W^{j+1}$, where $W^j = span\{\Psi_k^j\}$ with Ψ the wavelet function.

Mallat also developed an efficient and very simple way to compute this multilevel transform based on filter banks. With this tool, one can compute the so called discrete scale coefficient c_k^j and wavelet coefficient d_k^j associate with discrete values of scale j and position k. Roughly speaking, the basic ingredients to compute one level step of this transform are the low filter (h) related to the analysing scale function and its relation with the high-pass filter (g) related to the analysing wavelet function. These filters are used to compute the scale coefficients and the wavelet coefficients as follows:

$$c_k^j = \sqrt{2} \sum h(m-2k) c_m^{j+1} \qquad (1)$$

and

$$d_k^j = \sqrt{2} \sum g(m-2k) c_m^{j+1} \qquad (2)$$

The multilevel transform is done by repeating this procedure recursively: convolute the scale coefficients with the filter and performing the downsampling procedure, i.e., removing one data point between two. Therefore in each scale decomposition levels the number of data is reduced by two. Following is a scheme for the DWT and its inverse (IDWT),

$$\left\{c^{j+1}\right\} \underset{IDWT}{\overset{DWT}{\leftrightarrow}} \left\{c^j, d^j, d^{j-1} \ldots, d^{j-j_0}\right\} .$$

The initial data is consider the first level scale coefficient c^{j+1}.

The wavelet coefficients have the property that their amplitudes are related to the local regularity of the analysed data (Mallat, 1989; Daubechies, 1992). This means that, where the data has a smooth behaviour, the wavelet coefficients are smaller, and vice-versa. This is the basic idea of data compression and the application we are doing here. The wavelet coefficient amplitudes are also related to the analysing wavelet order and the scale level.

There is not a perfect wavelet choice for a certain data analysis. However, one can follow certain criteria to provide a good choice, see for instance, Domingues *et al*. (2005).

In this work, we have chosen the Daubechies scaling function of order 2, with the choice that the wavelet function locally reproduces a linear polynomial. On one hand, high order analysing Daubechies functions are not adding a better local reproduction of the MC disturbance data. On the other hand, the analysing function of order 1 does not reproduce well these disturbances locally.

We have also observed that just one decomposition level is enough for the energy analysis methodology that we propose here, which corresponds to a pseudo-period of 48 s. The pseudoperiod is $T_a = (a\Lambda) / F_c$ where $a = 2^j$ is a scale, $\Lambda = 16\text{s}$ is the sampling period, Fc = 0.6667 is the center frequency of a wavelet in Hz (Abry, 1997). In Table 4, as a test, some decomposition levels and the Daubechies scaling function of order 1 to 4 are shown, where F_c = [0.9961; 0.6667; 0.8000; 0.7143]. Pseudo-periods (seconds) regarding the Daubechies orthogonal wavelets are presented. It also shows that the information here could be useful for studying fluctuations with different frequencies which is not done in this work.

Table 4. Pseudo-period (seconds) regarding the Daubechies orthogonal wavelets. In this work Λ=16s, j = 1 and db2 then pseudo-period is 48.0 seconds. The information here could be useful for studying fluctuations with different frequencies.

Level	Order			
j	1	2	3	4
1	32.1	48.0	40.0	44.8
2	64.3	96.0	80.0	89.6
3	128.5	192.0	160.0	179.2
4	257.0	384.0	320.0	358.4
5	514.0	768.0	640.0	716.8

The non zero values of the low filter h for Daubechies order 2 analysing wavelet are:

$[h_0,h_1,h_2,h_3]$=0.4829629131445,0.8365163037378, [0.2241438680420, -0.1294095225512] and $[g_0, g_1, g_2, g_3] = [h_0, -h_1, h_2, -h_3]$ is the high-pass band filter (Daubechies, 1992, p.195).

In this case, we are using an orthogonal transform. The orthogonal property is very important here, because with it we with it, we can guarantee a preserving energy property in the wavelet transform similarly to the Parseval theorem for Fourier analysis (Daubechies, 1992). Therefore the total energy of the signal is equal to the superposition of the individual contributions of energy of their wavelet coefficient in each decomposition level (Holschneider, 1991).

In the characterization of a SW disturbance, we perform one decomposition level, and we compute the square of wavelet coefficients (d^1 or $d1$) (energy content on that level), as in Mendes da Costa (2011); Mendes *et al*. (2005), and its mean value D_{d1} is:

$$D_{d1} = \frac{\sum_{i=1}^{N/2} d1_i^2}{N/2}, \text{where } N = length(f(t)) \quad (3)$$

This value was calculated in the three regions, for each IMF components (B_x, B_y, B_z). Its values are influenced by the fluctuations amplitude in the physical system studied. It is lower at a system in stationary state with minimum energy. If the system has a strong external perturbation then the D_{d1} value increases.

The MCs have flux-rope-like topology and form a large-scale winding of a closed magnetic structure that could be nearly force-free. And it is possible to see anisotropy of magnetic field fluctuations in an average interplanetary MC at 1 AU (Narock and Lepping, 2007). We do not expect to find the same behaviour in all three components by the existence of anisotropy. An average value ($\langle D_{d1} \rangle$) of wavelet coefficient D_{d1} in the three magnetic field components are calculated:

$$\langle D_{d1} \rangle = \frac{1}{3}\sum_{i=1}^{3} D_{d1}^{(i)}, \quad (4)$$

where the angle brackets $\langle \ldots \rangle$ denote an average of the D_{d1} in IMF components ($i = 1, 2, 3 = B_x, B_y, B_z$). Its value is useful to compare the fluctuations between SW regions. From a physical point of view, this technique is useful to find candidate regions in the IMF dataset with more perturbations. The $\langle D_{d1} \rangle$ value increases with the degree of disorder and it is maximum for completely random systems.

The treatment procedure is able to characterize regular/non regular behaviour existing in experimental data to identify the transition between regions with these two primary behaviours in objective bases. The SW time interval is separated into three new time intervals (windows) corresponding to the preceding sheath or pre-MC, the MC itself, and the SW after the MC or post-MC.

The criterion to select a precise data window after the MC is empirical. Each post-MC region was selected with the same length of the cloud regions. The main effort is to study SW data interval containing the ICMEs, where a shock event and a cloud region were reported. Arbitrary

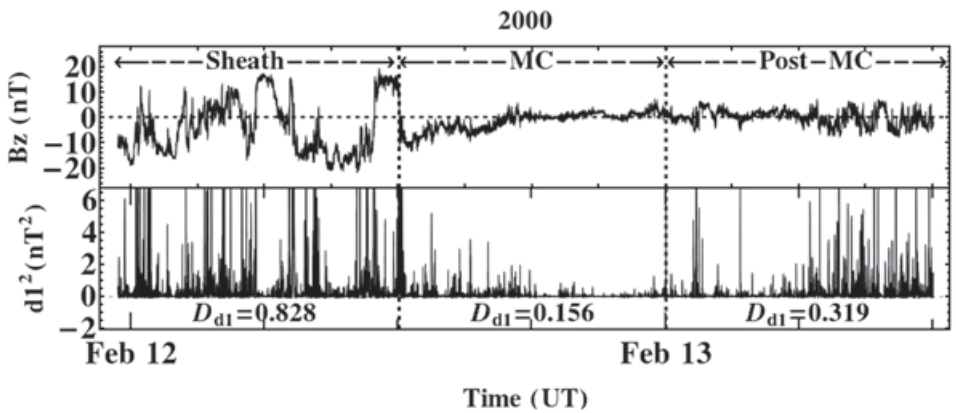

Figure 1. At the top, IMF B_z (in GSM system) versus time from the ACE spacecraft with 16s time resolution, at February 11; 23:23 UT-February 13; 12:00 UT; 2000. At the bottom, the square of the first decomposition level of wavelet coefficient $d1^2$ versus time for the sheath region (left of the first vertical dashed line), the MC (middle between the vertical dashed lines), and the quiet SW (right of the second vertical dashed line). The lower values of D_{d1} are noticed inside of MC region.

selection of post-MC region could affect the results, because this region could be disturbed by other processes unrelated with the MC itself. Thus, the physics of the system should not be changed in the proposed methodology. Further analyses of complicated events can indeed help to understand the true processes occurring in the interplanetary medium. In an evident way, showing the behaviour in the different regions is valuable because only then will be possible to justify that wavelet coefficients may help to find boundaries. A zoom in treatment in the fluctuations from variables with random variations (i.e., IMF) could help to separate disturbance processes, e.g., MC-candidate event inside of an ICME. Our hypothesis is that wavelet coefficients help to identify boundaries in the SW data, specifically the shock waves and the leading edge of ICMEs.

Results and Discussion

We present two case studies based on the analysis of Huttunen *et al*. (2005), where we have applied this methodology to analyse MC periods (events 14 and 16, Table 1). The study is extended to a total of 41 cases shown in the table, although the results are not presented individually here. In this section, a discussion is done to reach an interpretation.

February 11-13, 2000 ICME event

In Figure 1, at the top, we show the time series of IMF B_z component measured by the ACE spacecraft at the date February 11; 23:23 UT-February 13; 12:00 UT; 2000. The data was measured in GSM coordinate system with resolution time of 16s. The three regions under study are separated by two vertical dashed lines. At the bottom, we show the square of the first decomposition level of wavelet coefficients, $\mathrm{d}1$, and results of D_{d1}. The mean of wavelet coefficient D_{d1} in time series at plasma sheath is 0.828 nT^2. The result is that the lower D_{d1} (0.156 nT^2) corresponds to the MC.

Table 5. Mean D_{d1} of wavelet coefficients.

Events	$D_{d1}B_x$	$D_{d1}B_y$	$D_{d1}B_z$	$\langle D_{d1}\rangle$
Feb 11-13, 2000				
Sheath	0.524	0.814	0.828	0.722
MC	0.093	0.124	0.156	0.124
Post-MC	0.177	0.247	0.319	0.248
Jul 11-14, 2000				
Sheath	0.279	0.270	0.625	0.391
MC	0.016	0.032	0.042	0.030
Post-MC	0.233	0.230	0.458	0.307

In Table 5, the results of D_{d1} for the three components of $\vec{B}$ are presented. Seen in the figure, the MC regions in the three components always have the lowest D_{d1} value. While the higher D_{d1} values in all components correspond to the sheath region.

As a previously known feature, the larger amplitude of the wavelet coefficients, $\mathrm{d}1$, are indeed associated with abrupt signal locally. From a visual inspection of data, detections may not be an easy task; but the wavelet transforms aids to find those kinds of phenomena.

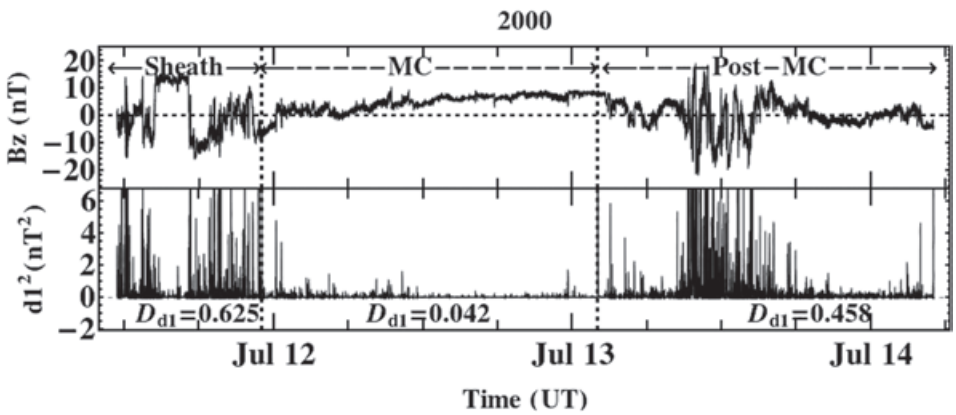

Figure 2. (At top, IMF B_z (in GSM system) versus time from the ACE spacecraft with 16s time resolution, at July 11; 11:22 UT-July 14; 05:00 UT; 2000. At bottom, the square of the first decomposition level of wavelet coefficient $d1^2$ versus time for the sheath region (left of the first vertical dashed line), the MC (middle between the vertical dashed lines), and the quiet SW (right of the second vertical dashed line). The high amplitude of $d1^2$ inside the third region (Post-MC) is because other event arrived. The lower values of D_{d1} is noticed inside of MC region.

July 11-14, 2000 ICME event

In Figure 2, a similar study is done. At the top, we show the time series of IMF B_z component measured by ACE spacecraft at the date July 11; 11:22 UT-July 14; 05:00 UT; 2000. The three regions under study are separated by two vertical dashed lines. At the bottom, the square of first decomposition level of wavelet coefficient versus time is plotted.

The statistical mean of the wavelet coefficient D_{d1} in the sheath region is 0.625 nT^2. Again the lower D_{d1} (0.042 nT^2) corresponds to the MC region; and the higher D_{d1} (0.625 nT^2) corresponds to the sheath region. The highest amplitude of $d1^2$ inside the third region (Post-MC) is due to the arrival of other event (event 17 in Table 1).

Related to this case, the results of D_{d1} for the three components of $\vec{B}$ are presented in Table 5. Also seen in the earlier figure, the MC region in the three components always has the lowest D_{d1} value. While the highest D_{d1} value in all components correspond to the sheath region.

The tendency of the MC events to have lower values of D_{d1} in comparison with the processes of the other regions. This feature is clearly identified by using this approach, which can be added to the usual features (Burlaga *et al*., 1981) established earlier for the MCs. Also, we found higher D_{d1} values in the sheath. The higher amplitudes values of the wavelet coefficients indicate singularity patterns which are identified in the sheath region (see top panel on Figures 1 and 2).

41 ICMEs events

Aiming to a conclusive analysis, the calculations D_{d1} for the three IMF components are done for the other cases of Table 1. The procedure is identical to the one used in the previous studies.

In Figure 3, the $\langle D_{d1} \rangle$ values versus number of events were plotted respectively as squares, cross-circles symbols, and triangles symbols, correspond respectively to the sheath, MC and Post-MC regions. We can compare the $\langle D_{d1} \rangle$ values of the three regions for every event. The $\langle D_{d1} \rangle$ values are higher in the sheath region in 35/41 or 85.4% events. This does not occur in the events numbered as 4; 5; 6; 13; 24; 34 in Table 1, where the highest values are found in the "Post-MC" regions. The explanation is that Post-MCs as shown in Figure 2, there may be an arrival of a shock or an ICMEs. However, the magnetic field fluctuation in the sheath is always greater than one in the cloud that follows. In particular, the magnetic field fluctuation in some MC regions (events numbered as 9; 19; 17; 20; 21; 31; 41) is greater than one in the SW that follows. We can learn that fluctuations are not low in all MCs, in some cases waves can penetrate from the sheath to the cloud. In this paper, the goal is to test the usefulness of this wavelet technique to study fluctuations in the SW data in order to explore any intrinsic physical process.

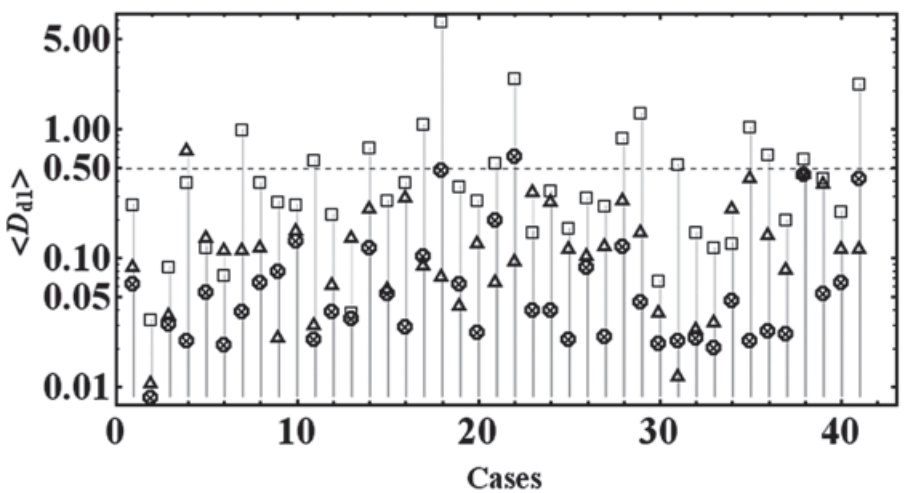

Figure 3. The $\langle D_{d1} \rangle$ values versus number of events were plotted respectively as squares, cross circles symbols, and triangles symbols, correspond to the sheath, MC and Post-MC regions. The y axis is plot with a logarithmic scale, because is best to visualization.

Figure 4 shows a histogram constructed from the occurrence frequencies of the $\langle D_{d1} \rangle$ values. The $\langle D_{d1} \rangle$ values for the sheath, MC and Post-MC regions are plotted respectively as grey, black, and white bins. In this figure, 63.4% of the MCs are located in the first two sets of bars on the left, while there are 4.9% and 24.4% of the sheaths and Post-MC regions respectively. The wavelet coefficients are low in some sheath regions. This means that if an ICME is not moving faster than the surrounding SW (Klein and Burlaga, 1982; Zhang and Burlaga, 1988; Burlaga, 1988), the sheath region does not present a very corrugated feature in the magnetic field. In principle, the identification by visual inspection could be more difficult to be done under these conditions. Conversely, in the last four sets of bars we have 75.6% of the sheaths and only 12.2% of the MCs regions. The results presented in the two previous case studies are confirmed: the largest amplitudes of the magnetic field fluctuations are in the sheath, and the lowest ones are during the MC. However, we do not have well defined $\langle D_{d1} \rangle$ values to identify the three different regions. Figure 4 only allows the comparison between values from the three regions in the same event. We can conclude that there is not a well-defined fluctuations pattern inside of MCs. The fluctuations could depend on the SW in the environment where the MC is expanding.

Figure 4 shows that due to the overlapping observed between the three distributions, this technique could not be used to identify boundaries automatically. It provides an objective analysis technique that helps in reducing the effort to find the boundaries inside of ICME, fundamentally the cloud boundaries. This technique could be useful to help a specialist to find boundaries when working with IMF dataset.

As in Table 5, the higher D_{d1} values are found in B_z component for every region. By direct visual inspection, most of the time, this detection is not possible. However, the wavelet transform enables finding this phenomenon easily. The B_z component is very important in the magnetic reconnection at Earth's magnetopause. An open question could be asked: how important are the fluctuations for the geoeffectiveness? We think that this is an important example of application of this technique in order to evaluate the SW fluctuations. Also, the wavelet coefficients can help to obtain a better visualization of the shock and to identify the initial border of the MC.

The wavelet coefficients recover the expected behaviours of the physical processes underlying in the magnetic records. This is understandable, because the MC has a geometric structure in form of flux-rope, unlike the sheath region and the "quiet" SW. The sheath is naturally a turbulent region, presenting many fluctuations in the IMF data with large D_{d1} values. A smoother magnetic field is the cause of the low values of D_{d1} in the MCs regions. The existence of MCs with large values of the wavelet coefficients was unexpected result in this study. We have found five MCs with this feature, and further they will deserve specific studies. The SW after the MC can present an extended quiet behaviour, or an increasing of random characteristics, or even turbulences from an arrival event (for the latter, e.g., the events 16 and 20). Sometimes, the Post-MC region has a large $\langle D_{d1} \rangle$ value due to the existence of a reverse shock.

If this technique is applied to a large dataset of SW IMF, the wavelet coefficients could be also large in other regions in which there are no ICMEs. On other hand, the wavelet coefficients are relatively lower in quiet SW regions. Although it does not allow identifying

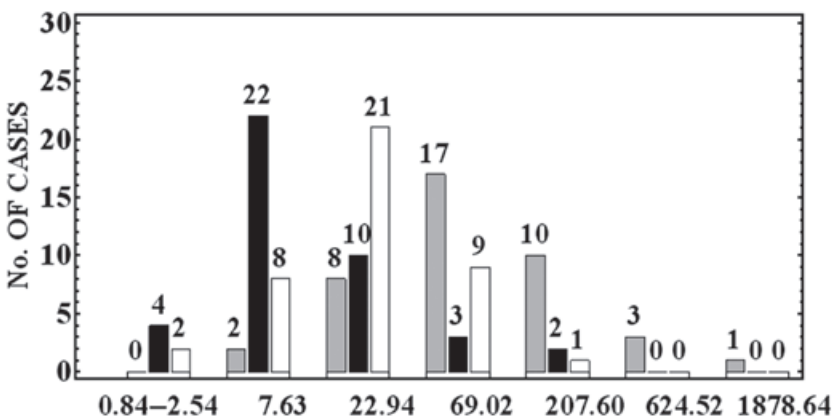

Figure 4. A histogram is constructed from a frequency table of $\langle D_{d1} \rangle$ values; the abscissa axis was normalized by 0.01. The $\langle D_{d1} \rangle$ values for the sheath, MC and post MC, the three select regions, plotted as the grey, black and white.

clouds automatically, it is an useful tool for experts. Because, this technique can be used as auxiliary tools to find cloud boundaries, when, for example, the minimum variance analysis (MVA) is used. In fact, we have used for this purpose. In our opinion, the presentation of this tool for the Space Physics Community could "open doors" for other applications. For example, we believe that it might be useful to study Alfvén waves, where fluctuations in the SW with different pseudo-frequencies can be investigated.

Application to identify the shock and leader edge of ICME

The formation of a sheath implied in the existence of a shock waves. If we cannot find a shock then the sheath is not defined. However, if the MC is moving at the same speed as the ambient SW but still expanding, it will disturb both the SW ahead and behind, creating sheath-like structures (though they may not be bounded by a shock front). This study considers the events of MCs not associated with evident shock waves, presented in Table 3 (see event 3). With illustrative purpose, a case study is presented for the date June 24; 12:00 UT-June 25; 16:00 UT; 1998. The criteria to select the data interval after the MC are the same used previously. The duration time in regions at 41 sheaths is less than one day, and then a region with this equivalent duration from the initial time of the cloud is chosen.

In Figure 5, the above interval at the date June 23; 12:00 UT-June 26; 16:00 UT; 1998 is shown. Each panel presents respectively, from top to bottom, B_x, B_y and B_z time series respectively. At the bottom of the respective panels, the square of the first decomposition level of wavelet coefficients, d1, versus time is plotted. The two vertical dashed lines correspond to the MC region delimitations identified by Huttunen *et al*. (2005). The wavelet coefficients allow for a zoom in on the fluctuations of magnetic components. As larger amplitudes in the wavelet coefficients are observed inside the initial border of MC, then we think that this boundary should be redefined. So, the leader edge at date June 24; 16:32 UT 1998 is redefined. The second vertical thick line corresponds to the previous data.

Also, wavelet coefficients could be used to identify sheath like structures. However, the confirmation on the type of electrodynamical discontinuity implies the use of plasma data. So, a probable discontinuity at date June 24; 04:00 UT 1998 was identified. Thus, with the help of SW plasma parameters, an interplanetary sheath-like structure can be associated to this event. The first vertical thick line corresponds to the start of its location.

In Figure 5 (all panels), the D_{d1} values in each regions are shown. We found higher D_{d1} values in the sheath-like structures while the lower values correspond to cloud region. The results related to this part are consistent with the earlier results.

In conclusion, this methodology has a practical application. Maybe other applications for Space Physics Community uses will be found, mainly taking into account fluctuations that occur in several frequency ranges.

Conclusions

We deal with time series of SW for a group of magnetic clouds in order to analyse the fluctuations of the IMF B_x, B_y and B_z components. The mathematical property chosen here was the statistical mean of the wavelet coefficients ($\langle D_{d1} \rangle$) which was obtained by applying the discrete orthogonal wavelet transform using Daubechies wavelet of order two (i.e. Daubechies scale filters order 2, db2) to the components of the IMF as recorded by the instruments of the MAG on-board of the ACE S/C at the L1 point.

The main point in the use of the amplitude of the Daubechies wavelet coefficients is that they represent the local regularity present in the signal in study (Mallat, 1989). They were constructed to express the local approximation error between a certain local polynomial reproduction and the signal itself. This is used to identify local regularity in high order derivatives in the analysed signal. The local regularity changes can be therefore highlighted by means of the amplitude wavelet coefficients. It is not easy or even possible to see discontinuities in high order derivatives that cause disturbances by visual inspection of the signal. For instance, using Daubechies wavelet of order 2, discontinuities higher than the first derivatives can be detected and measured, respectively. We use that propriety of local regularity identification to highlight possible regions of regularity on the magnetic field at three different regions around an ICME event measure at IMF datasets. The results show that there is, apparently, a clear distinction between the values of the wavelet coefficients obtained along the different parts of the passing magnetic structure (ahead of the MC, i.e., the sheath; the MC itself; and after the passage of the MC (Post-MC)). The measurements show that $\langle D_{d1} \rangle$ exhibits the lower values during the passage of the MC. Also, we found higher values in the sheaths.

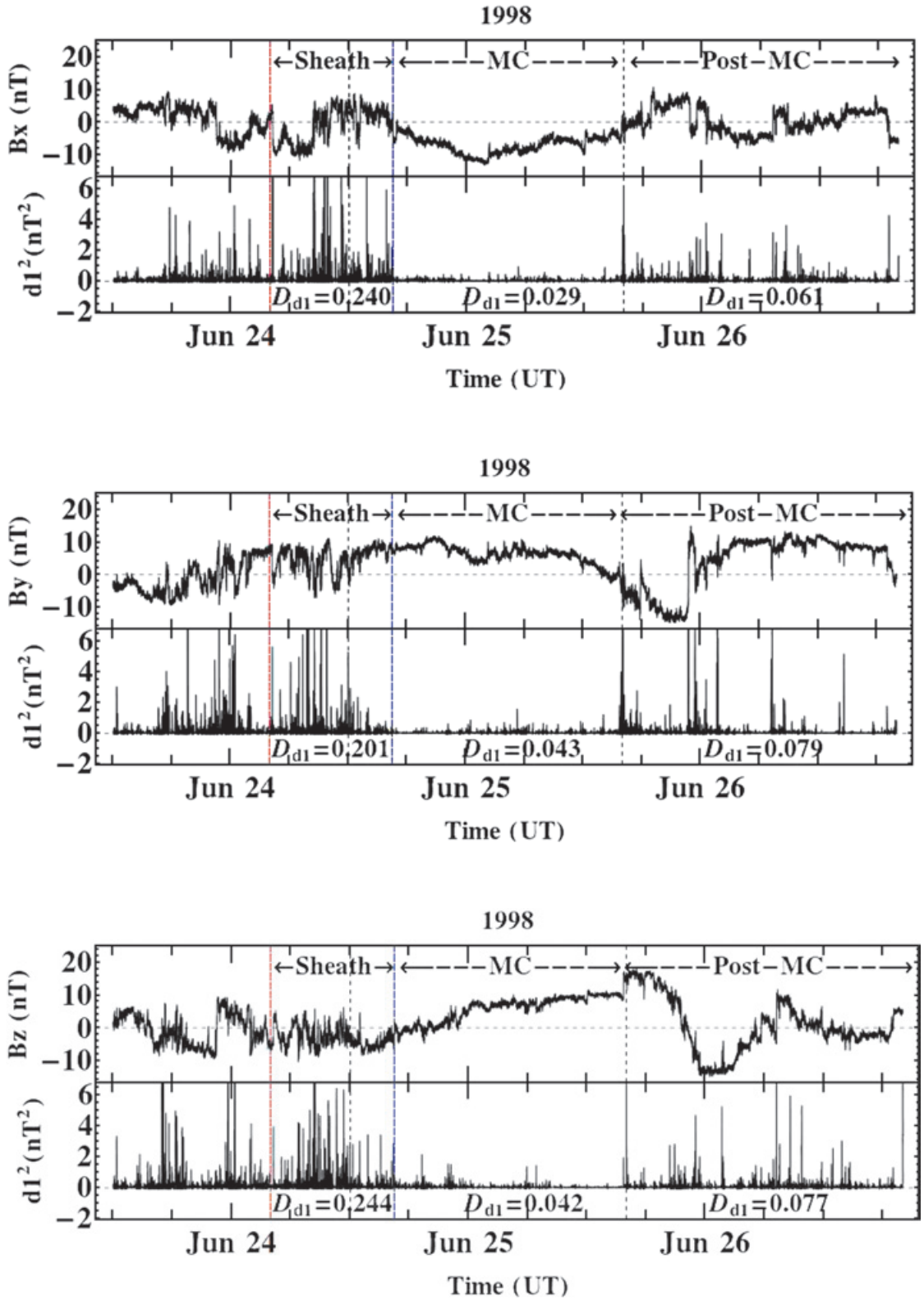

Figure 5. (top the panel) At top, IMF B_x (in GSM system) versus time from the ACE spacecraft with 16 s time resolution, at date June 23; 12:00 UT-June 26; 16:00 UT; 1998; at bottom, the square of the first decomposition level of wavelet coefficient $d1^2$ versus time. Also, the other two components must be analysed, as is shown in the middle and bottom panels.

Using assumptions that concern the physics of MC, the analyses developed in this work show that a smoothed magnetic configuration (i.e., few magnetic fluctuations) in MC is the main reason of the lower values of wavelet coefficients during it. This study has been performed only for specific types of ICMEs, all of which were structures that appeared to be MCs. This tool allows for the comparison of the existing fluctuation of SW magnetic field, i.e., B_x, B_y and B_z, which it is not an easy task under simple visual inspection. The B_x component has lower fluctuations, or singularities, and the B_z component the higher ones.

We can identify the effect of shock waves in the change of the local regularity of the IMF component using its $d1^2$ time series, shows that the amplitude of the wavelet coefficients decreases at transient regions in MC boundaries identified by other authors. Therefore, the behaviour expected inside of MCs is the decrease of entropy and variance respectively, and then the fluctuations should be lower than outside them. The previous behaviour is not true for all the cases because some another phenomenon could also be present. However, in this study this was verified for 32/41 or 78% of the cases. We can learn that fluctuations are not low in all magnetic clouds, in some cases waves can penetrate from the sheath to the cloud. The fluctuations could depend on the solar wind in the environment where the cloud is expanding.

This is an objective analysis technique provided to find the boundaries of magnetic clouds related to ICMEs. The procedure identifies transitions in the IMF regularity for different regions existing in the solar wind, which highlight cloud regions. It can be very useful for specialists, because the wavelet coefficients have the advantage to find some discontinuities (transients) that are not easy to be seen in the IMF data by simple visual inspection.

By now, only assumptions for proper MCs were validated. Maybe this methodology could be extended to identify features of some other specific fluctuation patterns in the IMF, such as CIR, heliospheric current sheath crossings or ICMEs without MC signatures which has not yet been done.. Such an approach aiming at new facilities for the Space Physics community efforts seem to be an important contribution.

Acknowledgments

This work was supported by grants from CNPq (grants 483226 /2011-4, 307511 /2010-3, 306828 /2010-3 and 486165 /2006-0), FAPESP (grants 2012 /072812-2, and 2007 /07723-7) and CAPES (grants 1236-83 /2012 and 86 /2010-29). A.O.G. thanks the CAPES and CNPq (grant 141549/2010-6) for his PhD scholarship and CNPq (grant 150595/2013-1) for his postdoctoral research support. V. E. Menconi thanks to the grants FAPESP 2008/09736-1, CNPq 3124862012-0 and 455097/2013-5. We also wish to thank the anonymous referees for improvement of this paper.

Appendix A. The wavelet coefficients in a discontinuous function.

The local regularity changes can be therefore highlighted by means of the amplitude wavelet coefficients. Using the signal presented in (Daubechies, 1992, p.301), we constructed the following example to illustrate the propriety.

Considering,

$$f(x)=\begin{cases} 2e^{-|x|} & if \quad x\le -1, \\ e^{-|x|} & if \quad -1<x\le 1 \\ e^{-x}[(x-1)^2+1] & if \quad x\ge 1; \end{cases},$$

This function is continuous except in x = -1, the first derivative of it is discontinuous at that point and in the point x = 0 and the second derivative is discontinuous at these

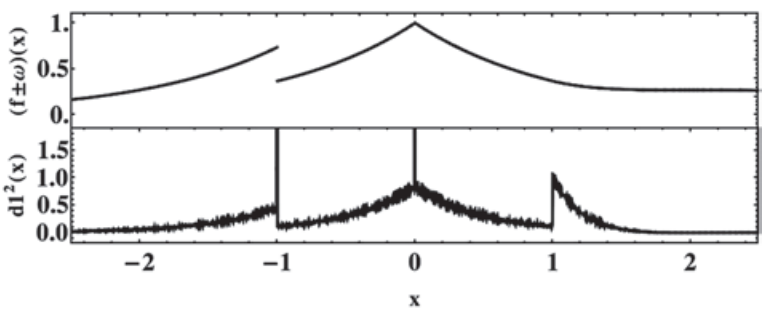

Figure A.6. At top, the signal $f(x)\pm\omega(x)$ versus x was plotted, where $\omega(x)$ is a white noise. At the bottom, the square of the first decomposition level of wavelet coefficients $d1^2(x)/10^{-12}$ versus x was plotted.

points. We compute one decomposition level of discrete orthogonal wavelet transform using a Daubechies wavelet of order 2. The result is presented in the Figure A.6, the larger amplitude of the wavelet coefficients, identifies the three points where the signal has changes in the local regularity.

Bibliography

Abry P., 1997, Multirésolutions, algorithmes de décomposition, invariance d'échelles, diderot Edition. Ondelettes et turbulence. Paris.

Borovsky, J.E., 2012, The velocity and magnetic field fluctuations of the solar wind at 1 AU: Statistical analysis of Fourier spectra and correlations with plasma properties. *Journal of Geophysical Research,* 117, A5.

Bothmer, V., Schwenn, R., 1998, The structure and origin of magnetic clouds in the solar wind. Annales Geophysicae 16, 1–24, 10.1007/s00585-997-0001- x.

Burlaga, L., 1988, Magnetic clouds and force-free fields with constant alpha. J*ournal of Geophysical Research*, 93, 7217.

Burlaga, L., Behannon K., 1982, Magnetic clouds: Voyager observations between 2 and 4 AU. *Solar Physics*, 81, 181.

Burlaga L.F., 1995, Interplanetary Magnetohydrodynamics. Oxford Univ. Press, New York.

Burlaga, L. F., Sittler, E., Mariani, F., Schwenn, R., 1981, Magnetic loop behind an interplanetary shock: Voyager, Helios and IMP 8 observations. *Journal of Geophysical Research*, 86, 6673–6684.

Celletti A., Giorgilli A., 1990, On the stability of the lagrangian points in the spatial restricted problem of three bodies. *Celestial Mechanics and Dynamical Astronomy*, 50, 1, 31–58.

Dal Lago A., Gonzalez W., Gonzalez A., Tsurutani B.T., 2000, Magnetic field and plasma parameters for magnetic clouds in the interplanetary medium. *Geofísica Internacional*, 39, 1, 139–142.

Dal Lago A., Gonzalez W.D., Gonzalez A., Vieira L.E.A., 2001, Compression of magnetic clouds in interplanetary space and increase in their geoeffectiveness. *Journal of Atmospheric and Solar-Terrestrial Physics*, 63, 451–455.

Dasso S., Mandrini C., Démoulin P., Luoni M., Gulisano A., 2005, Large scale MHD properties of interplanetary magnetic clouds. *Advances in Space Research*, 35, 711–724.

Daubechies I., 1992, Ten lectures on wavelets. Society for Industrial and Applied Mathematics, Philadelphia, PA, USA.

Démoulin P., Dasso S., 2009, Causes and consequences of magnetic cloud expansion. *Astronomy and Astrophysics*, 498, 2, 551–566.

Domingues M.O., Mendes O., Mendes da Costa A., 2005, Wavelet techniques in atmospheric sciences. Advances in Space Research, 35 5, 831– 842.

Echer E., Alves M., Gonzalez W., 2005, A statistical study of magnetic cloud parameters and geoeffectiveness. Journal of Atmospheric and Solar- Terrestrial Physics 67, 10, 839–852.

Farrugia C.J., Osherovich V.A., Burlaga L., 1995, Magnetic Flux Rope Versus the Spheromak as Models for Interplanetary Magnetic Clouds. *Journal of Geophysical Research*, 100, A7, 12293–12306.

Gonzalez W.D., Tsurutani B.T., 1987, Criteria of interplanetary parameters causing intense magnetic storms (Dst<-100nT). *Planetary and Space Science*, 35, 9, 1101–1109.

Gosling J., 1990, Coronal mass ejections and magnetic flux ropes in interplanetary space. In: Russel, C. T., Priest, E. R., Lee, L. C. (Eds.), Physics of Magnetic Flux Ropes. AGU Geophys. Monogr., p. 343.

Gosling J., 1998, Overexpanding coronal mass ejections at high heliographic latitudes: Observations and simulations. *Journal of Geophysical Research*, 103, A2, 1941–1954.

Holschneider M., 1991, Inverse Radon transforms through inverse wavelet transforms. Inverse Problems 7, 6, 853.

Hubbard B.B., 1997, The World According to Wavelets: The Story of a Mathematical Technique in the Making. A K Peters Ltd.

Huttunen K.E.J., Schwenn R., Bothmer V., Koskinen H.E.J., 2005, Properties and geoeffectiveness of magnetic clouds in the rising, maximum and early declining phases of solar cycle 23. Annales Geophysicae, 23, 625– 641.

Kim H.-J., Lyons L., Boudouridis A., Lee D.-Y., Heinselman C., Mc-Cready M., 2009, Evidence that solar wind fluctuations substantially affect the strength of dayside ionospheric convection. *Journal of Geophysical Research*, 114, A11305, 14.

Klein L.W., Burlaga L.F., 1982, Interplanetary magnetic clouds at 1 AU. *Journal of Geophysical Research*, 87, 613–624.

Lepping, R., Burlaga, L., Szabo, A., Ogilvie, K., Mish, W., 1997. The Wind magnetic cloud and events October 18-20, 1995: interplanetary properties and as triggers for geomagnetic activity. *Journal of Geophysical Research*, 102, A7, 14, 049–14,063.

Lepping R.P., Berdichevsky D., Pandalai S.G., 2000, Interplanetary magnetic clouds: Sources, properties, modeling, and geomagnetic relationship. *Recent research developments in geophysics*, 77–96 Eng.

Lepping R.P., Jones J.A., Burlaga L.F., 1990, Interplanetary magnetic clouds at 1 AU. *Journal of Geophysical Research*, 95, 11957.

Lundquist S., 1950, Magnetohydrostatic fields. *Ark Fys*, 2, 361–365.

Lyons L., Kim H.-J., Xing X., Zou S., Lee D.-Y., Heinselman C., Nicolls M., Angelopoulos V., Larson D., McFadden J., Runov A., Fornacon K.- H., 2009, Evidence that solar wind fluctuations substantially affect global convection and substorm occurrence. *Journal of Geophysical Research*, A11306, 14.

Mallat S.G., 1989, Multiresolution Approximations and wavelet orthonormal bases of L2, R, 315, 1, 69–87.

Mendes O.J., Domingues M.O., Mendes da Costa A., 2005, Wavelet analysis applied to magnetograms. *Journal of Atmospheric and Solar-Terrestrial Physics*, 67, 1827–1836.

Mendes da Costa A., Oliveira Domingues M., Mendes O., Marques B., Christiano G., 2011, Interplanetary medium condition effects in the south Atlantic magnetic anomaly: A case study. *Journal of Atmospheric and Solar-Terrestrial Physics*, 73, 11-12, 1478–1491.

Narock T.W., Lepping R.P., 2007, Anisotropy of magnetic field fluctuations in an average interplanetary magnetic cloud at 1 AU. *Journal of Geophysical Research*, 112, A06108, 6.

Ojeda G.A., Calzadilla M.A., Lazo B., Alazo K., Savio O., 2005, Analysis of behavior of solar wind parameters under different IMF conditions using nonlinear dynamics techniques. Journal of Atmospheric and Solar- Terrestrial Physics, 67, 17-18, 1859–1864.

Ojeda G.A., Mendes O., Calzadilla M.A., Domingues M.O., 2013, Spatio-temporal entropy analysis of the magnetic field to help magnetic cloud characterization, *J. Geophys. Res. Space Physics*, 118, 5403-5414, doi:10.1002/jgra.50504.

Osherovich V., Burlaga L.F., 1997, Magnetic Clouds. In: Crooker, N., Joselyn, J., Feynman, J. (Eds.), Coronal Mass Ejection. Vol. 99. AGU,Washington, D. C., p. 157.

Siscoe G., Odstrcil D., 2008, Ways in which ICME sheaths differ from magnetosheaths. *Journal of Geophysical Research*, 113 A00B07, 1–10.

Smith C.W., L'Heureux J., Ness N.F., Acuña M.H., Burlaga L.F., Scheifele J., 1998, The ACE Magnetic Fields Experiment. *Space Science*, 86, 613–632.

Tsurutani B.T., Gonzalez W.D., 1992, Great magnetic storms. *Geophysical Research Letters*, 19, 1, 73–76.

Tsurutani B.T., Gonzalez W.D., Tang F., Akasofu S.I., Smith E.J., 1988, Origin of Interplanetary Southward Magnetic Fields Responsible for Major Magnetic Storms Near Solar Maximum (1978-1979). *Journal of Geophysical Research*, 93, 8519–8531.

Wu C.-C., Lepping R.P., 2002a, Effect of solar wind velocity on magnetic cloud-associated magnetic storm intensity. *Journal of Geophysical Research*, 107, A11, 1346–1350.

Wu C.-C., Lepping R.P., 2002b, Effects of magnetic clouds on the occurrence of geomagnetic storms: The first 4 years of Wind. J*ournal of Geophysical Research*, 107 A10, 1314–1322.

Zhang G., Burlaga L.F., 1988, Magnetic clouds, geomagnetic disturbances and cosmic ray decreases. *Journal of Geophysical Research*, 88, 2511.

Geofísica Internacional (2014) 53-2: 117-133

Original paper

Morphologic analysis of the temporal change of forest cover

Jorge Lira

Received: November 22, 2012; accepted: July 25, 2013; published on line: April 01, 2014

Resumen

En este trabajo se presenta un análisis morfológico de cobertura forestal en un lapso de doce años. Se emplearon dos imágenes multiespectrales LANDSAT TM-4 de los años 1989 y 2001. Estas imágenes cubren un área forestal donde han ocurrido cambios significativos en tales años. Estas imágenes fueron expandidas en términos de variables canónicas que describen la respuesta espacial-espectral de las masas forestales. Las imágenes fueron modeladas como un campo vectorial de tantas dimensiones como bandas empleadas en el análisis. Se construyó un campo vectorial usando las bandas de variables canónicas.El conjunto de variables canónicas fue usado para cuantificar el cambio vectorial de las masas forestales. Este cambio vectorial cuantifica el grado de alteración de las masas forestales. Se empleó un algoritmo de crecimiento de regiones para segmentar las áreas ocupadas por el bosque. Este algoritmo emplea como entrada las variables canónicas. El resultado de tal segmentación es una imagen binaria llamada el bitmap. A partir de este bitmap, se llevó a cabo un análisis morfológico del área ocupada por el bosque. Se empleó un DEM generado a partir de un par interferométrico del satélite RADARSAT-1 para realizar una referencia cruzada con los bitmaps. Esta referencia cruzada conduce a la determinación de las elevaciones a las cuales ocurren los cambios de las masas forestales.

Palabras clave: cobertura forestal, variables canónicas, morfología, crecimiento de regiones.

Abstract

A morphologic analysis of forest cover in a time span of twelve years is presented in this work. Two multispectral LANDSAT TM-4 images of the years 1989 and 2001 were used. These images cover a forest area where significant changes have occurred in such years. These images were expanded in terms of canonical-expansion variables that describe the spatial-spectral response of the forest masses. The images were modeled as a vector field of as many dimensions as the number of bands employed in the analysis. A vector field was constructed using canonical-variable bands. The set of canonical variables for each year was used to quantify a vector change of the forest masses. This vector change quantifies the degree of alteration of the forest masses. A region-growth algorithm was used to segment the areas occupied by the forest. This algorithm uses as input the canonical variables. The result of such segmentation is a binary image named the bitmap. From this bitmap, a morphologic analysis of the area occupied by the forest was undertaken. A DEM generated from a radar interferometric pair of the RADARSAT 1 satellite, was used to perform a cross-reference with the bitmaps. This cross-reference leads to the derivation of the elevation of occurrence of changes in the forest masses.

Key words: forest cover, canonical variables, morphology, region growing.

J. Lira
Instituto de Geofísica
Universidad Nacional Autónoma de México
Ciudad Universitaria
Delegación Coyoacán, 04510
México D.F., México
Corresponding author: jlira@geofisica.unam.mx

Introduction

The analysis of vector change is used in this work to quantify the change of forest cover in the environs of Mexico City. The vector change is combined with morphologic analysis to derive quantitative evolution of the forest cover. A number of methods of vector change have been published in the literature (Allen and Kupfer, 2000; Fraser *et al*., 2005; Nackaerts *et al*., 2005; Sanchez Flores and Yool, 2007).

A number of change indices have been used to quantify change of temporal phenomena such as deforestation, desertification, urban growth or land cover change (Johnson and Kasischke, 1998; Le Hégarat-Mascle and Seltz, 2004; Cakir *et al*, 2006). A detailed account of change detection methods is given in Coppin *et al*. (2004). Several methods of change detection in remote sensing are given in Canty (2007). Recent advances in tropical forest cover used parametric classification and change vector analysis to detect unchanged and changed areas in the tropical forest of Amazonia (Raši *et al*., 2013).

In the present work, a multispectral image is modeled as a vector field of as many dimensions as bands employed in the analysis (Lira and Rodriguez, 2006; Lira, 2010). In this model, a pixel is defined as a vector of an equal number of elements as the number of bands. Two LANDSAT TM-4 images are used in this model to obtain the change of forest cover in a time span of twelve years. A co-registration of the images was applied in order to implement our method and to evaluate the forest cover change in the time span.

In the present research, the vector change that experiences the vector field associated to the image was considered (Lambin and Strahler, 1994; Warner, 2005; Sanchez and Yool, 2007; Kontoes, 2008). A set of variables were calculated from a canonical-expansion of the image (Lira and Garcia, 2003). This expansion produces three basic canonical variables that characterize the spatial-spectral state of the forest cover. The use of variables to study land cover change, as a basis for change vector analysis, has been proposed (Lambin and Strahler, 1994; Lambin and Ehrlich, 1997). The original Landsat bands define a 6-dimensional vector field. Instead, the canonical variables define a 3-dimensional vector field.

The set of variables were used in a region-growth algorithm to segment the forest cover. This segmentation produced a two-class image named the bitmap. The bitmap depicts the area of the forest cover and the rest of the image. From the bitmaps of the images, morphologic change was evaluated. A digital elevation model (DEM) was constructed using an interferometric pair of the RADARSAT 1 satellite. The DEM was combined with the bitmaps to derive conclusions on morphologic change of forest cover.

In the present work, one vector field was considered: the vector field formed by the canonical variables. Principal component analysis (PCA) was applied to the set of variables of both images. From PCA, changes of the vector field were assessed. The analysis of vector change based on PCA is used there upon and conclusions on the forest cover change were derived. In the ensuing section of methods, details are provided on the vector field analysis.

Materials and methods

Materials

Two multi-spectral LANDSAT TM-4 images are used in this research. From these images, an area was extracted; the resulting sub-images are dubbed 1989 and 2001. Figure 1 depicts a false color composite of the images of 1989 and 2001. Table 1 shows basic technical details of these images. With the exception of band 6, all the bands of the images were used in our research analysis. Band 6 is not included in the analysis due to a different pixel size.

These images cover an area located to the east of Mexico City where a forest mass surrounds two volcanoes. This forest mass is formed by a mixture of coniferous trees, namely pine, oyamel and cedar (Hernandez García and Granados Sánchez, 2006). From March 1989 to January 2001, this forest mass has experienced a change in extension, morphology and heterogeneity (Rzedowski and Rzedowski. 2005; Hernandez García and Granados Sánchez, 2006). This forest masses will be referred in this research as forest cover. In addition to the LANDSAT TM-4 images, an interferometric pair from the RADARSAT 1 satellite was considered (Table 2). From this interferometric pair, a digital elevation model (DEM) was extracted.

The LANDSAT TM-4 images were geometrically corrected and corregistered using the ephemerides of the orbit. On the generation of the DEM from the RADARSAT 1, ground control points were used to corregister

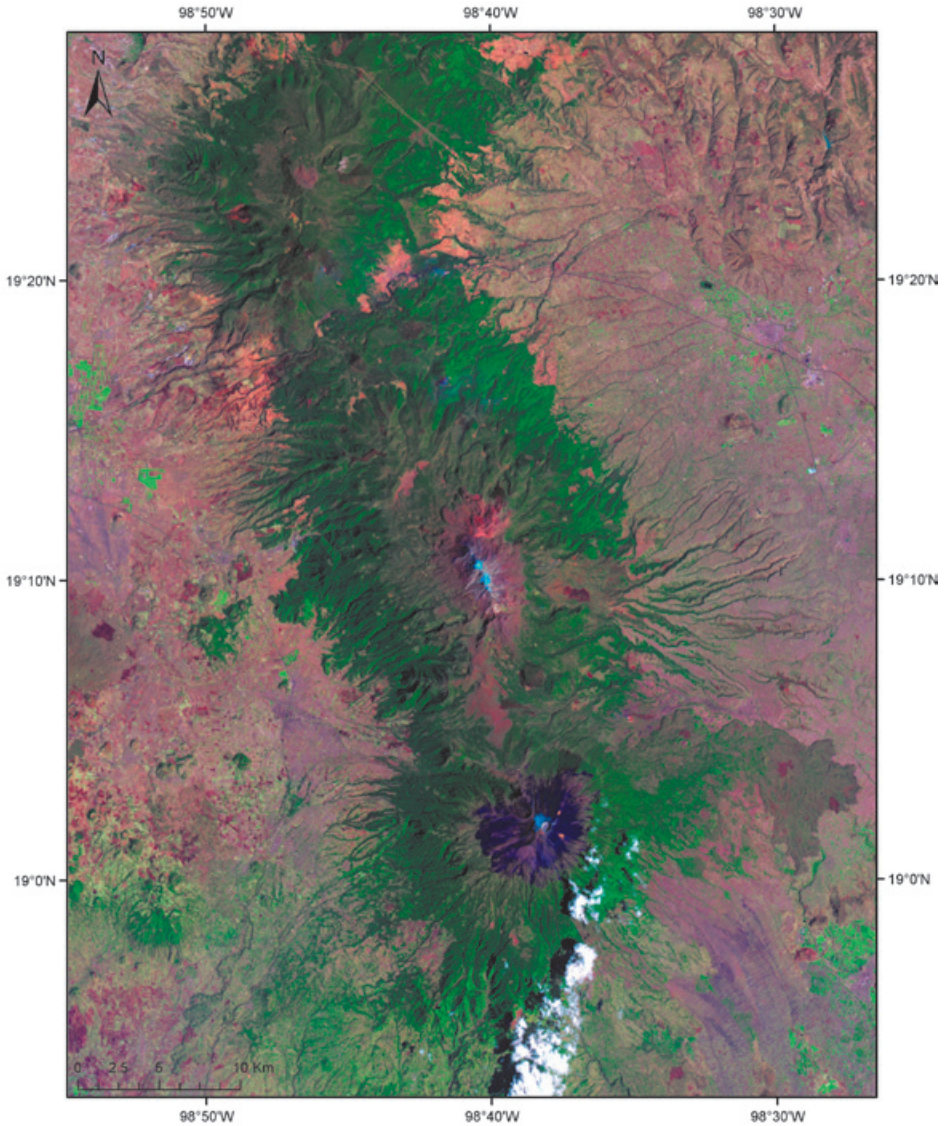

Figure 1. RGB = [7,4,1] of the images of 1989 (a) and 2001 (b).

Table 1. Basic technical details of multi-spectral Landsat TM-4 images.

Image	Date	Path/Row	Pixel (m^2)	Dimension (pixels)	Bands (μm)
1989	March 7, 1989	26/47	28.5 × 28.5	1904 × 2380	1) 0.45-0.52 2) 0.52-0.60 3) 0.63-0.69 4) 0.76-0.90 5) 1.55-1.75 6) 10.4-12.5 7) 2.08-2.35
2001	January 4, 2001	26/47	28.5 × 28.5	1904 × 2380	1) 0.45-0.52 2) 0.52-0.60 3) 0.63-0.69 4) 0.76-0.90 5) 1.55-1.75 6) 10.4-12.5 7) 2.08-2.35

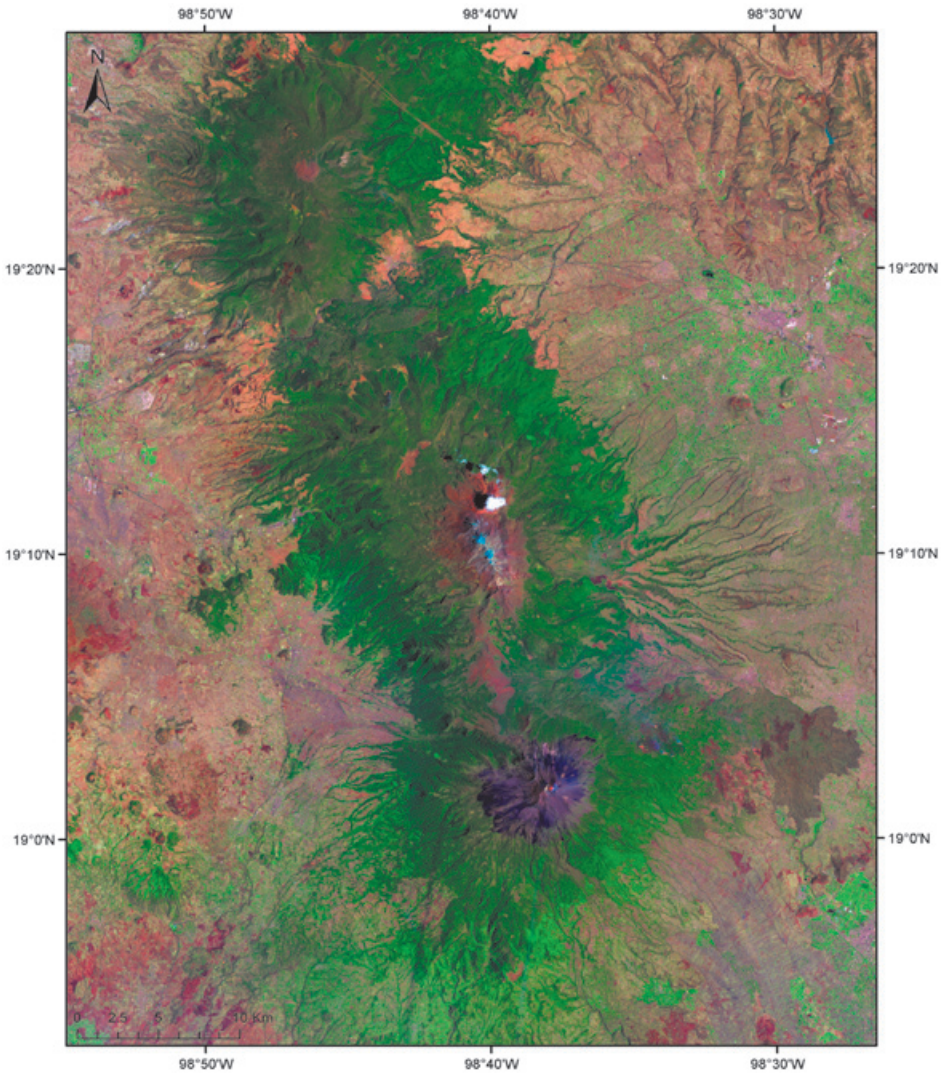

Figure 1b.

the interferometric pair. In this sense, the DEM produced by the interferometric pair was corregistered with the LANDSAT TM-4 images. Both, the LANDSAT TM-4 images and the DEM were resampled to have the same pixel dimension of 28.5 × 28.5 m^2.

Methods

In order to quantify the temporal change of the forest cover, two multi-spectral images were considered. On the grounds of these images, a model to characterize the spatial-spectral state of the forest cover was defined. The model was defined by means of a set of variables. Using the model, a segmentation of the area covered by the forest cover was undertaken. The segmentation based on this model results in a binary image dubbed the bitmap as explained in section 2.2.3. The validity of the model was assessed on the grounds of a multivalued probabilistic logic combination of the variables that define the model as explained in section 3.3. The bitmap was used to derive morphologic parameters that quantify the temporal change of the forest mass (Section 3.4). A method of vector change by means of the principal component analysis was considered to quantify the degree of forest cover change (Section 2.2.4). Details of the above rationale follow (Figure 2).

Table 2. Basic technical details of interferometric RADARSAT 1 images.

Image 1	Image 2	Pixel (m^2)	Size (km^2)	Looks	Band
May 19, 1998	July 6, 1998	24 × 24	144.74 × 226.89	4	C(5.6 cm)

The selected variables that describe the spatial-spectral behavior of the forest cover are Reflectance of vegetation, Texture and the Greenness band of the Kauth and Thomas transformation. These variables define the spatial-spectral state of the forest cover. The texture determines the spatial roughness of vegetation, and Reflectance and Greenness establishes the spectral state of vegetation. Details of the calculation of these variables are provided in section 2.2.1. Such variables form a canonical expansion of the image (Lira and Garcia, 2003). In brief, the model is designed as (a) A canonical expansion of the multispectral image, (b) A set of variables to describe the spatial and spectral behavior of the forest cover and (c) To define a vector field of three dimensions from which vector change can be assessed.

A segmentation of forest cover was achieved using the variables as input to a hierarchical region-growth algorithm RHSEG (http://techtransfer.gsfc.nasa.gov/RHSEG). The result is a segmented image with a certain number of regions (Tilton *et al*., 2006). Details of this segmentation are provided in section 2.2.3.

RHSEG stands for Recursive Hierarchical Segmentation. This algorithm establishes a segmentation hierarchy where an image is segmented at different levels of detail. Segmentation at coarser levels of detail can be generated from merges of regions at finer levels of detail. In this procedure, an object in the image is represented by multiple image segments in finer level of detail in the segmentation hierarchy. In region-growing, spatially adjacent regions iteratively merge to represent and object with spatial-spectral homogeneity (Tilton *et al*., 2006).

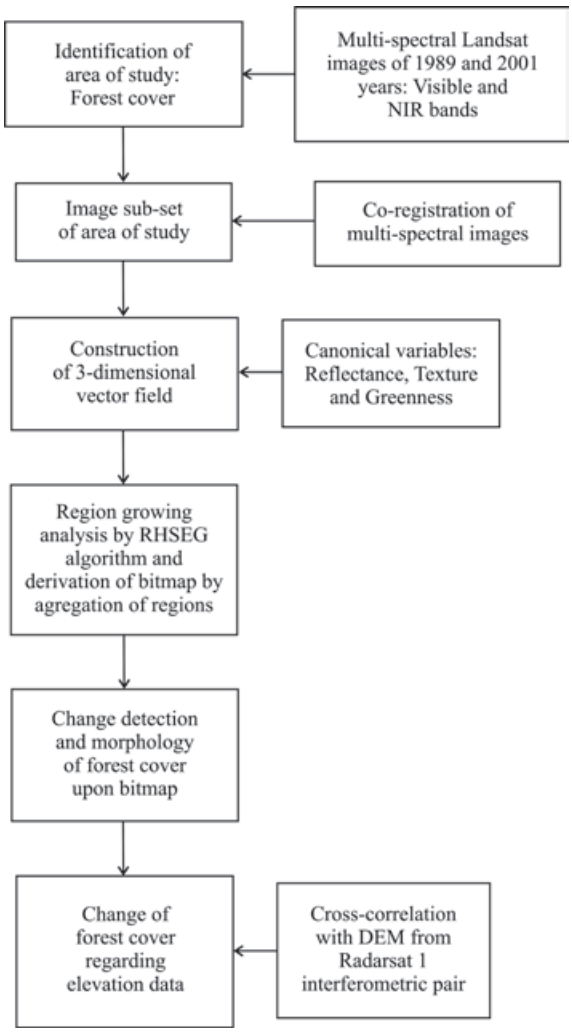

Figure 2. Workflow of the methodology of analysis.

The morphology of the forest cover was calculated using a group of morphologic parameters. A large number of connected areas dubbed patches form the forest cover. The evaluation of the morphology consists in the calculation of two groups of parameters, a) the number of patches and its area and b) the heterogeneity of the patches. The first group is to assess the extension of the forest cover and the second group is to assess the complexity of the landscape form by the forest cover. The calculation of the two groups of parameters for the images 1989 and 2001, permit the quantification of the evolution of the extension of the forest cover and the change of its heterogeneity. Morphologic parameters were calculated using the Fragstats software (http://www.umass.edu/landeco/research/fragstats/fragstats.html). Details are given in section 3.4.

Since PCA is used to quantify the temporal vector change, no radiometric normalization was required for the variables that define the

spatial-spectral model (Canty, 2007, Chapter 8). Details of this are provided in section 2.2.2. Once the images were corregistered, PCA was applied to the vector field formed by the variables of both images. Section 2.2.4 describes such change. Figure 2 depicts the workflow of the methodology above described.

In order to corroborate that the selected variables adequately depicts the state of the forest cover a multivalued probabilistic logic is employed. The variables of the two images are combined by means of multivalued probabilistic logic (Nilson, 1986) to generate an image where the change of the forest cover is described. Section 2.2.5 provides details of such combination.

Canonical expansion

A canonical expansion is a representation of the image in terms of a set of variables with low or null correlation among them (Lira and Garcia, 2003). The variables selected for such expansion were Reflectance, Texture and Greenness of the forest masses. The calculation of these variables was the following. The Greenness is the second band of the Kauth and Thomas transformation of the LANDSAT TM-4 image. The Reflectance of the forest cover is derived using a variant of the principal component analysis (Lira, 2006). In this variant, a set of pixels related only to the forest cover is manually extracted from the image. The covariance matrix of such set is calculated. The set of eigenvectors is obtained from this covariance matrix. These eigenvectors define a kernel of transformation. This kernel is then applied to the whole image. The result is the variant of the principal component analysis related only to the forest cover. The Texture is generated using a divergence operator applied upon the first three principal components of the LANDSAT TM-4 images (Lira and Rodriguez, 2006). These variables represent the spatial-spectral state of the forest masses. Figure 3 shows a false color composite of canonical variables for the images of 1989 and 2001. Let these variables be named as follows: X_1 – Greenness, X_2 – Reflectance and X_3 – Texture. These variables form an expansion of the image in agreement with the following expression

$$g_i\ (k,l) = \mu_i + \sum_{j-1}^{m} a_{ij} X_j\ (k,l)\,,$$

$$\forall\ i = 1, 2... \text{ n and } k, l = 1, 2... \text{ M, N} \qquad (1)$$

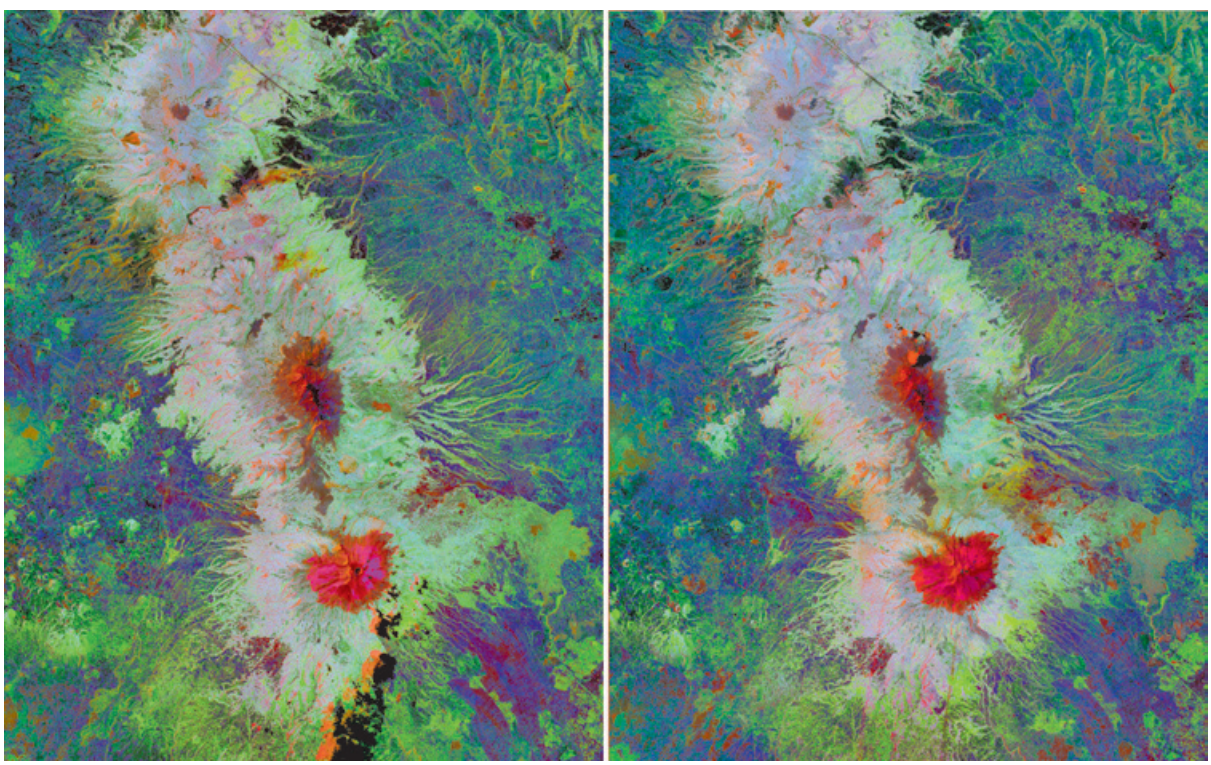

Figure 3. RGB false color composite of canonical variables for the 1989 (left) and 2001 (right) images.

Where (k, l) are the coordinates of a pixel in the image, μ_i is the mean of the image bands and (M, N) are the dimensions of the image. The index i is a band of the image, while j is a dummy index. The coefficients a_{ij} in this case are set to one. Hence, the image g is expressed as a linear combination of the variables above-mentioned. When the correlation between variables X_i is low, expression (1) approximates a canonical expansion of the image (Dougherty 1999). The moderate correlation (Table 3 and 4) among these variables for the images used in this work corroborates that expression (1) is approximately valid as a canonical expansion of the images. A linear histogram expansion was applied to the three variables to have the digital range [0,255]. No units were associated to the variables.

Radiometric normalization and co-registration

Although the same sensor produces the images used in this research, the conditions of illumination and geometry of acquisition are not exactly the same. From one date to the other, the solar illumination is different due to variations in the elevation angle and changes of the azimuth angle of the Sun. Even more, the satellite orbit experiences small fluctuations that lead to a geometry of different observation for the acquisition of the images. Due to this, it is necessary to carry out a co-registration process of the images. The co-registration is made by means of an orthorectification model using the satellite ephemerides applied to each image. The radiometric normalization is not required since the vector change is assessed using the PCA applied upon the ensemble of spectral variables of both images (Canty, 2007, Chapter 8). The combined histogram of the variables for the images of 1989 and 2001 show that a radiometric normalization is achieved (Figure 4). To obtain the combined histogram, an RGB false color composite of the canonical variables was prepared. This RGB is an image of 24-bits depth. Then, a compression of 24-bits to 8-bits was applied. The histogram of the compressed image is the combined histogram. The co-registered bands were used in turn to derive the above-described variables.

Generation of a bitmap

The region-growth algorithm RHSEG was applied to the set of canonical variables above-mentioned. This algorithm was applied to each group of variables for the images of 1989 and 2001. The region-growth algorithm generated a segmented image where certain regions are associated with the forest masses. In an iterative process, the regions were grouped until reaching a binary image that represents a thematic map dubbed the bitmap. This iterative process consists in the aggregation of regions related to the forest cover. Regions not associated to the forest cover are grouped into a single class dubbed rest of the image. The identification of regions related to forest cover is done on the grounds of the image obtained by multivalued probabilistic logic (section 2.2.5). The part of the clouds in the image 1989 is entirely over the forest masses; therefore, that cloud-region was integrated into the class forest cover. This procedure was carried out manually.

This bitmap is a binary image with two values or states: 1 – forest cover, and 0 – rest of the image. The bitmap set the grounds for the quantification of the associated morphologic

Table 3. Linear regression between canonical bands of image 1989.

Canonical band	First component	Texture	Greenness
First component	1.0000	0.3802	0.6828
Texture	0.3802	1.0000	0.2142
Greenness	0.6828	0.2142	1.0000

Table 4. Linear regression between canonical bands of image 2001.

Canonical band	First component	Texture	Greenness
First component	1.0000	0.3248	0.6145
Texture	0.3248	1.0000	0.1773
Greenness	0.6828	0.1773	1.0000

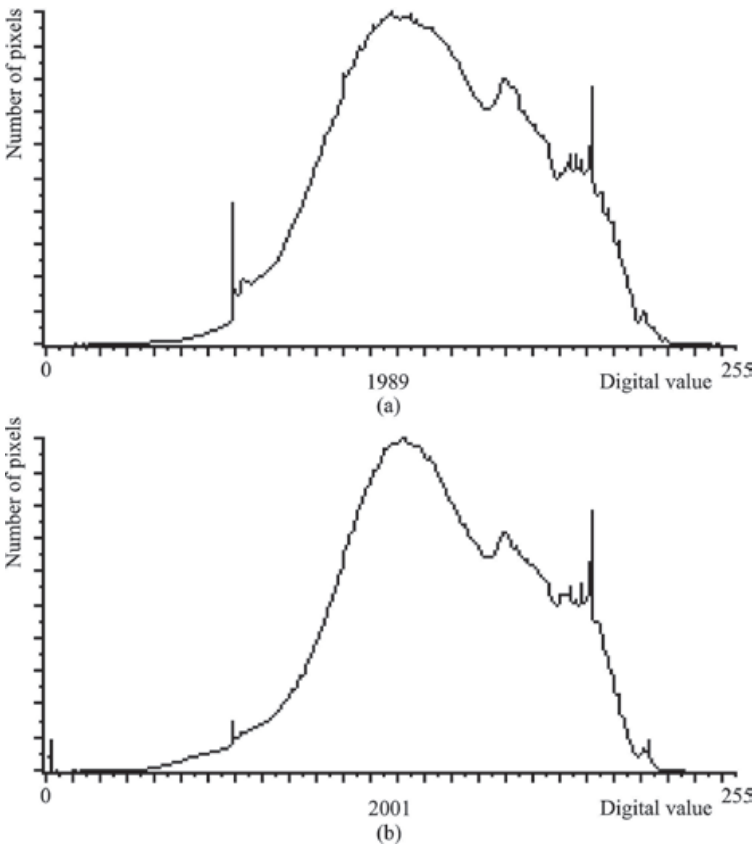

Figure 4. Combined histogram of indicators of image 1989 (a) and image 2001 (b).

parameters of the forest cover as explained in section 3.4. Figure 5 displays the bitmap of the images of 1989 and 2001. The bitmaps were also used to assess the temporal change of the forest cover as explained in sections 2.2.5, 3.1 and 3.2.

Vector change

In a multispectral image $g_\eta(r)$ of η bands, a pixel is a vector of η elements

$$r = \{b_1, b_2 \ldots b_\eta\} \quad (2)$$

Where b_k is the value of the pixel in the k − band. The interval of variation of b_k is $0 \leq b_k \leq 2^{n-1}$, where n = 8 in most cases. The set of vectors $\{r_i\}$ forms the vector field associated to the multispectral image (Lira and Rodriguez, 2006; Lira 2010), represented as

$$U = \{r_i\} \quad (3)$$

Where the hooks {} indicate the set of vectors associated to an image. Let r_i be the vectors of the vector field of the 1989 image and r_j those of the 2001 image. According to this, two vector fields are considered. The region of the vector field associated to the forest masses experience a change from the year 1989 to 2001. A measurement of such change is required to asses the modification of the forest cover.

The vector change can be measured in several ways: (a) By means of a measurement of similarity between the vectors $\{r_i\}$ and $\{r_j\}$ (Sanchez Flores and Yool, 2007; Warner, 2005). (b) Using the principal component analysis of the whole ensemble of bands of the two images (Canty, 2007). (c) Using the principal component analysis of the set of canonical variables of the two images.

The principal component analysis was applied on two sets of bands, namely

(i) Principal component analysis of the ensemble of bands.

The principal component analysis was applied to the ensemble of bands of the images 1989 and 2001. None of the first three components shows valuable details to quantify the change of the forest cover.

(ii) Principal component analysis of the set of canonical variables.

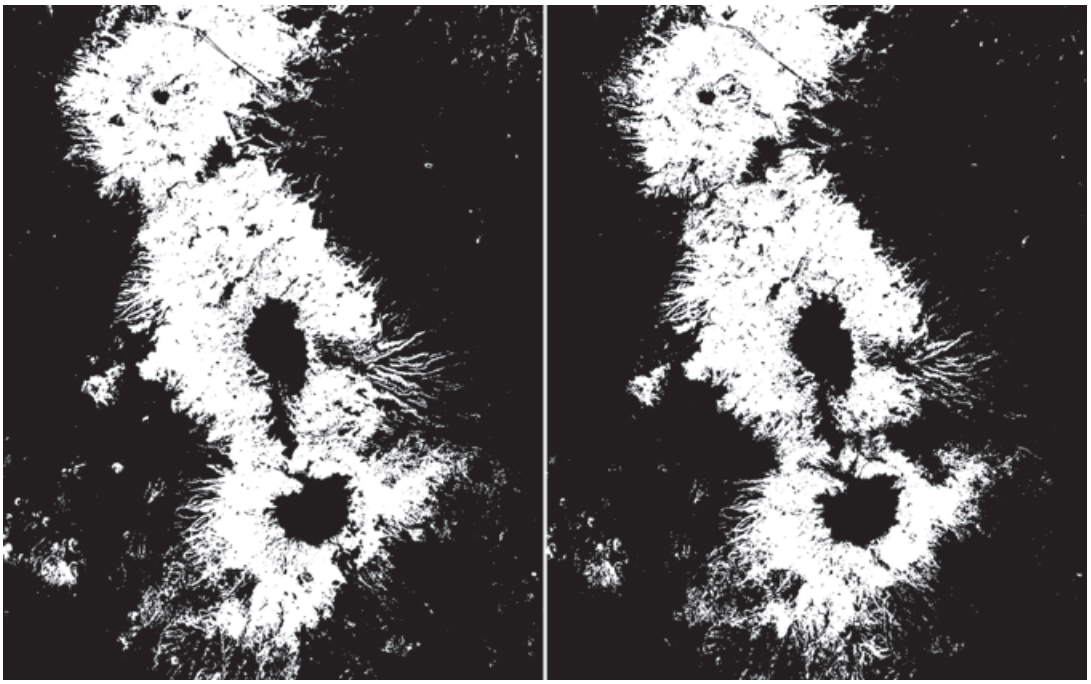

Figure 5. Bitmap of the images of 1989 (left) and 2001 (right).

The vector change was measured using the principal component analysis of the ensemble of canonical variables of the images 1989 and 2001. Six canonical variables, three variables from the image of 1989 and three from the image of 2001 determine such ensemble. Therefore, a 3-dimensional vector field is defined for 1989 and a 3-dimensional vector field for 2001. This vector field experiences a change from 1989 to 2001. This vector field change can be measured by the use of principal component analysis applied on the ensemble of 6-canonical variables for 1989 and 2001. The first component carries most of the variance of the vector change from 1989 to 2001. Figure 6 shows the first principal component of the vector change.

The regions of the vector field that did not experience a change from 1989 to 2001 have a high degree of similarity. Those that did change have a low similarity. That change is depicted in the first principal component. In figure 6, the values of the measurement of similarity and principal components are standardized at the interval [0, 255], where zero indicate no change and 255 the maximum change. This is translated into an image where forest cover change is gradually appreciated from dark tones to bright tones. Forest cover alteration is appreciated in bright tones, the brightest, the greater the change.

Multivalued probabilistic logic

The canonical expansion produced three variables X_i that characterize the spatial-spectral state of the forest vegetation of the scene. These variables can be combined using multivalued probabilistic logic (Nilsson, 1986) by means of the expression

$$X = 255 - \prod_{i=1}^{3} (255 - X_i) \qquad (4)$$

Where X is the resulting image of such combination. Image X is the probability of occurrence of forest cover.

Equation (4) requires the variables X_i to be considered as probabilities. To accomplish this, it is assumed that the pixel distribution values of the variables X_i are probabilities. In this sense, the higher the value of the pixel in X_i, the higher the probability. The histogram of X_i characterizes such probability distribution. The higher the value of a pixel in X_i the higher the probability of occurrence of a forest cover. Therefore, the multivalued logic allows the corroboration that the selected variables characterize the forest cover properly. Figure 7 shows the multivalued probabilistic logic for the set of variables of the images of 1989 and 2001. The results for the multivalued probabilistic logic are high probability for forest

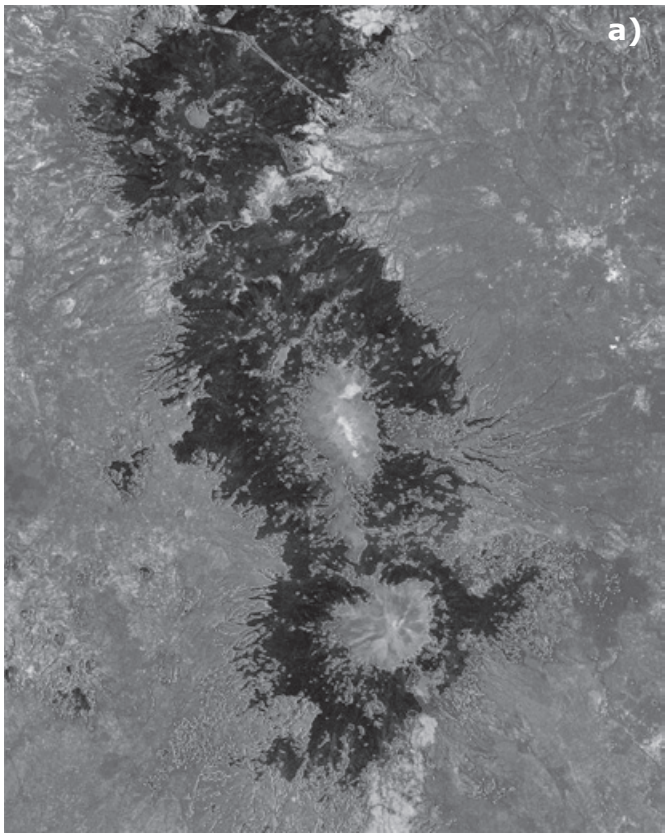

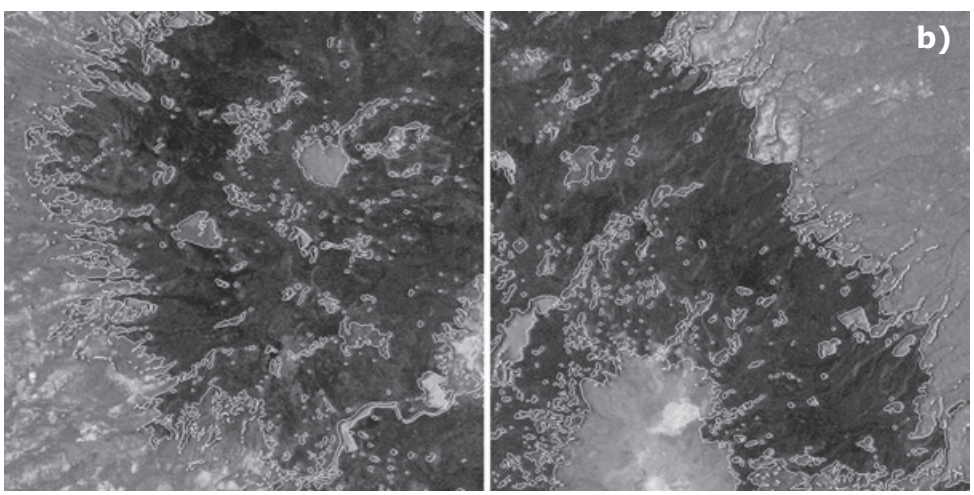

Figure 6. (a) First principal component of vector change. Forest cover alteration is appreciated in bright tones, the brightest, the greater the change. Forest mass appears in medium and dark gray. (b) Amplification of two selected zones from the top left (left) and from the middle (right) of figure 6a.

zones (dark tones) and low probability for the rest of image (medium and bright tones). In multivalued probabilistic logic, distinctive probabilities occur for the forest masses and the rest of the image.

Digital elevation model

An interferometric pair from the RADARSAT 1 satellite was used to generate a digital elevation model (DEM) of the area of study. This interferometric pair was acquired from the Alaskan Satellite Facility by means of an ASF Project Agreement. Table 2 shows basic parameters of this interferometric pair.

The DEM is depicted in figure 8. A cross-reference of this DEM with the bitmaps that depict the forest cover change (Figure 5) permits the estimation of the elevations of the forest masses and an identification of the areas of forest loss. With the cross-reference, forest loss-type may be related to altitude as explained in section 3.5.

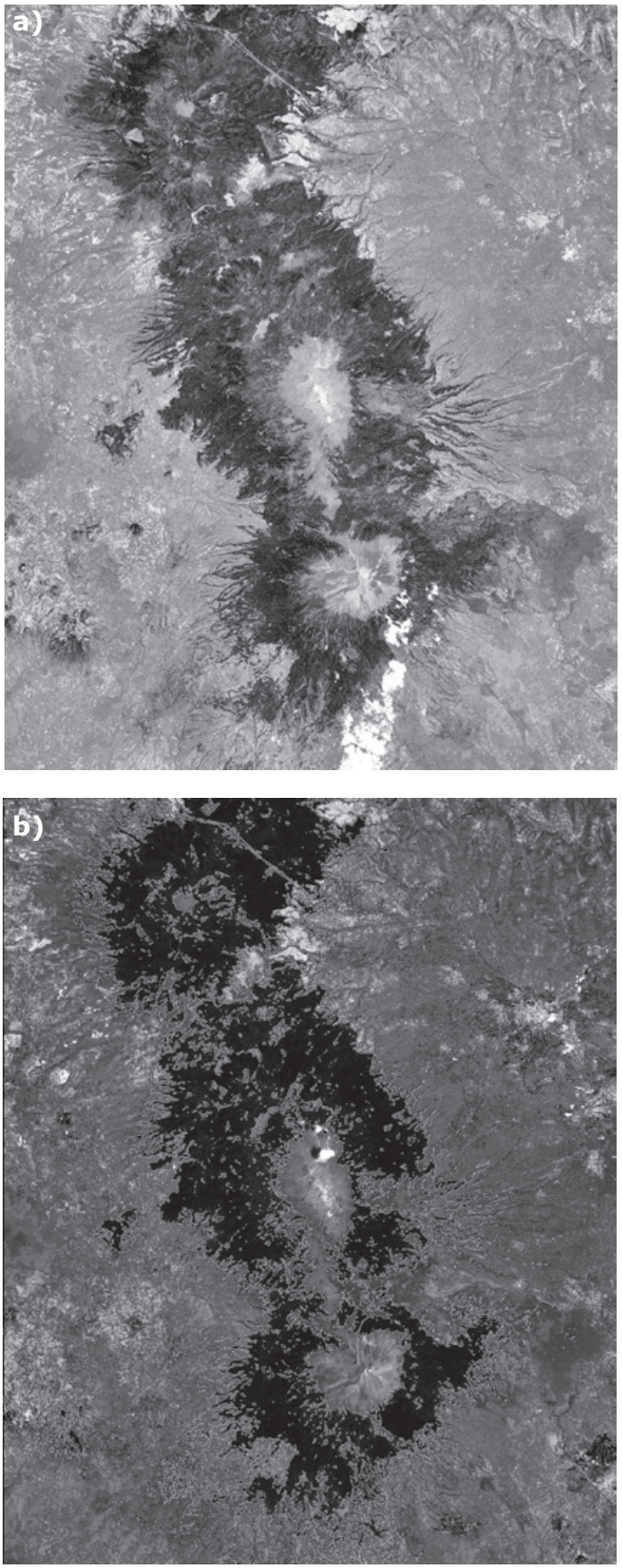

Figure 7. Multivalued probabilistic logic of 1989 (a) and 2001 (b).Forest masses appear in dark gray. Borders from the bitmap of 2001 are overlaid with the probabilistic logic of 2001.

Results

Production of a bitmap

The classification with the region–growth algorithm using the canonical variables produced the bitmap of the years 1989 and 2001. The bitmap was used as the basis to evaluate the morphology of the forest areas (Figure 5 and Table 5). Figure 9 depicts an overlay of the bitmaps of 1989 and 2001. The forest cover change is shown in red. The reduction of forest masses occur in the perimeter and in numerous spots within the forest.

Vector change

Two methods were considered using the principal component analysis applied to the original bands or to the set of variables (section 2.2.4). Best result was obtained with the set of six canonical variables from the images 1989 and 2001. As figure 6 shows, the bright spots that indicate forest change match well with the borders of the bitmap of 2001. In this figure, the perimeter of the forest cover coincides well with the edges produced by the bitmap.

Figure 6 is an overlay of the first principal component of the ensemble of canonical variables with the bitmap of 2001. In this component, forest cover changes are depicted in varying shades of gray. Instead, the bitmap depicts the total forest loss. Therefore, some of the gray shades indicating medium or moderate forest cover change are not marked by the bitmap. These results corroborate that the use of variables, instead of the original bands, is an appropriate model of the spectral response of the forest cover.

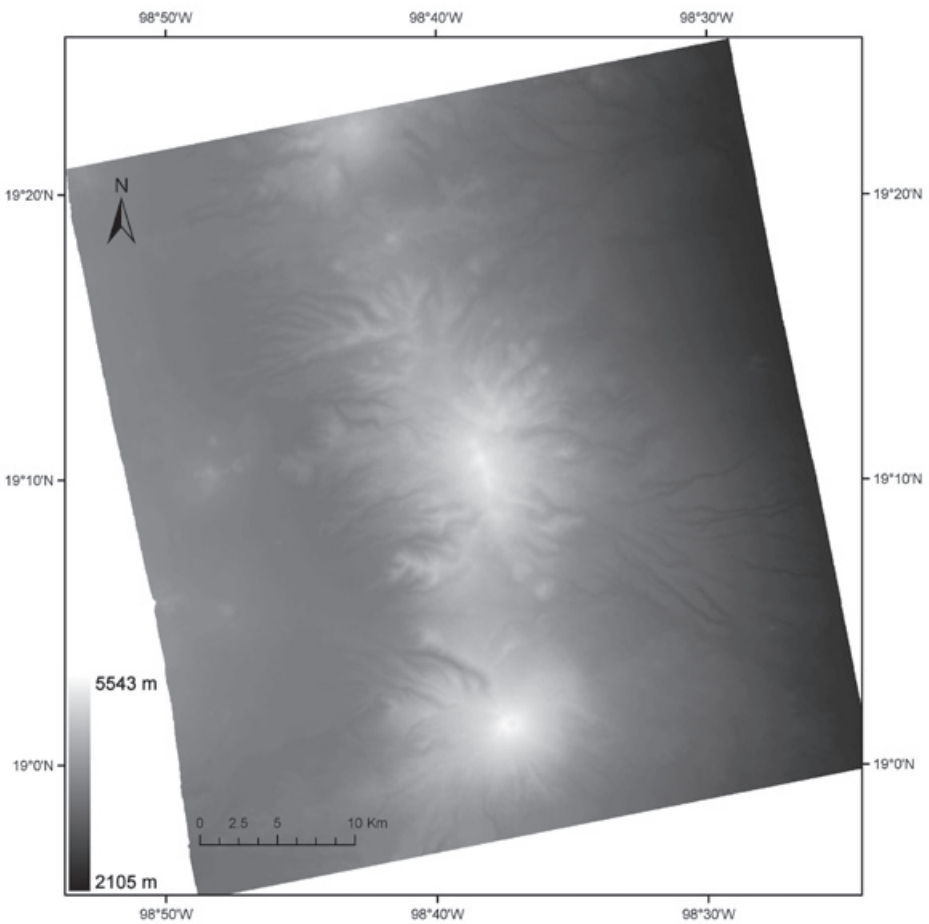

Figure 8. Digital elevation model derived from a RADARSAT 1 interferometric pair. Elevation scale is shown on the left-bottom.

Table 5. Morphologic parameters of the forest areas.

Image	Patches	Area (m^2)	Density/patches (m^{-2})	Form/landscape	Perimeter/Area (1/m)
1989	3,691	1,028,905,504	1.0049	53.9582	1.3341
2001	4,002	926,230,606	1.0896	58.8024	1.3267

Multivalued probabilistic logic

The combination of the variables of forest cover with multivalued probabilistic logic produced an enhancement of the forest zones and an inhibition of the rest of the image. This corroborate that the selected canonical variables are well adapted to characterize the spatial-spectral response of the forest masses (Figure 7). The histogram of the probabilistic image is bimodal with a sharp decrease around digital value of 80. A sharp change in gray shades from forest cover to non-forest occurs in this probabilistic image. The borders coincide well with the multivalued probabilistic logic of image 2001. Therefore, when the borders from the bitmap of 2001 are overlaid with the probabilistic logic of 2001 such sharp changes is identified.

Morphology of forest cover

With the bitmap associated to the segmentations of the forest cover, it is feasible to quantify the morphologic parameters of the forest zones. These morphologic parameters are area, number of patches, density of patches, form of the landscape and fractal dimension. The first three parameters determine the extension of the forest cover. The last two parameters describe the complexity of the forest cover.

Table 5 summarizes the values of these parameters. The area associated to each pixel is 28.5 × 28.5 m^2 = 812.25 m^2. The definition and units of these parameters is the following

• Area - Number of pixels of the forest area of the bitmap multiplied by the area associated

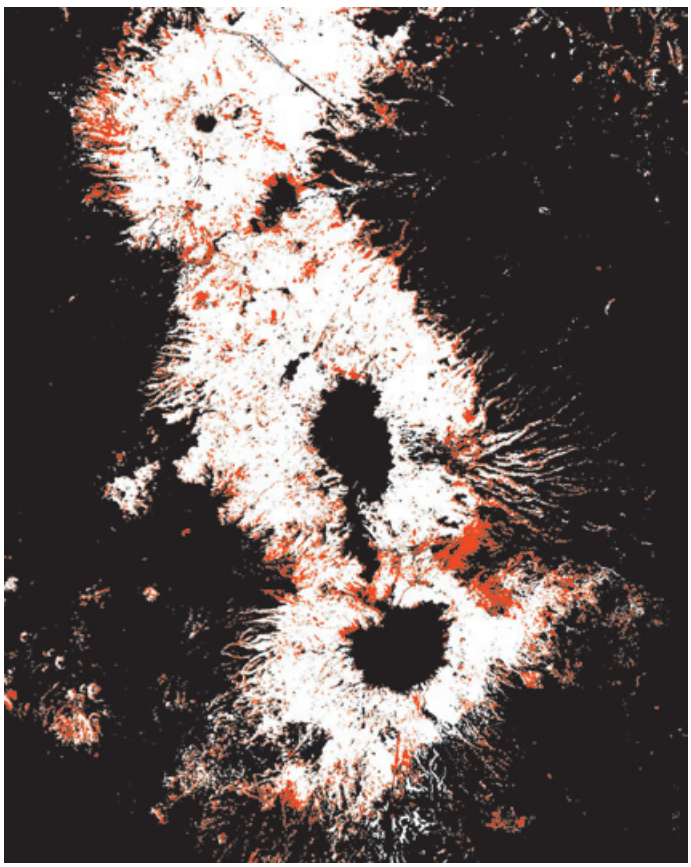

Figure 9. Overlay of bitmaps of 1989 (white plus red) and 2001 (white). Change appears in red.

to the dimension of the pixel. This quantity is expressed in m^2.

• Patches - Number of connected zones under connectivity 8 that include the forest area. This quantity is dimensionless.

• Density of patches - Number of patches divided by the forest area. This quantity is expressed in m^{-2}.

• Form of the landscape - Measure of the aggregation or desegregation of patches. As the value of this parameter increases, the patches become increasingly disaggregated. This quantity is dimensionless.

• Perimeter/Area, fractal dimension - Double of the slope of the line of regression of the logarithm of the patch area against the logarithm of the patch perimeter. This quantity is expressed in 1/m.

From the year 1989 to the year 2001, the forest area was reduced by 102,674,898 m^2 (Table 5). The fragmentation and reduction of the forest areas is the result of illegal cutting, fires and plagues (Aceves Pastrana, 2005).

The values of the morphologic parameters of table 5 prove clearly that the forest area (the landscape) becomes more complex as forest mass is lost. A great number of patches of diverse size form the forest areas depicted in the bitmap; the set of patches is equal to the total area occupied by the forest mass. For a quad-core i7 PC running at 3.4 GHz at 64-bit operating system, the total computing time for the images used in the present investigación is less than 10 minutes.

Cross-reference of DEM with forest cover

A cross-reference of DEM with forest cover (bitmap) is shown in figure 10. Table 6 resumes forest changes related to the elevation of the study area. The boxes in figure 10 indicate several zones of major forest change (Table 6).

As figure 10 shows, minor changes in the forest areas occur in the periphery and in numerous spots inside the forest. Major changes are localized in two zones: to the north and to the southeast in two large gullies. The forest cover of the study area occurs in the environs of two major volcanoes. The elevation variation in this area is from the hills at 2105 meters to the summit of the highest volcano at 5543 meters. The forest cover are present from the hills to an altitude of about 4000 meters. A cross-reference of DEM with the bitmap allows the localization of forest cover in relation to the altitude of the study area. Therefore, on the grounds of this cross-correlation the elevation of forest change occurrences can be identified. Table 6 has three columns. The left column shows five selected areas where forest change occurs. The column on the middle indicates the elevations of that change, and the column on the right the degree of change.

Conclusions

A segmentation of the areas that occupy the forest masses in a zone to the east of the Mexico City generated a binary image dubbed the bitmap. This bitmap was produced using an algorithm of region−growth that employs as input the canonical variables that characterize the state of the spatial-spectral response of the forest masses. From the bitmap, it is possible to obtain the morphologic variables that describe the spatial structure of the forest areas. The associated vector change to the vector fields of the images of two dates in a lapse of twelve years allows the quantification of the degree and location of the change of the forest mass. The use of a DEM obtained from an interferometric pair allows the identification of elevation-related spots where changes in forest cover occur. A search of the social, geographic and physical situation of the forest masses in area of study (Aceves Pastrana, 2005) complement the image analysis developed in this research. From these bases the following conclusions are derived

i). Such fragmentation is heterogeneous, within the forest mass and some edges of the forest area. The density of patches increases since the area is reduced and the number of patches increases (Table 5), this result in an increase of heterogeneity of the landscape formed by the forest cover patches.

ii). The morphologic structure of the areas becomes more complex as the forest area fragments. The form of the landscape (Table 5) gives the measurement of the complexity of the forest area. The value of this parameter increases from 1989 to 2001 indicating that the complexity of the forest cover area has increased.

iii). The forest spots are reduced in a considerable area. The area of the forest cover is reduced by slightly more than 100 km2 (Table 5).

iv). The canonical variables describe better the spatial-spectral state of the forest areas than the original bands. The application of principal

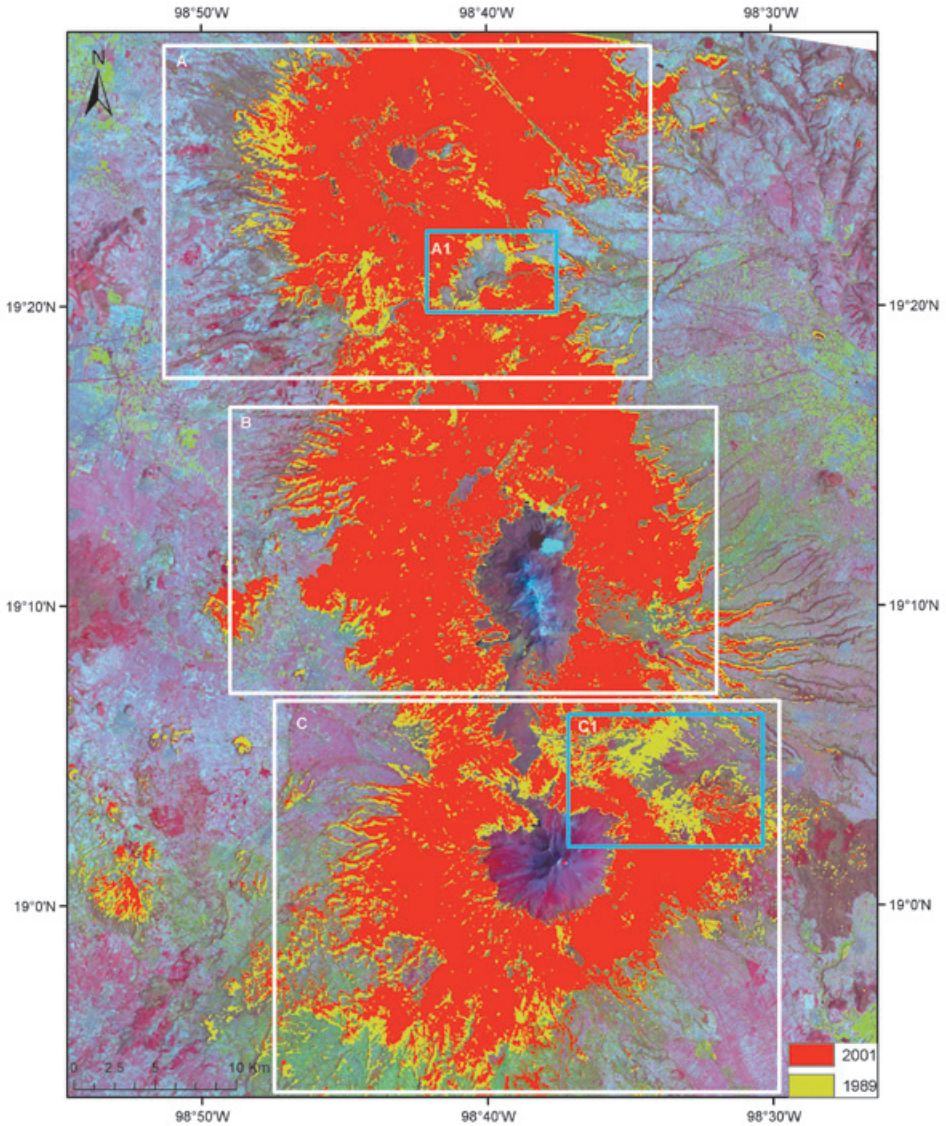

Figure 10. Cross-reference of DEM with bitmaps of 1989 (yellow plus red) and 2001 (red). Yellow depict change areas. Boxes show three alteration zones (see table 6).

Table 6. Modification of forest areas in relation to the elevation.

Year 1989 – Zone	Height (m)	Observations
A	2650 –3960	minor changes
A1	3050 – 3960	mayor change
B	2550 – 3960	minor changes
C	2500 – 3830	minor changes
C1	3050 – 3830	minor change
Year 2001 – Zone	**Height (m)**	**Observations**
A	2850 – 3950	minor change
A1	3160 – 3960	mayor change
B	2550 – 3960	minor change
C	2600 – 3830	minor change
C1	3250 – 3830	mayor change

component analysis to the ensemble of the 12-bands of the images of 1989 and 2001 did not produce meaningful results. The canonical variables are designed to characterize the spatial (texture) and the spectral (reflectivity and greenness) response of the forest cover.

v). The multivalued probabilistic logic corroborates that the canonical variables provide an adequate description of the forest areas.

vi). The cross-reference with the DEM identified small spots of deforestation at higher altitudes and mayor changes of forest cover at lower altitudes (Table 6).

Acknowledgment

The author thanks Professor J. Tilton for a temporal license of the region-growth software RHSEG. The author thanks the Alaska Satellite Facility for the free-delivery of radar images.

References

Aceves Pastrana P.E., 2005, Deforestación en México, Módulo Conocimiento y Sociedad, Universidad Autónoma Metropolitana, Unidad Xochimilco, 71 pp.

Allen T.R., Kupfer J.A., 2000, Application of Spherical Statistics to Change Vector Analysis of Landsat Data: Southern Appalachian Spruce-Fir Forest, *Remote Sensing of Environment*, 74, pp. 482 – 493.

Cakir H.I., Khorram S., Nelson S.A.C., 2006, Correspondence Analysis for Detecting Land Cover Change, *Remote Sensing of Environment*, 102, pp. 306 – 317.

Canty M.J., 2007, Image Analysis, Classification and Change Detection in Remote Sensing, CRC Press.

Coppin P., Jonckheere I., Nackaerts K., Muys B., 2004, Digital Change Detection Methods in Ecosystem Monitoring: A Review, *International Journal of Remote Sensing*, 25, pp. 1565 – 1596.

Dougherty E.R., 1999, Randomn Processes for Image and Signal Processing, SPIE Press.

Fraser R.H., Abuelgasim A., Latifovic R., 2005, A Method for Detecting Large-Scale Forest Cover Change Using Coarse Spatial Resolution Imagery, *Remote Sensing of Environment*, 95, pp. 414 – 427.

Hernández García M.A., Granados Sánchez D., 2006, El Parque Nacional Iztaccihuatl - Popocatepetl - Zoquiapan y el Impacto Ecológico - Social de su Deterioro, *Revista Chapingo*, 12, pp. 101 - 109.

Johnson R.D., Kasischke E.S., 1998, Change Vector Analysis: A Technique for the Multispectral Monitoring of Land Cover and Condition, *International Journal of Remote Sensing*, 19, pp. 411 – 426.

Kontoes C.C., 2008, Operational Land Cover Change Detection Using Change Vector Analysis, *International Journal of Remote Sensing*, 29, pp. 4757 – 4779.

Lambin E.F., Strahler A.H., 1994, Change-Vector Analysis in Multitemporal Space: A Tool to Detect and Categorize Land-Cover Change Processes Using High Temporal-Resolution Satellite Data, *Remote Sensing of Environment*, 48, pp. 231 – 244.

Lambin E.F., Strahler A.H., 1994, Indicators of Land-Cover for Change-Vector Analysis in Multitemporal Space at Coarse Spatial Scales, *International Journal of Remote Sensing*, 15, pp. 2099 – 2111.

Lambin E.F., Ehrlich D., 1997, Land-Cover Changes in Sub-Saharan Africa 1982 – 1991: Application of a Change Index Based on Remotely Sensed Surface Temperature and Vegetation Indices at a Continental Scale, *Remote Sensing of Environment*, 61, pp. 181 – 20.

Le Hégarat-Mascle S., Seltz R., 2004, Automatic Change Detection by Evidential Fusion of Change Indices, *Remote Sensing of Environment*, 91, pp. 390 – 404.

Lira J., 2010, Tratamiento Digital de Imágenes Multiespectrales, UNAM (Electronic Book: www.lulu.com).

Lira J., García E., 2003, Characterization of Vegetation in the South of México by Means of a Canonical Expansion, *International Journal of Remote Sensing*, 24, pp. 1083 – 1093.

Lira J., Rodriguez A., 2006, A Divergence Operator to Quantify Texture From Multi-spectral Satellite Images, *International Journal of Remote Sensing*, 27, pp. 2683 – 2702.

Lira J., 2006, Segmentation and Morphology of Open Water Bodies From Multi-spectral

Images, I*nternational Journal of Remote Sensing*, 27, pp. 4015 – 4038.

Nackaerts K., Vaesen K., Muys B., Coppin P., 2005, Comparative Performance of a Modified Change Vector Analysis in Forest Change Detection, *International Journal of Remote Sensing*, 26, pp. 839 – 852.

Nilsson N.J., 1986, Probabilistic logic, *Artificial Intelligence*, 28, pp. 71 – 87.

Raši R., Beuchle R., Bodart C., Vollmar M., Seliger R., Achard F., 2013, Automatic Updating of an Object-Based Tropical Forest Cover Classification and Change Assessment, IEEE *Journal of Selected Topics in Applied Earth Observations and Remote Sensing*, 6, pp. 66 - 73.

Rzedowski G.C., Rzedowski J., 2005, Flora Anerogámica del Valle de México. 2a. ed., Instituto de Ecología, A.C. y Comisión Nacional para el Conocimiento y Uso de la Biodiversidad, Pátzcuaro (Michoacán), 1406 pp.

Sanchez Flores E., Yool S.R., 2007, Sensitivity of Change Vector Analysis to Land Cover Change in an Arid Ecosystem, *International Journal of Remote Sensing*, 28, pp. 1069 – 1088.

Tilton J.C., Lawrence W.T., Plaza A.J., 2006, Utilizing hierarchical segmentation to generate water and snow masks to facilitate monitoring change with remotely sensed image data: GIScience and Remote Sensing, 43, 39-66.

Warner T., 2005, Hyperspectral Direction Cosine Change Vector Analysis, *International Journal of Remote Sensing*, 26, pp. 1201 – 1215.

Geofísica Internacional (2014) 53-2: 135-151

Original paper

Hydrogeologic characterization of the abandoned mining site of Castelejo, Portugal by VLF-EM & RMT-R geophysical surveying

Vitor Manuel Gomes de Oliveira*, Luís Filipe Tavares Ribeiro and María Catarina Rosalino da Silva

Received: November 27, 2012; accepted: August 28, 2013; published on line: April 01, 2014

Resumen

Hay alrededor de 175 minas abandonadas en Portugal, de las cuales unos 60 son antiguas explotaciones de uranio. La mina de uranio Castelejo está ubicada a unos 2 km al W de Vila Cortês da Serra, en el distrito de Guarda, en la cuenca del río Mondego. En términos geológicos, la mina se localiza en un granito de grano medio e dos micas con tendencia porfiroidal. La explotación comenzó con dos minas a cielo abierto entre 1979 y 1990, que produjeron alrededor de 132 toneladas de U_3O_8. Desde 1992, la producción comenzó a llevarse a cabo a través de la lixiviación *in situ* con H_2SO_4 de materiales de bajo contenido en uranio. La circulación de las aguas superficial y subterránea está estructuralmente condicionada por la fracturacion intensa en la zona. Dos campañas geofísicas de exploración se llevaron a cabo a fin de caracterizar el sistema de fracturas. La primera fue una investigación con el método VLF que nos permitió identificar los principales sistemas de fallas que pueden proporcionar rutas para el flujo de las aguas subterráneas. A partir de la segunda campaña, que fue un estudo llevado a cabo con el método RMT en una caja de falla que reproduz o gradiente natural de la mina, se obtuvieron las resistividades y espesores del material de granito intemperizado. Los perfiles obtenidos muestran que la resistividad disminuye con el aumento de profundidad.
Este aspecto puede deberse a causas naturales - el material que llena la caja de falla es más intemperizado en profundidad que en la superficie - o puede indicar contaminación en profundidad, debido al drenaje ácido de las minas.

Palabras clave: prospección geofísica, acuífero fisurado, agua de mina, VLF, RMT-R.

Abstract

There are about 175 abandoned mining sites in Portugal, of which about 60 are old uranium workings. The Castelejo mine is an old uranium located about 2 km W of Vila Cortês da Serra, in Guarda district, on the River Mondego basin. In geologic terms, the mine is located in medium-grained two-mica monzonitic granite, with porphyroidal tendency. Exploitation started with two open cast mines between 1979 and 1990 which produced about 132 tonnes U_3O_8. From 1992, production started to be carried out through the *in situ* H_2SO_4 leaching of the mine's low-grade materials. The superficial and groundwater circulation are structurally conditioned by the intense fracturing in the area. Two exploratory geophysical field campaigns were conducted in order to characterize the fracturing. The first was a VLF survey that allowed us to identify major fault systems that may provide paths for groundwater flow. From the second campaign, which was an RMT survey conducted at a fault gauge which records the mine natural gradient flow, we obtained the resistivities and thicknesses of the weathered granite material. The profiles obtained show that resistivity declines with increasing depth.
This fact may arise from natural causes – the material which fills the fault gauge is more weathered at depth than on the surface – or it may indicate contamination at depth, due to acid mine drainage.

Key words: geophysical surveying, fissured aquifer, mine water, VLF, RMT-R.

V.M.G. Oliveira
L.F.T. Ribeiro
CVRM
Instituto Superior Técnico
Universidade de Lisboa
Av. Rovisco Pais, Lisboa Portugal
*Corresponding author: vgomesoliveira@ist.utl.pt

M.C.R. Silva
Centro de Geología
FCUL, Edifício C6
Campo Grande
Lisboa, Portugal

Introduction

The activities developed by mining are, from the very start of operations, capable of degrading the surrounding environment and causing major environmental modifications, unless they are properly monitored and then controlled in accordance with the data gathered from the monitoring.

Main modifications to the environmental balance generally result from digging a part of the land surface, as well as from the production of deposits of varying kinds of waste and / or sterile minerals (tailings) and from the chemical products used in ore separation / purification (Younger *et al*., eds, 2002). All these modifications cause hydrological and hydrogeological impacts (on superficial and ground water), geochemical impacts (on sediment, ground and alluvium) and biochemical impacts (on living beings) (Lottermoser, 2003).

The characteristics and consequences of these impacts diverge according to when they are produced, and they can cause sporadic and /or diffuse pollution.

Sporadic pollution occurs when the mine is being worked; if there is a control system in operation (monitoring) the pollution can be prevented from spreading.

Diffuse pollution tends to occur once a mine has been abandoned. As a rule (Rapantova *et al*., eds, 2008) when a reasonably long time is spent on closing down a mine there is no longer any concern with monitoring, which is only undertaken when it is active.

This attitude disregards possible subsequent risks to the closed down mine without taking any type of prevention to forestall them, and therefore it contributes to the propagation of the contamination.

The environmental liabilities of mining are expressed, as a rule, by the incidence of abnormal (very high) concentrations of heavy metals in the sediments, ground and alluvia, as well as in the water within the area of influence of this activity (Rapantova *et al*., eds, 2008). The presence of these elements is essentially due to the leaching of the materials inside the mine and to erosion and leaching processes acting on the tailing materials extracted from the mine (Younger *et al*., eds, 2002). In fact, in open cast mining these elements are vulnerable to the action of the wind and the rain, which are their main vehicles of dissemination.

In many cases of mine exploration, the action of the water over the tailings and other mine wastes causes a phenomenon known as acid mine drainage (AMD). This phenomenon particularly occurs in metal ore workings in which sulphide is exposed to oxidating environments, or when acid leaching from poor ore with a view to its concentration and subsequent recuperation occurs (Lottermoser, 2003). When the mine is definitely abandoned and if the evolution of the characteristics and the processes of environmental alteration are not controlled the ominous consequences will get worse as years go by. One of the best-known is the contamination of the surface water and groundwater, which occurs both during the phase of functioning and after the mine's closure.

The hydrogeological impact is a serious problem in almost all underground mines and in open cast mines, too. A series of measures can help to avoid or reduce this contamination. Thus, when the mine is abandoned it is essential to have the most accurate knowledge possible of the hydrogeology, the geology, the mineralogical composition of the materials, and the method of extracting and processing the ore to enable the prevention, correction and mitigation of environmental degradation caused by the operation.

The method used to decommission a mine directly influences the local hydrogeological conditions. In conjunction with the operation there are often problems of mining subsidence, which occurs because methods of dismantling are used that do not consider the full extent of the galleries.

When in operation we can see, in brief, the following effects:

- Differential settlements
- Fractures on the ground
- Lowering of groundwater levels
- Reduced flow of aquifers or even their exhaustion
- Contamination of water.

It can be said that during the course of its history Portugal several times gained importance for major mining, and it is even one of those countries in which mining carried out by Romans is well documented (Ferreira, 1971; Carvalho *et al*., 1971).

From north to south Portugal 55 Roman mining operations were recorded, and we think there were others that have not been

surveyed. They were mostly for gold and several remained in operation until very recent times (Nunes, 1983).

Identification of fracturing

Geophysical surveying has long been used to characterize fracturing in various geological formations. Particularly in mining areas, where fractures are often related to mineralized veins, the joint use of geophysical and other methods enables one to characterize the ore potential of an area of interest (Kearey *et al*., 2002).

Geophysical surveying today has a very broad range of applications: from mining to civil engineering, through archaeological, environmental, geological and hydrological investigations to aquifer characterization.

In addition to obtaining different kinds of information of geological interest and detecting geological structures that may contain water (e.g. faults and fractures), geophysical surveying is also used to map and monitor the presence and behavior of contaminants in groundwater, ranging from saltwater intrusion in coastal aquifers to the presence of contaminants from mining, industrial or agricultural operations (Kearey *et al*., 2002; Oliveira, V., 2010).

Several geophysical methods can be applied to characterize soil and groundwater contamination, particularly those using ground-penetrating radar (GPR) devices, magnetometers or conductivimeters (Daniels *et al*., 1995; Milson, 2003).

Using more than one surveying method improves the accuracy of interpretations, so as in the work described here, it is possible to geologically characterize the suspected area of contamination using one method and to adopt another to detail its intensity and spread. In this study we use two electromagnetic methods, adapted and refined at the University of Neuchâtel, where they are starting to be used in the characterization of karst discontinuities (Thierrin *et al*., 1988; Turberg *et al*., 1992).

Risks associated with abandoned U mining sites

Some of the risks associated with abandoned uranium mining sites are usually identified through an ecological and human risk-assessment process. In general terms, once the ore has been milled it becomes yellowcake, a U_3O_8 concentrate, through a series of processes that include crushing, leaching, drying and filtering the initial material.

The composition of the tailings produced over all these processes is represented in Table 1.

Tailings pose several risks and threats, some of which are (see Figure 4):

Table 1. Properties of uranium mill tailings (adapted from USEPA 2007).

Type of tailing	Size (μm)	Composition
Sand	75 - 500	SiO_2 plus ≈ 1 weight % Al, Fe, Mg, Ca, Na, K, Se, Mn, Ni, Mo, V silicates and metal oxides; approximately 0.004-0.01 weight % U_3O_8; with H_2SO_4 leaching process: 26-100 pCi ^{226}Ra/g and 70-600 pCi ^{230}Th/g;
Slime	45 - 75	SiO_2 and Na, Ca, Mn, Mg, Al, Fe silicates and metal oxides; Concentration of U_3O_8 and ^{226}Ra ≈ 2 x concentration in sands; with H_2SO_4 leaching process: 150-400 pCi ^{226}Ra/g and 70-600 pCi ^{230}Th/g;
Liquid	-	with H_2SO_4 leaching process: pH 1.2-2.0; $Na+$,NH_4+, SO_4^{2-}, $Cl-$, PO_4^{3-}; dissolved solids ≈ 1 weight %; approximately 0.001-0.01 weight % U_3O_8; 20-7500 pCi ^{226}Ra/l and 2000-22000 pCi ^{230}Th/l;

a) Radon exhalation

Radon (^{222}Rn) is a dangerous radioactive gas which migrates to the surface of a tailings pile through a process of diffusion and is then released into the atmosphere.

One of the most feared characteristics of Rn is the danger that it poses to the lungs if inhaled. According to USEPA (2007), Rn can affect the health of people living many kilometers from a tailings pile.

b) Gamma radiation

The radioactivity present in the tailings, mainly due to the uranium decay products of radium (^{226}Ra) and thorium (^{230}Th) can be harmful to those directly exposed to the emitted radiation.

c) Dust blowing

The action of the wind over the tailings causes dust blowing. Dust blowing can spread many kinds of contaminants in the air. This risk worsens after the closure of the mine, as the tailings materials dry out.

d) Dam failure

Dam failure, although rare, might be caused by anthropogenic or natural factors. Among the former, bad conception or design of the dam can be blamed while natural disasters – earthquakes, rainfall, snowfall or flooding are examples of natural causes.

e) Seepage

Groundwater contamination may be a major problem when considering the risks associated with uranium mill tailings.

In fact, there is a strong relationship between the geological environment of the mine and its surroundings and the migration of contaminants to the aquifer, as we can also see in this study.

The hydrology of the site is also crucial, along with the chemistry and type of the tailings (sand, slime or liquid and their composition, see Table 1 for details). The soil composition and the characteristics of the mining processes (e.g. underground or surface mining, use of acid leaching) are likewise important. The acid leaching poses an additional problem related to the increased solubility caused in some products, thereby facilitating their migration to groundwater.

f) Other risks

Among the risks not illustrated in Figure 4, the improper use of tailings must be mentioned.

Actually the use of sandy tailings as building materials raises the danger of radiation exposure for the inhabitants of such buildings.

Study Area

Current situation in Portugal

In Portugal there are about 175 abandoned mine workings, dozens of which are currently undergoing environmental restoration. About 60 are former uranium mines, which are for the most part located in very intense fractured zones.

1907 is the year of the discovery of the Urgeiriça uranium-radium deposit. Only radium was exploited until 1944, when the exploitation and production of uranium began, which had place in Urgeiriça until the operation was closed in 2001 with the ending of processing of ore.

The uranium workings were abandoned with the decline of its economic and strategic interest, and the last mines of this radioactive metal were closed in the early 1990s.

The present work concerns an old mine site at Castelejo, an ancient uranium exploitation, located about 2 km W of Vila Cortês da Serra in Gouveia municipality, Guarda district, and connected to the Mondego River basin through the Paço Stream (Figure 8-B).

At present, the area is being environmentally rehabilitated by the Portuguese state-owned enterprise charged with the environmental rehabilitation of old abandoned mining areas. Exploitation started with two open cast pits (now both flooded) between 1979 and 1990 which produced about 132 tonnes of U_3O_8. From 1992 up to 1997 production started to be done through in situ H_2SO_4 leaching of the poor material taken from the mine itself, as well as that from other workings located nearby. This latter process was responsible for the production of (more or less) a further 22.5 tonnes U_3O_8.

The coordinates of the central point of the mine, located between both open skies, referring to the Unified European Reference System (ED50) are: latitude 40º 33’ 20’’N and longitude 7º 33’ 5’’W (Figure 8-B).

Geology

Mainland Portugal is formed by an ancient and hardened core, usually called the *Hercynian Massif*, part of the so-called Hesperian Massif, and by land coverage (Figure 1-A and B).

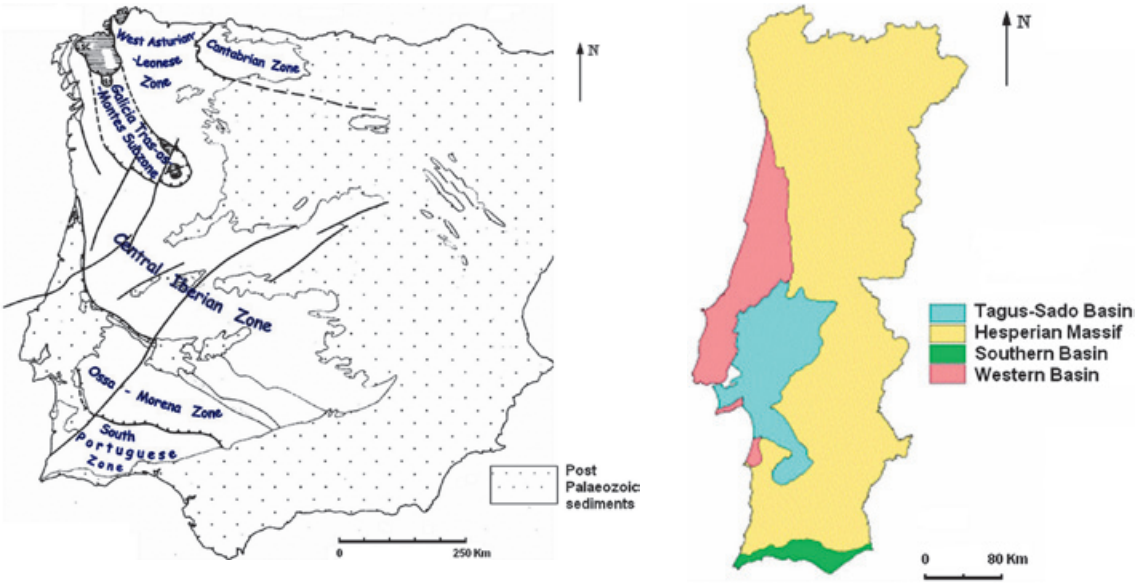

Figure 1. a) Paleogeographic and tectonic zones of the Hesperian Massif. Adapted from Ribeiro *et al*. 1979. b) Major hydrogeological units of portuguese metropolitan territory. Adapted from SNIRH, Instituto da Água, 2009

The *Hercynian Massif* comprises ante-Mesozoic lands, and consists of sedimentary, eruptive and metamorphic rocks (Ribeiro *et al*., 1979).

The land coverage includes sedimentary and some Meso-Cenozoic eruptive rocks which form the western and southern edges of the country, as well as modern deposits, consisting of alluvial flood plains and different beach levels, which result from various basins of sedimentary filling (Teixeira, 1966; Ribeiro *et al*., 1979; Figures 1-A and B).

The Hesperian Massif is crossed by the Central Cordillera, a ENE-WSW lying mountain range, which divides it into two: the north Meseta (Meseta signifies Little Table, so the expression has an essential geomorphological meaning) with an average altitude of 800 meters, and the south Meseta, with an average altitude of about 400 m.

The formations that form the Hesperian Massif, mainly schists, granites and graywackes, suffered the action of Caledonian, Hercynian and Alpine orogenies, although the Hercynian orogeny is the one whose effects are better documented here.

In the Iberian Peninsula, the Hercynian orogeny began in the Middle Devonian and continued until the Late Carboniferous period (Ribeiro *et al*., 1979).

Although it has developed over several stages, two main phases can be distinguished (dated by the presence of unconformities in the outer zones or by radiometric dating of certain granites (Araújo, M.A. (2002); Abranches, M.C.B. *et al*. (1982)):

- First one, which ran from Middle Devonian to Visean
- Second, a phase dating from Westphalian.

The orogenic actions caused folding in a general NW-SE orientation, as well as synorogenic magmatism and regional metamorphism.

Between the Late Westphalian and Late Permian periods the Hercynian chain suffered uplifts, the results of erosion and post-tectonics intrusive actions, mainly consisting of alkaline and calc-alkaline granitoid rocks, which gave rise to considerable filonian mineralization.

The last stages of Hercynian orogeny induced intense fracturation in the Massif, causing various movements of uplifting and sinking.

During the Cenozoic era the Hesperian Massif suffered fracturation again, now predominantly in the NE-SW direction, as a result of the Alpine orogeny actions that occurred (Ribeiro *et al*., 1979).

In geological terms (see Figures 2 and 3) the Castelejo mine is located in medium-grained two-mica monzonitic granite, with porphyritic tendency.

Various granitic intrusions occurred in the late Hercynian age (the mineralizations that occurred are related to quartz veins and usually consist of uranium phosphates - torbernite, autunite and sabugalite - secondary minerals derived from uraninite and other uranium weathering product compounds).

The distribution of U in Portugal

Most known uraniferous deposits lie in central Portugal, in the region covered by the four districts (a district corresponds to an administrative territorial division) of Viseu, Guarda, Coimbra and Porto, although the largest number of mining operations are concentrated in the first two districts (which are, in general terms, presented in Figure 2).

The uranium deposits are related to post-tectonic Hercynian magmatism, usually in the form of monzonitic granite intrusions, medium to coarse-grained, two-mica and having a porphyritic tendency.

They usually lie in a NE-SW direction. Most deposits are related to quartz veins installed in fractures in granites.

There are various opinions about the genesis of uranium deposits. In brief, most

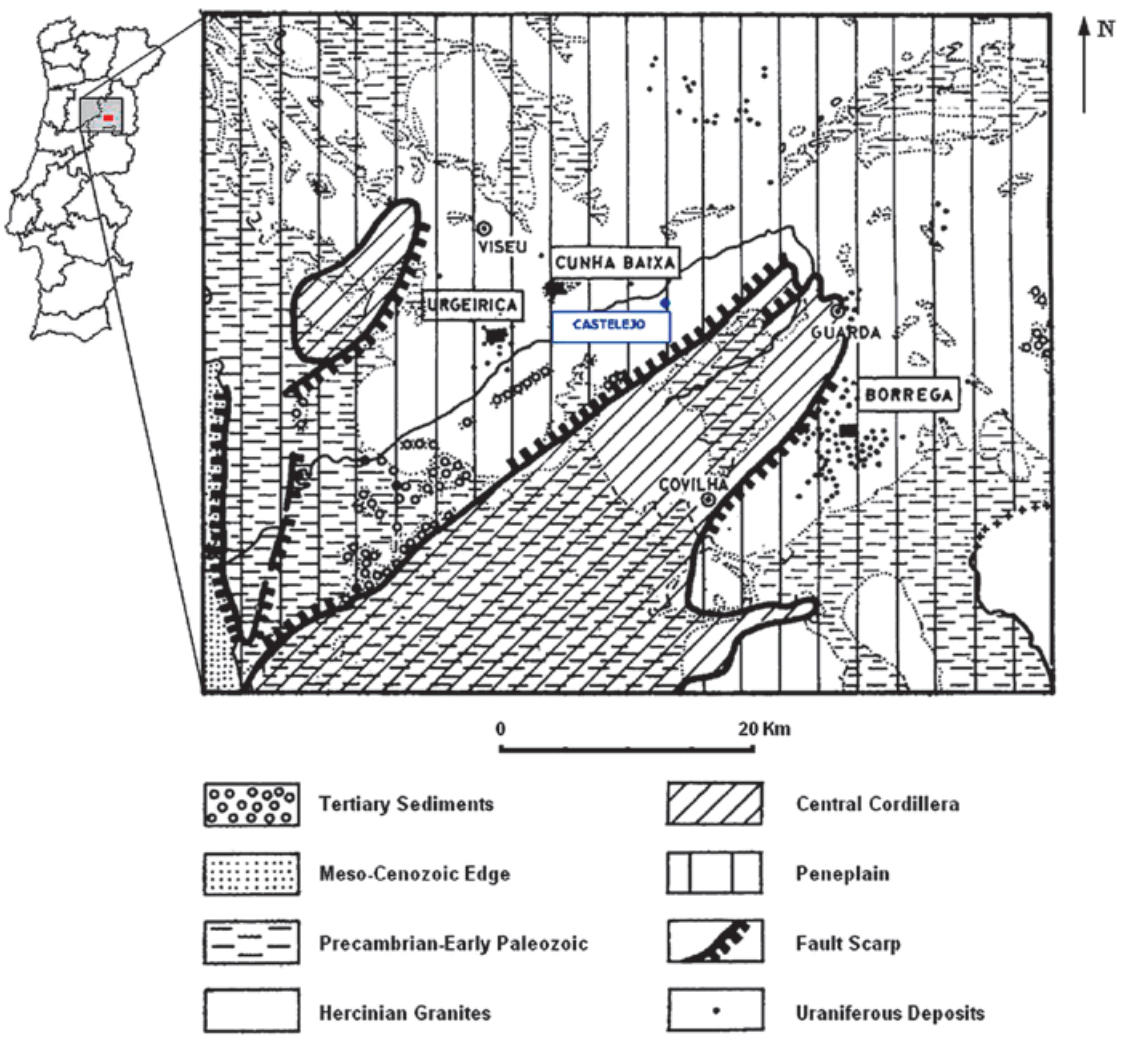

Figure 2. "Beiras Uraniferous Region". On the map of Portugal (left), the Castelejo mine locates at the red rectangle (adapted from *Ferreira, 1971*).

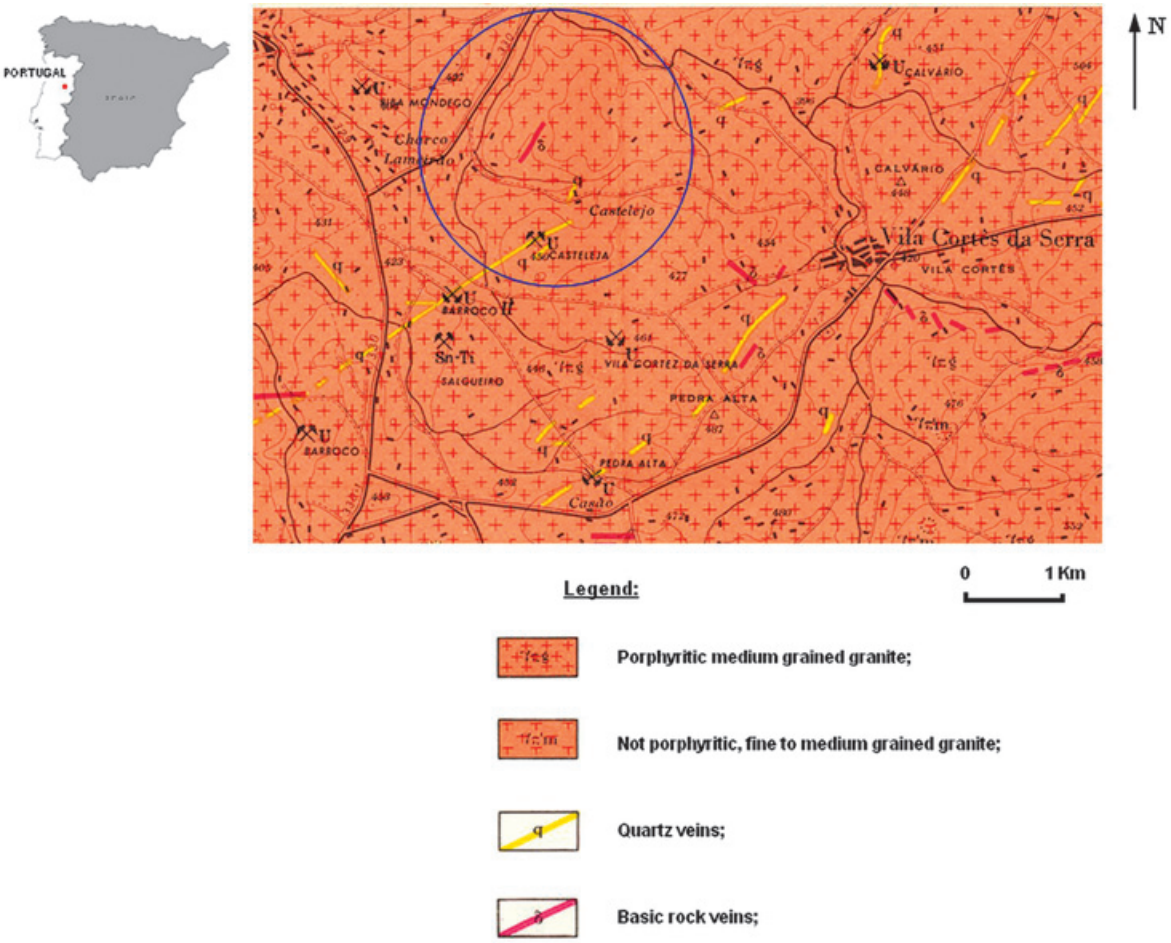

Figure 3. Castelejo mine geological setting

authors (Cerveira, A., 1951; Neiva, J.M.C., 1995) albeit with slight variations, considered primary deposits as coming from hydrothermal deposits, while the secondary deposits - impregnation deposits - are considered as coming from the leaching of the first and subsequent precipitation in favourable structures.

Scope of the study

The superficial and groundwater circulation is structurally conditioned by the intense fracturing in the area (Teixeira, C. *et al*., 1967). To characterize the fracturing, two superficial geophysical exploration field campaigns were conducted. The first consisted of a very low frequency (VLF) survey that enabled the identification of major fault systems that may constitute prime pathways for groundwater flow. The second campaign was a radio magnetotelluric (RMT) survey conducted at a fault gauge fulfilled with weathered granite material. This fault gauge collects the mine's natural gradient flow, and from the survey we have obtained the resistivities and thicknesses of the weathered material.

EDM, the Portuguese state-owned enterprise, in charge of the environmental rehabilitation of the old abandoned mining areas, has been monitoring several water points (wells and piezometers) located in the vicinity of the old Castelejo mine on a more or less regular basis since 1991. However, the collected data are difficult to process since neither the piezometer geometrical characteristics nor its depths of abstraction are known. Besides, data collected over time vary both quantitatively as qualitatively, which makes data analysis difficult.

Furthermore, the collected data relate to two different realities – dug wells and drilled wells - and it is reasonable to apply them a conceptual model based on the supposition that they concern two equally different aquifers: a porous aquifer located near the surface, in the superficial zone of granite weathering, taken as an unconfined aquifer and shown up by countless flooded zones and superficial abstractions detected in the field, and a fissured aquifer, located under the first one in a deeper fractured rock zone, taken as a confined aquifer (Afonso, M.J.C. 2003; Carvalho, J.M., 2006).

Therefore, in view of the hydrogeological characterization of the former mining area and the identification of main drainage pathways, supplementary data was needed to enable us to confirm (or not) the layout of the several unpublished reports. For this, two geophysical surveys were undertaken, using two different geophysical methods. This was intended to supplement the information obtained in each campaign.

main fractures identified in the initial study performed, which was based on photogeological analysis of the studied area.

Materials and Methods

Bases and methods

It is common to be faced with problems of several orders when approaching the hydrogeological study of fractured rocks with a view to their hydraulic characterization.

In the case of granitic rocks, in particular, which, when fresh, are practically impermeable to water, it is well known that its secondary porosity, namely due to several physical processes, can very often play a determinant role in water circulation.

The circulation of the water in this type of rock prompts a fundamental question, which is linked to the identification of the fractures from where the drainage can proceed: these fractures are not always easy to identify, bearing in mind the thickness of the covering layer that sometimes overlies the rock (Afonso, M.J.C. 2003).

So, we need to resort to indirect survey methods that enable us to identify any abnormalities of hydrogeological interest.

The methods used in the current work are very low frequency – electromagnetics (VLF-EM) and radio magnetotelluric – resistivity (RMT-R). Both methods are based on radio waves from low frequency to very low frequency – from 12 kHz to 300 kHz in both methods – which are emitted by antennas located all over the world (Thierrin, J. *et al*., 1988; Turberg, P. *et al*., 1992; Turberg, P., 1993).

These waves also propagate in the basement, with the depth of penetration of their generated primary field being given by :

$$P = 503\sqrt{\frac{\rho_a}{F}} \qquad (1)$$

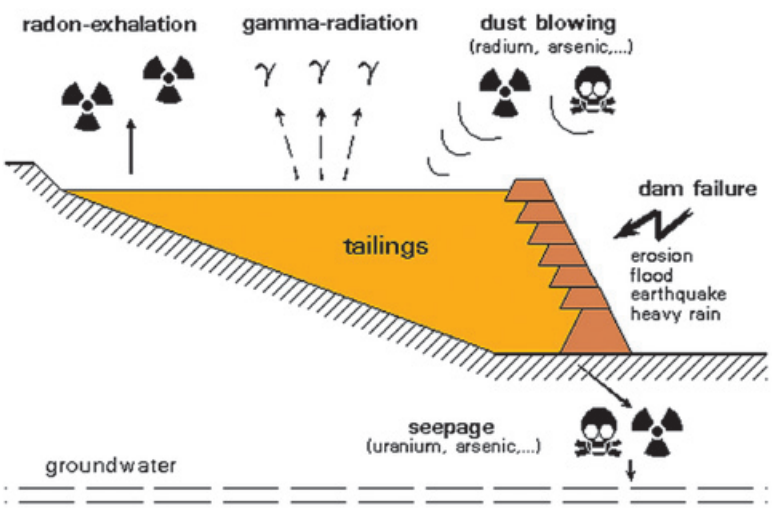

Figure 4. Some ecological and human risks associated with uranium mill tailings (adapted from http://www.wise-uranium.org/uwai.html).

where :

P - depth of penetration of the primary field generated by the radio waves (m)
ρ_a - apparent resistivity (ohm.m)
F - wave frequency (Hz).

But these waves also give rise to a secondary electromagnetic field, which depends on the nature of the material crossed and can be detected at the surface (Thierrin, J. *et al*., 1988; Turberg, P. *et al*., 1992). Consequently the resultant electromagnetic field consists of the sum of the primary and secondary fields, which are distinguished by intensity, phase and direction.

VLF-EM Method

With the VLF-EM method, special, well-adjusted devices make use of one horizontal axis coil to measure the intensity of the primary electromagnetic field (Hp), while the intensity of the secondary field (Hs) is measured through one vertical axis coil.

The equipment used was specifically developed for hydrogeological purposes by Prof. Imre Müller, of the Centre of Hydrogeology of the University of Neuchâtel (Müller, I., 1983).

It differs from commercial appliances since it continuously registers the variation of the signal. The joint use of a data logger and a GPS secures the right location of registered anomalies (Müller, I., 1983; Thierrin, J. *et al*., 1988; Turberg, P. *et al*., 1992).

The vertical components are either in phase or out of phase relative to the primary field.

The expression of the results is given by the relation Hs/Hp %, as illustrated in Figure 5.

The method permits detection of the presence of electricity-conducting bodies such as faults filled with clay materials exhibiting equally great sensitivity to other important hydrogeologic characteristics, such as lateral facies variations (Dill, A. *et al*., 1998).

The method has the additional advantage of not requiring contact with the ground –once the antenna is automatically oriented, it can be used manually or installed in vehicles.

RMT-R Method

The RMT-R method measures the electric field, E_x , in the direction of propagating radio waves (e.g. in the emitter antenna direction). The electric field is measured between two electrodes inserted in the ground at a certain distance from each other (in our work this distance is 5 meters).

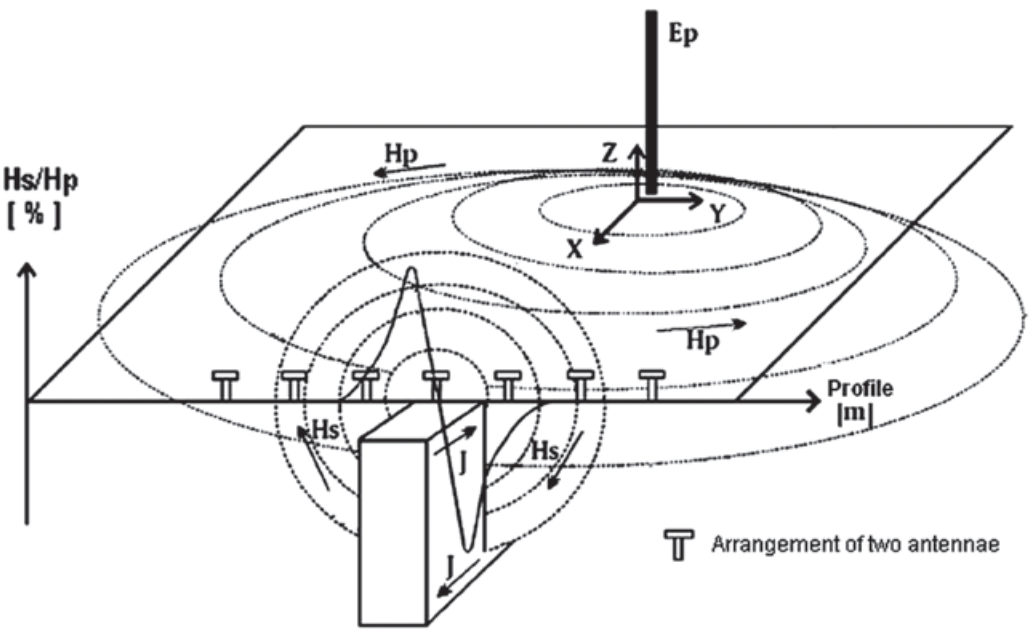

Figure 5. Basis of VLF-EM method, adapted from Turberg and Müller (1992) Reproduced from *Dill et al*. (1998).

The RMT-R method also measures the magnetic field, H_y , which is measured through a coil whose horizontal axis is normal to the emitter antenna direction.

The apparent resistivity, ρ_a, results from the application of equation (2):

$$\rho_a = \frac{E_x}{H_y}^2 \frac{1}{2\pi \ _0 F} \qquad (2)$$

where:

E_x - electric component of the resultant field (Volt/m)

H_y - magnetic component of the resultant field (Ampere/m)

μ_0 - permeability of free space (Henry/m).

F - wave frequency (Hz).

This method also measures the phase-shift, ϕ, between the electric and magnetic components. The phase-shift enables inference of the stratigraphic characteristics of the place under study: there will be a conductive layer over a resistive one if $\phi < 45º$, there will be a resistive layer over a conductive one if $\phi > 45º$, and the medium is considered homogeneous if $\phi = 45º$.

Given the fact that emitter antennas being located far apart from the receiver device, we could consider all directions of propagation as essentially parallel, which in practice reduces to only one direction. Once the device allows the simultaneous measurement of 4 frequencies, we can interpret it as supplying information from 4 depths (see Figure 6). An inversion program (FITVLF2) for the personal computer was used to obtain the real resistivities and the thicknesses of the layers traversed. Although its description is beyond the scope of this article, detailed information about the method of inversion and its implementation can be found at Fischer, G. *et al*. (1981), Fischer, G. (1985) and Thierrin, J. (1992).

Since it is a quick method that enables measurements (soundings) to be taken at 5 m intervals it allows the detection of heterogeneities, and it is possible to infer the permeability of the formations from their resistivity values, although this has not been done in the present study.

Multidirectional soundings can also be carried out to get information about the anisotropy of the studied medium.

Results and Discussion

VLF-EM

In Figure 8 we present a photographic map of the places surveyed by VLF-EM method.

The marked points show the paths walked along and color gradation indicates that the relation Hs/Hp % is (the deeper the color, the stronger the relationship Hs/Hp %):

- red color – positive Hs/Hp % relationship;
- blue color – negative Hs/Hp % relationship;
- white color - near zero Hs/Hp % relationship.

All profiles were carried out at 16 kHz frequency and some important conclusions can be drawn from their interpretation (see Figure 8).

Very negative or very positive values (Hs/Hp <-40 % or Hs/Hp> 40 %) correspond to measurements taken under the influence of high tension power lines and so they must not be considered. Negative Hs/Hp % values are usually related to major resistivity layers, whereas positive Hs/Hp % values indicate major electricity conductivity layers (for instance, the presence of clay materials).

Successive inflections of Hs/Hp % indicate fracture zones, the more important the greater the registered amplitude.

In Figure 9 we present a summarized interpretation of the obtained results, in order to illustrate the stated above. The joint interpretation of the VLF-EM results with information gathered on EDM internal reports and field reconnaissance data made it possible to draw a map summarizing the fractures in the studied area, from which main drainage trends can be established (see Figure 10, wherein places where the presence of water was noted are marked in blue).

RMT-R

Apparent resistivity and phase difference between the electric and magnetic fields were measured in RMT-R survey profiles. These profiles were defined in the sectors marked with circles, and they were quite enlightening (see Figures 10 and 11).

Figure 6. Basis of RMT-R method, adapted from Thierrin and Müller (1988). Reproduced from *Dill et al. (1998).*

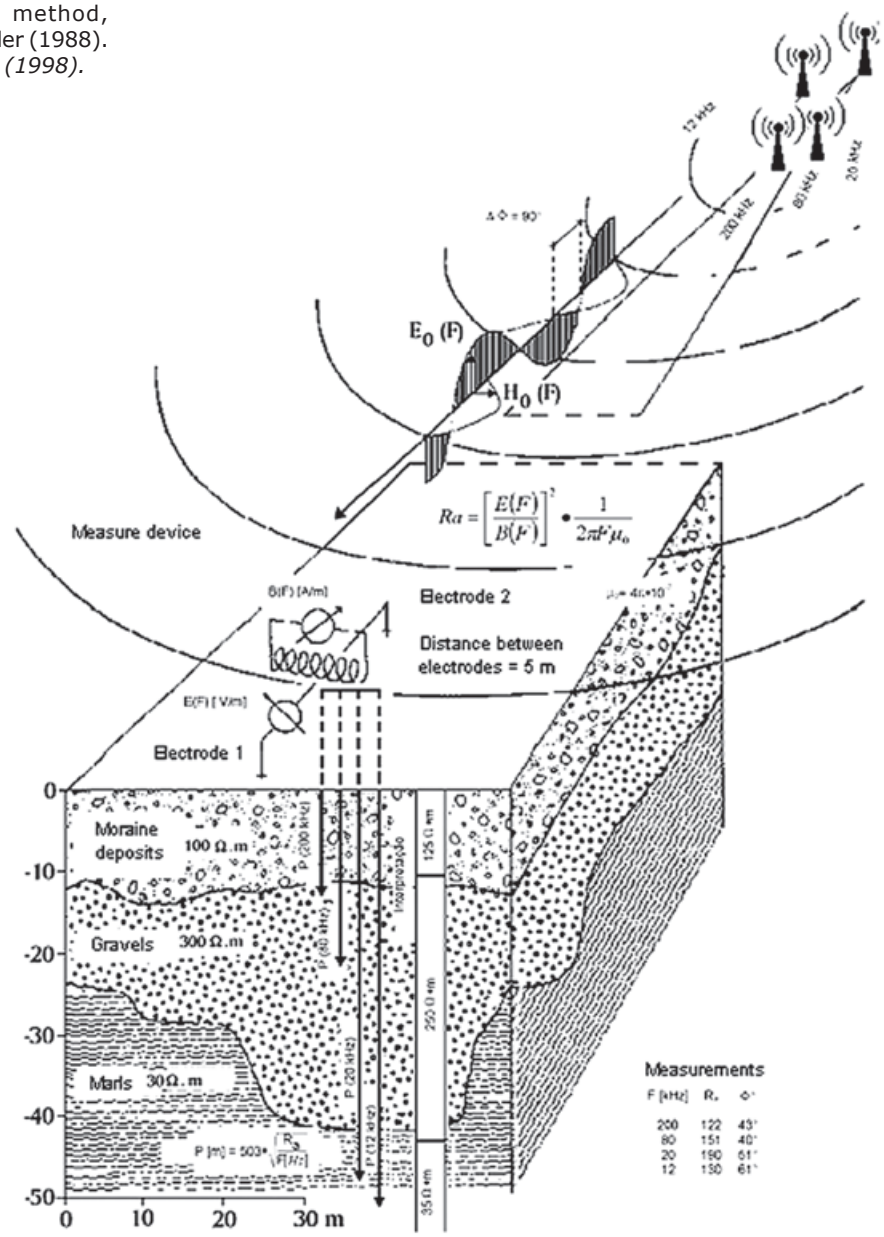

Figure 7. VLF-EM method: equipment adapted to a vehicle (Castelejo mining site).

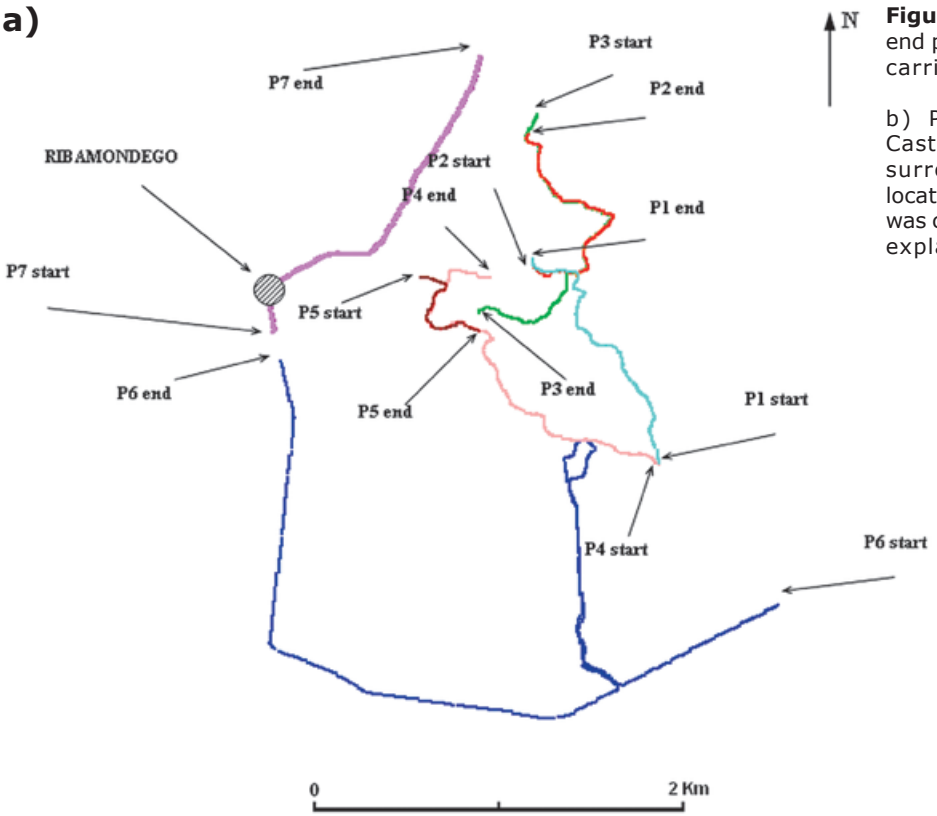

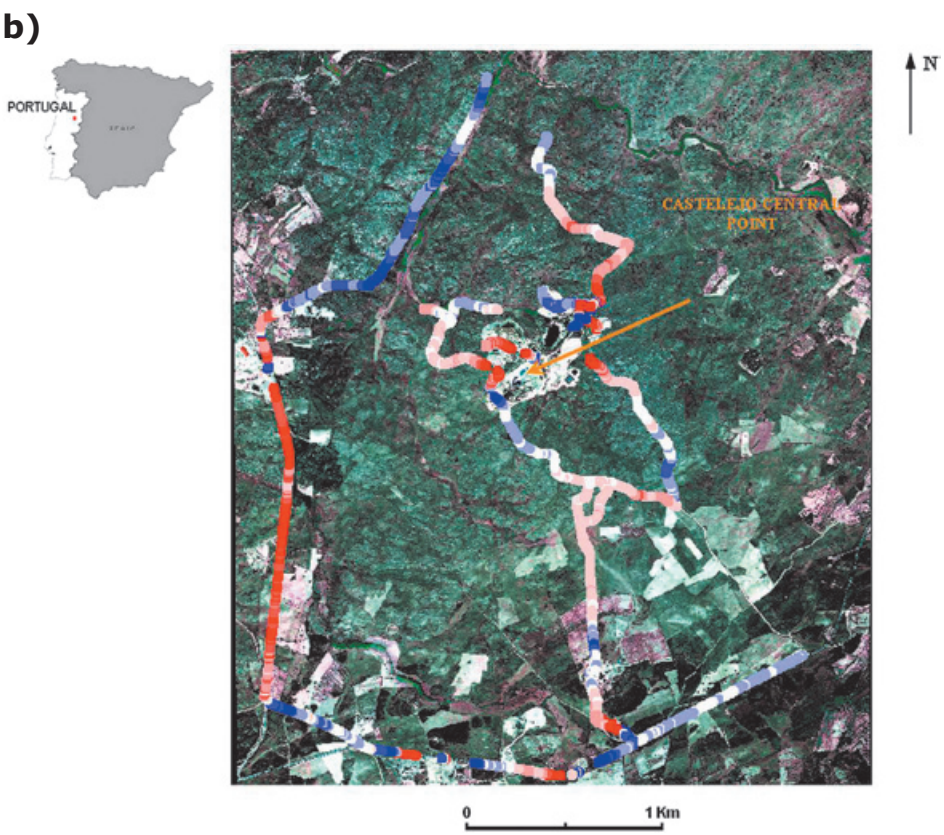

Figure 8. a) Start point and end point of the seven profiles carried out in the VLF-EM survey
b) Photographic map of Castelejo former mine site surroundings, with profile location where VLF-EM survey was conducted (color variation explained in the text; P – Profiles).

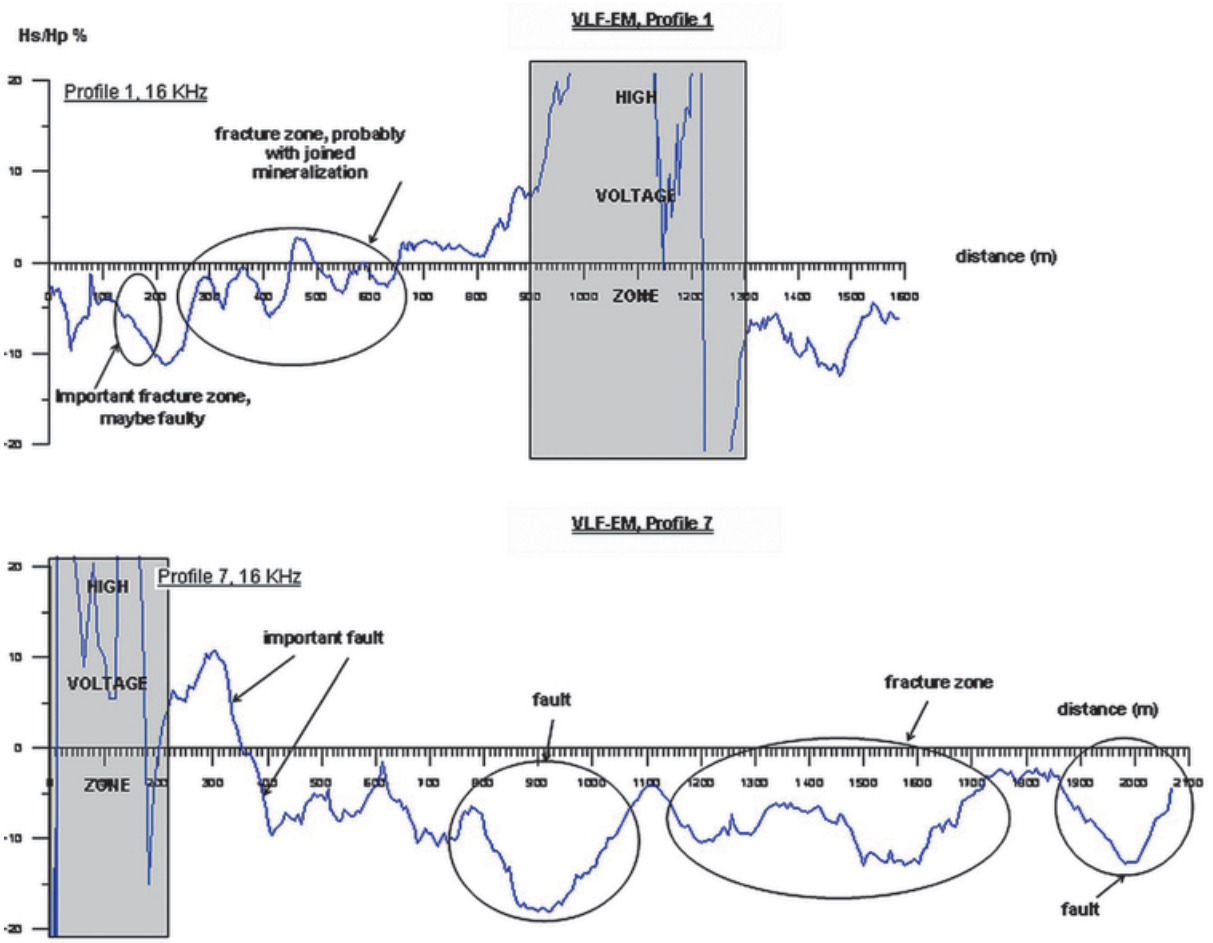

Figure 9. Interpretation of the results of the VLF-EM survey profiles.

In particular, the profiles located NW of the mining site, in the Castelejo Valley (see Figure 12), have revealed very interesting features.

After processing the obtained results using an inversion program (Fischer, G., 1985), the real resistivities and thicknesses of the different layers were computed (Figure 13). Mid sector values were calculated next.

We noted that all the profiles defined along the Castelejo Valley exhibit a decrease in resistivity with depth. Once we are away from the mineralized vein, this may suggest either more alteration of granites with depth, or a situation of deep-contamination.

The profile P1 reproduced in Figure 13 (referring to deep pink points in Figures 10 and 11) is located near the old mining site: resistivity values correspond to those obtained for almost unweathered granite blocks (with resistivity values > 1000 Ω.m) immersed in a weathered matrix (with resistivity values ≈ 700 Ω.m).

On the other side, the profile P6, also reproduced separately in Figure 13 (here referring to light green points in Figures 10 and 11) is located along the main fault valley near the confluence with the mine stream: resistivity values corresponding to a situation of very weathered rock material, decreasing with depth.

The profiles carried out along the valley that spreads out WNW from washing pools, indicate that this is a fault valley, filled in with erosion material. As before mentioned, all profiles show a decrease of resistivity not only with depth but also as we go away from the mine towards the main fault valley (e.g. from P1 to P6, see figure 12).

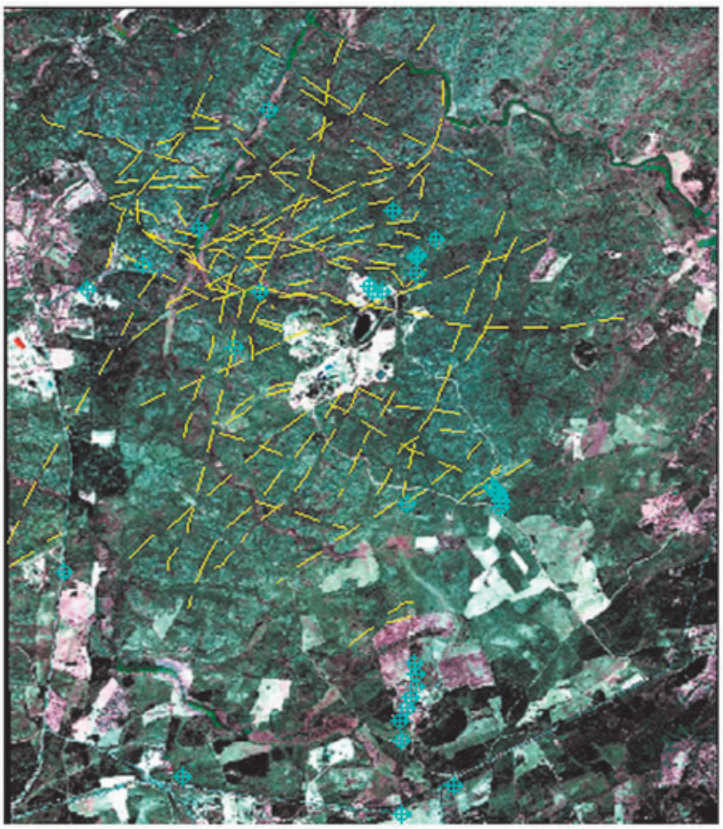

Figure 10. Fracture map of the studied area.

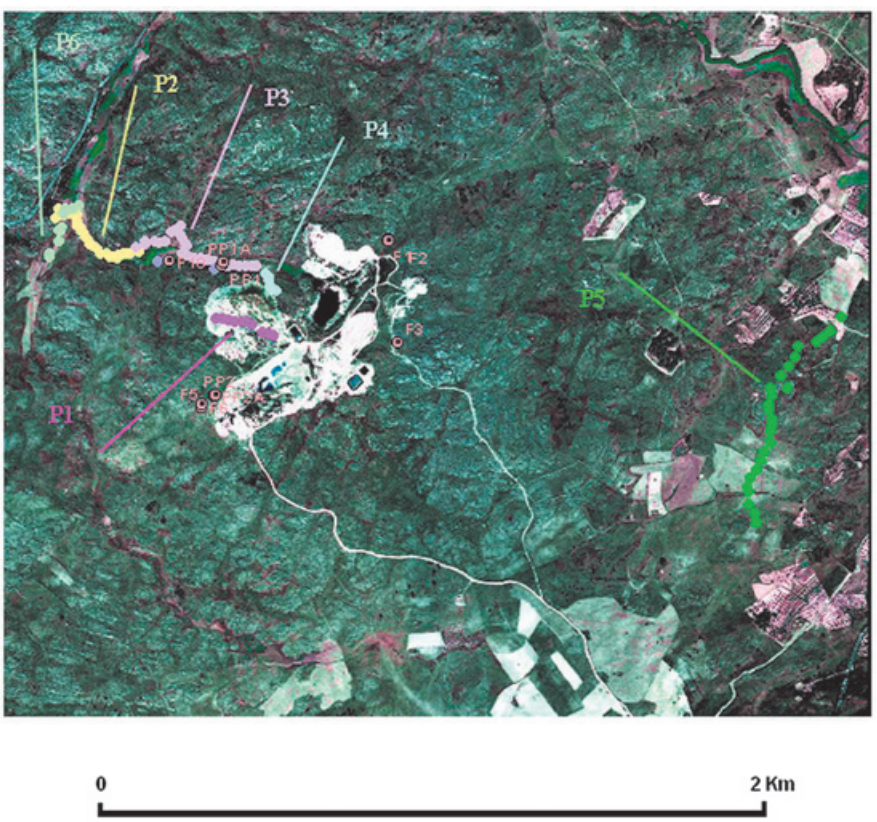

Figure 11 – Location of all RMT-R profiles performed in the surroundings of Castelejo mining site (P – Profiles).

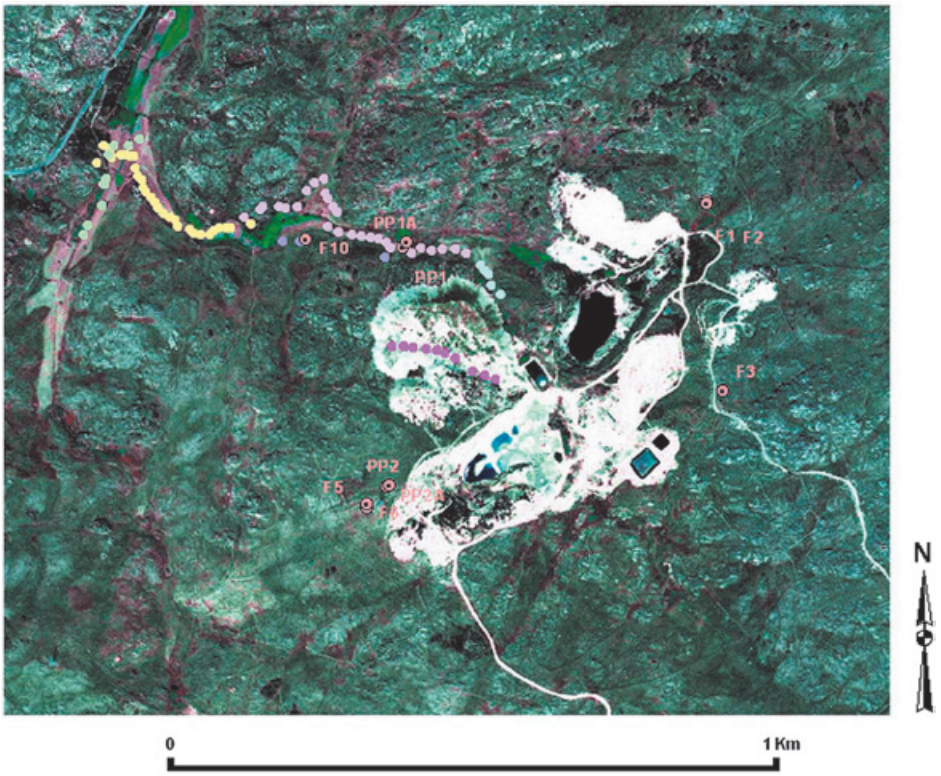

Figure 12 – Location of RMT-R profiles performed in the Castelejo Valley.

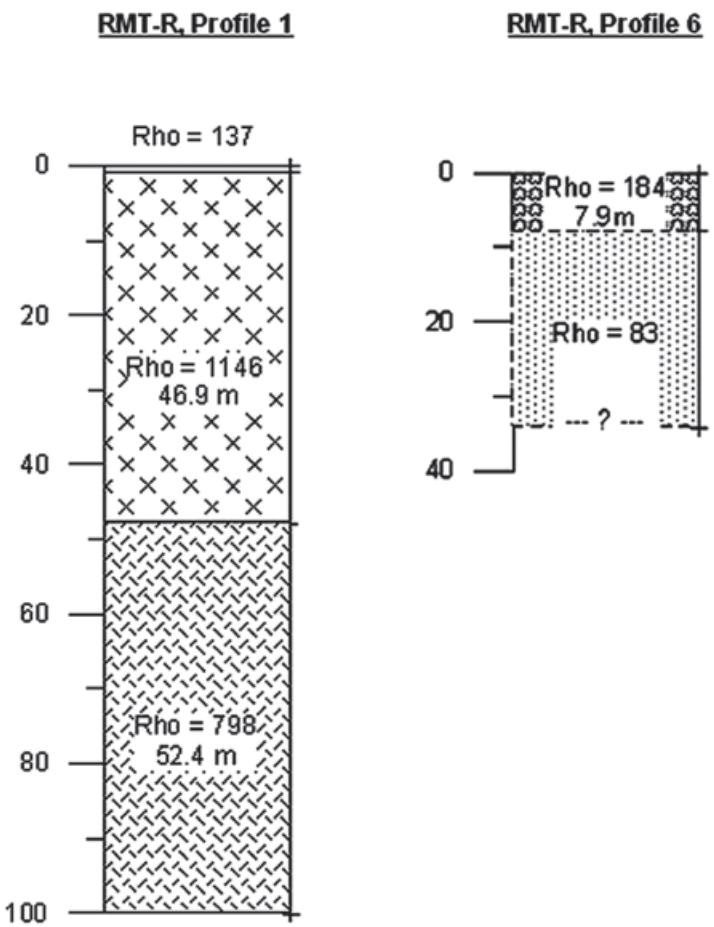

Figure 13. The profile P1 is located near the old mining site, with resistivity values.

Conclusions

At the beginning of the study it was known the situation in terms of regional tectonics, which was known complex for being associated with a number of episodes of tardi-Hercynian fracturing, as well with the Alpine tectonics.

In order to better characterize the underlying geology of the old Castelejo mine, two geophysical surveying campaigns were conducted at the site. Both the results of the first campaign (VLF-EM results) and the references consulted, particularly in EDM internal reports, pointed to the presence of faults and fractures which might constitute the main pathways of superficial and underground drainage.

In the second campaign, measurements of RMT-R were performed to the WNW and ESE of the centre of exploration. Apparent resistivity and phase difference between the electric and magnetic fields were the measured values. The obtained values were projected graphically and processed, after which real resistivities and thicknesses were determined through the use of an inversion program.

After matching the literature data with the data obtained during field work, it was concluded that the direction of maximum compressive stress, s_1, located NNW-SSE to NW-SE, where extension fractures are developed, should be the one wherein groundwater flows more easily, since the larger openings of the fractures provide a better flow.

However, it was not possible to establish a direct correspondence between real resistivity values and permeability values, which, although outside the scope of this article, may be relevant for v.g. hydrogeological purposes.

All profiles also reveal a singular situation – their resistivity values decrease with depth.

This can be due to natural causes (more weathered layers) or it can indicate a situation of deep contamination with acid drainage (increased mineralization).

In fact, we are in the presence of a former uranium exploration, in which ore acid leaching took place in a flooded open sky, with a number of negative implications in the surroundings, particularly over groundwater. Treatment operations of the mine water still occur. However, any risks to populations seem weak, given the isolation of the area in terms of population.

Also the use of water seems to be aimed to agricultural purposes rather than for human consumption.

This point will be addressed in the future through the implementation of a hydrochemical monitoring plan.

Acnowledgements

The assistance of Amélia Dill was deeply appreciated

References

Abranches M.C.B., Canilho M.H., 1982. Determinação de idade pelo método do Rb-Sr de granitos antigos portugueses. *In* Memórias da Academia das Ciências de Lisboa. - Tomo XXIV (1981/82), p. 17-32

Afonso M.J.C., 2003, Hidrogeologia de rochas graníticas da região do Porto (NW de Portugal). *Cadernos Lab. Xeolóxico de* Laxe. A Coruña. 28, pp. 173-192.

Araújo M.A., 2002, Tópicos da Matéria da disciplina de Geografia Física de Portugal. *http://web.letras.up.pt/asaraujo/geofis/geofis.html.*

Carvalho D., Goinhas J., Schermerhorn L., 1971, Principais jazigos minerais do Sul de Portugal. I Congresso Hispano-Luso-Americano de Geologia Económica, Livro-Guia da Excursão nº 4, Direcção-Geral de Minas e Serviços Geológicos, Lisboa, 94 pp.

Carvalho J.M., 2006, Prospecção e pesquisa de recursos hídricos subterrâneos no Maciço Antigo Português : linhas metodológicas. Tese de Doutoramento, Universidade de Aveiro, 312 pp.

Cerveira A., 1951, Sobre a metalogenia do urânio em Portugal. *Boletim da Sociedade Geológica Portuguesa*, 8, 3, pp.141-182

Daniels J., Roberts R., Vendl M., 1995, Ground penetrating radar for the detection of liquid contaminants. *Journal of Applied Geophysics,* 33, Elsevier, 13 pp.

Dill A., Müller I., Costa A.M., Monteiro J.P., 1998, Importância do uso de métodos geofísicos electromagnéticos Very Low Frequency Electromagnetics (VLF-EM) e Radio Magnetotelluric-Resistivity (RMT-R) no estudo de aquíferos cársicos do Alentejo e do Algarve. 4º Congresso da Água, A.P.R.H., Lisboa, 10 pp.

Ferreira M.P., 1971, Jazigos uraníferos portugueses, jazigos de Au-Ag-sulfuretos do Norte de Portugal. I Congresso Hispano-Luso-Americano de Geologia Económica, Livro-Guia da Excursão nº 5, Direcção-Geral de Minas e Serviços Geológicos, Lisboa, 81 pp.

Fischer G., Schnegg P.-A., Peguiron M., Le Quang B., 1981, An analytic one-dimensional magnetotelluric inversion scheme. *Geophysical Journal of the Royal Astronomical Society,* 67 2, John Wiley & Sons Ltd, pp. 257-278.

Fischer G., 1985, Some Remarks on the Behaviour of the Magnetotelluric Phase. *Geophysical Prospecting*, 33 (5), John Wiley & Sons Ltd , pp. 716-722.

Kearey P., Brooks M., Hill I., 2002, An Introduction to Geophysical Exploration. Blackwell Science Ltd., 281 pp.

Lottermoser B., 2003, Mine wastes, characterization, treatment and environmental impacts. Springer-Verlag Berlin Heidelberg, 277 pp.

Milsom J., 2003, Field geophysics. John Wiley & Sons Ltd, West Sussex, England, 249 pp.

Müller I., 1983, Anisotropic properties of rocks detected with electro-magnetic VLF (Very Low Frequency). International Symposium on Field measurements in Geomechanics. Zurich, Switzerland, special publ., pp. 273-282.

Neiva J.M.C., 1995, Jazigos portugueses de minérios de urânio. *Memórias* 4, IV Congresso Nacional de Geologia, Museu e Laboratório Mineralógico e Geológico, Faculdade de Ciências, Universidade do Porto, pp. 575-579

Nunes A., 1983, A geologia económica e a indústria mineira através dos tempos. *Geonovas* 5, pp. 67-114.

Oliveira V., 2010, Modelação hidrogeológica da área mineira abandonada de Castelejo (Guarda). Tese de Doutoramento. Faculdade de Ciências Universidade de Lisboa, 211 pp.

Rapantova N., Hrkal Z., (editors), 2008, Mine water and the environment. Proceedings of 10th Internacional Mine Water Association Congress. VSB-Technical University of Ostrava, Faculty of Mining and Geology. Olomouc, Czech Republic, 628 pp.

Ribeiro A., Antunes M.T., Ferreira M.P., Rocha R.B., Soares A.F., Zbyszewski G., Moitinho de Almeida F., Carvalho D. e Monteiro, J.H., 1979, Introduction à la géologie générale du Portugal. Serviços Geológicos de Portugal, Lisboa, 114 pp.

Teixeira C., 1966, A evolução do território português no decurso dos tempos geológicos. Palestra *Rev. Ped. Cult.*, 28, Lisboa, pp. 111-157.

Teixeira C., Carvalho B., Santos P., Peres M., Barros R., 1967, Carta geológica de Portugal à escala 1:50.000, Folha 17-D (Gouveia) e notícia explicativa. Serviços Geológicos de Portugal, Lisboa, 28 pp.

Thierrin J., Müller I., 1988, La méthode VLF-Résistivité multifréquence, un example d'exploration hydrogéologique dans un synclinal crétacé à la Brévine (Jura neuchâtelois). *Annales Scientifiques de l'Université de Besançon*, Mémoire Hors de Série, nº 6, Quatrième Colloque d´Hydrogéologie en Pays Calcaire, Besançon, France, 17-25.

Turberg P., 1993, Apport de la cartographie radiomagnetotellurique a l´hydrogeologie des milieux fracturés. Thèse de Doctorat. Faculté des Sciences de l'Université de Neuchâtel, Suisse, 233 pp.

Turberg P., Müller I., 1992, La méthode inductive VLF-EM pour la prospection hydrogéologique en continu du milieu fissure. *Annales Scientifiques de l'Université de Besançon*, Mémoire Hors de Série, nº 11, Cinquième Colloque d´Hydrogéologie en Pays Calcaire et en Milieu Fissuré, Neuchâtel, Suisse, 207-214.

United States Environmental Protection Agency, 2007, Technical report on technologically enhanced naturally occurring radioactive materials from uranium mining – Volume 2: investigation of potential health, geographic and environmental issues of abandoned uranium mines. U.S. Environmental Protection Agency, Office of Radiation and Indoor Air, Radiation Protection Division, Washington, DC, USA.

Younger P., Robins N., (editors), 2002, Mine water hydrogeology and geochemistry. *Geological Society Special Publication*, 198, London, 396 pp.

Geofísica Internacional (2014) 53-2: 153-162

Original paper

Sensitivity of the surface temperature to changes in total solar irradiance calculated with the WRF model

Carolina Cipagauta*, Blanca Mendoza and Jorge Zavala-Hidalgo

Received: January 14, 2013; accepted: September 03, 2013; published on line: April 01, 2014

Resumen

En este trabajo se estima la sensibilidad de la temperatura del modelo WRF a cambios en la Radiación Solar Total (RST). Las simulaciones se realizaron para una región centrada en el Atlántico norte, incluyendo partes del Este de Norteamérica, Oeste de Europa y Noroeste de África. Para esto, se realizaron 4 simulaciones iguales, donde el único parámetro que se modificó fue la RST. Adicionalmente, se realizó una quinta simulación donde se cambiaron las condiciones iniciales atmosféricas, para comparar el efecto del cambio de la RST sobre la temperatura con el de un cambio en el día de inicio de la integración. Se compararon promedios mensuales de temperatura para cada simulación obteniéndose que tanto los cambios en las condiciones iniciales como los de la RST tienen un impacto medible en la temperatura de la región de estudio. Se presenta también una estimación de la sensibilidad del modelo usando parámetros adimensionales. Con estos experimentos numéricos encontramos algunos rasgos que permitirían distinguir entre los efectos de cambios de la RST y en las condiciones iniciales sobre la temperatura. Sin embargo, los cambios debidos al RST son de la misma magnitud que los cambios debidos a las variaciones en las condiciones iniciales. Se observa también que, en promedio y sobre toda la malla, la temperatura promedio no sufre cambios significativos ni ante cambios de la RST ni ante los de las condiciones iniciales.

Palabras clave: WRF, sensibilidad de la temperatura, radiación solar total, Atlántico Norte, técnica de parámetros adimensionales.

Abstract

The temperature sensitivity of the WRF model to changes in Total Solar Irradiance (TSI). The simulations were performed for a region centered over the North Atlantic Ocean, including portions of Eastern North America, Western Europe and Northwest Africa. Four simulations were run with different TSI values. Also, a fifth simulation was performed in which we varied the initial atmospheric conditions, in order to compare the effect on the temperature of both, changes in the TSI and initial atmospheric conditions. Comparing temperature monthly averages we found that changes in TSI and in the initial conditions have a measurable impact on temperature in the region of study. The sensitivity of the model using non-dimensional parameters was also estimated. The numerical experiments show some features that might allow to distinguish between the effects on the temperature due to changes in TSI from those caused by initial conditions. However, TSI changes are of the same order of magnitude than those of disturbances in the initial conditions. We also found that the mean monthly values of temperature over the full grid, did not present significant variations due to changes of either initial conditions or TSI.

Key words: WRF model, sensivity temperature, total solar irradiance, North Atlantic, non-dimensional parameters technique.

C. Cipagauta*
Posgrado en Ciencias de la Tierra
Universidad Nacional Autónoma de México
Delegación Coyoacán, 04510
México D.F., México
*Corresponding author: carocipa@gmail.com

B. Mendoza
Instituto de Geofísica
Universidad Nacional Autónoma de México
Delegación Coyoacán, 04510
México D.F., México

J. Zavala-Hidalgo
Centro de Ciencias de la Atmósfera
Universidad Nacional Autónoma de México
Delegación Coyoacán, 04510
México D.F., México

Introduction

Before the spatial era, it was believed that the solar radiation reaching the top of the atmosphere was constant with an approximate value of ~1370W/m^2. Since 1978, the radiometers on board of satellites have shown that the solar radiation is not constant, as it presents an increase of ~0.1% between the minimum and the maximum of the 11-years solar activity cycle (Fröhlich, 2000). The Total Solar Irradiance (TSI) is the total electromagnetic power emitted by the Sun per unit area of cross section arriving at the mean Earth-Sun distance [Tiwari and Ramesh, 2007].

The TSI variations can affect the Earth´s climate through their direct influence on the mean global temperature or in some other indirect ways (e.g. Gray *et al*., 2010). General Circulation Models (GCM) estimate that a 2% increase of the TSI could produce an increase of ~4ºC in temperature. If we assume a linear scale, then 0.1% would produce a temperature increase of 0.2ºC [CGER,1994]. Comparing this temperature change with the temperature increase in the range of 1.5ºC to 4.5ºC estimated by the IPCC [2007], we could conclude that the temperature changes due to the 11- year TSI cycle change is small.

The stratospheric changes induced by the solar activity can influence the troposphere and the climate. Simulations using GCM suggest that solar UV changes modify the stratospheric ozone content and the temperature, affecting its latitudinal gradient. This modifies the stratospheric winds altering the tropospheric stability and impacting in several tropospheric dynamic processes including the intensity of the Hadley cell in low and subtropical latitudes and the low extra-tropical pressure systems. Although some GCM climatic simulations estimate a decrease of mean global temperature of 0.46ºC for a 0.25% TSI reduction, some surface regions could cool and others could heat more than 1ºC as a result of the advective changes produced by the differential heating of land and oceans [Haigh *et al*., 2005; Meehl *et al*., 2008; Barriopedro *et al*., 2008; Lee *et al*., 2008].

The aim of this paper is to estimate the sensitivity of the surface terrestrial temperature to changes in the TSI using the Weather Research and Forecasting Model (WFR). Although the WRF model can estimate other variables (Cipagauta *et al*., 2013), we choose the temperature as it is the most widely used climatic variable. We applied the model under several conditions: We use a regional model to observe the impact on México, although the boundary conditions constrain the behavior of the region, it allows us to use a higher resolution. The WRF model is applied only to the atmosphere, the sea surface temperature is prescribed. Finally, due to the computational cost required for each experiment the model was only ran for a single year.

The Weather Research and Forecasting Model (WRF)

The WRF model is a next-generation mesoscale non-hydrostatic numerical weather prediction system designed to serve both operational forecasting and atmospheric research needs. Several institutions support the WRF project in order to achieve a better understanding of atmospheric processes and improved weather prediction [Skamarock *et al*., 2008]. In this study we used the WRF version 3.1.1 with the Advanced Research WRF (ARW) core. In all the simulations we applied Mercator projection and the schemes described in Skamarock *et al*. [2008] as follows:

- WRF Single-Moment 3-class for microphysics in a simple and efficient scheme that considers ice, snow and the Graupel processes, which are adequate for real mesoscale simulations.

- The Kain-Fritsch scheme for cumulus parameterization.

- The Yonsei University (YSU) scheme for the planetary boundary layer.

- The Rapid Radiative Transfer Model (RRTM) for the long-wave radiation.

- The Dudhia scheme for the short-wave radiation.

Sensitivity of the surface temperature

Four numerical simulations were run to investigate the impact of TSI on surface temperature. A fifth experiment was introduced to compare temperature sensitivity to changes in TSI and initial boundary conditions. We aim to estimate the variability of the temperature in each case. The simulation that corresponds to the base year represents the typical conditions of the region of interest. To study the sensitivity of the WRF model surface temperature due to TSI variations, we used non-dimensional parameters that estimate the surface temperature change as responses to radiation variations.

Description of Non-dimensional parameters technique

To relate TSI and temperature, we applied the radiative balance equation, widely used in atmospheric models. This relation is basically the Stephan-Boltzman expression for the black body radiation

$$(1-\alpha)S = 4\sigma\bar{T}^4 \qquad (1)$$

where α the planetary albedo, S the solar radiation, σ is the Stephan-Boltzman constant, and T is the mean effective planetary temperature.

From equation (1), we calculated a non-dimensional parameter defined as

$$\beta_T = 1 - k_1 \frac{\partial T}{\partial S} \qquad (2)$$

where k_1 is a constant to be selected and T is the mean effective temperature. This parameter is a measure of the sensitivity of the corresponding variable [Szirtes, 2006].

In equation (2) the partial derivative is estimated by keeping as constants the other variables that could depend on T, and k_1 is choose in such a way that β_T is non-dimensional. Using equation (1) we find the partial derivative in (2), then we choose k_1 as the inverse value of the partial derivative evaluated in a reference condition of radiation and temperature. Then the sensitivity parameter associated to temperature becomes:

$$\beta_T = 1 - \left(\frac{T_0}{T}\right)^3 \qquad (3)$$

where T is the model temperature for the radiative condition of our interest, T_0 is the temperature of the base radiation. T and T_0 can be daily or monthly averages, obtained from the model for different zones as well as over the full region of study, depending on the spatial and temporal behavior that we choose to examine

Simulation configuration

We choose a base year: September 1st of 1983 to August 31st of 1984. In this year the Sun was in the descending phase of its activity cycle showing intermediate activity, as it is approximately half way between the maximum and the minimum of solar activity. The simulation grid (see Figure 1) consists of a single domain centered over the North Atlantic Ocean between 0-100ºW and 5-60º N, with a resolution of 30 km, the region includes portions of Eastern North America, Western Europe and Northwest Africa. The initial and boundary conditions were taken from the NCEP/NCAR reanalysis project (Kalnay *et al*., 1996). We focus the analysis on five zones of the domain, where the surface temperature

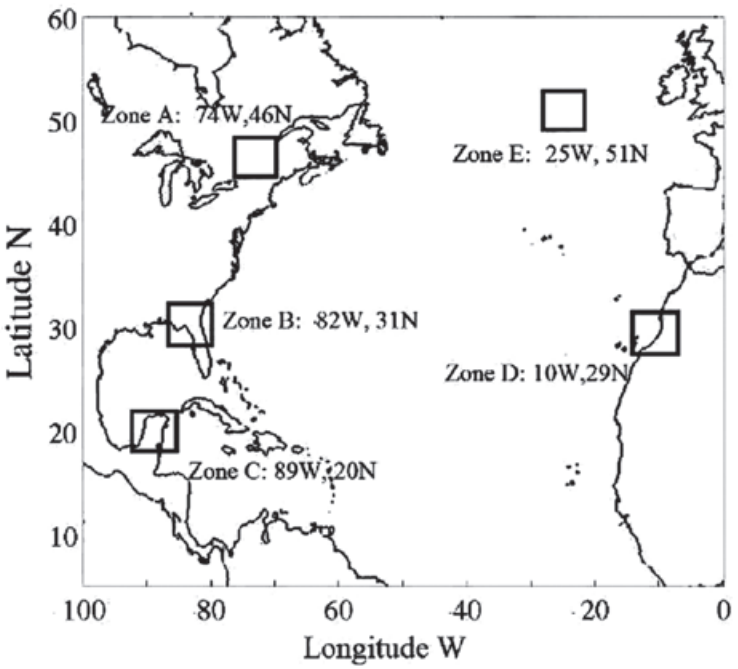

Figure 1. Domain used in the numerical simulations. We divided the domain in five zones, the corresponding coordinates appear in the center of the squares.

variations appear more noticeable. One exception was zone C, which was chosen due to the locations particular interest in this study.

The intent of this study was to analyze temperature sensitivity to TSI variations using WRF model. Four simulations were run, each one with a fixed TSI value that vary among the simulations according to Table 1. The first simulation corresponds to the control experiment or base year, with a fixed TSI value similar to the one measured for the year 1983, which was a year half with a value between the maximum and the minimum of the 11-years solar cycle phase (http://www.pmodwrc.ch/php?topic=tsi/composite/SolarConstant). The measurements since the satellite era (1978) indicate that the TSI increase between the minimum and the maximum of the 11-years solar activity cycle ~0.1%, this is mainly due to an interplay between superficial magnetic dark features such as sunspots and bright features such as faculae and network elements (Fröhlich, 2006). A higher solar activity year (HR) with a TSI increased by 0.05% corresponds to the second simulation. A year of lower solar activity (LR) with a TSI reduced by 0.05% corresponds to the third simulation. The fourth simulation was run with an estimate of the TSI for the next two solar activity cycles (Mendoza *et al*., 2010). This estimate indicates a period of lower solar activity and therefore lower solar irradiance. We named this numerical experiment as the future minimum radiation (FMR). Finally we performed a fifth simulation, using the control (base year) experiment but introducing the atmospheric conditions of the 2nd of September, 1983 as the initial conditions. We run this last simulation in order to compare the effects due to the TSI changes against the effects due to a variation of initial conditions.

Table 1. TSI values used in the four WRF simulations.

Experiment	TSI (W/m^3)
Base	1366.2
HR	1366.8
LR	1365.5
FMR	1364.9
CI	1366.2

We performed two different analyses with the surface temperature model results using monthly and daily averages. In the first analysis we calculated the monthly average differences between the HR, LR and FMR and the base year, those are D_HR for HR-Base, D_LR for LR-Base and finally D_FMR for FMR-Base, respectively. In the same way we indicate as D_IC the monthly average differences between the year with the changed initial conditions and the base year, that is D_IC = IC-Base. The second analysis is based on the calculation of the non-dimensional sensitivity parameter. We averaged the daily and monthly surface temperature means over the region of study. This average is used to calculate the sensitivity parameter through Equation (3), we take T_0 as the base year temperature over the whole domain and T is the model temperature over the whole domain.

Results

The monthly mean surface temperature differences (D_HR, D_LR, D_FMR and D_IC), from September 1983 to August 1984, for each simulation are shown in figures 2, 3 and 4. Larger changes occur in latitudes higher than 30º N. The changes are observed on the Eastern US and Canada and Northwest Africa. In low latitudes (5º - 10º N) the differences are smaller compared to those observed at higher latitudes. Larger positive differences occur in November and June on the Eastern US and Canada and negative differences, also in November, occur on Northwest Africa.

In these plots, variations of surface temperature are noticeable for each case during the year of study. However, the variations observed for D_HR, D_LR and D_FMR are of the same magnitude as those corresponding to variations in the initial conditions D_IC. Then to determine if the model is more sensitive either to TSI changes or to changes in the initial conditions, we use the technique of dimensionless parameters.

In Figures 2-4 we also see variations in some continental zones in low latitudes. Those changes are usually smaller than in higher latitudes. When we calculate the monthly surface temperature averaged over the full area of study (see Figure 5a), i.e. the simulation grid, the five simulations do not show meaningful differences; i.e. the base, HR, LR and FMR have the same monthly mean temperature over the full grid. This can be due to the fact that the zones where there are large differences are small compared to the zones where the differences are smaller. If we compute the monthly average for each one of the five zones (A, B, C, D and E) we found larger monthly differences. For instance in zones A, C, D and E there is a difference of

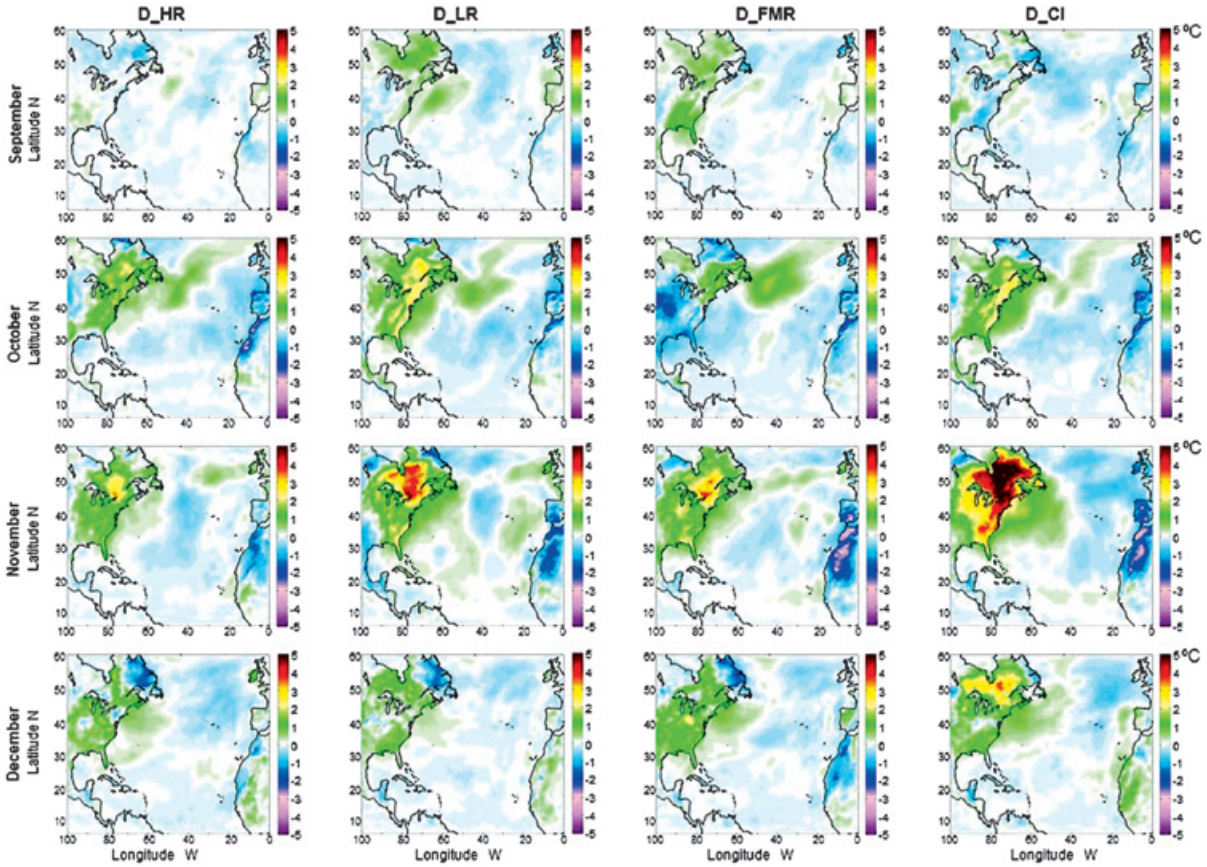

Figure 2. Average monthly surface temperature differences (ºC) for September, October, November and December, 1983. The first column shows D_HR, the second D_LR, the third D_FMR and the fourth D_CI.

at least 1ºC in November and June, while in January and March the differences are smaller (see figs. 5b, 5d, 5e and 5f).

To quantify these differences the daily and monthly temperature sensitivity of the WRF model to changes in TSI using Equation (5) was computed. To calculate the daily sensitivity (Figure 6) over the area of study (Figure 5a) and the five zones (Figures 5b to 5f), we use T_0 as the base year daily average temperature of the area, and T as the daily average temperature in the area for the different TSI values. Also, the monthly temperature sensitivity over the area of study (Figure 7a) and the five zones (Figures 7b to 7F) was computed; here T_0 is the base year monthly average temperature and T is the monthly average temperature in the area for the different TSI values. In Figures 6 and 7, the curves for the various numerical experiments are different. Although the variations are small we notice that the temperature was more sensitive in November and June as we also notice in Figures 2 to 4. The average sensitivity of the temperature for each of the simulations is shown in Table 2. Figures 6 and 7 show that the sensitivity is positive for the various TSI, but it is negative for changes of initial conditions during November and June.

Finally, to complement the analysis made for the temperature, although is not the main purpose of this article to do a comprehensive analysis of all the variables that are available from the numerical simulations, we present results of: latent heat, sensible heat, surface pressure, and precipitation. Figure 8 shows the monthly average differences between the HR, LR and FMR and the base year, those are D_HR for HR-Base, D_LR for LR-Base and finally D_FMR for FMR-Base, respectively of the variables mentioned above (Cipagauta *et al*., 2013). Since our temperature analysis reveals that the month of November 1983, has larger differences with respect to the base year, we restrict the presentation of the results of the additional variables to this month. These results show that changes in the TSI modify

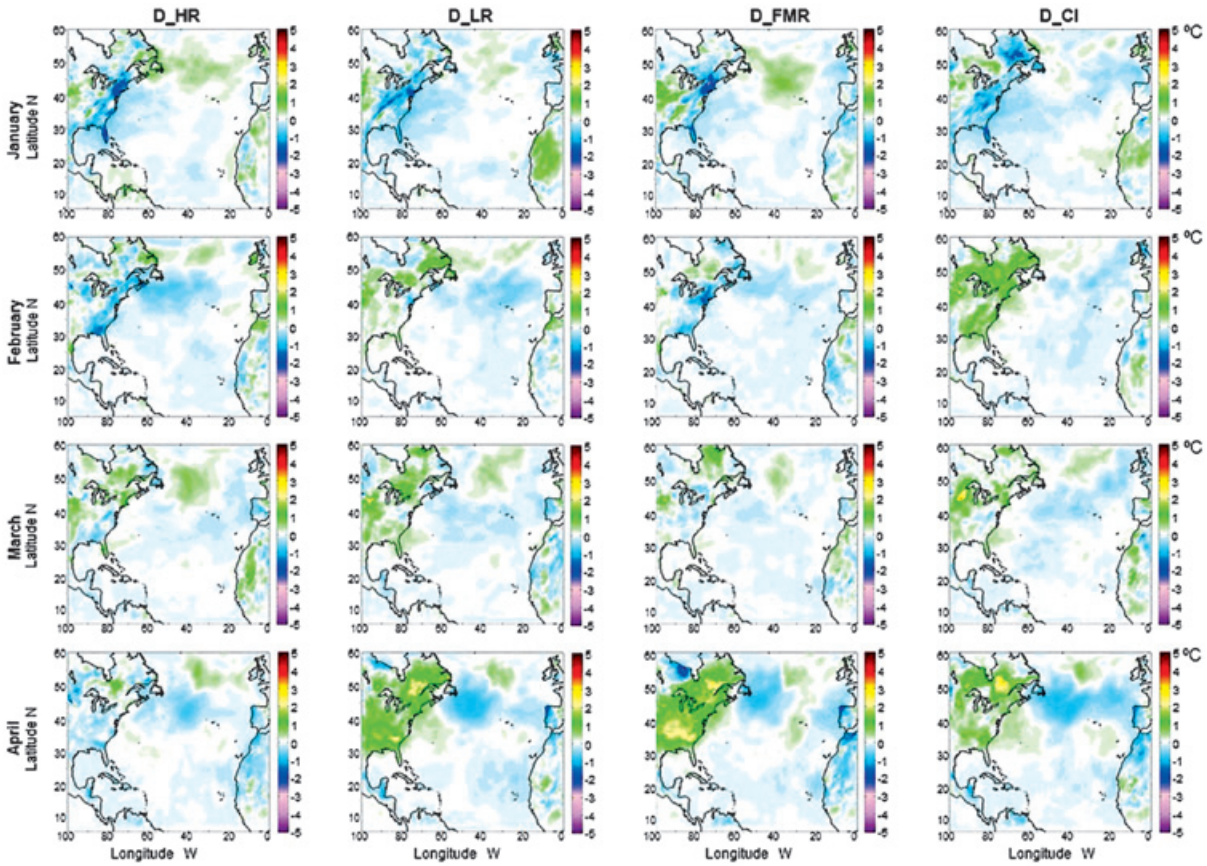

Figure 3. Average monthly surface temperature differences (ºC) for January, February, March and April, 1984. The first column shows D_HR, the second D_LR, the third D_FMR and the fourth D_CI.

the temperature as well as other variables. Figure 8 shows that the largest changes in these variables also occur at higher latitudes. Changes of latent heat, sensible heat, and surface pressure occur mainly in the ocean rather than in the continents.

Conclusions

Based on predictions of GCM and the supposition of linearity, it was expected that an increase (decrease) in TSI would cause an increase (decrease) in surface temperature. However, Figures 2 to 4 show that this is not the case, for instance, in November and June for the three different values of TSI the temperature in Northeast EU and Canada increases, but the temperature change is larger for the FMR, while in Northwest Africa for the three scenarios of TSI there is a decrease in temperature, being larger during the FMR. Some studies using GCM suggest that some regions of the Earth´s surface could cool and others could heat by least 1ºC as a results of changes caused by the differential heating of the land and ocean [Haigh *et al*.,2005; Meehl *et al*., 2008; Barriopedro *et al*., 2008; Lee *et al*.,2008]. Our results seem to support this suggestion.

However, temperature variations observed in the numerical experiment IC, are similar to those that occurred in experiments in which the TSI was varied, in the sense that the changes are observed in the same zones and of the same order of magnitude. However, the calculated model sensitivity shows that the sign corresponding to the TSI variations is opposite to the sign of the change in initial conditions (Figure 6a, 7a). This would suggest that in this model the temperature changes observed due to different conditions of TSI are different from variations in the IC. Although we have only one IC experiment, this gives an idea of the order of magnitude expected for the differences that can be found for a small change in the initial conditions.

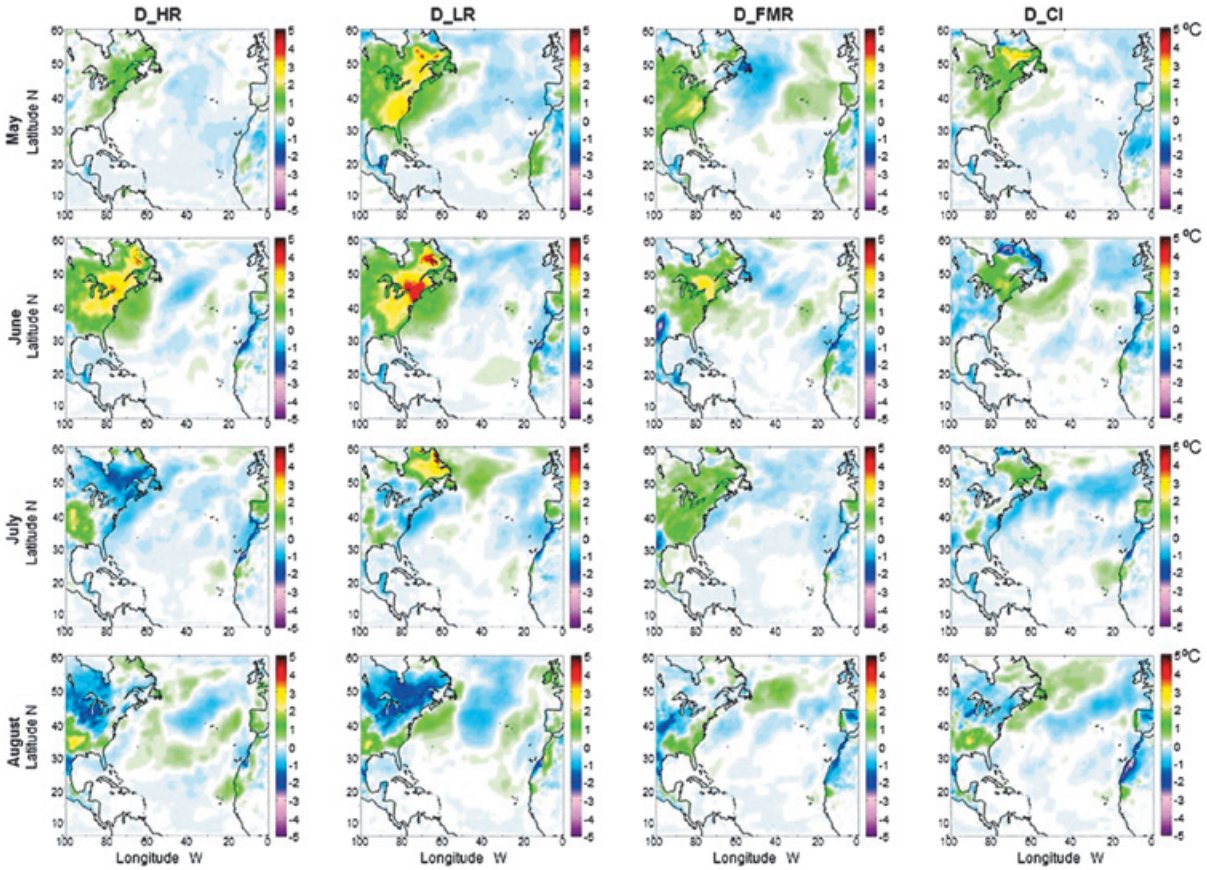

Figure 4. Average monthly surface temperature differences (ºC) for May, June, July and August 1984. The first column shows D_HR, the second D_LR, the third D_FMR and the fourth D_CI.

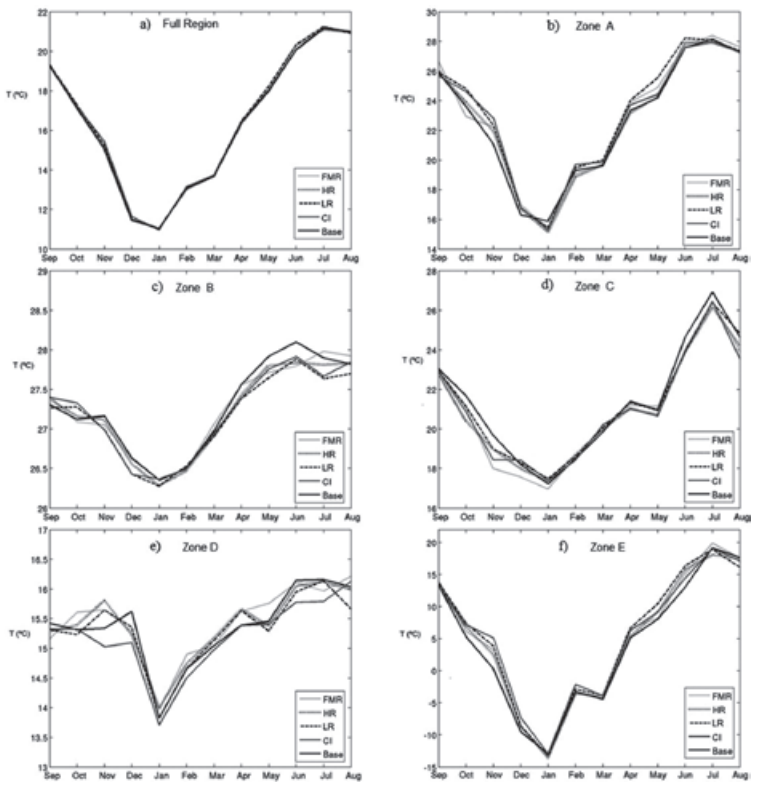

Figure 5. Monthly average temperature (ºC) for five simulations in: a) The whole area of study. b) Zone A. c) Zone B. d) Zone C. e) Zone D. f) Zone E.

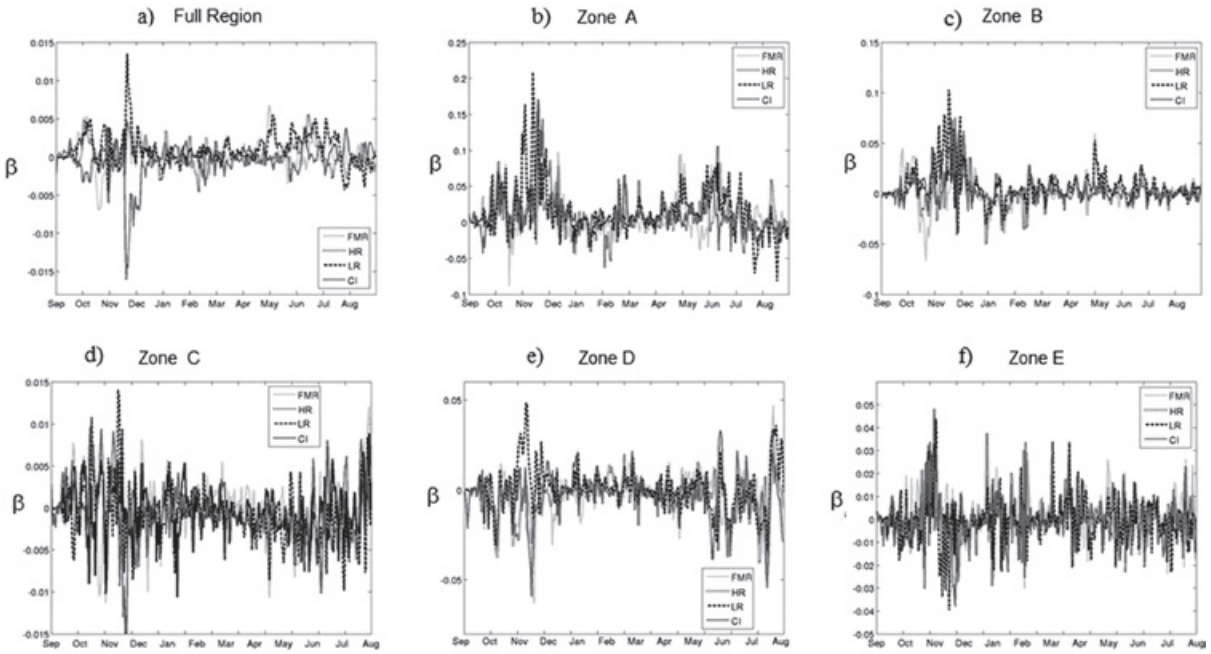

Figure 6. Monthly temperature sensitivity in: a) The whole area of study. b) Zone A. c) Zone B. d) Zone C. e) Zone D. f) Zone E.

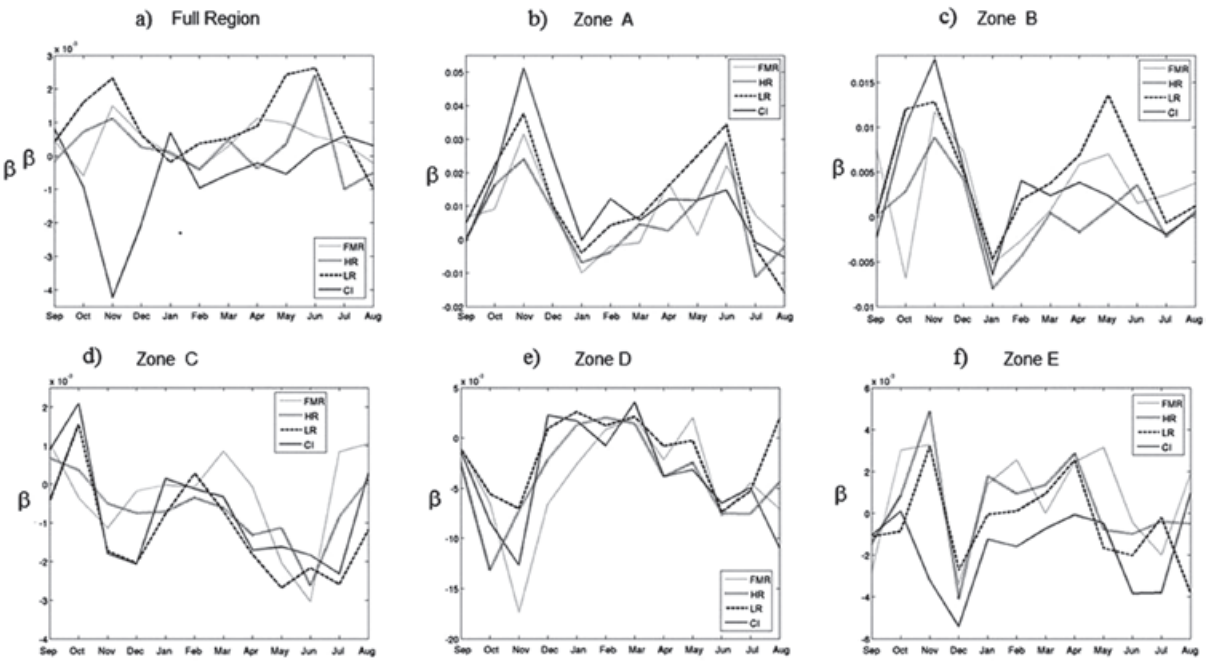

Figure 7. Daily temperature sensitivity in: a) The whole area of study. b) Zone A. c) Zone B. d) Zone C. e) Zone D. f) Zone E.

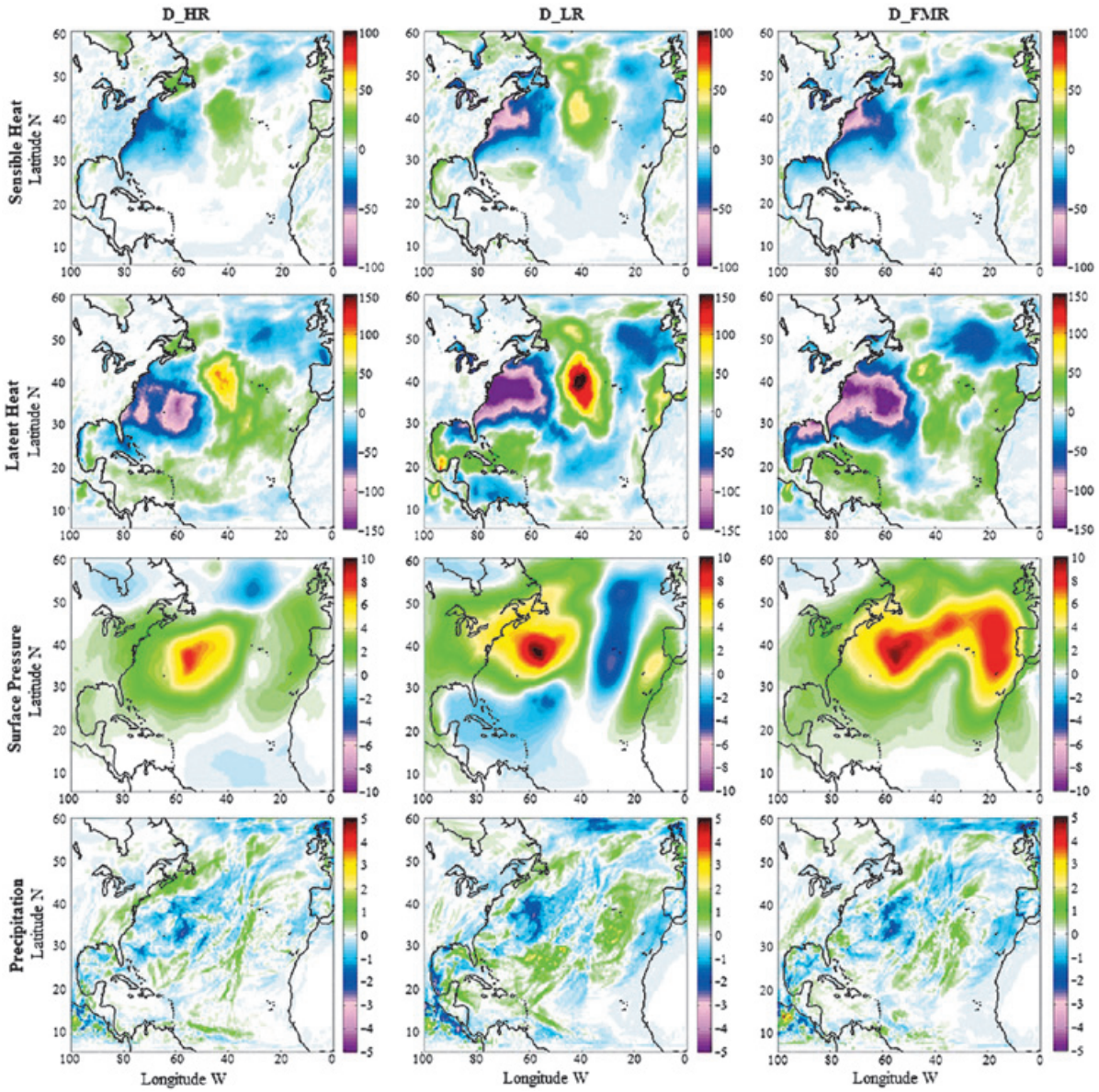

Figure 8. Average monthly differences a) Sensible Heat. b) Latent Heat. c) Surface Pressure. d) Precipitation, for November, 1983. The first column shows D_HR, the second D_LR, the third D_FMR.

Therefore, we conclude that changes in TSI produce changes similar to those of a disturbance in the initial conditions, but do not lead to significant changes in the conditions of the average temperature. Probably significant temperature variations will be produced if larger TSI changes occurred. To have more conclusive results concerning the sensitivity of the model to TSI variations leading to effects on weather, it will be desirable to couple the WRF model with an ocean model in order to allow the ocean heat content change under different TSI conditions. Our results are relevant for climate change experiments using the technique of downscaling [Giorgi *et al*, 2009] because it highlights the importance of using coupled ocean-atmosphere models to get a better temperature setting.

References

Barriopedro D., García-Herrera R., Huth R., 2008, Solar modulation of northern hemisphere winter blocking. *J. Geophys. Res.*, 113(D14118),. doi: 10.1029/2008JD009789.

Cipagauta C., 2013, Sensibilidad del modelo WRF a cambios en la RST en el Atlántico Norte. Ph.D. Thesis. Universidad Nacional Autónoma de México. (under review)

CGER., 1994, Commission on Geosciences, Environment and Resources, Board on Global Change, National Research Council, Solar Influences On Global Change. The National Aca-demies Press.

Fröhlich C., 2006, Solar irradiance variability since 1978 - Revision of the PMOD composite during solar cycle 21. Space Science Reviews 125: 53-65.

Giorgi F., Jones C., Asrar G., 2009, Addressing climate information needs at the regional level: the CORDEX framework. *WMO Bulletin* 58, 3.

Gray L.J., Beer J., Geller M., Haigh J.D., Lockwood M., Matthes K., Cubasch U., Fleitmann D., Harrison G., Hood L., Luterbacher J., Meehl G.A., Shindell D.B., van Geel B., White W., 2010, Solar influences on climate. *Rev. Geophys*,48, RG4001.

Haigh J., Blackburn M., Day R., 2005, The response of tropospheric circulation to perturbations in lower stratospheric temperature. *J. Climate*, 18:3672–3685.

IPCC. Climate Change 2007: The Physical Science Basis - Contribution of Working Group I to the Fourth Assessment Report of the Intergovernmental Panel on Climate Change. Edited by S. Solomon *et al*., Cambridge Univ. Press, Cambridge, U.K.

Kalnay *et al*., 1996, The NCEP/NCAR 40-year reanalysis project, *Bull. Amer. Meteor. Soc*., 77, 437-470.

Lee T., Zwiers F., Tsao M., 2008, Evaluation of proxy-based millennial reconstruction methods. *Clim. Dyn.*, 31, 263–281.

Meehl G., Arblaster J., Branstator B., 2008, and Loon H. V. A coupled air-sea response mechanism to solar forcing in the Pacific region. *J. Climate*, 21:2883–2897.

Mendoza B., Mendoza V.M., Garduño R., Adem J., 2010, Modeling the Northern Hemisphere temperature for solar cycles 24 and 25. *J. of Atmos*. And Solar-Terr. Phys. 72: 1122-1128.

Skamarock W., Klemp J., Dudhia J., Gill D., Barker D., Duda M., Huang X., Wang W., Powers J., 2008, A description of the Advanced Research WRF Version 3. NCAR TECHNICAL NOTE.

Szirtes T., 2006, Applied dimensional analysis and modeling. Second. Edition, Elsevier.

Tiwari M., Ramesh R., 2007, Solar variability in the past and paleoclimate data pertaining to the southwest monsoon. *Current Science*, 93, 4,25.

Geofísica Internacional (2014) 53-2: 163-181

Original paper

A multivariate Bernstein copula model for permeability stochastic simulation

Victor Hernández-Maldonado*, Martín Díaz-Viera and Arturo Erdely

Received: February 25, 2013; accepted: September 03, 2013; published on line: April 01, 2014

Resumen

En este trabajo se presenta un método no paramétrico general de simulación estocástica conjunta de propiedades petrofísicas utilizando la cópula Bernstein. Este método consiste básicamente generar simulaciones estocásticas de una determinada propiedad petrofísica (variable primaria) modelando la dependencia empírica subyacente con otras propiedades petrofísicas (variables secundarias), mientras también es reproducida la dependencia espacial de la primera.
Este enfoque multivariado provee una herramienta muy flexible para modelar las complejas relaciones de dependencia de las propiedades petrofísicas. Tiene varias ventajas sobre otros métodos tradicionales, ya que no se limita al caso de la dependencia lineal entre las variables, y tampoco requiere de la suposición de normalidad y/o existencia de momentos.
En este trabajo este método es aplicado para simular un perfil de permeabilidad utilizando la porosidad vugular y velocidad de onda de corte (Ondas S) como covariables, en una formación carbonatada de doble porosidad a escala de pozo. Los valores simulados de la permeabilidad muestran un alto grado de precisión en comparación con los valores reales.

Palabras clave: permeabilidad, porosidad, velocidad de onda de corte, dependencia multivariada, cópula de Bernstein, simulación geoestadística.

Abstract

This paper introduces a general nonparametric method for joint stochastic simulation of petrophysical properties using the Bernstein copula. This method consists basically in generating stochastic simulations of a given petrophysical property (primary variable) modeling the underlying empirical dependence with other petrophysical properties (secondary variables) while reproducing the spatial dependence of the first one.
This multivariate approach provides a very flexible tool to model the complex dependence relationships of petrophysical properties. It has several advantages over other traditional methods, since it is not restricted to the case of linear dependence among variables, it does not require the assumption of normality and/or existence of moments.
In this paper this method is applied to simulate rock permeability using Vugular Porosity and Shear Wave Velocity (S-Waves) as covariates in a carbonate double-porosity formation at well log scale. Simulated permeability values show a high degree of accuracy compared to the actual values.

Key words: permeability, porosity, shear wave velocity, multivariate dependence, Bernstein copula, geostatistical simulation.

V. Hernández-Maldonado*
M. Díaz-Viera
Instituto Mexicano del Petróleo
Eje Central Lázaro Cárdenas 152
07730, México, D.F.
*Corresponding autor: vmhernann@yahoo.com.mx

A. Erdely
Programa de Actuaria
Facultad de Estudios Superiores Acatlán
Universidad Nacional Autónoma de México
México D.F.

Introduction

Integrated Reservoir Modeling (IRM) is the most accepted way to obtain the spatial distribution of petrophysical properties in oilfields (Cosentino, 2001). An important and common task performed in this method is the estimation of permeability, because it is well known that this petrophysical property is quite informative about the oil flux patterns in a reservoir. However, it is difficult to obtain direct information about permeability, and therefore it is necessary to find models of dependence with another petrophysical property (such as porosity, water saturation, etc.) in order to have an estimation of its profile (Landa *et al*., 1996).

The linear regression approach is the most common way to model permeability values using other petrophysical properties as covariates (Balan *et al*., 1995). To meet the requirement of linearity it is common to perform transformations which imply that the final result could be biased when it is back transformed; there are approaches that, in order to fit linear models, apply logarithmic transformations to induce this behavior, for example, to use the Cokriging method it is necessary to have a linear relationship since it requires the linear corregionalization model (Sanjay and Journel 1994).

The main disadvantage of linear dependency models is their lack of ability to capture and model the dependence structure or pattern (Al-Harthy *et al*. 2005). In other words, traditional methods cannot capture the complex variability of data, in terms of variance or standard deviation; hence, the predicted permeability will not reproduce extreme values of the real data. In other words, these approaches will not be able to represent impermeable barriers or high permeability zones, and from a fluid flow point of view this aspects are the most important characteristics that determine the patterns of fluid movement. In this context, the predicted permeability profile, using linear estimators, will not be an effective approximation due to its oversmoothing nature.

On the other hand, model-free function estimators like artificial neural networks are very flexible tools that have been used to model permeability. However, neural networks have some disadvantages too. First, the training process has to be done with caution and can be a lengthy process. The good results obtained by this technique are reached using a comprehensive training data set, which is not always available. On the other hand, failing in correctly calibrating the network may result in aberrant results. Another point to take into consideration is that the methodology is not yet an "off the shelf" application and requires expertise by the geoscientist (Cosentino, 2001).

Another alternative are Bayesian methods; however, the traditional framework of the Bayesian analysis is based on the multivariate normal distribution where the lower and upper tails are symmetrical. Armstrong *et al*. (2004) proposed an alternative Bayesian analysis that is based on Archimedean copulas where the joint distribution does not have to be normal and there is flexibility to have a lower tail or upper tail dependence based on the specific type of copula.

Constructing numerical models of the reservoir that honor all available data (core measurements, well logs, seismic and geological interpretations, etc.) having sparse knowledge of rock properties, leads us to consider the stochastic simulation approach (Deutsch, 1992). This is not a new concept (Haldorsen and Damsleth, 1990; Journel and Alabert, 1990), stochastic models of physical systems are used extensively in many disciplines.

Stochastic simulation is the process of building alternate, equally probable models of the spatial distribution of a random function. It is said that a simulation is conditional if the resulting realizations honor the raw data values at their locations. The most straightforward algorithms for generating realizations of a multivariate Gaussian field is provided by Sequential Gaussian Simulation (SGS) and Sequential Indicator Simulation (SIS), which are extensively used to perform permeability simulations (Holden *et al*. 1995). However despite of their improvements (Journel and Zhu, 1990; Suro-Perez, 1990) these methods are limited to cases when the spatial continuity is characterized by stationary two-point statistics and to data that is defined on the same support (Deutsch, 1992).

A competitive and more systematic method for predicting permeability may be achieved by applying stochastic joint simulations, in which the correct specification of dependence pattern between petrophysical properties is crucial (Deutsch and Cockerham, 1994). According to Deutsch this approach basically consists of an annealing geostatistical cosimulation of porosity-permeability using their empirical joint distribution.

A modification of Deutsch's methodology was presented by Díaz-Viera and Casar-González, (2005). Here, it was proposed the use of a bivariate t-copula to construct the joint distribution function between porosity and permeability rather than use the joint distribution function of the sample data, the dependence structure was specified by matching concordance measures such as Kendall's τ and Spearman's ρ. The above methodology was applied to simulate permeability from the porosity profile in a double porosity carbonate systems, restricted to one-dimensional case at well-log scale (Díaz-Viera *et al*. 2006).

While Díaz-Viera and Casar-González proposal can reproduce adequately the observed data, and also their extreme values using a t-copula, the critical problem is that the applied copula is parametric, and consequently, it is based on a given distribution function, the student t. In that sense, expecting a single copula family to be able to model any kind of dependency relationship seems to be too restrictive, at least for the petrophysical properties under consideration. It does not mean that parametric copulas have not practical use. It means that petrophysical properties modeling, where dependence structure can be complex or non linear, using parametric copulas could be available but in a very complicated form, Sancetta and Satchell (2004).

The copula approach has been successfully used to model dependence patterns in few areas of oil industry, for example, for field development decision process (Accioly and Chiyoshi 2004) or to model dependence in petroleum decision making (Al-Harthy *et al*. 2005).

In a recent work we use the copula approach to model the bivariate dependence between petrophysical properties in a complete nonparametric fashion (Hernández-Maldonado *et al*. 2012), it means we did not impose a priori a parametric joint distribution function to characterize the dependence structure of the sample; instead, we used a bivariate Bernstein copula function to model the intrinsic distribution of data values. In this work we introduce a multivariate method for estimating empirical dependence among several petrophysical properties using a nonparametric copula. The dependency model obtained is then used to stochastically simulate one property (primary variable) given other ones (secondary variables). Here, we apply a method widely used in geostatistics, the Simulated Annealing method, which is a global optimization framework where we can add restrictions to simulation. In this case, in addition of using multivariate dependence by sampling the empirical copula model, a spatial correlation function (a variogram) for the secondary variable is imposed. Additionally, if any raw data of the primary variable is available, it can be exactly honored, that is, the method can be conditional.

In this paper this method is applied to simulate rock permeability using a trivariate copula model where permeability is described by Vugular Porosity and Shear Wave Velocity. It is introduced a two stage simulation method in a multivariate fashion to model stochastically the spatial distribution of permeability at well log scale. Conditional and nonconditional simulations, and the median of simulations are performed in order to show the results that this method provides; also it is established that, as far as more descriptive variables integrate the Bernstein copula it will reproduce permeability values in a very precise form, consequently it will not be necessary to perform many simulations to reduce small scale variability.

Brief introduction to multivariate copulas

The main disadvantage of dependency models based on a linear regression approach is their lack of ability to capture and model more general dependence structure. As an alternative a copula can model the joint distribution of petrophysical properties in better ways. The essence of the copula approach is that a joint distribution of random variables can be expressed as a function of the marginal distributions (Al-Harthy *et al*., 2005).

According to Sklar's theorem (Sklar, 1959), the underlying copula associated to a multivariate random vector $(X_1, X_2, ..., X_m)$ represents a functional link between the joint probability distribution and the univariate marginal distributions $F_1, F_2, ..., F_M$ respectively:

$$H(x_1, x_2, ..., x_m) = C(F_1(x_1), F_2(x_2), ..., F_{\mathrm{m}}(x_m)) \quad (1)$$

For all $x_1, x_2, ..., x_m$ in the extended real numbers system, where $C:[0, 1]^m \rightarrow [0, 1]$ the underlying copula is unique whenever X_1, X_2, and X_m are continuous random variables. Therefore, all the information about the dependence between continuous random variables is contained in their corresponding copula. Several properties may be derived for copulas (Nelsen, 2006), and among them

we have an immediate corollary from Sklar's theorem: X_1, X_2 and X_m are independent continuous random variables if and only if their underlying copula is $C(u_1,...,u_n)=u,...,u_n$.

Let S=$\{(x_{11}, x_{21}, \ldots x_{m1}), \ldots, (x_{1n}, x_{2n}, \ldots x_{mn})\}$ be n observations of a random vector (X_1, X_2, ..., X_m). We may obtain empirical estimates for the marginal distributions X_1, X_2, ..., X_m by means of:

$$\hat{F}_j(x) = \frac{1}{n}\sum_{k=1}^{n} 1\{x_{jk} \le x\} \tag{2}$$

where stands for an indicator function which takes value whenever its argument is true, and otherwise. It is well-known (Billingsley, 1995) that the empirical distribution $\hat{F}_j$ is a consistent estimator of F_j that is, F_j that is $\hat{F}_j(t)$ *i*s a converges almost surely to $F_j(t)$ *as* $n \to \infty$ all *t.*

Similarly, we have the empirical copula (Deheuvels, 1979), a function C_n with domain $\left\{\frac{1}{n} : i = 0,1,...,n\right\}^m$ (where n is the sample size) defined as

$$C_n\left(\frac{v_1}{n},...,\frac{v_m}{n}\right) = \frac{1}{n}\sum_{k=1}^{n} 1\{rank(x_{1k}) \text{ £ } v_1,...,rank(x_{mk}) \le v_m\} \tag{3}$$

and its convergence to the true copula has also been proved (Fermanian *et al*., 2004). The empirical copula is not a copula, since it is only defined on a finite grid, not in the whole unit hypercube $[0, 1]^n$, but by Sklar's Theorem (Sklar, 1959) C_n may be extended to a copula.

Sklar's theorem is completely general and a joint distribution function can be constructed using the copula function. The copula separates the marginal distributions from correlation and the copula itself can capture the dependence structure. This is an essential property of copulas.

A general example of a multivariate copula model that describes the relationship of three random variables (a trivariate copula) according to Sklar's theorem is shown:

$$H(x_1, x_2, x_3) = C(F_1(x_1), F_2(x_2), F_3(x_3)) \tag{4}$$

There are different classes and families of copulas but, for this study, we will work with the Bernstein copula, which is a nonparametric copula since it is a nonparametric smoothing based on the empirical copula.

Joint stochastic simulation method using a multivariate Bernstein copula

The method presented here basically consists in generating a stochastic simulation of a primary variable, where the joint distribution function of its covariates is modeled using a nonparametric copula. In other words, the spatial dependence and dependence pattern between variables are decoupled; in this context, the Bernstein copula only models the dependence between variables and the spatial dependence is modeled by a variogram applying the Simulated Annealing method.

Basically this proposal is a two-stage modeling algorithm method; first, the pattern relationship between petrophysical properties under study; and second, the spatial structure. In the first stage it is modeled the dependence structure of petrophysical properties using a multivariate nonparametric copula (the Bernstein copula), then a geostatistical simulation of primary variable is performed using simulated annealing technique, whose objective function is the variogram model (Deutsch and Cockerham, 1994). A detailed description of each step of the algorithm will be described.

Multivariate Bernstein Copula Modeling.

Each petrophysical property is modeled as an absolutely continuous random variable X with unknown marginal distribution function F. For simulation of continuous random variables, the use of the empirical distribution function (2) is not appropriate since $\hat{F}_j$ is a step function, and therefore discontinuous, so a smoothing technique is needed. Since our main goal is to simulate a primary variable using more than one descriptive variable, it will be better to have a smooth estimation of the marginal quantile function $Q(u) = F^{-1}(u) = inf\{x:F(x)\ge u\}, 0\le u\le 1$ which is possible by means of Bernstein polynomials as in Muñoz-Pérez and Fernández-Palacín (1987).

$$\tilde{Q}_n(u) = \sum_{k=0}^{n} \frac{1}{2}\left(x_k + x_{k+1}\right)\binom{n}{k} u^k \left(1 - u\right)^{n-k} \tag{5}$$

For a smooth estimation of the underlying copula we make use of the Bernstein copula (Sancetta and Satchell, 2004; Sancetta, 2007):

$$\tilde{C}_B\left(u_1,...,u_m\right) = \sum_{v_1=0}^{n_1} \ldots \sum_{v_m=0}^{n_m} \alpha\left(\frac{v_1}{n_1},...,\frac{v_m}{n_m}\right) P_{v1,m1}\left(u_1\right)...P_{vm,nm}\left(u_m\right) \tag{6}$$

where;

$$P_{v_j,m_j}(u_j) = \binom{n_j}{v_j} u_j^{v_j}(1- u_j)^{n_j - v_j} \qquad (7)$$

For every (u_1, ..., u_m) in the unit hypercube $[0, 1]^m$, and $\alpha\left(\frac{v_1}{n_1},...,\frac{v_m}{n_m}\right)$ is the empirical copula, defined in (3).

For example, the trivariate Bernstein copula model derived from (6) is:

$$\tilde{C}_B(u,v,w) = \sum_{i=0}^{n}\sum_{j=0}^{n}\sum_{k=0}^{n} C_n\left(\frac{i}{n},\frac{j}{n},\frac{k}{n}\right)\binom{n}{i}u^i(1- u)^{n-i} \binom{n}{j}v^j(1- v)^{n-j}\binom{n}{k}w^k(1- w)^{n-k} \qquad (8)$$

Sampling algorithm of a Bernstein copula model

For a pair of random variables (X_1, X_2) with joint distribution function H and underlying copula *C* we need to generate an observation of uniform (0, 1) random variables (U, V) whose joint distribution function is C and then transform those uniform variables as in step 3 of the sampling bivariate algorithm. For generating such pair *(u, v)* it is used a conditional distribution method, this method needs the conditional distribution function for *V* given $U = u$, which we denote as $c_u(v)$:

$$c_u(v) = \frac{\partial \tilde{C}_B(u,v)}{\partial u} \qquad (9)$$

where $\hat{C}_B$ is the bivariate Bernstein copula model, obtained by (6).

To simulate replications from the random vector with the dependence structure estimated from the observed data S:={(x_{11}, x_{21}), ..., (x_{1n}, x_{2n})} it is applied the following algorithm:

Sampling bivariate algorithm:

1.Generate two independent and continuous Uniform (0,1) random variates *u* and *t*

2.Set $v = c_u^{-1}(t)$; where c_u is defined in (9).

3.The desired pair is $(x_1, x_2) = (\tilde{Q}_n(u), \tilde{R}_n(v))$ where $\tilde{Q}_n$ and $\tilde{R}_n$ according to (5), are the estimated and smoothed quantile functions X_1 of X_2 and, respectively.

For the multivariate case we must solve equations that represent conditional distribution functions for W given $U=u, V=v$.

To simulate replications from the random vector with the dependence structure estimated from the observed data S:={(x_{11}, x_{21}, x_{31}), ..., (x_{1n}, x_{2n}, x_{3n})} it is applied the next algorithm.

Sampling trivariate algorithm:

1.Generate three independent and continuous Uniform (0, 1) random variables *u* and t_1, t_2.

2.Set $v = c_u^{-1}(t_1)$ where c_u is defined in (9).

3.Set $w = c_{uv}^{-1}(t_2)$ where

$$c_{uv}(w) = \frac{\frac{\partial \tilde{C}_B(u,v,w)}{\partial u\,\partial v}}{\frac{\partial \tilde{C}_B(u,v,1)}{\partial u\,\partial v}} \qquad (10)$$

where is the trivariate Bernstein copula model (8).

4.The desired vector is $(x_1, x_2, x_3) = \left(\tilde{Q}_n(u), \tilde{R}_n(v), \tilde{H}_n(w)\right)$ where $\tilde{Q}_n(u), \tilde{R}_n(v)$ and, $\hat{H}_n(w)$ according to (5), are the estimated and smoothed quantile functions of X_1,X_2 y X_3, respectively.

Simulated Annealing method.

To perform stochastic simulations of a primary variable it is applied a method widely used in geostatistics, the Simulated Annealing method, which is a global optimization framework where we can add restrictions to simulation. In this case, in addition of using multivariate dependence by sampling the copula model, a spatial correlation function (a variogram) for the secondary variable is imposed. Additionally, if any raw data of the primary variable is available, it can be exactly honored, that is, the method can be conditional.

A more detailed explanation of each single step of simulated annealing method, as well as technical terminology, can be found in Dréo *et al*. (2006), Dafflon et. al., (2009a, 2009b), Dafflon and Barrash (2012), Hernández-Maldonado *et al*. (2012), Deutsch (2002). In this work, we will just briefly mention its steps.

a.Generating an initial configuration, known as "seed". An initial configuration is the starting point of the simulation, also, it can be

considered as a "possible solution" of the spatial disposition of the primary variable. There are some ways of proposing this configuration, see Deutsch (2002), Dréo et al. (2006). One of most popular of them is just proposing random numbers with uniform distribution. We decided to use the multivariate Bernstein copula sampling algorithm (section 3.1.1) to obtain this starting point in order to have a better approximation of the final solution.

b.Defining the objective function. Since we use the Bernstein copula we do not have to include univariate histograms into the objective function because they are reproduced automatically; in the same way, as Bernstein copula models the dependence structure between variables, it is not necessary to include neither a correlation coefficient. In other words, in order to satisfy the spatial distribution of the primary variable, we are able to propose an objective function that consists only in one term (11) the variogram function

$$FO = \sum_i \frac{[\gamma^*(h_i) - \gamma(h_i)]^2}{\gamma(h_i)^2} \qquad (11)$$

Where:

$$\gamma(h) = \frac{1}{2N(h)} \sum_{i=1}^{N(h)} [Z(x_i + h) - Z(x_i)]^2 \qquad (12)$$

$$T_0 = \left(- \frac{\Delta E}{log(\tau_0)} \right) \qquad (13)$$

c.Measuring the initial configuration energy. By (12), it is calculated the variogram of the initial configuration and it is compared to the variogram of the real configuration (11), this value is the energy of the starting point, and the main idea is that it must be decreased during the simulation procedure, see Deutsch (2002). This step gives us an idea of the seed´s quality, if we use random numbers to generate it, its measured energy will be very high, however, as long as this method uses a sample given by the Bernstein copula the initial energy is significantly small.

d.Obtaining the initial temperature and the annealing schedule. The initial temperature is obtained by (13):

The annealing schedule is obtained following the procedure proposed by Dréo et al. (2006).

e.Ending up a realization. The simulation ends whenever the objective function error is reached, or an accumulation of 3 stages without change occurs, or when the maximum number of attempted perturbations is reached.

It is shown a diagram of the method to perform multivariate stochastic simulations in, Figure1.

Case study

It will be modeled the Permeability of double porosity carbonate formations of a South Florida Aquifer in the western Hillsboro Basin of Palm Beach County, Florida. Based in the algorithm described in Section 3, we propose a copula-based approach to model the relationship between permeability, porosity and Shear Wave Velocity (S-waves). The dependency model obtained will be then used to stochastically simulate permeability using Porosity and Shear Wave velocity.

Data description

The characterization of this aquifer for the borehole and field scales is given in Parra *et al*. (2001), Parra and Hackert (2002), and a hydrogeological situation is described by Bennett *et al*. (2002). The interpretation

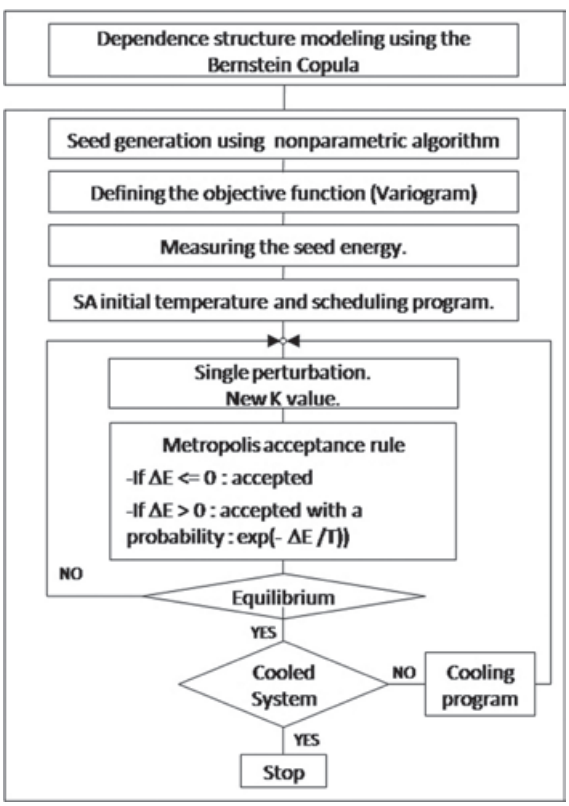

Figure 1. Diagram of the two-stage method to perform multivariate stochastic simulations using multivariate Bernstein copula.

of the borehole data, the determination of the matrix and secondary porosity and secondary-pore types (shapes of spheroids approximating secondary pores) were presented by Kazatchenko *et al*. (2006), where to determine the pore microstructure of aquifer carbonate formations the authors applied the petrophysical inversion technique that consists in minimizing a cost function that includes the sum of weighted square differences between the experimentally measured and theoretically calculated logs as in Kazatchenko *et al*. (2004).

In this case the following well logs were used for joint simultaneous inversion as input data: resistivity log, transit times of the P- and S-waves (acoustic log), total porosity (neutron log), and formation density (density log). To calculate the theoretical acoustic and resistivity logs the double-porosity model for describing carbonate formations was applied: Kazatchenko *et al*. (2006).

This model treats carbonate rocks as a composite material that consists of a homogeneous isotropic matrix (solid skeleton and matrix pore system) where the secondary pores of different shapes are embedded. The secondary pores were approximated by spheroids with variable aspect ratios to represent different secondary porosity types: vugs (close-to-sphere shapes), quasi-vugs (oblate spheroids), channels (prolate spheroids), and microfractures (flattened spheroids) Kazatchenko *et al*. (2006).

We used the results of inversion obtained by Kazatchenko *et al*. (2006) for carbonate formations of South Florida Aquifer that includes the following petrophysical characteristics: matrix porosity, secondary vugular and crack porosities (Figure 2).

The secondary-porosity system of this formation has complex microstructure and corresponds to a model with two types of pore shapes: cracks (flattened ellipsoids) with the overall porosity of 2% and vugs (close to sphere) with the porosity variations in the range of 10-30%.

Statistical data analysis.

Given multivariate data, it is common to start choosing as explanatory variables those who exhibit higher dependence with the variable that is to be explained. We measured the dependence between the petrophysical properties in terms of the dependence index Φ proposed by Hoeffding (1941), which satisfies all desirable properties for a dependence measure for continuous random variables, see Nelsen (2006).

From all possible explanatory variables (PHITOT, PHIMAT, PHICR, PHIV, VS Meas, VP meas) for permeability (K), for the first explanatory random variable it was chosen relative vugular porosity (PHIV) since it exhibited the highest dependence $\Phi\ (PHI, K)=0.71$ (on a [0,1] scale). In choosing a second explanatory random variable we need, in addition, to have a high dependence with permeability, and the lowest possible dependence with the first explanatory variable (PHIV), otherwise it would mean that it is quite similar to it and it will add no significant information to what the first one already can provide. Under this criteria, the second best choice was Share Wave Velocity (VS meas),

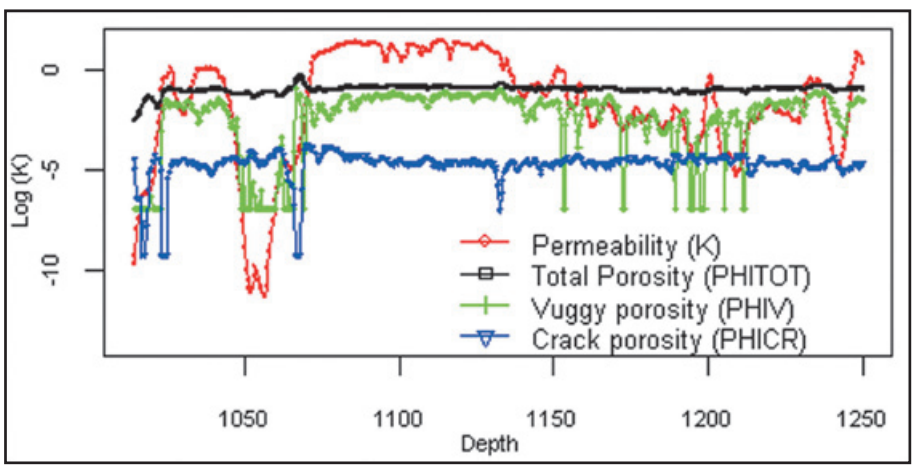

Figure 2. Crack porosity (PHICR), vuggy porosity (PHIV), total porosity (PHITOT) and permeability (K).

with $\Phi\ (VS\ meas,\ K) = 0.60$ and $\Phi\ (PHIV,\ VS\ meas) = 0.55$

Table 1 shows all dependence index Φ of explanatory variables that are the results of inversion obtained by Kazatchenko *et al*. (2006); Total porosity (PHITOT), Matrix porosity (PHIMAT), Crack porosity (PHICR), Vugular porosity (PHIV), Share Wave Velocity (VS Meas), P-Wave velocity (VP meas).

In table 1 explanatory variables are shown, using this information we confirm that PHIV has the highest dependence, but following the order of this table we should use as second explanatory variable PHITOT. We did not make this choice because, as we said before, a second explanatory variable needs to have a high dependence with permeability, and the lowest possible dependence with the first explanatory variable (PHIV). To see this behavior in table two we show the explanatory variables matrix dependence Hoeffding index.

We have chosen PHIV as the first explanatory variable; it means we must pay attention to the first line of table 2, and select the variable with the lowest dependence to PHIV. It should be PHICR but in Table 1 we see that this property offers poor information about K. Finally, we may choose VP meas but, VS Meas explains K in some better way (Table 1).

In Figure 3 it is shown a scatter-plot distribution and histograms of PHIV–K sample data taken from Kazatchenko *et al*. (2006), it shows their bivariate distribution. In Figure 4 it is shown a scatter-plot distribution and histograms of VS meas–K data values

Table 1. Dependence index Φ, Hoeffding (1941), for possible explanatory variables (PHITOT, PHIMAT, PHICR, PHIV, VS Meas, VP meas).

Explanatory variable	Corresponding Hoeffding index Φ vs. K
PHIV	0.71
PHITOT	0.62
PHIMAT	0.50
VS Meas	0.60
VP meas	0.55
PHICR	0.16

Bernstein Copula Model.

It is modeled the trivariate Bernstein Copula using relative vugular porosities (PHIV), Shear Wave Velocity (VS meas = velocity of S-waves measured) and K as absolutely continuous random variables X_1, X_2 and X_3, with unknown theoretical univariate distribution functions F_1, F_2 *and* F_3, *see (2). Observations of this random vector were obtained from Kazatchenko et al. (2006).*

We use (2) to estimate the empirical distribution function for each variable; however;

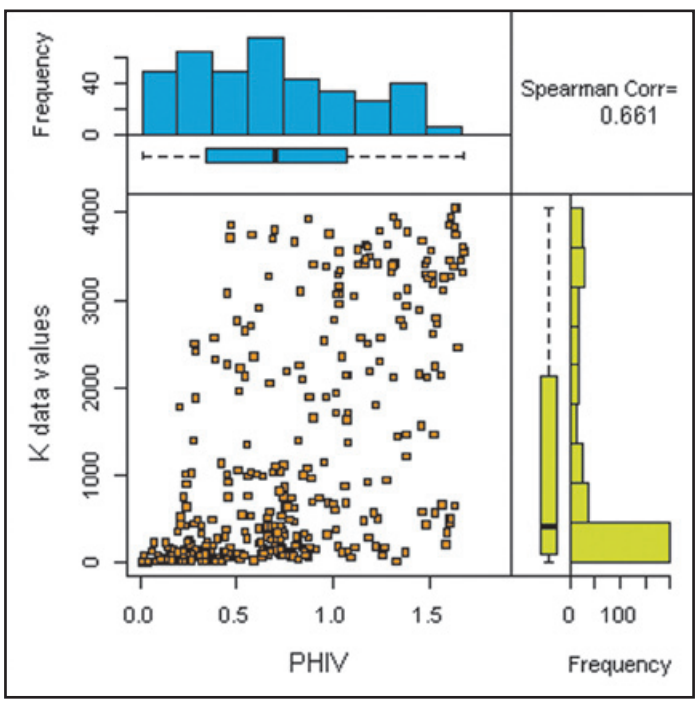

Figure 3. Scatter plot distribution and histograms of PHIV and K of real data values.

Table 2. Hoeffding dependence index Φ matrix, for possible explanatory variables (PHITOT, PHIMAT, PHICR, PHIV, VS Meas, VP meas).

Hoeffding index Φ	PHIV	PHITOT	PHIMAT	PHICR	VS Meas	VP meas
PHIV	1	0.88	0.72	0.34	0.58	0.57
PHITOT		1	0.43	0.32	0.64	0.61
PHIMAT			1	0.24	0.30	0.36
PHICR				1	0.31	0.20
VS Meas					1	0.32
VP meas						1

in order to model them as continuous random variables they should be smoothed using (5), since (2) is not appropriate because $\hat{F}_j$ is a step function and therefore discontinuous. The trivariate Bernstein copula model (8) will be used to sample data to stochastically simulate permeability.

Sampling from Bernstein copula.

In Figure 5 (left side) it is shown a scatterplot distribution and histograms of porosity–permeability real data (sample size of) taken from Kazatchenko *et al*. (2006). At the center of the same figure, it is shown a trivariate simulation of permeability values using vugular porosity and shear wave velocity as explicative variables. If we do not label these two scatter plots it would be difficult to know which one of them is the original one. In this case the multivariate Bernstein copula provides an acceptable the dependence structure for continuous variables with complex relationship. The right side of Figure 5 shows 3800 simulated values of permeability, according to some analysis, it shows more clearly percolation patterns.

Permeability simulations and discussion.

In this section spatial simulation will be performed using simulated annealing technique. Since multivariate dependence is modeled by the Bernstein copula, a spatial correlation function (the variogram) will be used as an objective function in the annealing algorithm.

We propose a copula-based nonparametric approach and simulated annealing technique to model the spatial distribution of permeability using as secondary variables, porosity and shear wave velocity (S-waves). In Figure 6 we can see a single nonconditional spatial simulation of permeability (K) in terms of depth. As we note the simulation (blue line) follows very close the real data behavior (red line), this is because we introduce more descriptive information into the Bernstein copula model. However, there is still a small-scale variability which does not exist in the original data values.

As a descriptive measure of the goodness of fit of predicted values of log-permeability (Log K) given values of the explanatory variables PHIV and VS meas, we calculated the Mean Squared Error (MSE) in each case:

$$\mathrm{MSE}\ (\log \mathrm{K}|\mathrm{PHIV}) = \frac{1}{n}\sum_{m=1}^{n}\left[z_m - \beta_{0.5}(x_m)\right]^2 \tag{14}$$

$$\mathrm{MSE}\ (\log \mathrm{K}|\mathrm{VS\ meas}) = \frac{1}{n}\sum_{m=1}^{n}\left[z_m - \beta_{0.5}(y_m)\right]^2 \tag{15}$$

$$\mathrm{MSE}\ (\log \mathrm{K}|\mathrm{PHIV,VS\ meas}) = \frac{1}{n}\sum_{m=1}^{n}\left[z_m - \beta_{0.5}(x_m, y_m)\right]^2 \tag{16}$$

where a lower value of MSE represents a better goodness of fit.

The simulated values of log K, given PHIV and VS meas (log *K* | *PHIV, VS meas),* show a MSE value of 0.5, which is very low compared to that obtained by Deutsch and Cockerham's method (1994), which MSE value is 7.76; also it is lower than the obtained one by Díaz-Viera and Casar-González method, where the MSE value is 5.5, details are shown in Hernandez-Maldonado *et al*., (2012). Finally, the MSE value for the trivariate copula simulation is lower than the MSE value of the bivariate copula simulation (log *K* | *PHIV)* (14), consequently it means that trivariate simulation has the best fitted values.

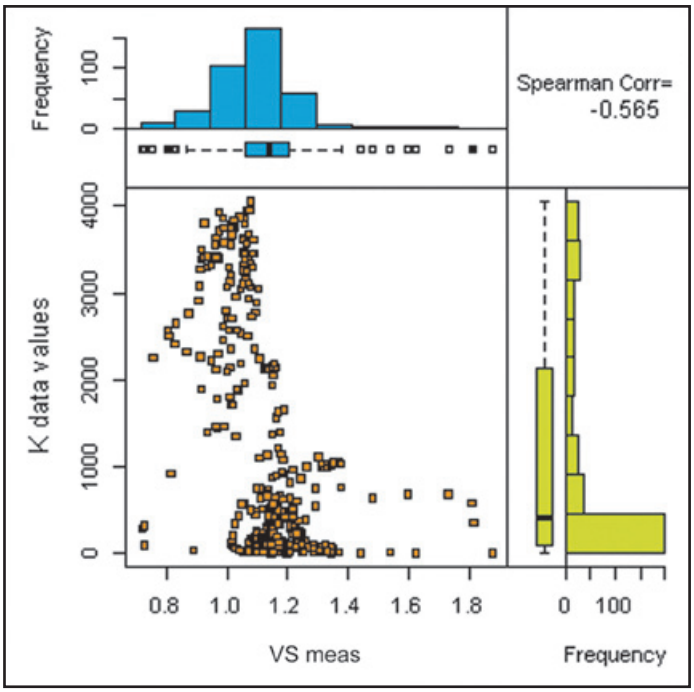

Figure 4. Scatter plot distribution and histograms of PHIV and K of real data values.

In terms of histograms, scatterplots and variograms, the proposed method shows very good agreement with the original data values. As we are using three variables, the scatterplots of permeability can be seen in terms of K-PHIV (Figure 7) and K-S-waves (Figure 8). The scatterplots of the original data values are shown in Figure 3 and Figure 4 respectively.

The variogram of the simulation (Figure 9) and its fitted model (Table 3), also shows good agreement with respect to real data (Figure 10). We can note that both variograms are almost equal, but in a detailed view, the empirical variogram of the simulated values is a little softer than the original one.

As we could anticipate, the dependence structure between these three petrophysical properties is well represented. The extreme values, and in general, all of most important statistics are quite well reproduced, (Figure 11). In order to reduce small-scale variability seen in Figure 6, a median of 10 nonconditional SA simulations was performed, Figure 12. Once again, the spatial structure, the histograms and the Scatter-plot reproduction shows a very good agreement respecting to real data, see also Figure 13 and Figure 14.

In Figure 12 we can see that for small values of K the simulation is not following real data values too closely, there are two

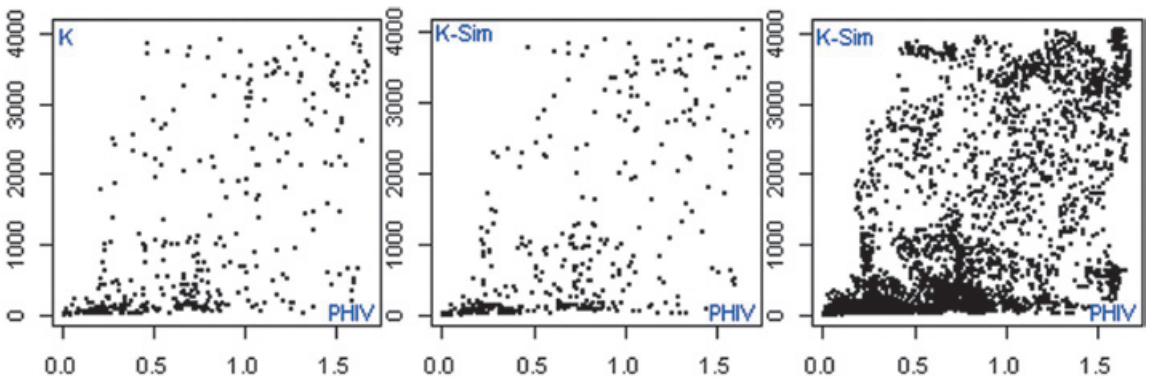

Figure 5. Scatter plot between Porosity and Permeability. Left, the 380 data values. Center, 380 simulated values using trivariate Bernstein copula. Right, 3800 simulated values.

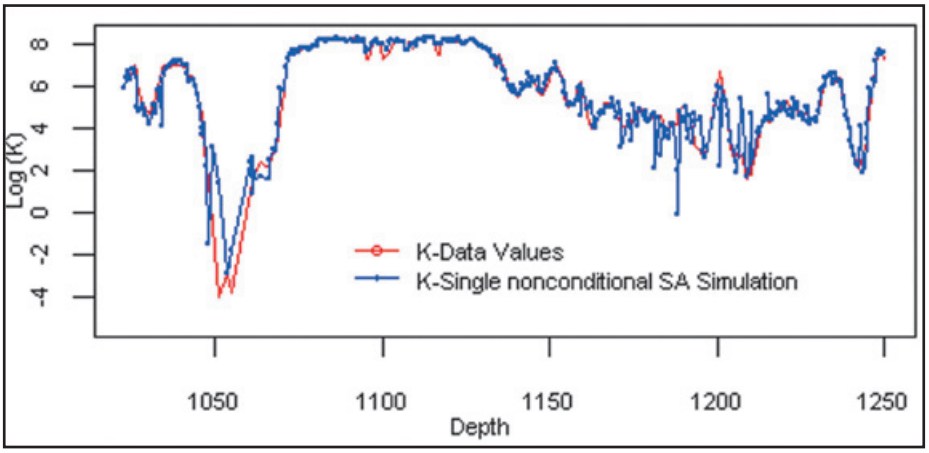

Figure 6. Single nonconditional simulation of permeability (K), using porosity and shear wave velocity (VS meas) as secondary variables.

Table 3. Variograms Models of the data values and single nonconditional SA simulation.

Configuration	Nugget	Sill	Range
Data values	0.00	2.61 x 106	85.07
Single SA nonconditional Simulation.	0.00	2.57 x 106	87.52
Median of 10 SA nonconditional Simulations.	0.00	2.51 x 106	87.27

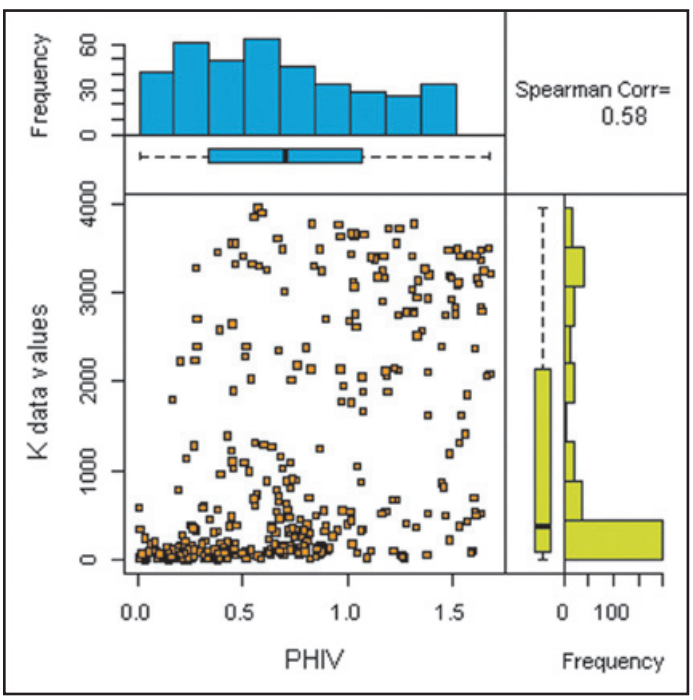

Figure 7. Scatter plot and histograms of PHIV and K (Simulated values).

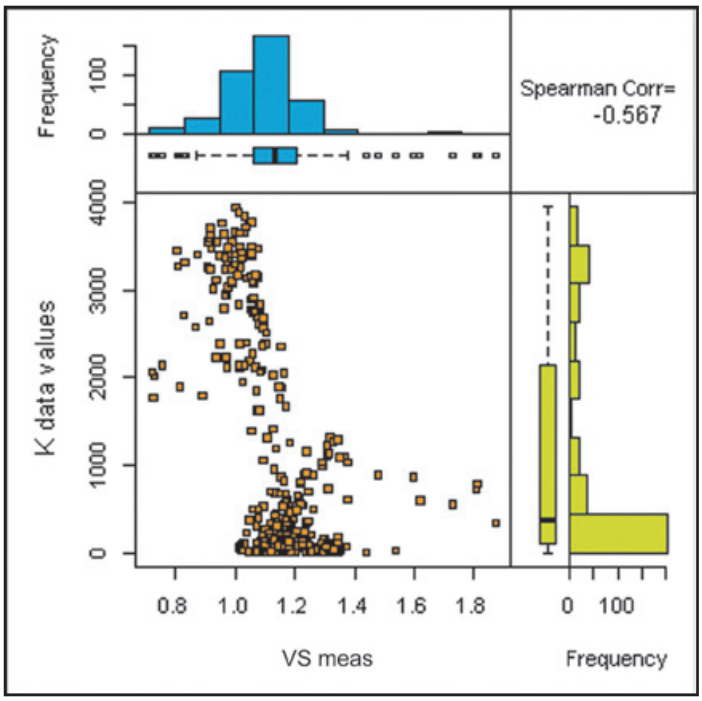

Figure 8. Scatter plot and histograms of VS Meas and K (Simulated values).

reasons. First, this "behavior" is observed in all simulation methods that were performed in order to compare the simulated values for the bivariate case of this proposal [Hernandez-Maldonado *et al*., (2012)]. In that work the most accurate results were shown by Bernstein copula. In this particular case is hard to have a simulation that follow too closely the behavior of the real data values, because there is very little information. And second, this is a median value of 10 different simulations, which means that each simulation has different degrees of accuracy, which is normal.

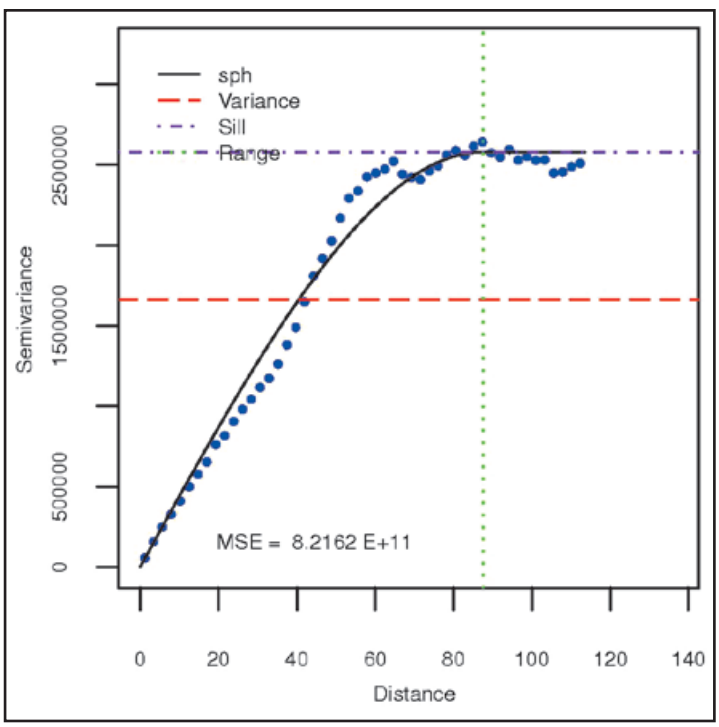

Figure 9. Estimated variogram and its fitted model for simulated K (Simulated values).

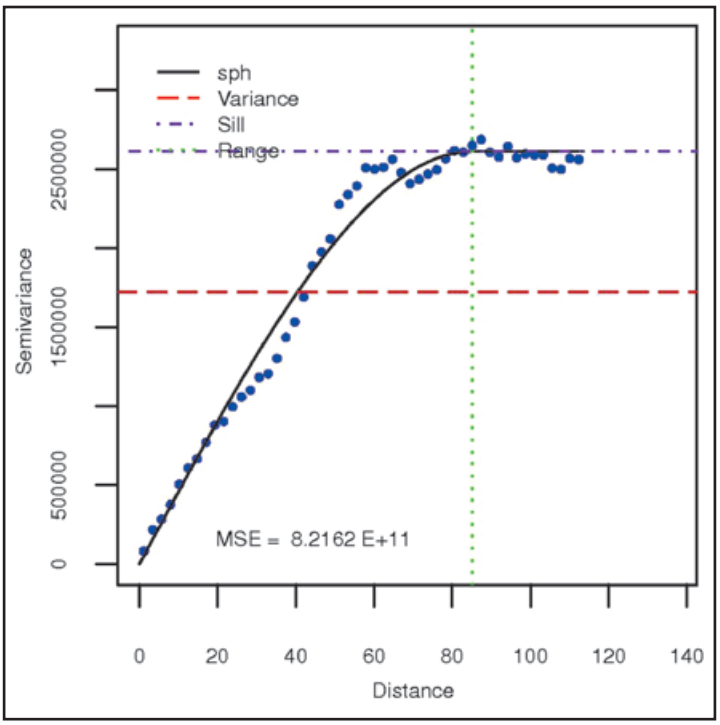

Figure 10. Estimated variogram and its fitted model for original K (Data values).

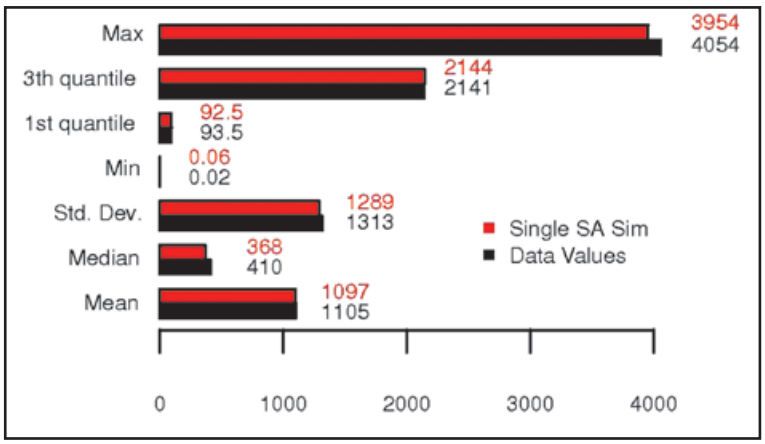

Figure 11. Statistical comparison of to the original data and a single trivariate SA simulation.

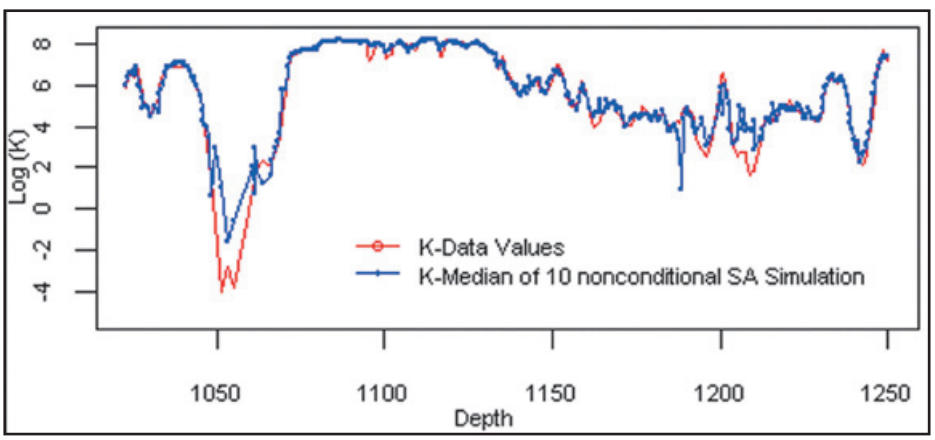

Figure 12. Median of 10 nonconditional simulation of permeability (K), using porosity and shear wave velocity (S-waves) as secondary variables.

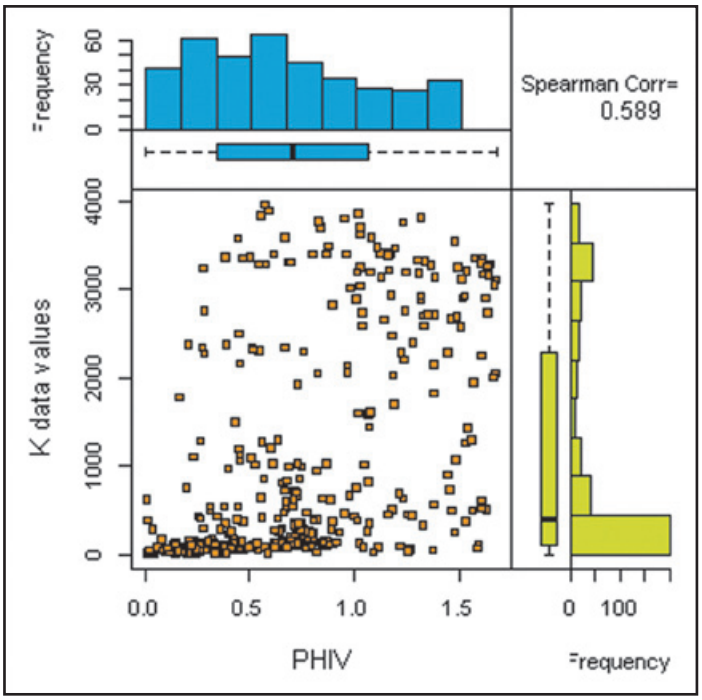

Figure 13. Scatter plot and histograms of PHIV and K simulated values (median of 10 simulations).

Figure 15 shows the variogram of this simulation and its fitted model. In contrast to Figure 10 (real data values) we can see that this method represents very well, the spatial structure of permeability.

The values of the variogram model for a single simulation and the median of 10 simulations are very close to the real data as well (Table 3). The same happens with their most important statistics (Figure 16).

Using (16) we can see that the MSE values between the real data and these nonconditional simulations are very similar (Table 4). It is an indicative that it is not necessary to perform

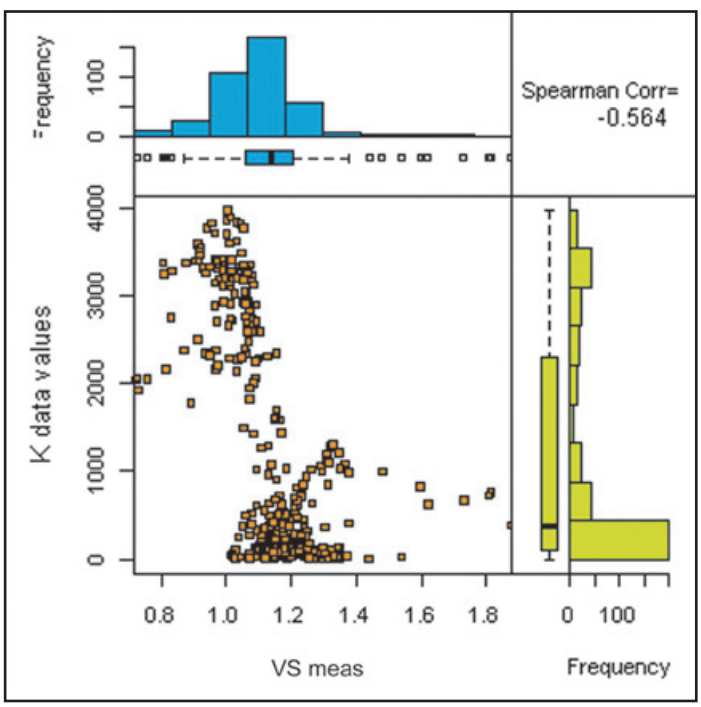

Figure 14. Scatter plot distribution and histograms of VS-meas and K simulated values (a median of 10 simulations).

many simulations to smooth the small-scale variability, and may be unnecessary.

Finally we perform conditional simulations and compare the MSE values in order to study the effect of different percentage of conditioning values. Figure 17 shows the results of the spatial distribution of the permeability in various percentages of conditioning values, from top to bottom order, it is conditioned to 10 percent, 50 percent and 90 percent of the conditioning data values. Note that results are, graphically, very similar to real data and their MSE values as well (see Table 5). This shows that the proposed method in a multivariate fashion does not require big amounts of conditioning data to have consistent results.

Table 4. MSE values of nonconditional simulations

Configuration	MSE
Single SA nonconditional Sim.	0.50
Median of 10 nonconditionals Sims.	0.35

The Bernstein copula (8) requires that the empirical copula be ready to be used all the time, hence, it is necessary to propose an efficient and fast algorithm in terms of data storage and computing speed to implement a multidimensional copula. We propose a procedure to efficiently implement a multidimensional empirical copula. Shortly described, this procedure fundamentally solves the two main disadvantages of using nonparametric copulas: it avoids redundant calculation, which increases its speed and just needs to storage the most important values of the generated hypercube.

Of course the method can be extended to more dimensions, but the purpose of the article is to show its application to a well log scale, where we have more control and better data quality. Its application to more dimensions will be the subject of future work.

Table. 5. MSE values of the single conditional simulations.

Configuration	MSE
Single SA nonconditional Sim.	0.50
Single SA 10% conditional Sim.	0.41
Single SA 50% conditional Sim.	0.36
Single SA 90% conditional Sim.	0.27

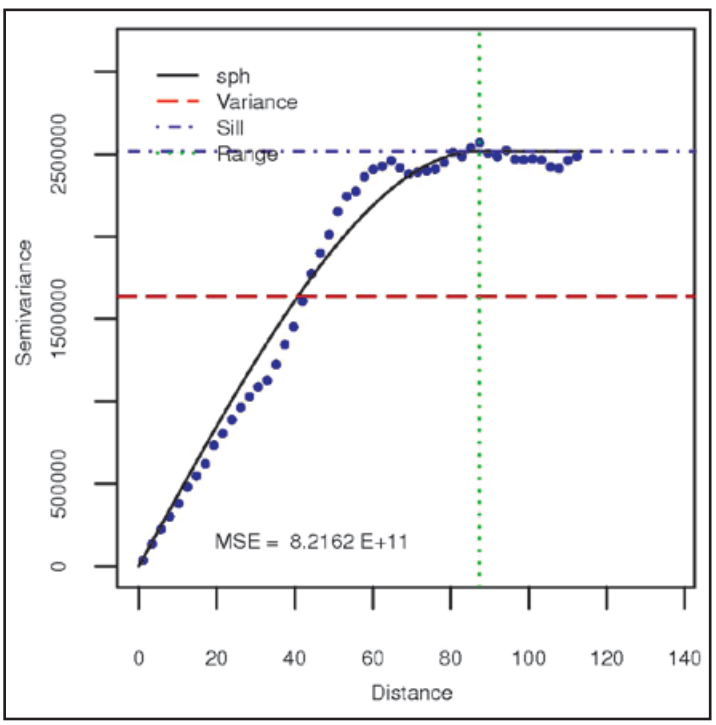

Figure 15. Estimated variogram and its fitted model for simulated K data values.

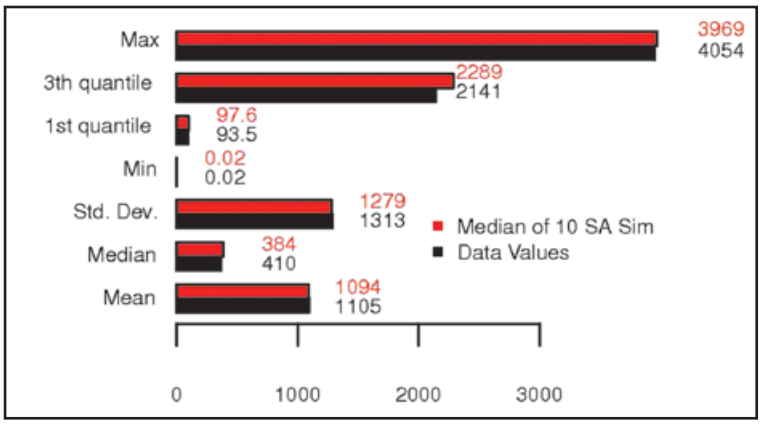

Figure 16: Statistical comparison of to the original data, and the median of 10 SA simulations.

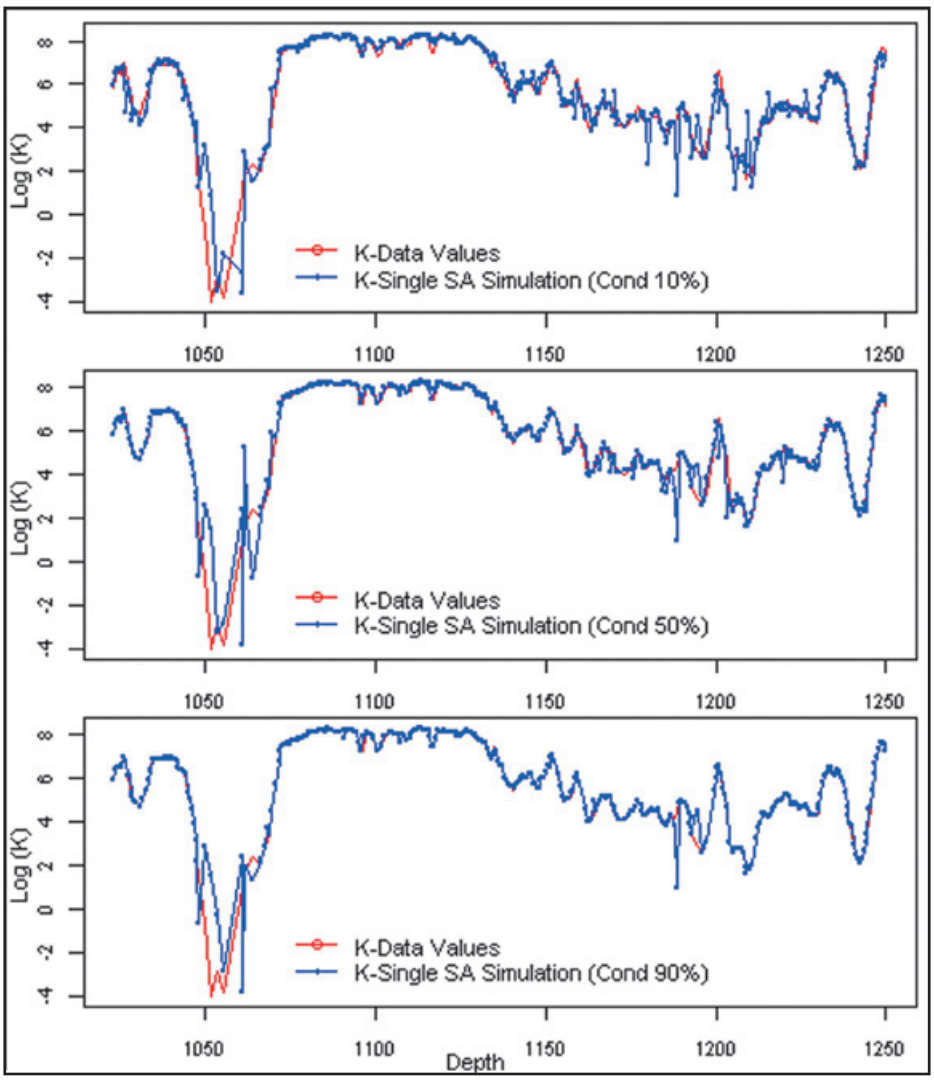

Figure 17. Spatial distribution of permeability in single conditional simulations using PHIV and VS meas as secondary variables. Conditioning levels (in top to bottom order) 10 percent, 50 percent and 90 percent.

Conclusions

From a methodological point of view, a multivariate copula approach provides a very flexible tool to model complex dependence relationships of petrophysical properties, such as porosity, permeability and shear wave velocity, without imposing strong assumptions of linearity or log-linearity, and/or normality when we are modeling them as random variables.

All the information about the dependence structure is contained in the underlying copula, and its estimation is being used, instead of the extreme information reduction that is done by the use of numerical measures such as the linear correlation coefficient, which under the presence of nonlinear dependence may become useless and/or quite misleading, see Embrechts *et al*. (1999, 2003). For this reason it is very important to extend the method to higher dimensions, because if we have more than one relevant explanatory variable, we may use this tool to take them into account.

The main advantage of the methodology used in this work is that it represents a straightforward way to perform nonparametric simulations, conditional and nonconditional. As we have said in the results of the application of this method, including more than one explanatory petrophysical property to leads to more accurate results. Consequently, it will not be necessary to perform many simulations (Figure 6 vs. Figure 12) or conditioning with high quantities of data values (Figure 17) to obtain acceptable results (Table 5).

This method has an important improvement with respect to the bivariate case, not only because it provides better results, but also it reduces the number of simulations to decrease the small scale variability. In other words it is not necessary to perform 10 or more simulations. Even more, it is not necessary to have a great number of conditioning values; the conditioned simulations did not show a lot of variation in terms of MSE values.

For future work, we think we can use a Bernstein copula to explore complex relationships between petrophysical properties and then fit, if possible, a semiparametric gluing copula, Siburg and Stoimenov (2008). Also, we consider we may use another optimization method which could give improved results, for example, we can implement genetic algorithms or Estimation of Distribution Algorithms (EDAs). It is very important to remark that the use of multivariate copulas leads to significant serious computational challenges, for this reason it is necessary to propose better ways to calculate them, for example parallel computing.

Acknowledgements

The present work was partially supported by the two following projects: IN110311 from Programa de Apoyo a Proyectos de Investigación e Innovación Tecnológica (PAPIIT) at Universidad Nacional Autónoma de México, and by 116606 (Y.00102) from Fondo Sectorial CONACYT-SENER-Hidrocarburos.

References.

Al-harthy M., Begg S., Bratvold, R., 2005, Copulas: A new technique to model dependence in petroleum decision making, *Journal of Petroleum Science & Engineering*, 57, 195-208.

Armstrong M., Galli A., Bailey W., Couet, B., 2004, Incorporating technical uncertainty in real option valuation of oil projects. *Journal of Petroleum Science & Engineering,* 44, 67–82.

Balan B., Mohaghegh S., Ameri S., 1995, State-of-The-Art in Permeability Determination From Well Log Data: Part 1.- A Comparative Study, Model Development. SPE 30978.

Bennett W.M., Linton P.F., Rectenwald, E.E., 2002, Hydrologic investigation of the Floridian aquifer system, western Hillsboro Basin, Palm Beach County, Florida, Technical Publication WS-8, South Florida Water Management District.

Billingsley P., 1995, Probability and Measure, 3rd edition. New York: Wiley.

Cosentino L., 2001, Integrated Reservoir Studies, second ed. Technip, Paris, France.

Dafflon B., Irving J., Holliger , K., 2009a, Simulated-annealing-based conditional simulation for the local-scale characterization of heterogeneous aquifers. *Journal of Applied Geophysics,* 68, 60-70.

Dafflon B., Irving J., Holliger* K., 2009b, Quantitative Integration of High-Resolution Hydrogeophysical Data: A Novel Approach to Monte-Carlo-Type Conditional Stochastic Simulations and Implications for Hydrological Predictions. *Journal of Earth Science*, 20, 580–591.

Dafflon B., Barrash W., 2012, Three-dimensional stochastic estimation of porosity distribution: Benefits of using ground-penetrating radar velocity tomograms in simulated-annealing-based or Bayesian sequential simulation approaches. *Water Resources Research*, 48:5.

Accioly R., Chiyoshi F., 2004, Modeling dependence with copulas: a useful tool for field development decision process, *Journal of Petroleum Science & Engineering,* 44, 83-91.

Deheuvels P., 1979, La fonction de dépendance empirique et ses porpriétés. Un test nonparamétrique d'independance, Acad. Roy. Belg. Bull. Cl. Sci. (5) 65(6): 274-292.

Deutsch C.V., 1992, Annealing Techniques Applied to Reservoir Modeling and the Integration of Geological and Engineering (Well Test) Data. PhD thesis, Stanford University, Stanford, CA.

Deutsch C.V., Cockerham P.W., 1994, Geostatistical Modeling of Permeability with Annealing Cosimulation (ACS). SPE 28413.

Díaz-Viera M., Casar-González R., 2005, Stochastic simulation of complex dependency patterns of petrophysical properties using t-copulas. Proc. IAMG'05: GIS and Spatial Analysis. 2, 749-755.

Díaz-Viera M., Anguiano-Rojas P., Mousatov, A., Kazatchenko, E., Markov M., 2006, Stochastic modeling of permeability in double porosity carbonates applying a Monte-Carlo simulation method with t-copula. SPWLA 47th Annual Logging Symposium.

Dréo J., Pétrowski A., Siarry P., Taillard, T., 2006, Metaheuristics for Hard Optimization, first ed. Springer-Verlag Berlin Heidelberg, Germany.

Erdely A., Díaz-Viera M., 2009, Nonparametric and semiparametric bivariate modeling of petrophysical porosity-permeability well log data. In: Copula Theory and Its Applications (P Jaworski *et al*. eds), Lecture Notes in Statistics - Springer. 198, 267-278.

Embrechts P., McNeil A., Straumann, D., 1999, Correlation: pitfalls and alternatives, Risk Magazine 5, 69-71.

Embrechts P., Lindskog F., McNeil, A.J., 2003, Modeling dependence with copulas and applications to risk management. In S. Rachev (ed) Handbook of Heavy-Tailed Distributions in Finance: 329-384. New York: Elsevier.

Fermanian J-D., Radulovic D., Wegcamp, M. 2004, Weak convergence of empirical copula processes, it Bernoulli 10, 547-560.

Haldorsen H., Damsleth E., 1990, Stochastic modeling. *Journal of Petroleum Technology*, 404-412, April.

Hernández-Maldonado V., Díaz-Viera M., Erdely, A., 2012, A joint stochastic simulation method using the Bernstein copula as a flexible tool for modeling nonlinear dependence structures between petrophysical properties. *Journal of Petroleum Science & Engineering,* 90-91 112-123.

Hoeffding W., 1941, Scale-invariant correlation theory. In N.I. Fisher and P.K. Sen (eds) The Collected Works of Wassily Hoeffding: 57-107. New York: Springer.

Holden L., Madsen R., Skorstad A., Jakobsen K. A., Tjolsen C. B., Vik S., 1995, Use of Well Test Data in Stochastic Reservoir Modelling. SPE annual Technical Conference and Exhibition held in Dallas, U.S.A., 22-25 October.

Journel A., Alabert F., 1990, New method for reservoir mapping. *Journal of Petroleum Technology*, 212-218, February.

Journel A., Zhu H., 1990, Integrating soft seismic data: Markov-Bayes updating, an alternative to cokriging and traditional regression. In Report 3, Stanford Center for Reservoir Forecasting, Stanford, CA.

Kazatchenko E., Markov M., Mousatov A. 2004, Joint inversion of acoustic and resistivity data for carbonate microstructure evaluation, it *Petrophysics*, 45, 130-140.

Kazatchenko E., Markov M., Mousatov A., Parra J., 2006, Carbonate microstructure determination by inversion of acoustic and electrical data: application to a South Florida Aquifer, it *J. Appl. Geophys*., 59, 1-15.

Landa J.L., Kamal M.M., Jenkins C.D., Horne R.N., 1996, Reservoir Characterization Constrained to Well Test Data: A Field Example. SPE Annual Technical Conference and Exhibition held in Denver, Colorado, U.S.A., 6-9 October.

Muñoz-Perez J., Fernández-Palacín A., 1987, Estimating the quantile function by Bernstein polynomials, *Computational Statistics and Data Analysis*, 5, 391-397.

Nelsen R.B., 2006, An Introduction to Copulas, second ed. Springer, New York.

Parra J.O., Hackert C.L., Collier H.A., Bennett M., 2001, A methodology to integrate magnetic resonance and acoustic measurements for reservoir characterization. Report DOE/BC/15203-3, National Petroleum Technology Office, Department of Energy, Tulsa, Oklahoma.

Parra J.O., Hackert C.L., 2002, Permeability and porosity images based on crosswell reflection seismic measurements of a vuggy carbonate aquifer at the Hillsboro site, South Florida, 72nd Annual Meeting of the Society of Exploration Geophysicists, Paper VCD P1.2.

Sancetta A., Satchell S., 2004, The Bernstein copula and its applications to modeling and approximations of multivariate distributions. Econometric Theory. 20, 535-562.

Sancetta A., 2007, Nonparametric estimation of distributions with given marginals via Bernstein-Kantorovic polynomials: L1 and pointwise convergence theory. *Journal of Multivariate Analysis*, 98, 7, 1376-1390.

Siburg K., Stoimenov P., 2008, A scalar product for copulas. *Journal of Mathematical Analysis and Applications*, 344, 429–439.

Suro-Perez V., 1992, Indicator Kriging and Simulation Based on Principal Component Analysis. PhD thesis, Stanford University, Stanford, CA.

Sklar A., 1959. Fonctions de répartition á n dimensions et leurs marges, Publ. Inst. Statist. Univ. Paris. 8, 229-231.

Geofísica Internacional (2014) 53-2: 183-198

Original paper

Joint interpretation of geoelectrical and volatile organic compounds data: a case study in a hydrocarbons contaminated urban site

Omar Delgado-Rodríguez*, David Flores-Hernández, Myriam A. Amezcua-Allieri, Vladimir Shevnin, Andrés Rosas-Molina and Salvador Marín-Córdova

Received: March 06, 2013; accepted: September 03, 2013; published on line: April 01, 2014

Resumen

Debido a la ocurrencia de un derrame de gasolina en un área urbana, los métodos de Tomografía de Resistividad Eléctrica (TRE), Perfilaje Electromagnético (PEM) y de medición de Compuestos Orgánicos Volátiles (COV) fueron utilizados para definir la pluma de contaminación y dirigir los trabajos de muestreo de suelo. Las anomalías COV (contaminación reciente) indicaron que una gasolinera localizada en el área de estudio es una fuente de contaminación activa. Las zonas con contaminación madura definidas con los métodos TRE y PEM correspondieron con anomalías de baja resistividad debido a los procesos de degradación de los hidrocarburos contaminantes. Los resultados alcanzados con los métodos TRE, PEM y VOC fueron integrados en un mapa, permitiendo la configuración final de las plumas de contaminación y la optimización de las perforaciones y el muestreo de suelo y producto libre. Análisis de laboratorio de las muestras de producto libre sugieren la existencia de más de un evento de contaminación en el sitio, con la presencia de contaminantes hidrocarburos frescos y degradados, clasificados en el rango de gasolina. Este estudio demuestra las ventajas de la aplicación conjunta de TRE, PEM y COV en sitios con fuentes de contaminación activa, donde se asume la existencia de hidrocarburos contaminantes recientes y maduros en el subsuelo.

Palabras claves: Benceno, Tolueno, Etilbenceno, Xilenos (BTEX), compuestos orgánicos volátiles (COV), contaminación por hidrocarburos, fuga de gasolina, tomografía de resistividad eléctrica (TRE), perfilaje electromagnético (PEM).

Abstract

As a result of a gasoline spill in an urban area, Electrical Resistivity Tomography (ERT), Electromagnetic Profiling (EMP) and Volatile Organic Compounds (VOC) methods were used in order to define the contamination plume and to optimize the drilling and soil sampling activities. The VOC anomalies (recent contamination) indicated that a gas station located at the study site is an active contamination source. The mature contaminated zones defined by ERT and EMP methods corresponded with low resistivity anomalies due to degradation process of the hydrocarbons contaminants. The ERT, EMP and VOC results were integrated on a map, allowing the final configuration of contamination plumes and the optimization of drilling and soil/free-product sampling. Laboratory analyses of free-product samples suggest the existence of more than one contamination event in the site, with the presence of recent and degraded-hydrocarbon contaminants classified in the gasoline range. This study shows the advantages of joint application of ERT, EMP and VOC methods in sites with active contamination source, where the existence of recent and mature contaminants in subsoil is assumed.

Keywords: Benzene, Toluene, Ethylbenzene, Xylenes (BTEX), hydrocarbons contamination, volatile organic compounds (VOC), gasoline spill, electrical resistivity tomography (ERT), electromagnetic profiling (EMP).

O. Delgado-Rodríguez*
D. Flores Hernández
M. A. Amezcua-Allieri
A. Rosas-Molina
S. Marin-Córdova
Instituto Mexicano del Petróleo (IMP),
Lázaro Cárdenas Norte 152,
San Bartolo Atepehuacan, 07730
México D.F.
Corresponding author: odelgado@imp.mx

V. Shevnin
Moscow State University
Geological Faculty
Department of Geophysics
Leninskie Gory, 119991
Moscow, Russia.

Introduction

Hydrocarbons are among the main factors of geological medium contamination. The effectiveness of electrical methods for the characterization, on surface and depth, of oil contaminated plumes has been reported by several authors (Vanhala, 1997; Modin *et al*., 1997; Atekwana *et al*., 2001; Osella *et al*., 2002; Delgado-Rodríguez *et al*., 2006; 2006a). Just after contamination, a high resistivity anomaly delimits the contaminated zone. Oil contaminants cause changes in physical, chemical and biological properties of soil (Sauck, 2000; Atekwana *et al*., 2001), mainly during the first four to six months after contamination. Abdel-Aal *et al*. (2004) found some important details on biodegradation process and changes in the electrical properties of contaminated zones. They demonstrated that the decrease of resistivity in soil contaminated by degraded hydrocarbons is mainly related to high surface conductivity in the pores of the affected rocks. Thus, the low resistivity anomalies are associated to the existence of mature hydrocarbon contamination. Electrical Resistivity Tomography (ERT) and Electromagnetic Profiling (EMP) are effective tools to mapping low resistivity anomalies caused by hydrocarbon contamination (Shevnin *et.al*., 2005).

ERT is applied in order to obtain a geoelectrical image of the sub-surface using electrical measurements made along profile at the surface. The application of ERT method is based on apparent resistivity determination with the help of linear array (e.g. Dipole-Dipole, Wenner-Schlumberger) of many electrodes connected to resistivity equipment. Resistivity data are then processed to obtain a resistivity cross-section (Loke, 2013). As a result of interpretation, true layers resistivity and their thickness are estimated.

The application of EMP method involves measuring the response of the subsurface to an electromagnetic field. An electromagnetic field is generated by a transmitter antenna, inducing eddy currents within the ground. These induced current generate a secondary magnetic field. Both primary and secondary magnetic fields are measured in a receiver antenna. The ground conductivity due to geological characteristics, conductive materials (metal objects) and contaminants can be calculated from the ratio of the secondary and primary magnetic fields (Keller and Frischknecht, 1966). The EMP results, although not providing detailed lithology (layers and their thicknesses) information, can quickly determine the horizontal changes in soil apparent conductivity (e.g. hydrocarbon contamination plume) at different study depths. The electromagnetic measurements are sensitive to buried elongated conductors such as metallic pipes, electric lines, sanitary sewer, etc. These are usually recognized by the large meter fluctuations which occur in short distance. When the antennas are oriented perpendicular to the elongated conductor's axis, a minimum conductivity value will be registered (reaching negative values). When the antennas are parallel and close to the conductor's axis, conductivity values will have a maximum (Geonics Limited, 2010). In this work, as part of the survey technique, to evaluate the magnitude of electromagnetic interference from metal objects in EMP measurements, soil conductivity measurements were performed to two orthogonal directions of the antennas.

Volatile organic compounds (VOC) are the most common contaminants encountered at hydrocarbon contaminated sites. VOC survey is applicable under a variety of geological setting. Accurate VOC determinations are needed to assess the extent of contamination to make decisions for appropriate remedial action. The evaluation of subsurface organic vapors is based on the physical phenomena of hydrocarbons volatilization given by the Henry law (Lin and Chou, 2006), as well as the site characteristics. It has been demonstrated that the analysis of gases or vapors is a good screening technique in hydrocarbon contaminated sites, with GWT depths between 2 to 10 m (API, 1991; Ochoa *et al*., 2007). Determination of VOC is usually performed in situ using a photoionization detector. Using this equipment, it is possible to detect a wide range of compounds in the gasoline to diesel range.

As a result of digging for a water cistern in a basement of an apartment building, a gasoline spill was detected. ERT and EMP methods were applied, as well as VOC measurements, in order to define the contamination plume and to guide the sampling activities. Through the application of the VOC, ERT and EMP methods, it was possible to calculate the dimensions of the affected area. Laboratory analyses of free-product samples suggest the existence of several contamination events with the presence of recent and mature hydrocarbon contaminants.

Site background

The site is located in a popular neighborhood of Mexico City between 2,240 and 2,244 m.a.s.l. The geological composition of the site belongs

to the sedimentary Mexico City basin and Texcoco ex-lake's west shore (Marín-Córdova *et al*., 1986). The stratification sequence showed low permeability clay and silt within fine and medium sand lenses. The groundwater table (GWT) was between 3.75 and 5.00 m in the central and northern portions of the site, meanwhile, in the southern portion, near to gas station, the GWT can reach up to 9.00 m depth. The permeability coefficient rate was 1.0 × 10-6 to 1.0 × 10-7 cm/s (low permeability).

A paved (main) street runs from southwest to northeast along 350 m (Figure 1). As a result of digging for a water cistern in a basement of an apartment building, a hydrocarbon spill with gasoline-like odor from a thin layer at an approximate depth of 5 m was detected. The spill point is about 100 m from a gas station, and about 50 m from small factories with solvents and fuel storage tanks, indicating the probable existence of active contamination sources (Figure 1). Indirect methods were applied to map the contaminated zones and to select the soil boring locations, defining a study area of 5.3 ha.

Application of geoelectrical and VOC methods: configuration of the contamination plume

Application of VOC measurements

Subsurface vapors were measured in situ to assess the content of VOC. The methodology to measure VOC has been tested and improved since 1992 to allow a rapid measurement (screening) of the most likely occurrence and distribution of hydrocarbons in the subsurface and thus select the sites to perform the drilling and soil sampling. Sampling equipment including a specialized hammer and a hammer sampler probe, allows by vacuum, the extraction of vapor from subsoil. VOC content in subsoil can then be determined using a portable photoionization detector (PID), which can measure concentrations from ppb to up to 10,000 ppm. Since the presence of VOC in the subsurface originated from the hydrocarbons contaminants are quantified, this method could be considered as semi-indirect. VOC were measured at 91 selected points.

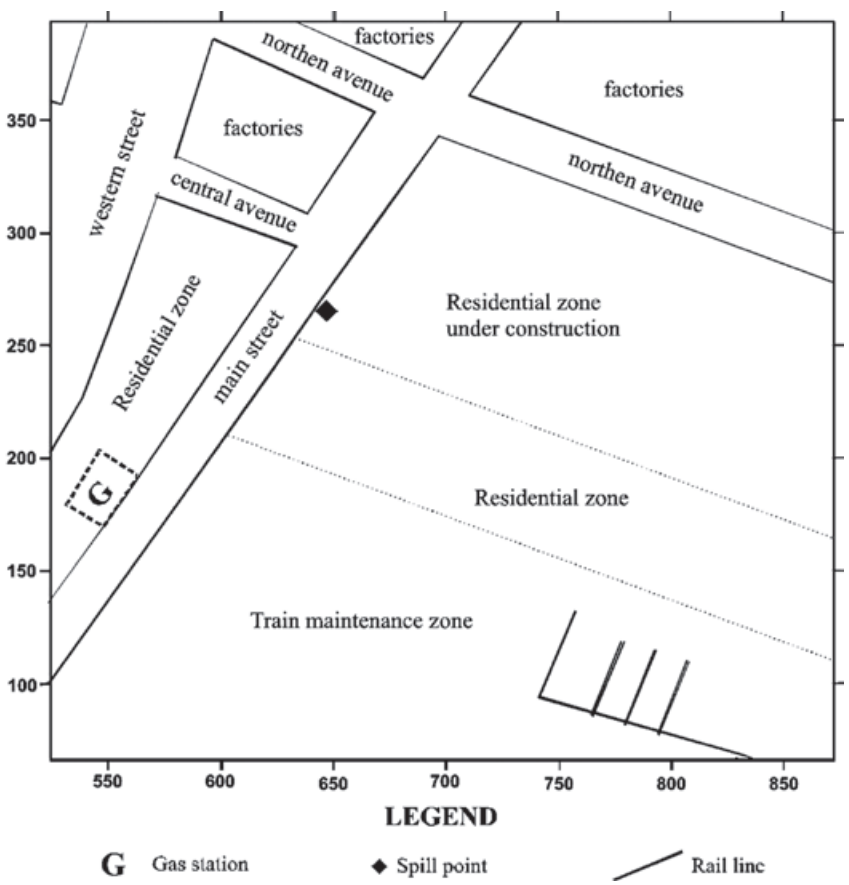

Figure 1. Scheme of the site.

Application of ERT method

Three ERT parallel profiles were performed on Main Street (Figure 1) in order to obtain resistivity anomalies associated with the presence of hydrocarbon-contaminated soils. A total of 64 ERT measurements points were settled. ERT survey was carried out using a great number (~50) of electrodes placed along each profile with a constant interval of 4 m, using AB/2 spacing of a Wenner-Schlumberger array from 6 to 42 m, ensuring a maximal study depth of 15 m. Spacing between sounding centers was 8 m.

Application of EMP method

Using the EM31-MK2 equipment (Geonics Limited, 2010), the horizontal changes in soil apparent conductivity for maximal study depth of 6 m is determined. Taking into account that in the most of the site the local GWT depth varies between 3.75 m – 5.00 m, it is feasible to use the EM31-MK2 equipment to detect the hydrocarbon contamination zones in soil, subsoil and groundwater, while in the southern end of the site (GWT depth = 9.00 m), EMP is feasible to detect the contamination in soil and subsoil, but not in the groundwater. The EMP survey was carried out considering the electromagnetic interference of the buried elongated conductors. According to our work experience using EM31-MK2 in urban and industrial sites (IMP 2006; 2006a; 2008; 2013; Mendez-Velarde *et al*., 2012), when the difference between conductivity values recorded to two orthogonal directions of the antennas is more than 10%, the EMP station is rejected and a new measuring point is selected, otherwise the average value can be used for the data reduction. In this way, we ensured that variations in the electromagnetic field are given only by variations in soil conductivity. After removing the measurement points affected by electromagnetic noise, 306 EMP data were recorded and an apparent resistivity map was made.

Results and discussion

The results of the application of ERT, EMP and VOC methods were processed using software SURFER 8 (Golden Software Inc., 2002) with minimum curvature algorithm. The minimum curvature gridding provides reasonable maps with satisfactory smoothing of the field lines (Briggs, 1974), widely used in the earth sciences (Ontario Geological Survey, 2003; Orfanos and Apostolopoulos, 2012), including geoelectric methods (Korhonen *et al*., 2005; Siemon, 2009).

VOC data interpretation

There are no national or international normative values that include normal or natural conditions of VOC for hydrocarbon contaminated soils. However, it has been observed that an anomalous value (greater than background) is evidence of contamination phenomena (Arpel, 1992). Fischer *et al*. (1996) studied a gasoline-contaminated site and they considered that VOC = 21 ± 2 ppm correspond to low contamination levels. Based on our experience (Ochoa *et al*., 2002; Delgado-Rodríguez *et al*., 2006, Mendez-Velarde *et al*., 2012), we had determined that in hydrocarbons contaminated sites VOC values greater than 20 ppm are associated with presence of hydrocarbons, either as free product, absorbed in the subsurface or dissolved in groundwater.

Fresh gasoline contamination presents high VOC (> 20 ppm) concentration. Low VOC (< 20 ppm) values could indicate the presence of clean soil or soil contaminated by mature hydrocarbons. Figure 2 shows some plumes with high VOC concentrations (dark zones, Figure 2), indicating the presence of fresh contaminants in the subsoil; one of them possibly related to the gas station.

In sites with an active contamination source it is possible to have both degraded contaminants (low VOC values) and fresh contaminants (high VOC values). In the spill point, such as in zone with clean soil, low VOC values are observed, indicating the possible existence of degraded hydrocarbon contaminants in the subsoil in zones with low values of VOC. Because of this, ERT and EMP methods are applied since they are effective for mapping mature contamination plumes.

Statistical analysis of ERT data

Figure 3 shows the statistical distribution (apparent resistivity vs. AB/2 distances) from 64 ERT measurements points. The legend represents the occurrence frequency values. In general, the apparent resistivity values are below of 20 Ohm.m, even in the vadose zone (minimal depth of GWT is 3.75 m), which means the clay content in soil is significant at different study depths. The mean curve (curve H, Figure 3) characterizes the subsurface up to 15 m depth by a three layer curve (type H) with low resistivity contrast. In most of the SEV, the resistivity decreases from 10 to 7.8 Ohm.m (first and second layer) which marks the transition from a semi-saturated to saturated clayey sediments, respectively, followed by a third layer (AB/2 > 30 m) with

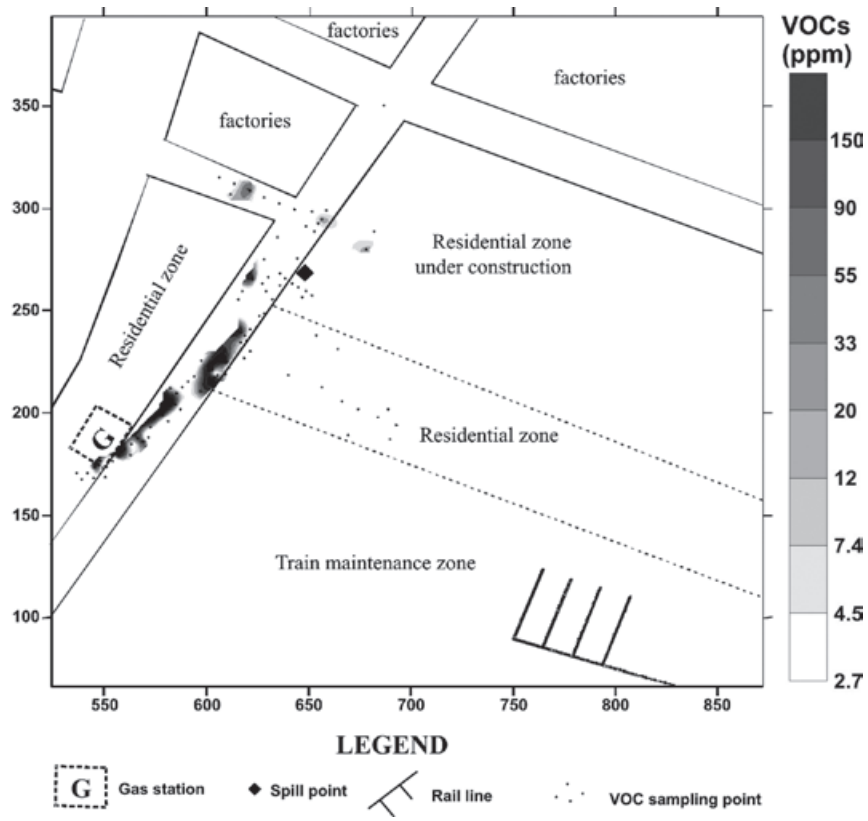

Figure 2. VOC map. The dark zones indicate the presence of recent hydrocarbon contamination.

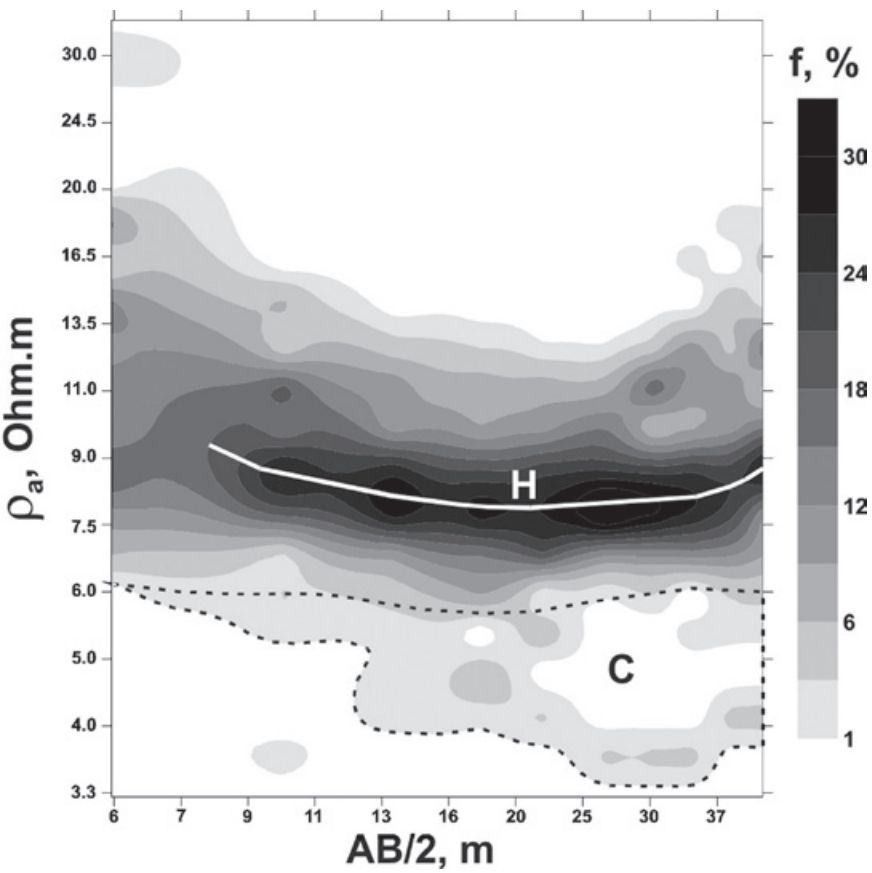

Figure 3. Statistical distribution of ERT data. (H) Mean resistivity curve for the study site. (C) Cloud of low apparent resistivity values separated from mean curve.

lower clay content (ρa ~ 9 Ohm.m). Apparent resistivity values below 6.4 Ohm.m are outlined in a cloud of data (dashed line contour, zone C, Figure 3), indicating the presence of low resistivity anomalies (mature contamination) for some ERT points, mainly for AB/2 > 10 m or study depth ≥ 5 m (second layer).

ERT data interpretation. Defining the geoelectric boundary between clean and contaminated soil

The RES2DInv software was used for the interpretation process and an interpreted geoelectrical section was obtained for each profile. The RES2DInv software uses the smoothness-constrained least-squares method inversion technique to produce a 2D model of the subsurface. Two different variations of the smoothness constrained least-squares method are provided; one optimized for areas where the subsurface resistivity varies in a smooth manner, and another optimized for areas with sharp boundaries (Loke and Barker, 1996). The obtained geoelectrical sections have the same number of layers with same thicknesses along each profile, giving great advantage to make interpreted resistivity maps for different study depths (e.g. groundwater table depth, contamination plume, etc).

Figure 4 shows the interpreted resistivity sections for ERT_1, ERT_2 and ERT_3 profiles with three main layers: a superficial resistive layer consisting of sandy-clayey deposits with resistivity range from 8 to 20 Ohm.m, a second layer where clay content increases with resistivity ranging from 1.5 to 9 Ohm.m and a resistive third layer given by the decrease in clay content with resistivity ranging from 8 to 35 Ohm.m.

Taking into account the existence of high clay content in the subsoil and the characterization of mature hydrocarbon contamination as low resistivity anomaly, we need to define the geoelectric boundary between clean and contaminated soil. For this purpose, we used in the present work a conductivity model for unconsolidated formations and the "PetroWin" software for calculation of the soil resistivity developed by Ryjov and Shevnin (2002). This model considers the geometrical microstructure of the components as well as electrochemical processes occurring in the soil for a wide range of the pore-water salinity and clay content. Once groundwater (or salinity) and soil resistivity are known, clay content and porosity are estimated for clean soil, and the geoelectric boundary is defined. The characteristics of the conductivity model, the procedure to determine the groundwater (from in-field measurements) and soil (from lab measurements) resistivity, and the equations for calculate the soil petrophysical parameters (including clay content and porosity) are explained in detail in Shevnin *et al*. (2006; 2007) and Delgado-Rodríguez *et al*. (2012).

In order to define the geoelectric boundary, four wells located far enough from the spill point (Figure 7B) were drilled in the residential zone under construction using a Geoprobe System (Figure 5). Four soil samples (one per

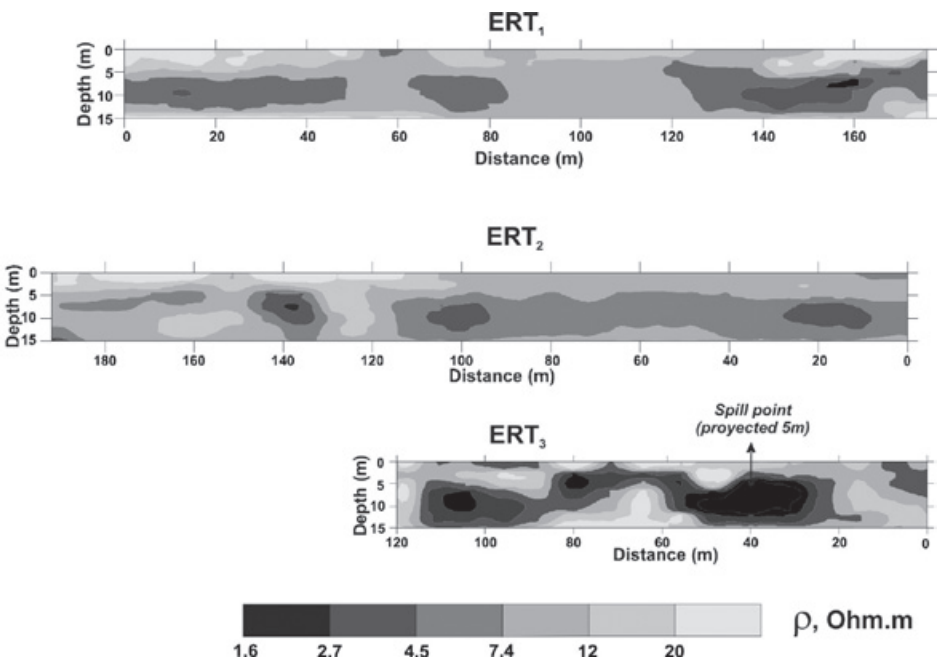

Figure 4. Interpreted resistivity section from ERT profiles with three layers. Low resistivity anomalies in the second layer indicate the presence of mature contamination.

Figure 5. Geoprobe System used to collect soil and groundwater samples

well) were collected from the layer noticeably more argillaceous, at depths of 6 to 7 m (second layer, Figure 4) and then analyzed in the laboratory, resulting in a clay content range between 37% and 50% (Table 1). Likewise, groundwater samples were collected from local aquifer, resulting in a mean resistivity values of 5.9 Ohm.m at 20 °C, which means a salinity of 1 g/l.

In Figure 6 the results of theoretical calculations with the "PetroWin" software are shown. Soil resistivity is considered as a function of water salinity (NaCl content at 20°C). Soil resistivity curves for different sand and clay proportions are displayed: curve for sand (in the upper part of Figure 3A, 0% clay, and 25% porosity) and curve for pure clay (in the lower part of Figure 3A, 100% clay, and 55% porosity). Water curve (dashed curve) gives us the relation between water resistivity and water salinity; while the vertical dotted line represent the groundwater salinity mean value of 1 g/l for the study area. Two horizontal dotted lines show the resistivity range 4.5 Ohm.m to 6.1 Ohm.m for soils with clay content between 37% -50% and pore-water salinity 1 g/l, being 4.5 Ohm.m the geoelectric boundary between clean and contaminated soil. Resistivity values less than 4.5 Ohm.m correspond to mature oil contaminated soils; however, low levels of hydrocarbons contamination may be present

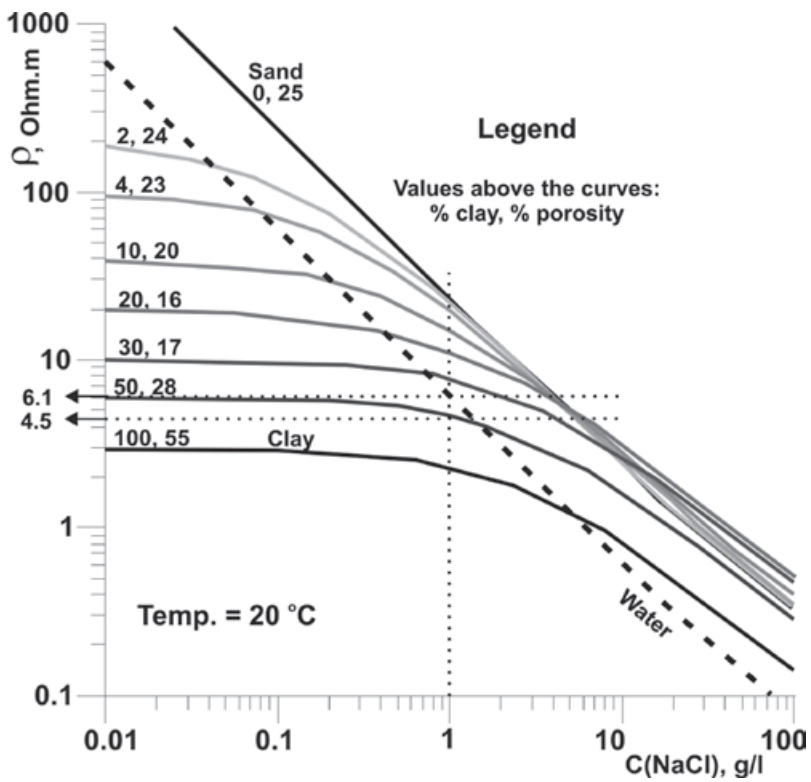

Figure 6. Experimental results and theoretical dependence of soil resistivity versus pore water salinity for different clay content in soils. Theoretical model: clay porosity = 55%, sand porosity = 25%.

Table 1. Clay content and sampling depth values of the clean soil samples. Clay content values were used to define the geoelectric boundary between clean and contaminated soils.

Clean soil sample	Clay content (%)	Sampling depth (m)
1	49	6.6
2	38	6.3
3	50	6.0
4	37	7.0

in soils with resistivity values within the aforementioned resistivity interval. Resistivity values greater than 6.1 Ohm.m indicate that there is no mature contamination.

The second layer presents low resistivity zones associated with the presence of mature hydrocarbons contamination. Using the interpreted information from Figure 4, the behavior of the resistivity on the second layer (local aquifer) can be mapped with high resolution. A map of interpreted resistivity for the second layer is shown in Figure 7A where the dark zones may indicate the presence of mature contamination.

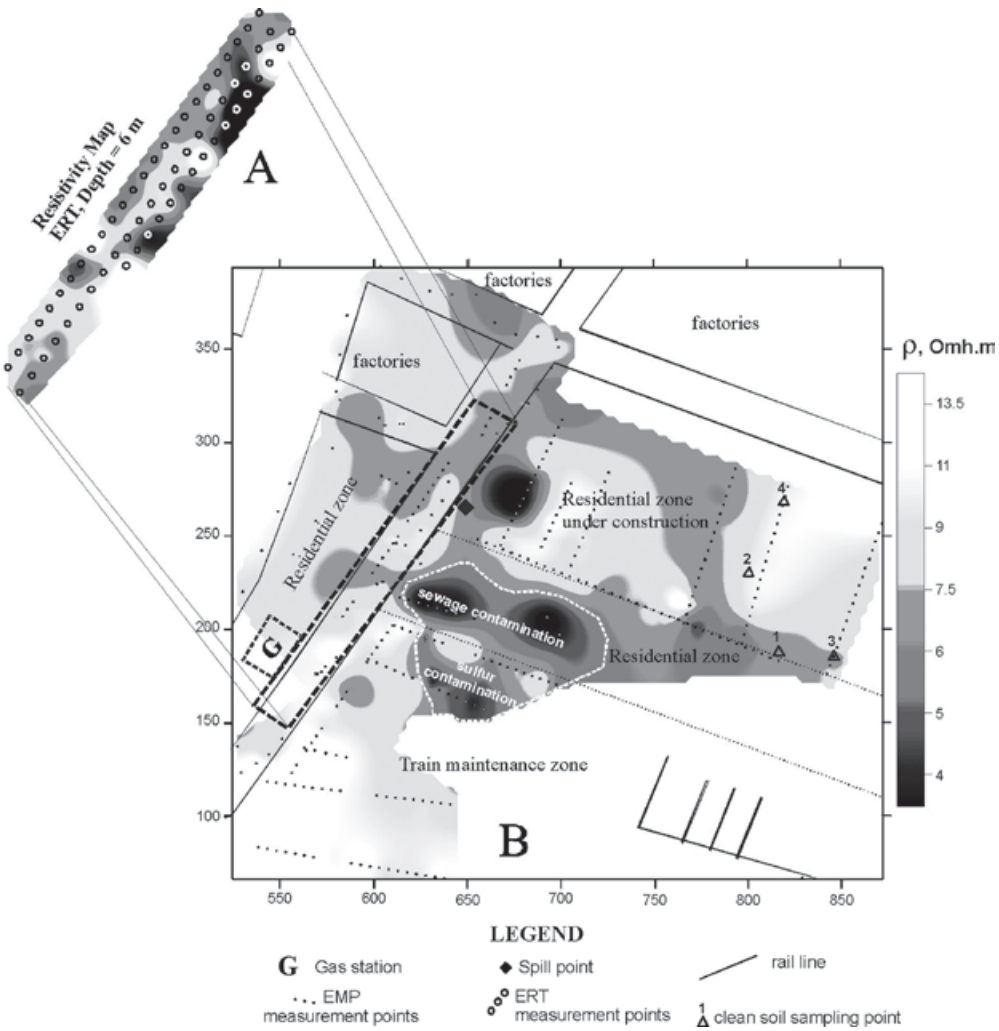

Figure 7. Resistivity maps. Interpreted resistivity map from ERT for depth= 6m. (B) Apparent resistivity map from EMP.

EMP data interpretation

The maximum study depth with EM31-MK2 is 6 m. Considering the conductive sediments of the site, the maximum study depth corresponding, in Figure 3 to AB/2 = 12 to 13 m, and higher values of the occurrence frequency, the ρa range from 7.5 to 9.5 Ohm.m is defined as representative of the lithological variations in the study site for study depth equal to 6 m.

Figure 7B shows the apparent resistivity map given by the EMP method. Three main (southern, central, and northern) low resistivity anomalies (dark zones, Figure 7B) are observed. The southern anomalous zone includes the railroad maintenance area (Figure 7B) where sulfur powder can be seen dispersed on the ground surface. Due to biodegradation processes, sulfur can cause an acidic environment, which generates salts in the subsoil and the consequent low resistivity anomaly. Therefore, the existence of chemical contamination is possible due to the presence of sulfur, therefore railroad maintenance area will be considered as contaminated by sulfur. The central anomalous zone is located within a residential zone (Figure 7B), coinciding with the drainage system. Due to land subsidence in the Valley of Mexico, frequently the drainage system, consisting of concrete pipelines, is broken and sewage leakages occur. In this case, we observed part of the sewage emerging on the terrain surface, resulting in low resistivity anomaly. Furthermore, the VOC values in this zone are almost zero (Figure 2), ensuring the absence of recent hydrocarbon contamination. Therefore, we propose that sewage is causing this low resistivity anomalies inside residential zone (Figure 7B). These two areas contaminated (by sulfur and sewage) should not be considered in the setting of hydrocarbon contamination plumes (see zone framed with dashed white line in Figure 7B).

The northern anomaly zone is located in the area where a new residential zone is being built, including the spill point (black diamond, Figure 7B). The cause of this anomaly zone is the presence of degraded hydrocarbons (mature contamination).

Zones with high apparent resistivity values indicate the absence of degraded hydrocarbon contaminants in the subsurface and the possible presence of recent hydrocarbons contamination. However, these high values are influenced by the superficial layer of subsoil. The superficial soil resistivity is determined not only by the clay content but also by its moisture, depending on the topographical elevations changes, masking the recent contaminants effect. This is why EMP method, as well as ERT, has low resolution in detecting fresh hydrocarbons contamination plumes.

In general, there is a good correspondence between ERT and EMP resistivity maps (Figure 7), showing possible migration routes of the contaminants in the subsurface.

Integrated data map from EMP, ERT, and VOC results.

High VOC values (high level of volatiles) indicate the presence fresh contamination in the subsurface. In contaminated zones (e.g. around of the spill point), where low VOC values (VOC ≤ 1.2 ppm) such as clean soil are observed, low resistivity anomalies (ρ ≤ 4.5 Ohm.m) confirm the existence degraded contamination. Due to this, it is necessary to integrate the geoelectric (ERT and EMP) and VOC methods results in order to define and to map all contamination plumes at the site and to focus the drilling and soil/free-product sampling.

To make the integral map, a grid of 5 × 5 m for the study site was created, and values (rather the logarithm of the values) obtained by each method were interpolated. The grid size is equal to the study area, with an approximate value of 5.3 ha. At each grid point, the applied methods receive a weight according to the interval wherein their values are (Table 2).

The parameters or variables that integrate the map are: gas concentration (VOC) in ppm, true resistivity (ERT) in Ohm.m and apparent resistivity (EMP) in Ohm.m. Each variable, depending on the values range, generates a weight (or degree of reliability, X_{ij}) of the anomalous zone. The obtained values of the indirect methods (ERT and EMP) receive weights between 0 and 5, while VOC, considered as semi-indirect method, their values receive a weight range between 0 and 7 (Table 2). Based on the petrophysical modeling performed in clean soil samples (Table 1, Figure 6), the ERT interval 6.1 Ohm.m ≤ ρ <14 Ohm.m gets weight 0 since it is not related to the presence of neither fresh or mature contaminant but rather is the sediments resistivity range of the site, while the other weights values are distributed as follows: 3 to 5 and 1 to 2, for low (high resolution) and high (lower resolution) resistivity anomalies, respectively. In a similar manner, based on the correspondence between apparent resistivity

Table 2. Weight assigned to each value range obtained from application of the EMP, ERT and VOC methods.

EMP		ERT		VOC	
ρ interval (Ohm.m)	**Weight (X_{ERT})**	**ρ interval (Ohm.m)**	**Weight (X_{EMP})**	**VOC interval (ppm)**	**Weight (X_{VOC})**
$\rho_a < 4.3$	5	$\rho < 3.2$	5	VOC < 20	0
$4.3 \leq \rho_a < 5.9$	4	$3.2 \leq \rho < 4.5$	4	20 ≤ VOC < 28	1
$5.9 \leq \rho_a < 7.5$	3	$4.5 \leq \rho < 6.1$	3	28 ≤ VOC < 37	2
$7.5 \leq \rho_a < 9.5$	0	$6.1 \leq \rho < 14.0$	0	37 ≤ VOC < 49	3
$9.5 \leq \rho_a < 13.0$	1	$14.0 \leq \rho < 19.0$	1	49 ≤ VOC < 67	4
$\rho_a \geq 13.0$	2	$\rho \geq 19.0$	2	67 ≤ VOC < 90	5
				90 ≤ VOC < 120	6
				VOC ≥ 120	7

and interpreted resistivity maps (Figure 7), EMP (apparent resistivity) values receive weights 1 and 2 to high resistivity anomalies and 3 to 5 to low resistivity anomalies. Taking into account the statistical distribution of the apparent resistivity values of the Figure 3, the interval 7.5 Ohm.m ≤ ρa < 9.5 Ohm.m receives weight 0. The index for VOC varies between 1 and 7 depending on the increase of VOC value from 20 to 179 ppm. VOC values less than 20 ppm will have weight 0 (Table 2).

The X_{ij} calculated for each method *i,* in each grid point *j* is multiplied by a coefficient MCi (MC_{VOC} = 5 for VOC, MC_{ERT} =4 for ERT and MC_{EMP} = 3 for EMP). Finally, the average of all the values resulting from the multiplication (integral parameter, IP) is calculated by the expression:

$$IP_j = \frac{\sum_{i=1}^{N_j} (X_{ij} * MC_i)}{N_j} \qquad (1)$$

Where: IP_j –integral parameter value of the grid point *j*.

X_{ij} –weight value calculated from field value of the method *i* in grid point *j*.

MC_i –multiplication coefficient for method *i*.

N_j –Total number of methods applied in grid point *j* ($N_j = 1, 2$ or 3).

It should be noted that the ranges and weights in Table (2) are valid for the site studied in the present study. New sites require a particular analysis of the obtained data, defining new ranges and assigned weights.

Tables 3 and 4 show the calculation procedure using equation (1) in grid portions corresponding to two small zones predominantly contaminated with fresh and mature hydrocarbons, respectively. Near to well S_1, the zone with fresh contaminants shows high VOC values (Table 3), while low resistivity and VOC values highlight in the zone with degraded contaminants located close to the spill point (Table 4).

The IP_j values are mapped and shown in Figure 8. Three contamination plumes are observed in the integrated map.

The first plume starts at the southwestern corner of the study area and extends down Main Street to the center of the site. Taking into account its connection with gas station and the high values of VOC in this plume (presence of fresh hydrocarbons), we can affirm that the gas station is an active contamination source. Four months after the completion of this work, as a result of an integrity testing of the underground storage tank, a gasoline leaking point was found and repaired in the gas station. The second plume, located in the residential zone under construction, is related with spill point, where medium and low values of VOC and low resistivity anomalies indicate the existence de mature hydrocarbon contamination. A third contaminated zone located in the central avenue is characterized by medium values of VOC and high resistivity values. This zone was related to the basement of a furniture factory, which uses solvents and white gas for painting and cleaning activities. The factory owner recognized that oil-based paints and solvents are poured directly on the soil (personal communication).

Table 3. Calculation of IP in a portion of the grid around the well S1, where the recent contamination is mainly characterized by high VOC values.

X	Y	EMP data	ERT data	VOC data	X_{EMP}* MC_{EMP}	X_{ERT} * MC_{ERT}	X_{VOC}* MC_{VOC}	N	IP
580	190	12.0	7.1	---	3	0	0	2	1.5
580	195	10.2	7.2	1.8	3	0	0	3	1.0
580	200	8.6	7.1	98.9	0	0	30	3	10.0
580	205	7.6	4.4	170.0	0	8	35	3	14.3
580	210	7.6	2.8	26.8	0	16	5	3	7.0
580	215	7.5	4.5	---	9	8	0	2	4.0

Table 4. Calculation of IP in a portion of the grid around the spill point, where mature contamination is characterized by low resistivity and VOC values.

X	Y	EMP data	ERT data	VOC data	X_{EMP}* MC_{EMP}	X_{ERT} MC_{ERT}	X_{VOC}* MC_{VOC}	N	IP
640	250	8.1	---	0.5	0	0	0	2	0.0
640	255	8.1	6.1	0.7	0	12	0	3	4.0
640	260	8.1	4.8	0.9	0	16	0	3	5.3
640	265	8.1	3.2	1.0	0	20	0	3	6.7
640	270	8.2	3.3	1.2	0	20	0	3	6.7
640	275	8.2	4.0	1.1	0	16	0	3	5.3

Verifying indirect results

Since benzene, toluene, ethylbenzene, and xylenes (BTEX) are some of the main VOC found in petroleum derivatives such as gasoline; we performed a measurement of the concentrations of each of their constituents in order to verify the anomalies. BTEX compounds are notorious due to the contamination of soil and groundwater by gasoline (EEA, 2010). Contamination typically occurs near petroleum and natural gas production sites, petrol stations, and other areas with underground or above-ground storage tanks, containing gasoline (EEA, 2010). Therefore, these compounds might be good indicator of recent contamination by gasoline. Although BTEX ratio were obtained to this purpose, it is acknowledge that inferring the age of a release based on BTEX ratios alone could be a valid approach only in well constrained situations, due to the rate of change of the gasoline BTEX ratio is affected by many site-specific variables. Another reason to measure BTEX in a gasoline contamination event was to comply with the current Mexican regulation (SEMARNAT, 2005).

In addition to BTEX, light oil fraction (LOF) was measured. LOF term refers to all volatile compounds which cover the range of carbon atoms from C_5 to C_{10}. The measurement of this fraction was performed to complement the measurement of all volatile compounds that may be present on the site, complying with current Mexican regulation on soil contamination.

Soil LOF Analysis

Using the integrated map (Figure 8), the drilling activities were conducted to the specific contaminated areas. Using a Geoprobe System (Figure 5), six monitoring wells were drilled up to 10 m of depth in strategic and topographic relevant points, taking into account the urban infrastructure and the access level to each point. Twenty two soil samples (Table 5) were collected in monitoring wells S_1-S_5 and S_x, (Figure 8). The analytical results revealed an irregular distribution of LOF depending on the depth ranges from bellow the detection limit to 11312 mg/kg. The maximal concentration (11312 mg/kg) of the site was detected in S_4 in the interval of depth 3 to 4 m. In well S_1, a concentration value of 1338 mg/kg was determinate for interval of depth 9.5 to 10 m, corresponding to the GWT depth in the southern end of the site. Other noticeable concentration

Table 5. Soil LOF concentration and sampling depth values. Grey rows show the maximal LOF concentrations for each well.

Well	X	Y	LOF (ppm)	Sampling Depth
S_1	589	208	678	5.50 - 6.00 m
			1338	9.50 - 10.00 m
			50	0.0 - 2.00 m
			834	2.00 - 3.00 m
			306	3.00 - 4.00 m
S_2	620	267	141	4.00 - 5.00 m
			62	5.20 - 5.80 m
			65	6.00 - 6.30 m
			BDL	6.80 - 7.00 m
S_3	654	281	50	0.0 - 3.80 m
			51	6.00 - 7.00 m
			38	1.50 a 1.90 m
			BDL	2.00 - 3.00 m
S_4	621	245	11312	3.00 - 4.00 m
			330	4.00 - 5.00 m
			86	5.00 - 6.00 m
			44	3.00 - 4.00 m
S_5	630.9	253.8	55	4.00 - 5.00 m
			33	5.00 - 6.80 m
			2071	3.15 - 4.00 m
S_x	616	294	301	4.00 - 4.40 m
			279	4.40 - 5.00 m

value (834 mg/kg) was determinate in well S_2 (Table 5). On the other hand, the well S_x shows significant value (2071 mg/kg) of LOF in sample of soil collected near to ground surface (depth ~1.2 m), as evidence of contamination by hydrocarbons poured on the terrain. LOF was very low in wells S_3 and S_5 (Table 5).

BTEX analysis in FP samples

One of the age-dating methods uses benzene plus toluene to ethylbenzene plus xylenes ratios (B+T/E+X). Use of this ratio minimizes uncertainties related to historical variations in BTEX composition of manufactured gasoline and provides a valuable tool for monitoring environmental changes in a dissolved gasoline plume with time (Stout *et al*., 2002). Although the rate of change of the gasoline BTEX ratio is affected by many site-specific variables, inferring the age of a release based on BTEX ratios alone could be a valid approach only in well constrained situations.

The samples of free product FP_1 and FP_2 collected in well S_1 and recollection trench, respectively (Figure 8), did not present significant changes in the B+T/E+X ratio (Figure 9). Observations revealed that fuels collected in monitoring S_1 were freshly released products by continuous leaking, as noted above. This could confirm that the free product fluid rapidly migrated to the GWT. Further work is needed to analyse if chemical substantial alteration occurred during its vertical migration into the soil or it may have remained in a relatively unaltered state.

BTEX ratio of free-phase gasoline sample FP_3, collected in the spill point (Figure 8) reached a value of 0.32, as shown in Figure 9. The significant decrease of BTEX ratio on free-phase in sample FP_3 implies a weathering by solubilisation, water washing or biodegradation process. Weathering and BTEX ratios imply that gasoline was transported to the water table and did not undergo substantial alteration during its vertical migration in the soil. Hence, a thin layer of free product was carried through sand lenses to the impermeable clay stratum. Therefore, when advanced alteration of the pattern has occurred due to environmental exposure, it is difficult to estimate, by composition of the free-phase, when the fuel was released. Lead and lead alkyls were absent in the free-phase sample, and is worth noting that regular unleaded gasoline was introduced in 1992.

Based on the results obtained from integral map (Figure 8) and BTEX analysis of FP samples (Figure 9), three contaminated plumes are characterized and showed in Figure 10.

Plume I. "Recent Infiltration Zone", corresponds to the most recent leakage of regular unleaded gasoline. The characteristics of the weathering processes (evaporation and solubilization) are not significant in the soil and FP samples. The contaminated plume I area is 1280 m^2, with a thickness according on sand layer thickness.

Plume II. Defined as "soil confined gasoline zone". It was contaminated by regular unleaded gasoline released within the last one to five years, based on the BTEX ratio analysis in FP samples. It showed a weathering process including evaporation, solubilisation, and biodegradation for a long time in a low permeability soil layer. Hydrogeology field analysis identified sand lenses confined in low permeability soil layers, the released gasoline could be trapped in a confined sand lens for years. However, site assessment work did not provide hydrogeochemical information from which reliable estimations about spill age could

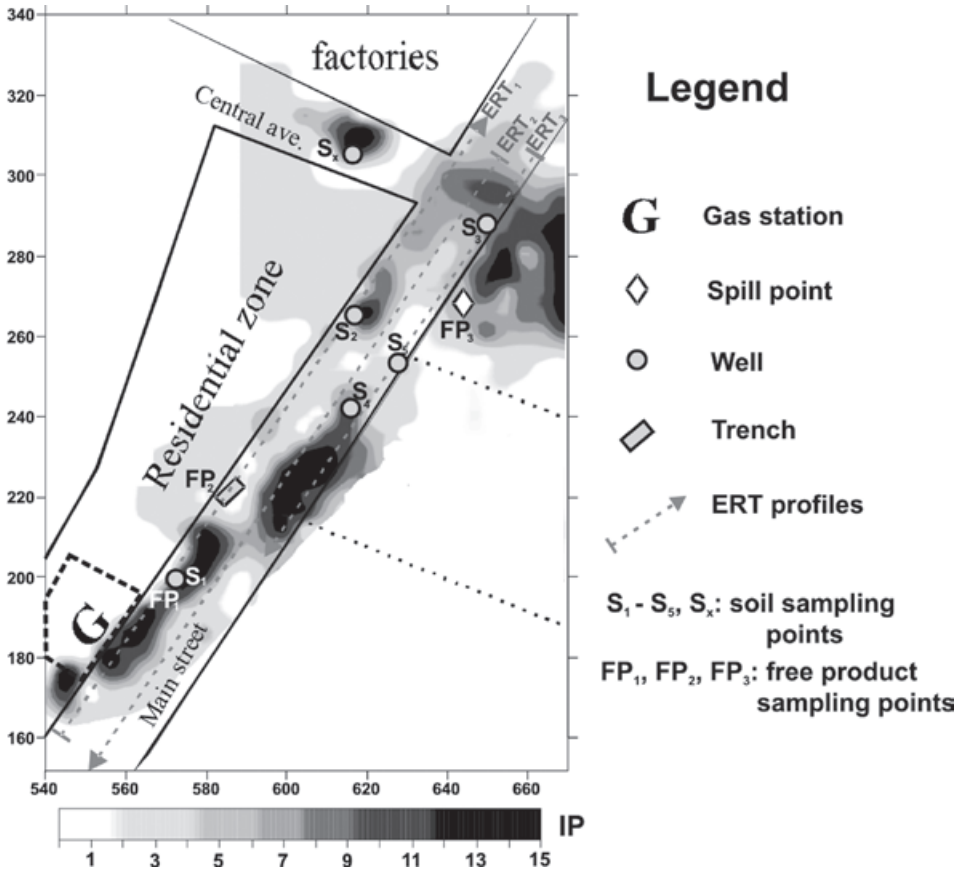

Figure 8. Integrated data map from indirect methods.

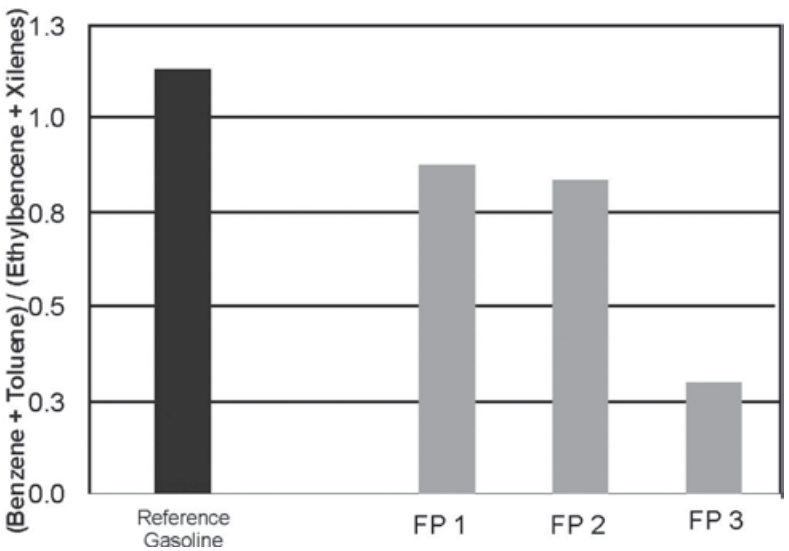

Figure 9. BTEX ratio of free-phase gasoline samples.

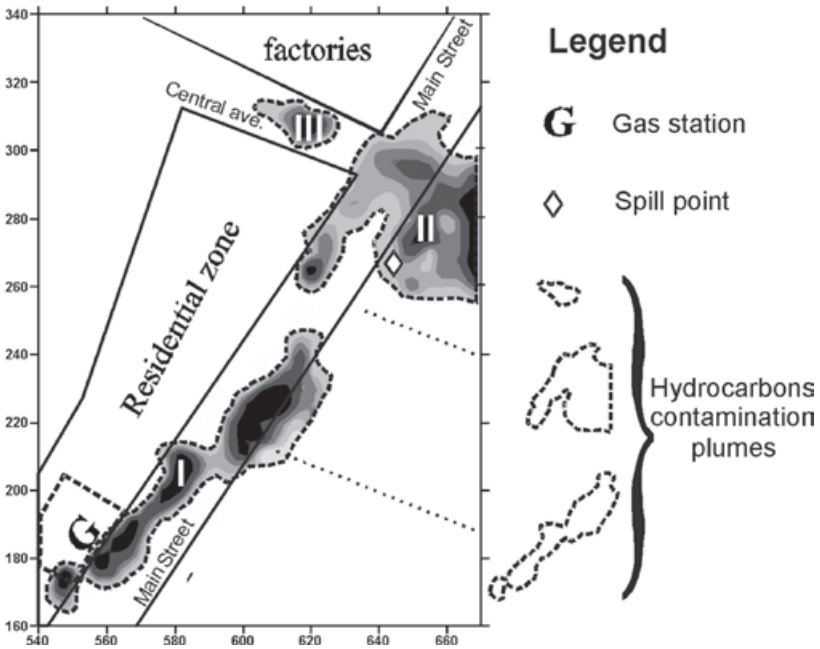

Figure 10. Map of hydrocarbons contamination plumes.

be drawn based on the BTEX ratios. The plume II area is 1152 m^2, with a volume according to sand lens thickness (~ 0.5 m).

Plume III. Zone characterized by a type of hydrocarbon different to the regular gasoline founded in plumes I and II. The composition of gasoline found in the shallower part of the subsurface (depth ~1.2 m) was similar to "white gas". Because of the chemical composition, weathering characteristics, contaminant transport, and hydrocarbons concentration in soils along the monitoring well S_x, plume III was considered an isolated event, not related with the other two plumes, covering a 160 m^2 area.

The sum of the areas of each contamination plumes is 2592 m^2, which almost represent 5% of the study area (5.3 ha), demonstrating the benefit of using indirect methods for the optimized selection of drilling points and soil sampling depths.

Conclusions

The indirect (ERT, EMP and VOC) methods are efficient tools for studying the hydrocarbons contaminated sites, reducing the number of drilling and soil samples. The high values of VOC mapped the presence of fresh gasoline in the subsoil and suggested that the gas station located at the study site is an active contamination source. Later, from an integrity testing, a gasoline leaking point was found in the underground storage tank of the gas station. However, the considerable degradation of the regular gasoline founded in the surrounding construction area indicates, at least, the existence of a previous contamination event.

The gas station is topographically located at an up gradient from the spill present in the nearby apartment construction. Therefore, gasoline released from buried pipeline would migrate toward the apartment construction area. Mature contaminated zones were defined by ERT and EMP methods as low resistivity anomalies. The ERT, EMP and VOC results were integrated on a map, allowing the final configuration of contamination plumes and the optimization of drilling and soil/free-product sampling.

The affected area by hydrocarbons can be separated in three plumes with different type of contaminants: Plume I, with recent release of regular gasoline, which is connected with the gas station as active contamination source; Plume II corresponds, according to geoelectrical and BTEX analysis results, to mature (weathering and biodegradation) hydrocarbons contamination due to regular unleaded gasoline released within the last one to five years; and a small Plume III, not related with the other two plumes mentioned above, caused by pouring of solvents and white gas on soil.

This study shows the advantages of joint application of ERT, EMP and VOC methods in sites with an active contamination source, where the existence of recent and mature contaminants in subsoil is suspected.

Bibliography

Abdel Aal G.Z., Atekwana E., Slater L.D., Atekwana E.A., 2004, Effects of microbial processes on electrolytic and interfacial electrical properties of unconsolidated sediments. *Geophys. Res. Lett*., 31, 12, 1-4.

API, 1991, An evaluation of soil gas and geophysical techniques for detection of hydrocarbons. API Publication Nº 4509, Washington, D.C., Health and Environmental Sciences Department, American Petroleum Institute, USA.

Arpel, 1992, Regional association of oil, gas and biofuels sector companies in Latin America and the Caribbean. Guide to solid waste management oil refinery, Canada.

Atekwana E., Cassidy D.P., Magnuson C. Endres, Werkema A.L., D.D. Jr., Sauck W.A., 2001, Changes in geoelectrical properties accompanying microbial degradation of LNAPL. In Proceedings of the Symposium on the Application of Geophysics to Engineering and Environmental Problems, Denver, Colorado, USA.

Briggs I.C., 1974, Machine contouring using minimum curvature. *Geophysics,* 39, 39-48.

Delgado-Rodríguez O., Shevnin V., Ochoa-Valdés J., Ryjov A., 2006, Geoelectrical characterization of a site with hydrocarbon contamination caused by pipeline leakage. *Geofísica Int*ernacional, 45, 1, 63-72.

Delgado-Rodríguez O., Shevnin V., Ochoa-Valdés J., Ryjov A., 2006a, Using electrical techniques for planning the remediation process in a hydrocarbon contaminated site. *Rev. Int. Contam. Ambient*., 22, 4, 157-163.

Delgado-Rodríguez O., Ladrón de Guevara-Torres M., Shevnin V., Ryjov A., 2012, Estimation of soil petrophysical parameters based on electrical resistivity values obtained from lab and in-field measurements. *Geofísica Internacional*, 51, 1, 5-15.

EEA, 2010, Benzene, toluene, ethylbenzene, xylene (as BTEX): European Environment Agency, http://glossary.eea.europa.eu/terminology/

Fischer M., Bentley A., Dunkin K., Hodgson A., Nazaroff W., Sextro J.D., 1996, Factors affecting indoor air concentrations of volatile organic compounds at a site of subsurface gasoline contamination. *Environ. Sci. Technol*., 30, 2948-2957.

Geonics Limited, 2010, EM31-MK2, Operating Manual, 51 pp., http://www.geonics.com

Golden Software Inc., 2002, Surfer. User´s Guide. Contouring and 3D mapping for Scientists and Engineers, 640 pp. http://gis.fns.uniba.sk/vyuka/DTM_ako_sucast_GIS/Kriging/2/Surfer_8_Guide.pdf

IMP, 2006, Proyecto F.21320 "Caracterización de la contaminación de suelos y agua freática en once diferentes sitios del D.D.V. Minatitlán – Villahermosa y D.D.V. Minatitlán – México". Dirección de Seguridad y Medio Ambiente, Instituto Mexicano del Petróleo.

IMP, 2006a, Proyecto F.21399 "Apoyo para la caracterización y restauración del área norte de la ex - Refinería 18 de Marzo". Dirección de Seguridad y Medio Ambiente, Instituto Mexicano del Petróleo.

IMP, 2008, Proyecto F.21472 "Evaluación del estado actual de la contaminación por hidrocarburos en el suelo y agua subterránea de la TAD de Azcapotzalco". Dirección de Seguridad y Medio Ambiente, Instituto Mexicano del Petróleo.

IMP, 2013, Proyecto F.23487 "Estudio de la contaminación por hidrocarburos en suelo y subsuelo del área de reconfiguración (CADI) de la Refinería Ing. Antonio M. Amor de Salamanca, Gto.". Dirección de Seguridad y Medio Ambiente, Instituto Mexicano del Petróleo.

Keller G.V., Frischknecht F.C., 1966, Electrical methods in geophysical prospecting, Oxford, Pergamon Press, 517 pp.

Korhonen K., Kuivamäki A., Ruotoistenmäki T., Paananen M., 2005, Interpretation of lineaments from airborne geophysical and topographic data. An alternative model within version Laxemar 1.2 of the Oskarshamn modelling project, *Geological Survey of Finland*, ISSN 1651-4416, SKB P-05-247, 39 pp., http://www.skb.se

Lin J. H., Chou M.S., 2006, Henry's law constant variations of volatile organic compounds in wastewater and activated sludge. *Aerosol and Air Quality Research*, 6, 2, 180-192.

Loke M.H., Barker R.D., 1996, Rapid least-squares inversion of apparent resistivity pseudosections by a quasi-Newton method. *Geophys. Prospect*., 44, 131-152.

Loke M.H., 2013, Tutorial: 2-D and 3-D electrical imaging surveys, 162 pp., www.geotomosoft.com

Marín-Córdova S., Aguayo C.J., Huízar A.R., Mandujano V.J., 1986, Geología en el Valle de México con fines geohidrológicos. Instituto de Geología, UNAM y CAVM.

Méndez-Velarde S.F., Ochoa-Valdés J., Delgado-Rodríguez O., 2012, Diseño de un plan de muestreo optimizado para la caracterización de hidrocarburos en suelos. Caso de estudio (48.6 hectáreas). SMA5, XVIII Foro de Avances de la Industria de la Refinación, Instituto Mexicano del Petróleo, México DF.

Modin I.N., Shevnin V.A., Bobatchev A.A., Bolshakov D.K. Leonov D.A., Vladov M.L., 1997, Investigations of oil pollution with electrical prospecting methods. In: Proceedings of the 3rd EEGS-ES Meeting, Aarhus, Denmark, 267-270.

Ochoa J., Méndez S., Valdés C., 2007, Aplicación del análisis de vapores orgánicos del subsuelo (gasometrías) en la caracterización de sitios contaminados por hidrocarburos. Derecho de Autor No. 03-2007-061912264100-01, Instituto Mexicano del Petróleo.

Ochoa J., Méndez S., Rosas A., 2002, Evaluación de la contaminación por hidrocarburos del subsuelo (gasometrías). El Petróleo de México, III, 2, 42-54.

Osella A., De la Vega M., Lascano, E., 2002, Characterization of a contaminant plume due to a hydrocarbon spill using geoelectrical methods. *J Environ. Eng. Geophysics*, 7, 78-87.

Ontario Geological Survey, 2003, Ontario airborne geophysical surveys, magnetic data, Oba-Kapuskasing area; Geophysical Data Set 1024 – Revised, 67pp.

Orfanos C., Apostolopoulos G., 2012, Analysis of different geophysical methods in the detection of an underground opening at a controlled test site. *Journal of the Balkan Geophysical Society*, 15, 1, 7-18.

Ryjov A., Shevnin V., 2002, Theoretical calculation of rocks electrical resistivity and some examples of algorithm's application. In Proceedings of the Symposium on the Application of Geophysics to Engineering and Environmental Problems (SAGEEP), Las Vegas, Nevada, USA.

Sauck W.A., 2000, A model for the resistivity structure of LNAPL plumes and their environs in sandy sediments. *J. App. Geophys*., 44, 151–165.

SEMARNAT, 2005, Norma Oficial Mexicana NOM-138-SEMARNAT/SS-2003, Límites máximos permisibles de contaminación en suelos por hidrocarburos y las especificaciones para su caracterización y remediación. Diario Oficial de la Federación.

Shevnin V. Delgado-Rodríguez O., Fernández-Linares L., Zegarra-Martinez H. Mousatov A., Ryjov A.A., 2005, Geoelectrical characterization of an oil contaminated site in Tabasco, Mexico. *Geofísica Internacional*, 44, 3, 251-263.

Shevnin V., Delgado-Rodríguez O., Mousatov A., Flores-Hernández D., Zegarra-Martinez H., Ryjov A.A., 2006, Estimation of soil petrophysical parameters from resistivity data: Application to oil-contaminated site characterization. *Geofísica Internacional*, 45, 3, 179-193.

Shevnin V., Mousatov A., Ryjov A.A., Delgado-Rodríguez O., 2007, Estimation of clay content in soil based on resistivity modeling and laboratory measurements. *Geophy. Prosp*., 55, 265-275.

Siemon B., 2009, Levelling of helicopter-borne frequency-domain electromagnetic data, *Journal of Applied Geophysics*, 67, 206–218.

Stout S.A., Uhler A.D., McCarthy K.J., Emsbo-Mattingly, 2002, Chemical Fingerprinting of Hydrocarbons. Introduction to environmental forensics, Academic Press, San Diego, California, 137-260.

Vanhala H., 1997, Laboratory and field studies of environmental and exploration applications of the spectral induced-polarization (SIP) method. Academic dissertation, for the degree of Doctor of Technology. Helsinki University of Technology.

Geofísica Internacional (2012) 53-2: 199-210

Original paper

Geological and geophysical data integration for delimitation of mineralized areas in a supergene manganese deposits

César Augusto Moreira*, Mario Rezende Borges, Glauber Matheus Lira Vieira, Walter Malagutti Filho and Mariana Aparecida Fernándes Montanheiro

Received: March 08, 2013; accepted: October 10, 2013; published on line: April 01, 2014

Resumen

Los métodos geofísicos constituyen una herramienta ampliamente utilizada en exploración mineral. Este trabajo presenta y discute los resultados de estudios geológicos y geofísicos desarrollados en un yacimiento de manganeso de origen supergénico, localizado en la región sudeste de Brasil. La zona mineralizada descrita en levantamientos geológicos fue caracterizada por bajos valores de resistividad (20Ω.m) y altos valores de cargabilidad (30ms), en un patrón similar al descrito en diversos trabajos en depósitos minerales de óxidos y sulfuros en rocas. Modelos geofísicos pseudo-3D permita la generación de mapas para diversas profundidades. Las áreas de alta cargabilidad y baja resistividad definen un patrón de mineralización gonditica con altos niveles de Mn. Áreas considerables con elevados valores de cargabilidad y baja resistividad probablemente resulten de la acumulación de hidróxido de manganeso y hierro, originados del intemperismo en cuerpos de mineral gonditico, disolución, percolación y precipitación.

Palabras clave: yacimiento, manganeso, supergénica, resistividad eléctrica, cargabilidad.

Abstract

Geophysical methods are widely used in mineral exploration. This paper discusses the results of geological and geophysical studies in supergene manganese deposits of southern Brazil. Mineralized zones as described in geological surveys were characterized as of low resistivity (20Ω.m) and high chargeability (30ms), pattern found also in oxides and sulfite mineral deposits. Pseudo-3D modeling of geophysical data allowed mapping at several depths. A relationship between high chargeability and low resistivity may define a pattern for high grade gonditic manganese ore. Large areas of high chargeability and high resistivity may result in accumulation of manganese and iron hydroxides, due to weathering of the gonditic ore, dissolution, percolation and precipitation.

Keywords: deposit, manganese, supergenic, electrical resistivity, chargeability.

C. A. Moreira*
W. Malagutti Filho
Departamento de Geologia Aplicada
Instituto de Geociências e Ciências Exatas
Universidade Estadual Paulista
Rio Claro, São Paulo State
Brazil
Corresponding author: moreirac@rc.unesp.br

M. Rezende Borges
Glauber Martins Lira Vieira
Mariana Aparecida Fernándes Montanheiro
Instituto de Geociências e Ciências Exatas
Universidade Estadual Paulista
Rio Claro, São Paulo State
Brazil.

Introduction

The Brazilian economy is traditionally based on mineral extraction for centuries mining attracted the first colonizers to move inland, during the period of Portuguese Colony and Empire. Territorial expansion was motivated by the search for valuable gems and minerals, especially in periods known as Diamond and Gold cycles.

Nowadays, Brazil is positioned among the top seven global economic powers, with a gross domestic product (GDP) based on the export of commodities like soy, beef and minerals such as iron, plus heavy industries, chemical industries and manufacturing.

World reserves of manganese ore is in seven countries, which together make up practically 98% of world deposits: Ukraine (24,14%), South Africa (20,69%), Australia (16,03%), Brazil (10,34%), India (9,66%), Gabon (8,97%) and China (7,59%) (DNPM, 2011).

The world production of manganese in 2010 was 14710 million tons, with Brazil the second largest producer (2,6 million tons), only next to China with 2,8 million tons. Domestic production increased 13% from 2009 to 2010 (DNPM, 2011).

The mining sector is the basis for several productive chains. It's comprises the steps of research, mining and processing. Its current share of gross domestic product (GDP) is 4.2% and represents about 20% of Brazilian exports; it generates 1 million direct jobs, equivalent to 8% of all industrial jobs (MME, 2010). Brazil also produces niobium, iron, bauxite and copper, as well as gold and gems (MME, 2010).

Of critical importance for the maintenance, development and economic growth in Brazil, the mining sector is dependent on basic geological research for the discovery of new mineral deposits. Mineral exploration includes a series of steps of planning and strategies based on the mineral input of interest, ranging from the genetic model and mode of occurrence in the geological environment, research methods and procedures, to economic constraints such as demand, market value and future projection.

Mineral exploration and research are essential for the recognition and incorporation of new reserves, in response to a growing demand for both the domestic market and for export and trade balance. The available tools include direct methods (geological mapping, probing, soil and rock sampling, chemical analysis) and indirect (analysis of remote sensing, geophysical methods) (Moon *et al.* 2007). Due to the low cost and the possibility to cover large areas, geophysical methods are an important tool in mineral research. Aerial geophysical surveys are employed in regional tasks, while detailing is obtained by ground survey. In the latter case, we may mention the use of Electrical and Electromagnetic methods in geophysical prospecting of mineral deposits consisting of sulfides and oxides, often preceded by magnetometric survey (Moon *et al.*, 2007; Telford *et al.*, 2004).

The Electrical Resistivity method has application in the surveys for disseminated manganese due to the characteristic of high electrical conductivity of this metal, often contrasting in relation to the rocks around. The Induced Polarization method is widely applied in this type of research because of the high polarizability of minerals disseminated in the geological environment. This method was developed and optimized primarily for exploration of disseminated sulphides.

Several studies have shown the advantages, disadvantages, benefits and limitations of uses of these geophysical methods mentioned in the detailing and analyzing the morphology of mineral deposits (Alis, 1990; Irvine & Smith, 1990; White *et al.*, 2001; Moreira & Ilha, 2011; Moreira *et al.*, 2012).

This paper discusses the results of geological and geophysical studies conducted in a manganese mine of supergene origin, located in southeastern Brazil. Methods of Electrical Resistivity and Induced Polarization were employed in this work. The main objectives are: to establish relationships between measured physical parameters and mineralized zones in oxides and hydroxides in mapped mining fronts and analysis of the morphology of mineral bodies from the analysis and interpretation of three-dimensional models in terms of electrical resistivity and chargeability.

Material and methods

Geology and genesis of minerals

The area of studies, known as the Córrego do Cocho mine near located in the city of Itapira, State of São Paulo, southeastern Brazil, 177 km from São Paulo city (Figure 1).

Mining activity in the Córrego do Cocho mine began in the early 90s by Mineração Itapira Ltd. The manganese mineral is extracted from the

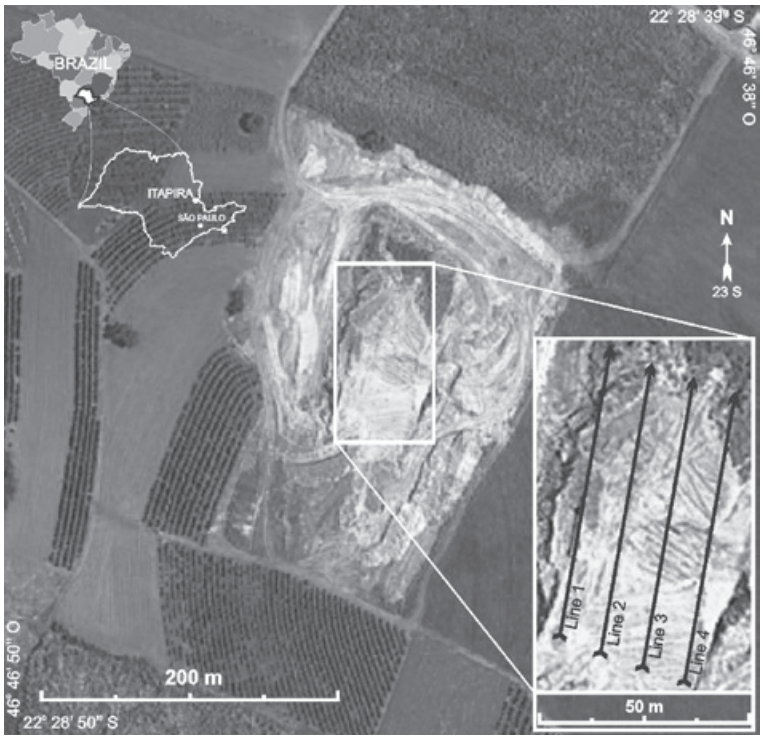

Figure 1. Location of the area of study, with positioning of lines of acquisition of geophysical data in the area of mining of manganese mineral.

mining fronts by direct excavation of saprolite material (Figure 2), which is a processed by homogenization, washing, crushing, grinding and concentration of the ore.

The regional geological context is the Ribeira Fold Belt, characterized by NE-SW trend with tectonic stacking to W toward São Francisco Craton. The lithotypes exhibit main deformation characterized by frontal collision and transpressive component. Transpressive shear zones and thrusts limit tectonic domains.

The Ribeira Fold Belt groups consists of two main lithostratigraphic units: the Amparo Complex and the Itapira Group.

The structures and rocks of the Amparo Complex reveal polymetamorphic classical evolution, initiated by sedimentation of clastic with clays concomitant with intrusions, extrusions and basic tuffs (Wernick, 1967). These rocks resulted in gneissic-migmatitic association of amphibolite facies and granulite in metamorphic event assigned to the

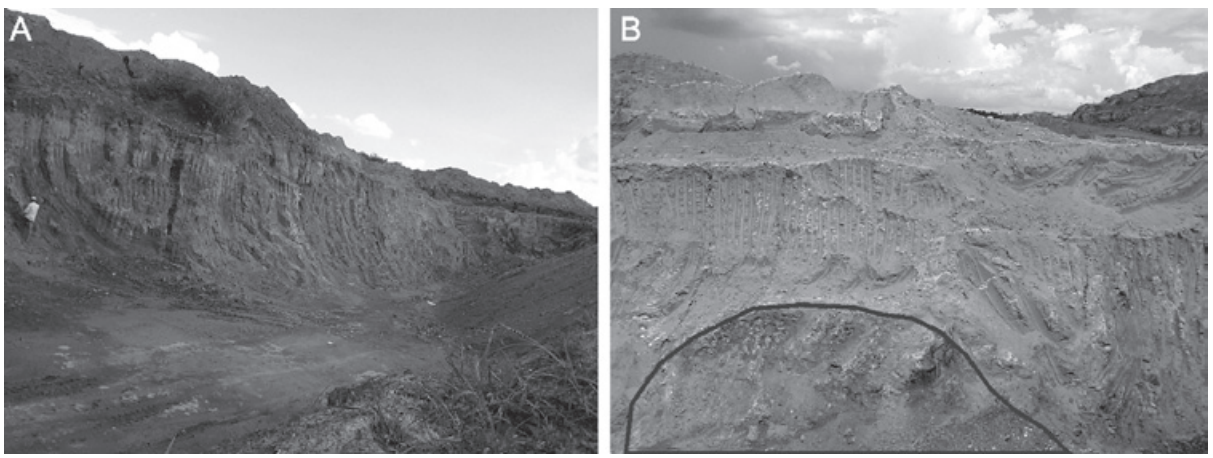

Figure 2. a) Mining front in activity. b) Detail of mineral body exposed.

Mesoproterozoic. In a successive event of tectonic deformation occur recrystallization and intrusion of large granitic masses, resulted in new migmatization of the Amparo Complex during the Brazilian Neoproterozoic Cycle (Wernick, 1978).

The Itapira Group is composed of metasedimentary rocks originated by prograding shallow platform sediments, composed predominantly of muscovite quartzites and paragneisses, and less frequently of migmatites, amphibolites, calc-silicate rocks, schists, metaultramafic rocks, marbles, metasediments of Eleuterio Formation and lenses of gondites (Zanardo, 2003, Angeli *et al.*, 2011).

In evolutionary terms, the Itapira Group is interpreted as a metavulcanosedimentary sequence of Proterozoic with syn-tectonic granitoids associated and subdivided into two distinct units (Oliveira *et al.*, 1998; Lazarini, 2000): a lower sequence consisting of pelites, greywacke, arkoses, intercalated with sediments of sandy clay, clay sandy clay, aluminous pelitic, marl, banded iron formations and manganifer sediments. The top sequence is composed of pelites, psamitic pelites, aluminous pelites, marls, limestone, marbles and manganifer sediments. The metasedimentary rocks of the Itapira Group, directly associated with gondites, represent metamorphic lithologies generated from a platform progradational sequence, consisting of muscovite schist, talc schist, muscovite quartzite, quartzite interbedded with mafic and ultramafic rocks, whose foundation is represented by migmatitic and gneissic rocks of the Amparo Complex. The evidence suggests an active tectonic environment with rapid transport of immature sediments of volcanic contribution to the genesis of manganifer protomineral in the area of studies (Verissimo, 1991).

More than a dozen gonditic bodies are discover in the region, which present a greater or lesser extent, classic profiles of weather alteration with enrichment in oxides and hydroxides of manganese. The genetic processes of supergene enrichment of the manganese protomineral are attributed to events that occurred between the Eocene and the Miocene, related to the formation of the South American Surface, attributed to climatic variations and tectonic reactivation (King, 1956).

The manganese protomineral found in the Itapira Group is classified by genesis as a silicate protomineral composed mainly of quartz and spessartine in approximately similar proportions, and calcium silicate protomineral, with quartz, spessartine, pyroxenes, amphiboles, plagioclase, carbonates and epidote.

In the Córrego do Cocho mine the silicate protomineral dominates, with textures and deformation structures in directions NW-SE and NE-SW, which occurs in paragneisses and quartzites spessartine, in the form of lenses aligned towards NE, corresponding to a single layer stretched and broken boudinage (Angeli *et al.*, 2011). The gneisses have leucocratic banded feldspathic quartz coarse-grained with fractures filled with oxides and hydroxides of manganese.

The mineral being exploited in mining fronts occurs in oxidized form, comprising oolites, pisolites and concretions near the surface, and massive mineral, banded and stained at depth. The main minerals are represented by spessartine, manganifer clinoamphiboles, rarely scapolite and piroxmangite. Litioforite also occurs and cryptomelane, pyrolusite, hausmannite, manganite and hollandita, plus nsutite, gahnite, jacobsite, yofortierite, psilomelana venular, woodrufite and todorokite (Angeli *et al.*, 1984).

Espessartine is the most abundant mineral, cemented by matrix rich in cryptomelane, whit occurs as amorphous crystals and preserve features related to the supergene alteration of espessartine. Psylomelane occurs in the shape of gray crystals, semi rounded, most frequently near the surface along the cryptomelane in both the matrix itself and close to the spessartine crystals. Total reserves of mineral for the Córrego do Cocho mine reach about 2.0 Mt, with 344,664 t of metal averaging a grade of 28% MnO2 (Angeli *et al.*, 2011).

Geophysical methods

We used methods of Electrical Resistivity and Induced Polarization, using the technique of electrical profiling.

Resistence is an intrinsic property in soil and rock, defined by current density over gradient of electrical potential. Resistivity changes an earth material, either vertically or laterally, produce changes in the relations between the applied current and the potential distribution as measured at the surface, and reflect changes in composition, extent, and physical properties of the subsurface materials. Properties that affect resistivity of a soil or rock include porosity,

water content, composition (clay mineral and metal content), salinity of pore water, and grain size distribution.

The Electrical Resistivity method is based on generating an electric field by injecting an electric current (I) through metal rods, called the transmitter circuit (Sheriff, 1989). The electric potential (ΔV) produced by this field is captured by a receiver circuit, which can also be represented by metallic rods or non-polarizable electrodes. Applying Ohm's Law the electrode spacing, represented by K factor, enables measuring the apparent resistivity parameter (*ρa*) for various depth levels (1):

$$\rho a = K \frac{V}{1} \qquad \Omega\,\mathrm{m} \qquad (1)$$

Induced polarization is a phenomenon of electric current stimulation observed by a voltage signal in the subsurface materials (Sumner, 1976). This method consists in using an electrodic transmission device for injecting a pulsed, periodic electric current intro the subsurface, the response is obtained via a receiver circuit consisting of non-polarizable electrodes.

Chargeability is defined by the transient potential variable between two points on the transient decay curve normalized by the primary potential (Lowrie, 2007). In a dipolar arrangement, the current electrodes form a transmitter pair, while the potential electrodes form a receiver pair. When the current is interrupted, the voltage across the potential electrodes does not drop immediately to zero. After an initial abrupt drop to a fraction of its steady-state value it decays slowly for several seconds. Conversely, when the current is switched on, the potential rises suddenly at first and then gradually approaches the steady-state value. The slow decay or rise of part of the signal is due to induced polarization, which results from two similar effects related to the rock structure: membrane polarization and electrode polarization. In this work chargeability measurements were performed in the time domain, in terms of milliseconds (ms), defined as:

$$M = \frac{1}{V_c} \int_{t2}^{t1} V_t \, dt \quad \mathrm{ms} \qquad (2)$$

Field work was, based on resistivity and chargeability measurements along a line, with the aim to investigate variations at one or more depth levels, through a dipole-dipole arrangement. This arrangement is characterized by the use of even by spacing electrodes, oriented and displaced linearly.

We adopted a 5m spacing between electrodes and investigation on 8 depth levels. The acquisition parameters were: 100mA current, a decay time of 10ms, single reading window with 100ms, acquisition time of 2s, four acquisition cycles and concomitant readings of resistance and chargeability. In chargeability readings, non-polarizable electrodes were used in a copper sulfate solution (Cu-CuSO4).

A Terrameter SAS 4000 resistivity meter was used, it consists of a single module for transmitting and receiving data with a resolution of 1 mV, 100W of power and four channels of reading, calibrated for transmission of periodic cycles of low frequency alternating current. This procedure enables the filtering of noise during data acquisition (ABEM, 2006). In the area of the mine 300 m of electrical routing were performed, divided in 4 lines of 75m in parallel arrangement in N17o direction and 10m spacing between lines (Figure 1).

Results

The field data were tabulated and processed initially by the RES2DINV program (Loke & Barker, 1996), models of inversion sections with a distance and depth were generated, together with topographic correction (Figure 3 and 4).

The inversion process consists in the superposition of a series of rectangular blocks connected to the field points in the pseudo section, i.e. the section generated by field data in theoretical depth. The depth of the bottom row of blocks is set to be approximately equal to the equivalent depth of investigation of points with the maximum space between electrodes (Edwards, 1977).

The subroutine of direct modeling is used to calculate the values for apparent resistivity, and a nonlinear least square optimization technique is used for reversal routine (DeGroot-Hedlin & Constable 1990, Loke & Barker, 1996). The result is presented in the form of sections with distance versus depth in terms of pseudo section, calculated section and inversion model. This paper presents only the inversion model in terms of resistivity and chargeability.

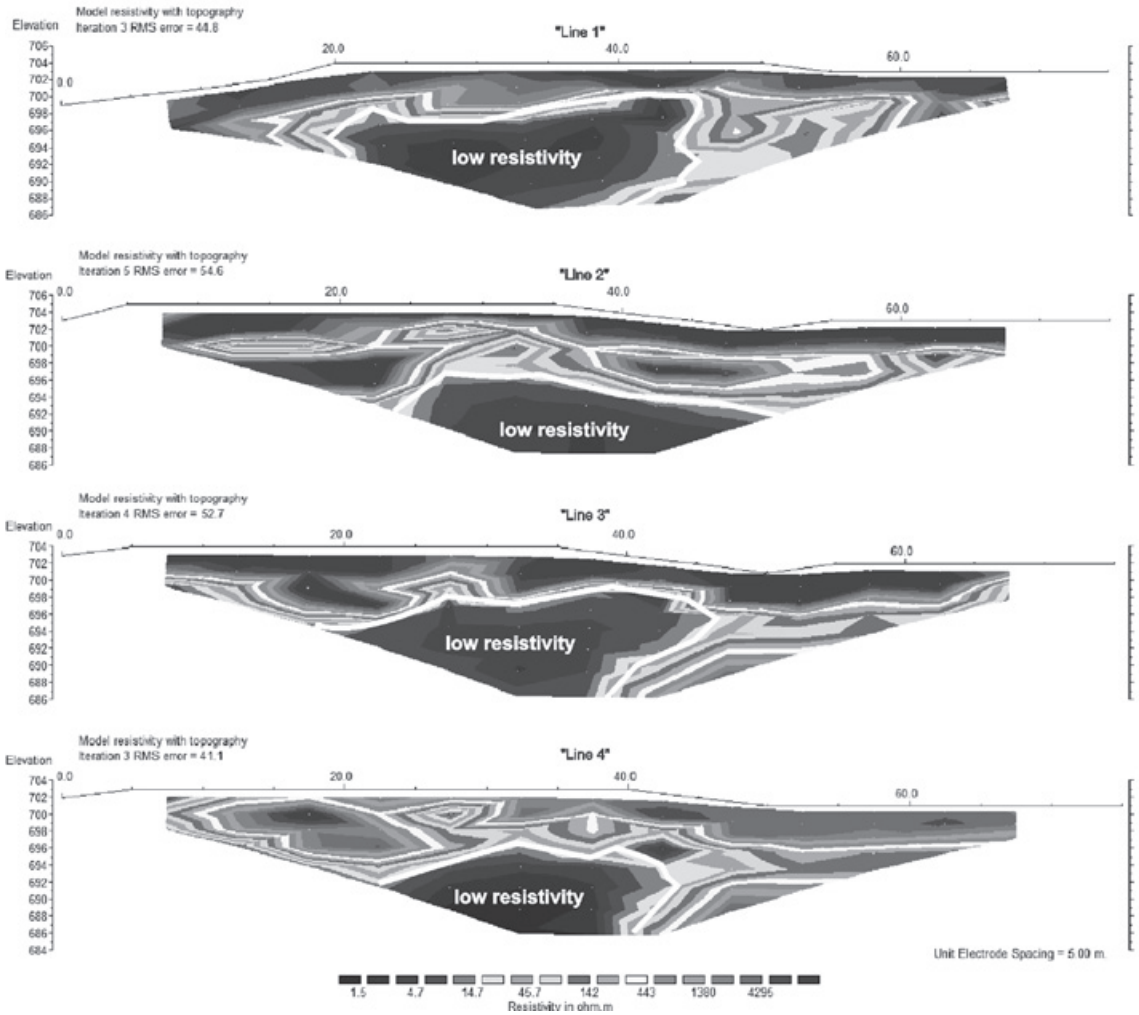

Figure 3. Resistivity inversion models

The relevant factor RMS error is a large contrast between maximum and minimum value measured, which hampes the optimization processing method (Figure 5).

Line 1 is located next to an active mining front, where there are outcrops of exposure of manganese ore. The georeferencing of the lines of electrical routing enabled to relate contrasting areas of physical parameters detected in inversion models, with zones of mineral concentration (Figure 6).

Concentration areas of high-grade minerals are characterized in the inversion model of line 1, as amounts of above 30ms chargeability and resistivity below 20Ω.m, in a pattern caused by oxides and hydroxides in soil and saprolite. This range characterizes disseminated sulphides and gold in various geological settings (Alis, 1990; Irvine & Smith, 1990; White *et al.*, 2001; Moreira & Ilha, 2011; Moreira *et al.*, 2012).

The central low resistivity portion is present in all resistivity section, though smaller variations in dimension. There is also correspondence in chargeability sections, characterized by high values beyond the limits of low resistivity areas, mostly in sections 2 and 4. The central area in sections corresponds to gonditc manganese ore concentrations exposed in mine front and directly correlated with the line 1.

However, the areas of high resistivity and high chargeability probably consist in manganese hydroxides from the destruction by weathering and hydration of the gonditic ore bodies, with dissolution and remobilization for vertical percolation and recristalization, in a similar processes found in gossans formations (Taylor, 2011; Biondi, 2003). These minerals are disseminated in depth and are characteristic of electric insulation, with in polarization intensity very similar to gonditic manganese ore.

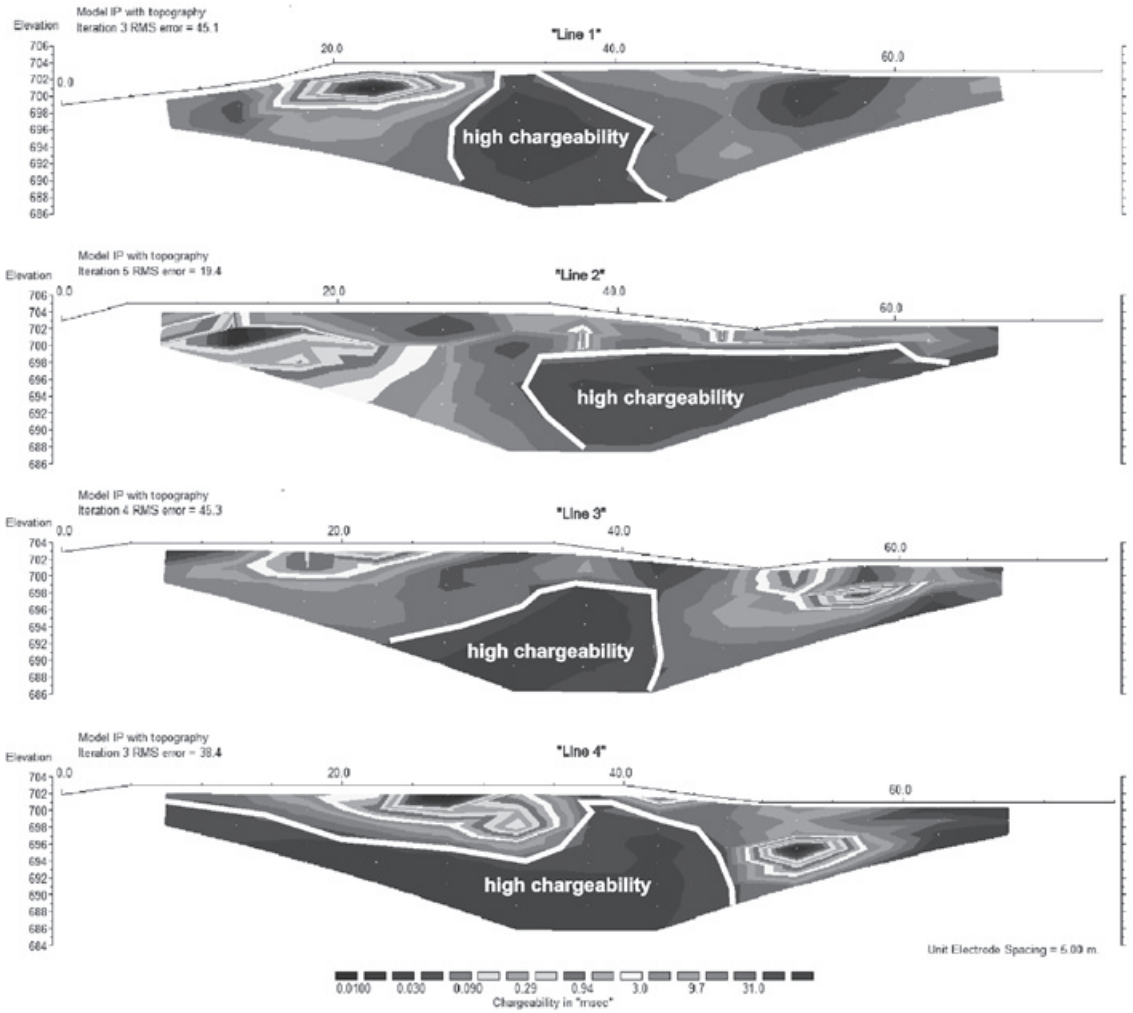

Figure 4. Chargeability inversion models with topography.

The values derived from inversion in terms of resistivity and chargeability were again tabulated and processed by Oasis Montaj platform, developed by Geosoft, for pseudo-3D modeling and 2D maps by interpolating previously processed data (Figure 7). These products were used for integration sections and presentation maps at relevant depths of pedogenetic mineralization, characterized by soils and saprolitic levels (Figure 8). Tridimensional presentation merely consists in pseudo-3D models.

Among the various algorithms available in the program, we adopt the method of minimum curvature for data interpolation. Interpolation is a mathematical procedure for adjusting a function of the unsampled points to values obtained from sampling points. Starting from the sampled points a lattice is defined with spacing relative to the points. The value of each node in the lattice is calculated by selecting closest known points, which are then filtered to smooth the resulting contours and allow the best fit to the original values.

The pseudo-3D model of electrical resistivity is characterized by high values of electrical resistivity at surface (above 1000Ω.m), with a gradual reduction in values accompanied by the increase in depth, especially for low values in shades of blue (below 100Ω.m). In the pseudo-3D model of chargeability with low values at the surface (below the 1ms), increase in depth, highlighted in shades of red (above the 30ms) in the area corresponding to the predominance of low resistivity values (Figure 7).

To verify the continuity of this pattern of values in other portions of pseudo-3D models, isovalues maps were generated for depths previously established, limited to 693m and 697m depths, rotated by angle and viewed from W to E (Figure 8).

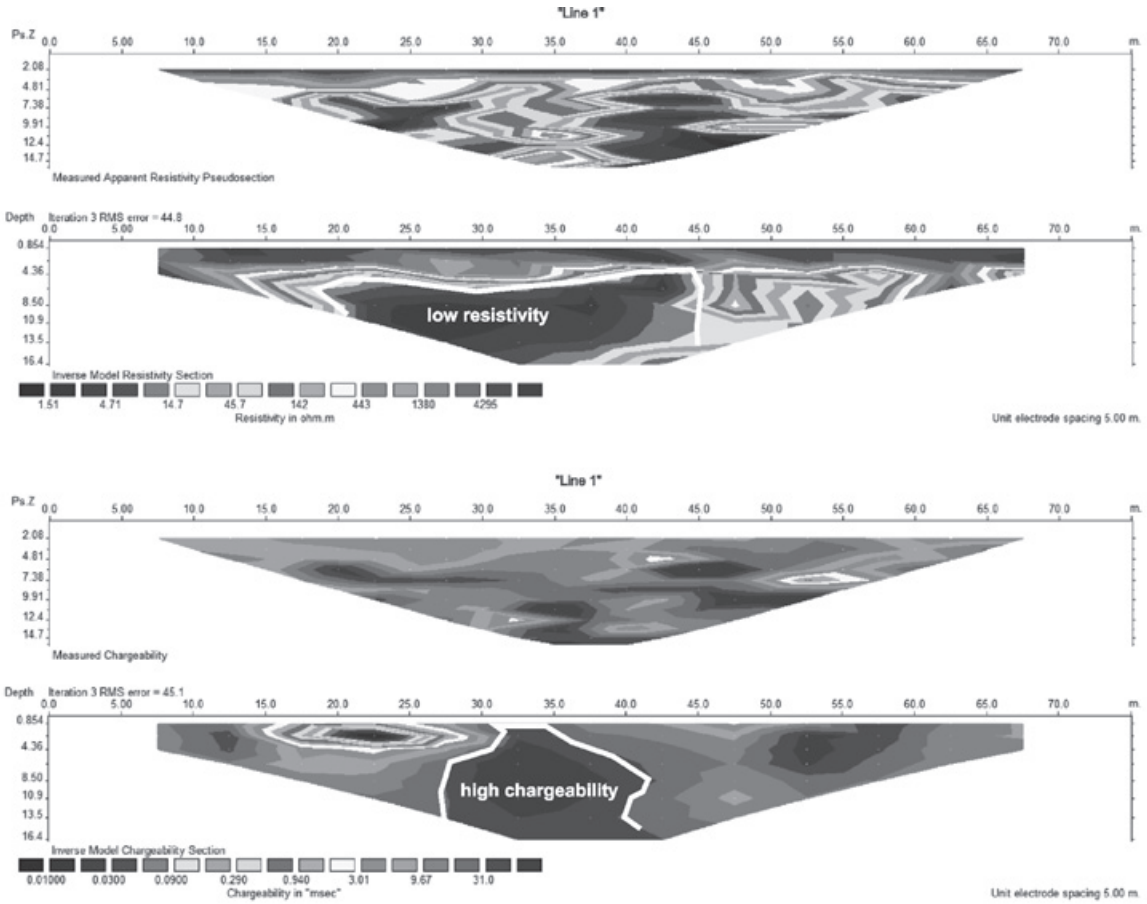

Figure 5. Resistivity measures and inverse model (above) and chargeability measures and inverse model (below) to Line 1.

A depth of 693m corresponds to the front mining ramp, where the mineralized bodies correspond to the inversion model of Line 1 outcrop. Between 697m and 693m little modified saprolite soil predominates, with fragments of rock, foliation and banding preserved and recognizable in the field, where the mineralized bodies present massive structure and intensely fracturing.

The depth of 697m represents the soil interval lacking fragments of rock, where manganiferous mineral concentrations occur as manganese hydroxides.The maps for both depths reveal no existence of low resistivity relations (above 100Ω.m) and high chargeability (above 30ms) for the other lines, coincidence being apparently limited to the western portion of the maps (position of line 1) (Figure 7).

The comparison of maps for 693m elevation reveals a central area with electrical resistivity quite homogeneous, corresponding to a domain with contrasting chargeability, where higher values in the central and east portions occur, coincident with lines 3 and 4, and moderate to low values west, coincident with lines 1 and 2. The comparison between the maps for 697m elevation also follows this pattern, although relatively higher electrical resistivity values predominate, besides relatively lower values of chargeability.

Electrical resistivity is sensitive to factors such as mineral content, porosity, grain size, presence of clay minerals, among others (Keller and Frischknecht, 1966). The materials that constitute the geological profile are basically represented by quartz and clay minerals derived from weathering of schists and quartzites, besides other minerals constituents of the mineralization.

The portions of soil near the surface are characterized by high resistivity values owing to absence of moisture, predominance

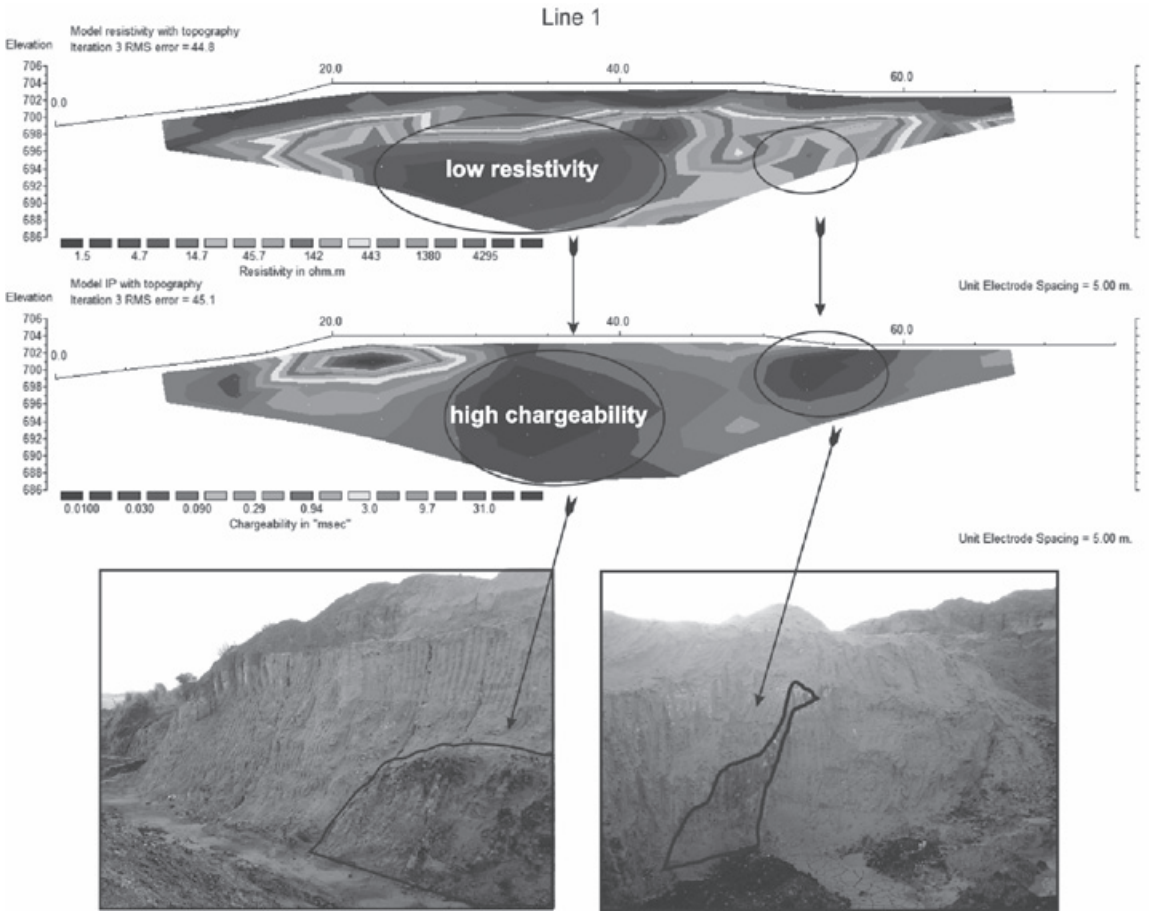

Figure 6 – Inversion models in terms of electric resistivity and chargeability, with emphasis on areas of low resistivity and high chargeability, related to mineralized zones exposed in front of mining located nearby.

of quartz and variable amount in hydrated minerals. While the silicates and hydroxides behave as electrical insulation, this mineral presents polarization intensity contrast.

The measures of chargeability are also partly influenced by geological conditioners similar to electrical resistivity, mainly mineral content. This aspect is determining for the polarizability of geological materials, very intense in disseminated sulfides, moderately intense for oxides and hydroxides and less intense in silicate minerals. Although there are processes of electrolytic polarization in the presence of moisture or clay, the polarizability is of little relevance to the presence of sulfides and metallic mineral responsible for the phenomenon of electronic polarization.

Thus, the areas of high chargeability revealed in the maps probably correspond to areas of manganese accumulation. The high grade Mn is found in gonditic ore bodies, characterized by high chargeability/low resistivity, whereas the disseminations in manganese hydroxides are represented by high chargeability/high resistivity, which consists in low grade in Mn, currently dumped as mine waste.

Conclusions

This paper shows that the combined use of geophysical methods correlated with geological descriptions of mineralized zones is a technically feasible procedure in in short term mine planning. The calibration of geophysical data with proven mineralized areas, can result in much higher detail when acquired only from surveys for sampling and chemical analysis, and thus in a relatively precise control of mining.

Understanding the existence and continuity of mineral bodies for grade control

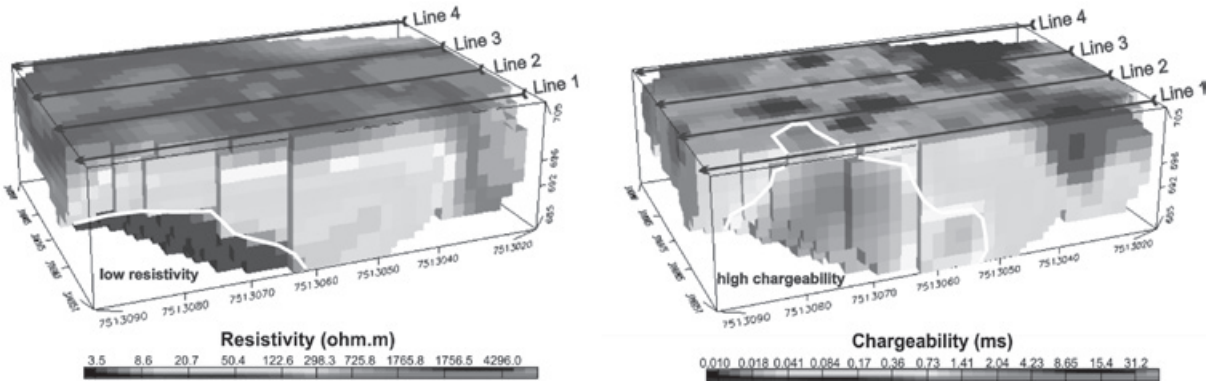

Figure 7. Pseudo-3D models for electrical resistivity and chargeability generated by interpolating lines of routing previously processed, with vision for east.

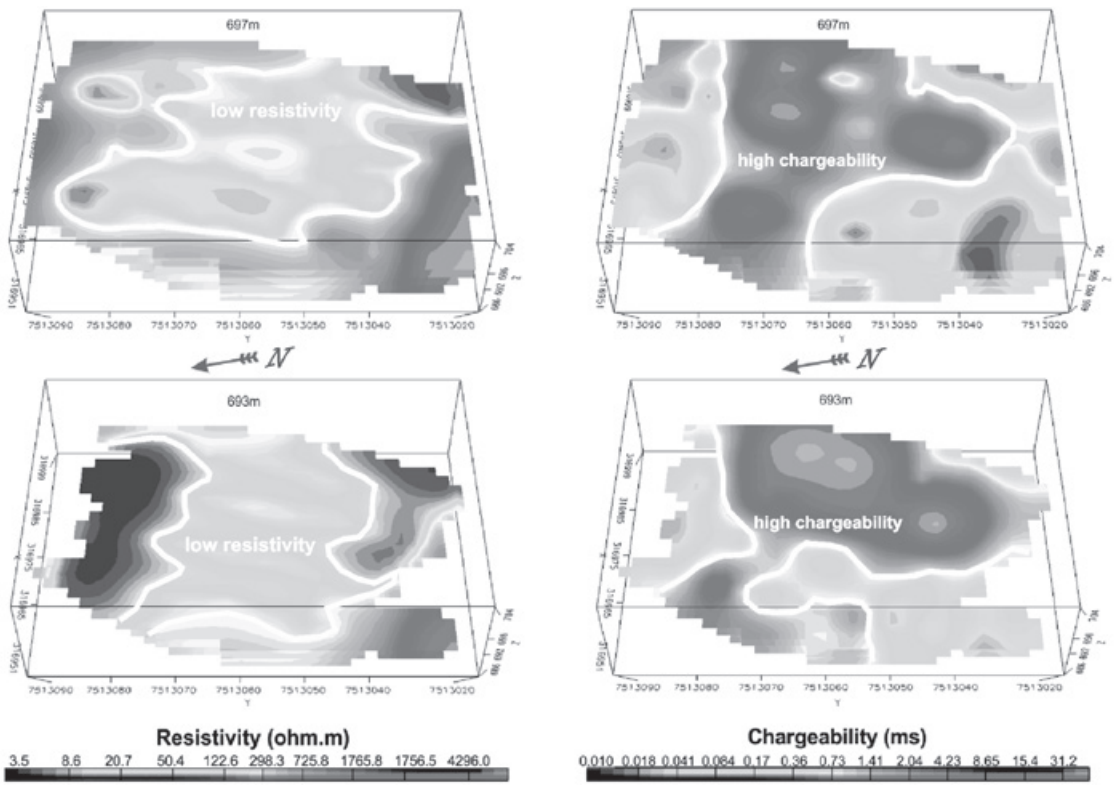

Figure 8. Maps of resistivity and chargeability for 693m and 697m quotas

in mining procedures is quite difficult even by conventional techniques of drilling and sampling, especially in complex deposits, with mineral distribution not linked to structural or stratigraphic controls. This procedure can result in errors when estimateding volumes.

In this paper a manganese deposit of supergene origin, with oxides and hydroxides of manganese disseminated in the interval of soil and saprolite, currently in the process of mining, besides structurally controlled mineral at greater depths, contained in schists and gneisses, was evaluated.

The application of geophysical methods of Electrical Resistivity and Induced Polarization in this complex geological context allowed the mapping of mineralized zones in interval of soil and saprolite. The initial calibration between areas of exposed mineral resulted in a geophysical signature of high chargeability

and low resistivity by high grade, as described in several studies of deposits of oxides and sulfides contained in rock.

The classic signature of oxide deposits in sulfide by means of the above mentioned geophysical methods can be expected for primary or non-weathered deposits. For the case of mineral deposits of secondary origin, whose genetic determinants are controlled by weathering processes, factors such as humidity, porosity and clay mineral content, have great influence on measurements of electrical parameters.

However, this pattern does not apply to the inner portions of the deposit, with considerable areas characterized by high chargeability and high resistivity. Due to evolution of the deposit and mineral neoformation processes, this pattern suggests that the presence of disseminations of manganese hydroxides is characterized by low grade.

Acknowledgements

The authors are thankful to Mineração Itapira Ltda for the availability of their installations and access to the mineral mining area and reviewer due to great contribution in the manuscript quality.

References

ABEM., 2006, Terrameter SAS 4000 / SAS 1000 - Instruction Manual, 136f.

Allis R., 1990, Geophysical anomalies over epithermal systems. *Journal of Geochemical Exploration*, 36, p. 339 – 374.

Angeli N., Carvalho S.G., Oliveira M.A.F., Choudhuri A., Saragiotto J.A.R., 1984, Caracterização das ocorrências de minério de manganês em parte da porção nordeste do Estado de São Paulo. In: Congresso Brasileiro de Geologia, 33. Rio de Janeiro. Anais. Rio de Janeiro: SBG, 8, p. 3710-3723.

Angeli N., Khan H., Ito G.M., Carvalho S.G., Jimenez-Rueda J., Penha U.C., 2011, Geologia e Caracterização Tecnológica do Minério de Manganês da Mina Córrego do Cocho, Itapira (SP). Geologia USP série Científica, 11, 3, p. 107-130.

Biondi J.C., 2003, Processos metalogenéticos e os depósitos minerais brasileiros. Oficina de Textos, São Paulo, 528 p.

DeGroot-Hedlin C., Constable S., 1990, Occam's inversion to generate smooth, two-dimensional models form magnetotelluric data. *Geophysics*, 55, p. 1613-1624.

DNPM - Departamento Nacional de Produção Mineral – MME - Brasil. Sumário Mineral, 2011, volume 31.

Edwards L.S., 1977, A modified pseudosection for resistivity and induced polarization. *Geophysics*, 42: 1020-1036.

Geotomo Software, 2003, Res2Dinv instructions manual, version 3.53.129p.

Irvine R.J., Smith M.J., 1990, Geophysical exploration for Epitermal deposits. *Journal of Geochemical Exploration*, 36, p.375 – 412.

Keller G.V., Frischknecht F.C., 1966, Electrical methods in geophysical prospecting. Pergamon Press, 562pp.

King L.C., 1956, A Geomorfologia do Brasil Oriental. *Revista Brasileira de Geografia*, Rio de Janeiro, 18, 2, p.147-265.

Lazarini A.P., 2000, Petrologia de metabasitos e ultrabasitos da região de Águas de Lindóia. 2000. Dissertação (Mestrado)- Instituto de Geociências e Ciências Exatas- Universidade Estadual Paulista (UNESP), Rio Claro, São Paulo.

Loke M.H., Barker R.D., 1996, Rapid least-squares inversion of apparent resistivity pseudosections by a quasi-Newton method. *Geophysical Prospecting*, 44, p. 131-152.

Lowrie L., 2007, Fundamentals of Geophysics. Cambridge University Press, New York, 393pp.

MME - Ministério das Minas e Energia – Brasil. 2010. Plano Nacional de Mineração 2030 (PMN – 2030). Brasília, MME, 178p.

Moon C.J., Whateley M.E.G., Evans A., 2006, M. Introduction to Mineral Exploration. 2o ed., Backwell Publishing, Oxford, 499 pp.

Moreira C.A., Ilha L.M., 2011, Prospecção geofísica em ocorrência de cobre localizada na bacia sedimentar do Camaquã (RS). *Revista da Escola de Minas*, Ouro Preto, 64, 3, p. 309-315.

Moreira C.A., Lopes S.M., Schweig C., Seixas A.R., 2012, Geoelectrical prospection of

disseminated sulfide mineral occurrences in Camaquã sedimentary basin, Rio Grande Sul State, Brazil. *Revista Brasileira de Geofísica*, 30, 2, p. 169-179.

Oliveira M.A.F., Zanardo A., Silva A.H.M., Lazarini A.P., 1998, Anfibolitos associados à Faixa Metamórfica Amparo – Itapira na região de Socorro – Amparo – Águas de Lindóia. In: Congresso Brasileiro de Geologia, 40, Belo Horizonte. Anais. Belo Horizonte: SBG/Núcleo MG, 1998. p. 456.

Sheriff R.E., 1989, Geophysical Methods, New Jersey, Prentice Hall, p.175-201.

Sumner J.S., 1976, Principles of induced polarization for geophysical exploration. *Elsevier Scientific*, Amsterdam, 277 pp.

Taylor R., 2011, Gossans and Leached Cappings – Fields Assessment. Springer-Verlag, Heidelberg, 165 pp.

Telford W.M., Geldart L.P., Sheriff R.E., 2004, Applied Geophysics. Cambridge University Press, New York, 2º ed., 774 pp.

Veríssimo C.U., 1991, Evolução geológica dos corpos de protominério e mineralizações de manganês associadas, porção leste de São Paulo e Sul de Minas Gerais. Dissertação (Mestrado) - Instituto de Geociências e Ciências Exatas, Universidade Estadual Paulista, Rio Claro.

Zanardo A., 2003, Pesquisa geológica e de matérias primas cerâmicas do centro nordeste do estado de São Paulo. Tese (Livre Docência) - Instituto De Geociências e Ciências Exatas, Rio Claro.

Wernick E.A., 1967, A geologia da região de Amparo, leste do Estado de São Paulo. Tese (Doutorado), Faculdade de Filosofia Ciências e Letras, Rio Claro.

Wernick E., 1978, Contribuição a estratigrafia do Pré-Cambriano do leste do estado de São Paulo e áreas vizinhas. *Revista Brasileira de Geociências*, São Paulo, 8, 3, p. 206-216.

Geofísica Internacional (2014) 53-2: 211-220

Original paper

Near-realtime source analysis of the 20 March 2012 Ometepec-Pinotepa Nacional, Mexico earthquake

Carlos Mendoza

Received: May 14, 2013; accepted: August 12, 2013; published on line: April 01, 2014

Resumen

Se aplica un procedimiento de inversión de falla finita para obtener un modelo de deslizamiento sobre el plano de falla para el sismo M_W 7.4 de Ometepec-Pinotepa Nacional del 20 de marzo 2012, utilizando ondas P telesísmicas registradas por la red del Global Seismographic Network. La inversión se hace en tiempo casi-real utilizando parámetros de la fuente reportados por el Servicio Geológico de Estados Unidos (USGS) y el proyecto del Global Centroid Moment Tensor (gCMT). La orientación de la falla y el ángulo de deslizamiento se obtienen del mecanismo del gCMT, asumiendo que la falla coincide con el plano nodal con bajo ángulo de buzamiento. Las dimensiones de la falla y la duración máxima de la función fuente se definen en base a la magnitud reportada para el evento. Datos telesísmicos obtenidos de la base de datos del Continuous Waveform Buffer del USGS se utilizan en la inversión con tiempos de inicio que corresponden a los arribos de la onda P implementados en el cálculo del hipocentro. La inversión se estabiliza aplicando una transición suave de deslizamiento a lo largo de la falla y una reducción simultánea del momento sísmico. Estas restricciones se implementan utilizando un peso de suavizamiento estimado directamente del problema inverso, permitiendo así la recuperación en un solo paso del patrón de ruptura menos complicado. La inversión de los registros en desplazamiento revela una simple ruptura circular similar al área de deslizamiento determinada por el USGS utilizando ondas de cuerpo y ondas superficiales, indicando que las ondas P telesismicas pueden identificar los rasgos principales de la fuente en tiempo casi-real. Inversiones adicionales realizadas utilizando registros en velocidad identifican una fuente mas detallada que cubre una zona elíptica de 2500 km^2 y que se extiende hacia arriba y hacia abajo del hipocentro a lo largo de la falla. Esta zona elíptica tiene dimensiones que cubren el área definida por dos fuentes separadas determinadas por otros investigadores utilizando datos locales y ondas sísmicas globales. Los resultados indican que los registros en velocidad podrian aportar mayor información sobre los detalles de la ruptura en inversiones realizadas en tiempo casi-real utilizando ondas P telesísmicas.

Palabras clave: earthquake source properties, finite-fault inversion, teleseismic P waves.

C. Mendoza
Centro de Geociencias
Universidad Nacional Autónoma de México
Campus Juriquilla
Querétaro, Qro.
Mexico
Corresponding author: cmendoza@geociencias.unam.mx

Abstract

We apply a single-step, finite-fault analysis procedure to derive a coseismic slip model for the large M_W 7.4 Ometepec-Pinotepa Nacional, Mexico earthquake of 20 March 2012, using teleseismic P waveforms recorded by the Global Seismographic Network. The inversion is conducted in near-realtime using source parameters available from the USGS/NEIC and the Global Centroid Moment Tensor (gCMT) project. The fault orientation and slip angle are obtained from the gCMT mechanism assuming that the fault coincides with the shallow-dipping nodal plane. The fault dimensions and maximum rise time are based on the magnitude reported for the event. Teleseismic data from the USGS/NEIC Continuous Waveform Buffer database are used in the inversion with record start times set to the P-wave arrivals used to compute the earthquake hypocenter. The inversion is stabilized by requiring a smooth transition of slip across the fault while minimizing the seismic moment. These constraints are applied using a smoothing weight that is estimated from the inverse problem, allowing the recovery of the least-complicated rupture history in a single step. Inversion of the deconvolved, ground-displacement waveforms reveals a simple, circular rupture similar in extent to the source identified by the USGS/NEIC using body- and surface-wave data, indicating that the teleseismic P waves can provide a first-order source model for the event in near-realtime. Additional inversions conducted using velocity records identify a more-detailed rupture model characterized by an elliptical 2500 km^2 source region extending updip and downdip from the hypocenter. This elliptical source preserves the orientation and overall dimensions of a dual-source slip model obtained recently by other investigators using local strong motions and global seismic waveforms. The results indicate that velocity waveforms could provide additional details of the earthquake rupture in near-realtime, finite-fault inversions using teleseismic P waves.

Key words: earthquake source properties, finite-fault inversion, teleseismic P waves.

Introduction

The rapid derivation of the extended properties of large earthquakes is an important component of earthquake early-alerting programs and is necessary for effective post-earthquake response. Preliminary earthquake source models are useful, for example, for estimating the ground motions expected in the epicentral region. Several international seismological agencies currently calculate preliminary fault-slip models for large earthquakes following their occurrence. The U.S. Geological Survey National Earthquake Information Center (USGS/NEIC), for example, provides fault-slip information following significant earthquakes using body- and surface-wave data recorded worldwide. Such timely analyses are not currently performed by researchers in Latin America.

The timely recovery of coseismic slip models requires the rapid acquisition and processing of the recorded seismic waveform data followed by the implementation of a waveform-inversion methodology usually based on a simplified parameterization of the earthquake source. Different data types, including regional records and teleseismic body- and surface-wave data, have been examined to rapidly infer the extended properties of large earthquakes using various inversion schemes (e.g., Mendoza, 1996; Ji *et al*., 2002; Dreger *et al*., 2005, Ammon *et al*., 2006; Hayes, 2011; Mendoza *et al*., 2011). Studies using teleseismic P waves (e.g., Mendoza *et al*., 2011; Mendoza and Hartzell, 2013) indicate that these data alone can be used to rapidly identify preliminary, first-order rupture models. These studies employ the kinematic, finite-fault inversion scheme of Hartzell and Heaton (1983) to model the earthquake source, with the coseismic slip computed in each of a fixed number of subfaults along a simple planar fault. The Hartzell and Heaton (1983) formulation generally requires running multiple inversions using varying amounts of stabilization to identify the simplest solution that reproduces the observed records. For near-realtime applications, Mendoza (1996) suggested running the inversion only once by fixing the seismic moment to a prescribed value. This approach was found to provide a preliminary image of the coseismic slip pattern for large earthquakes in the Mexico subduction zone, although the models exhibit significant fluctuations in slip due to the lack of spatial smoothing along the fault (Mendoza *et al*., 2011). More recently, Mendoza and Hartzell (2013) examined the multiple-inversion process of Hartzell and Heaton (1983) and found a relationship between the amplitudes of the observed teleseismic P-wave records and the amount of stabilization required to obtain the simplest rupture model. The relation allows an application of the methodology in a single step, using both moment-minimization and spatial-smoothing constraints estimated from

the inverse problem. Mendoza and Hartzell (2013) used this single-step approach to derive first-order slip models for several different-size events, including the 2011 M_W 7.1 East Turkey, the 2011 M_W 9.0 Japan, and the 2012 M_W 8.6 Northern Sumatra earthquakes using P-wave displacement records.

In this study, we use the single-step finite-fault inversion scheme of Mendoza and Hartzell (2013) to analyze the large M_W 7.4 interplate thrust earthquake that occurred in the Guerrero-Oaxaca border region, Mexico, on 20 March 2012 and examine the results to explore the development of an automated inversion process that could be implemented in near-realtime following the occurrence of large subduction earthquakes along the Middle America subdduction zone. The earthquake resulted from shallow subduction of the Cocos plate beneath North America and occurred in a section of the plate boundary that has experienced more than ten $M_W > 7$ events in the last century (UNAM Seismology Group, 2013). The earthquake caused extensive damage in the towns of Ometepec, Guerrero and Pinotepa Nacional, Oaxaca, and was also strongly felt in Mexico City (Juarez Garcia *et al*., 2012). Here, we present the results of a near-realtime application of the inversion procedure conducted the day of the event using teleseismic ground-displacement P waveforms, consistent with the data processing used by Mendoza and Hartzell (2013). We also perform additional inversions of the teleseismic dataset using velocity records to examine the extent to which principal features of the rupture history can be derived. We find that the velocity records provide more detail of the coseismic slip compared to the displacement waveforms, due to the higher frequency content. Thus, it would be useful to include these data in near-realtime analyses of the teleseismic P waves to derive provisional, first-order source models for large $M_W > 7$ interplate subduction earthquakes.

Inversion method

The method is based on the finite-fault waveform inversion scheme developed by Hartzell and Heaton (1983) and modified by Mendoza and Hartzell (2013) to identify the earthquake rupture history from the recorded teleseismic P waveforms in a single step. The method uses multiple consecutive slip intervals of finite duration to identify a long rise time, if required by the observations. In the analysis, a fault plane of prescribed orientation, dimensions, and depth is placed in the crustal structure of the source region and divided into a given number of subfaults. Fault dimensions are chosen to generously encompass the expected extent of rupture based on the moment magnitude of the earthquake. For the 2012 Ometepec-Pinotepa Nacional earthquake, the fault plane corresponds to the gently-dipping nodal plane in the Global Centroid Moment Tensor (gCMT) source mechanism (strike, dip, and rake of 295º/13º/91º), assumed to represent faulting along the Cocos-North America plate boundary. This gCMT mechanism was available from the USGS website the day of the event. The fault length and width were set to 140 km and 70 km, respectively, with the fault divided into 20 subfaults along the strike and 10 subfaults down the dip. The hypocenter was placed at the center of the fault at the 17-km depth computed by the USGS/NEIC.

Synthetic P-wave seismograms are then computed for each subfault at all the recording sites by summing the responses of a set of point sources distributed uniformly across each subfault, taking into account the time delays for a rupture front propagating at a prescribed rupture speed. The point-source responses are obtained using generalized ray theory (Helmberger and Harkrider, 1978) and a near-source crustal structure that corresponds to the upper 35 km of the AK135 velocity model (Kennett *et al*., 1995). The rupture velocity is fixed at 2.5 km/s, the value suggested by Mendoza and Hartzell (2013) corresponding to about 70% of the average crustal shear-wave speed in the velocity model. A boxcar source-time function is used to calculate the point-source responses, with the boxcar duration depending on the size of the event.

The synthetic records are placed end-to-end to form a matrix A of subfault synthetics. The observed records are similarly placed end-to-end for all stations to form the data vector b. Together, these form an overdetermined system of linear equations $Ax=b$ that is solved for the solution vector x whose elements correspond to the subfault slips required to reproduce the observations. Multiple slip intervals are accommodated by adding columns to the A matrix that are constructed by successively lagging the subfault synthetics by the width of the boxcar source-time function, resulting in a specified number of time windows that discretize the rise time on the fault. The inversion thus recovers the slip required of each subfault in each of the specified time windows. For the 2012 Ometepec-Pinotepa Nacional earthquake, we used five time windows of 1s duration, allowing up to 5s for the rise time at any point on the fault. This flexibility allows for the rise-time variations observed by Somerville *et al*. (1999) for earthquakes of this size.

In the Hartzell and Heaton (1983) formulation, the constraint equations λFx = 0 are added to the linear system to stabilize the inversion, where the smoothing weight λ controls the tradeoff between applying the constraints and fitting the observations. The constraints take two forms, with the linear system to solve given by

$$\begin{bmatrix} C_d^{-2}A \\ \lambda_1 F_1 \\ \lambda_2 F_2 \end{bmatrix} x = \begin{bmatrix} C_d^{-1}b \\ 0 \\ 0 \end{bmatrix}$$

where F_1 corresponds to the difference in slip between adjacent subfaults, thus requiring a smooth transition of slip from subfault to subfault. F_2 is the identity matrix, effectively reducing the length of the x vector and the total seismic moment. Cd^{-1} is a data covariance matrix that normalizes the data record at each station to its maximum amplitude. The coefficient matrix $Cd^{-1}A$ thus contains the observed-amplitude information following the data normalization process (Mendoza and Hartzell, 2013).

The linear system corresponds to a discrete ill-posed problem, which can be solved using Tikhonov-type regularization through an iterative L-curve analysis (Hansen, 1998). This iterative process recovers the simplest solution by identifying the optimum smoothing weight $\lambda_s=\lambda_1=\lambda_2$ that quantifies the balance between fitting the data and meeting the constraints (Mendoza and Hartzell, 2013). An independent estimate of this optimum smoothing weight, however, can be obtained from the average ($|a|_{avg}$) of the absolute values of the elements of the coefficient matrix using the relation $\lambda_s = 90\ |a|_{avg}$ (Mendoza and Hartzell, 2013). Thus, the amount of stabilization to apply can be estimated directly from the inverse problem and then used to invert the observed data, allowing the recovery of an earthquake source model in a single step. Note that the seismic moment could be fixed to a prescribed value, instead of minimizing the moment in the F_2 constraint. However, this would require a reevaluation of the relationship between the smoothing weight and the elements of the coefficient matrix to identify the proper smoothing value to use in the inversion.

Near-realtime source analysis

We applied the single-step inversion algorithm of Mendoza and Hartzell (2013) to the teleseismic P waves recorded for the 2012 Ometepec-Pinotepa Nacional earthquake to recover a first-order image of the rupture history the day of the event. The inversion uses the broadband, vertical (BHZ) waveforms recorded by stations of the Global Seismographic Network (GSN) with record start times corresponding to the P arrival times used by the USGS/NEIC to locate the events. The data were obtained from the USGS/NEIC Continuous Waveform Buffer (CWB) repository that are made available to the scientific community through dedicated client servers shortly after they are recorded at the various worldwide stations (ftp://hazards.cr.usgs.gov/CWBQuery/CWBQuery.doc). The data-retrieval procedure uses the phase-arrival times posted online by the USGS/NEIC following the earthquake (http://earthquake.usgs.gov/earthquakes) to request waveforms for stations located 25-95 degrees from the epicenter. Records from the available stations were then deconvolved to ground displacement, interpolated to a 1s time step, passband-filtered between 5 and 100s, and windowed to 50s record lengths. For the 2012 earthquake, a total of 26 teleseismic P-wave records were recovered from the CWB database (Figure 1 and Table 1) for use in the inversion. This data retrieval and waveform processing took less than 5 minutes on a 2-GHz Intel Core 2 Duo iMac desktop computer.

The slip model recovered for the earthquake using the deconvolved, teleseismic P-wave

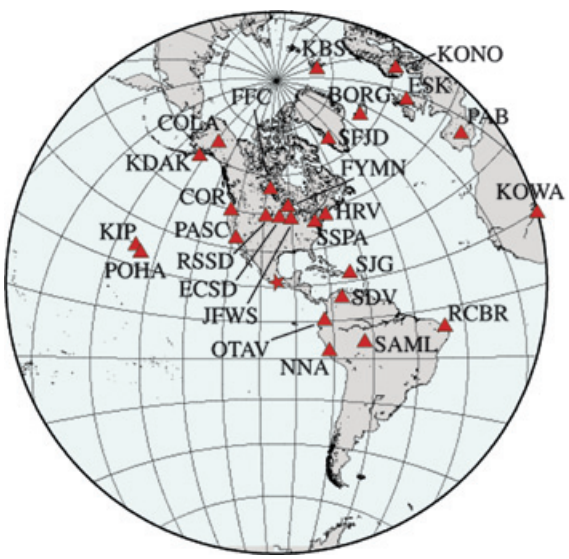

Figure 1. GSN stations (triangles) used to study the 20 March 2012 Ometepec-Pinotepa Nacional earthquake plotted relative to the USGS/NEIC epicenter (star).

Table 1. Stations used in teleseismic inversion.

Station	Distance (°)	Azimuth (°)
PASC	25.0	-42.1
BORG	69.5	26.5
ESK	79.3	35.4
FFC	38.1	-3.6
KDAK	57.3	-31.2
NNA	35.4	142.1
COLA	58.5	-22.4
COR	35.0	-32.0
HRV	34.4	36.0
KBS	77.5	10.7
KIP	56.5	-75.1
KONO	84.4	29.1
KOWA	89.8	75.0
OTAV	25.4	128.0
PAB	82.5	51.1
POHA	54.3	-77.4
RCBR	65.5	104.5
RSSD	27.8	-9.0
SAML	43.0	123.8
SDV	27.9	102.6
SFJD	58.9	19.8
SJG	30.6	82.5
SSPA	29.7	32.3
ECSD	27.0	2.5
EYMN	31.7	8.6
JFWS	27.0	12.9

displacement records is shown in Figure 2. This result was obtained within 1 minute following the processing of the observed records. The model shows a single, circular source centered at the earthquake hypocenter with a radius of about 30 km and a peak slip of 384 cm. The observed records are fit very well (Figure 3), although there are some misalignments at several stations (e.g.,BORG, KDAK, COR) that require small shifts to the USGS/NEIC P arrival times. Runs conducted after adjusting these record start times, however, yield slip models that are very similar to that shown in Figure 2.

The moment-rate function (Figure 4) shows a major 15s pulse with a seismic moment of 1.3 x 10^{27} dyne-cm (M_W 7.4) that corresponds to fault slip in the circular region near the hypocenter. There is also a second, smaller contribution to the total moment about 5s later due to slip beyond 50 km from the hypocenter. This second, small pulse has a minimal effect on the predicted teleseismic P waveforms and is attributed to the mapping of unmodeled, propagation effects onto the fault. That is, the observed records are fit just as well when slip from this outer portion of the fault is excluded from the source model. The circular, coseismic source region accounts for about 85 percent of the total calculated seismic moment of 1.5 x 10^{27} dyne-cm.

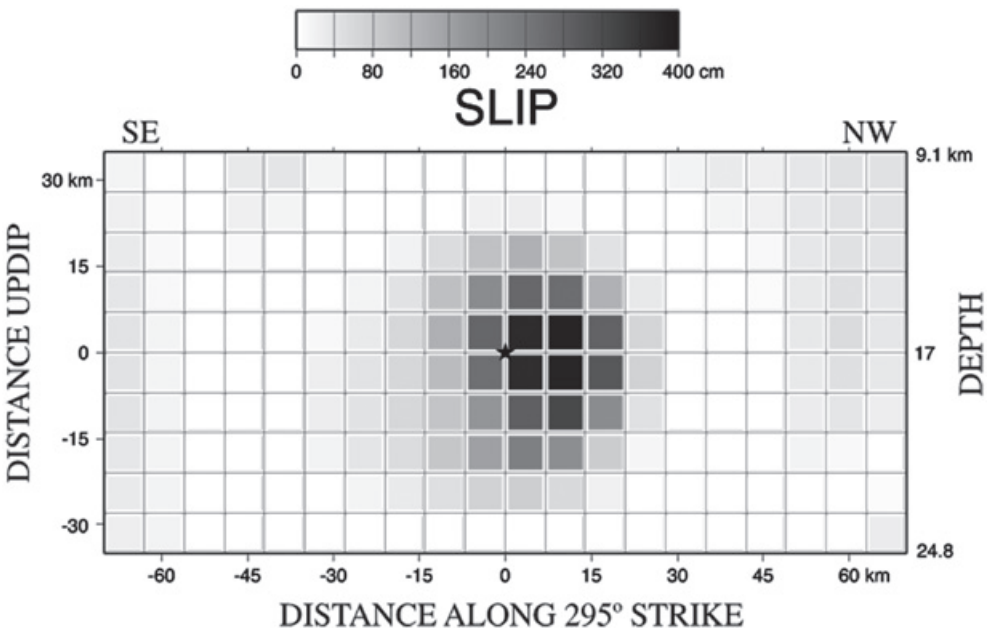

Figure 2. Slip model obtained for the 2012 Ometepec-Pinotepa Nacional earthquake from the inversion of the GSN teleseismic P-wave ground displacements filtered at 5-100s. View is from the top of the fault with distance measured from the hypocenter (star) placed at the 17-km depth obtained by the USGS/NEIC.

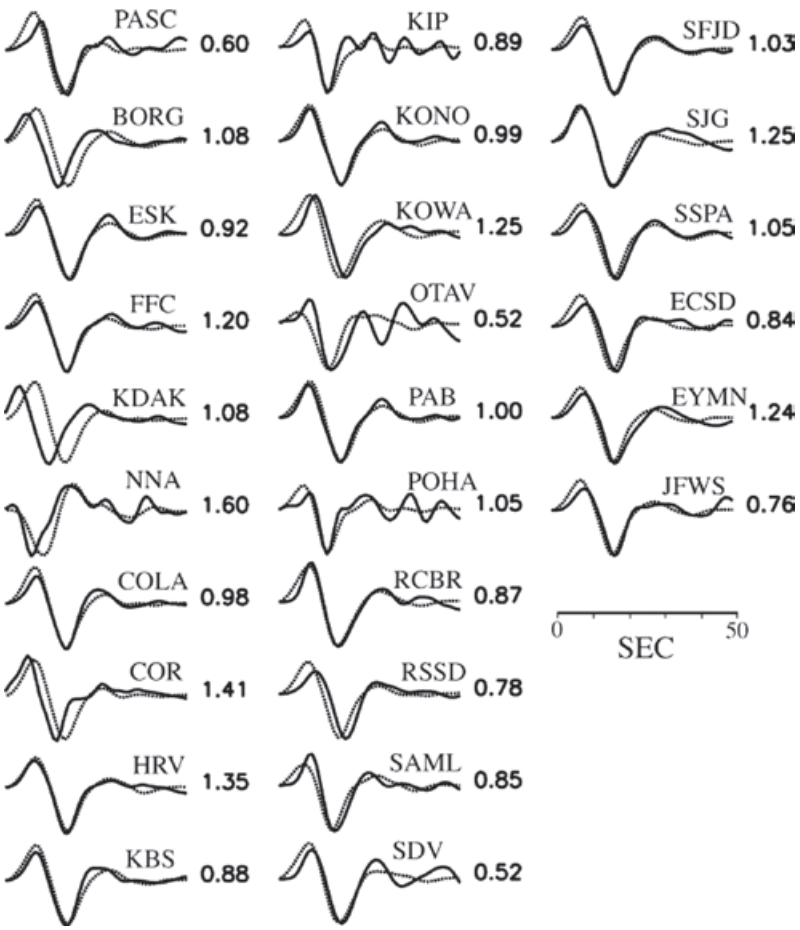

Figure 3. Fits between observed (solid) and predicted (dashed) teleseismic P-wave displacements corresponding to the slip model of Figure 2. Waveforms are normalized to their maximum amplitudes, and numbers to the right indicate the ratio of synthetic-to-observed amplitudes corresponding to a total moment of 1.5 x 10^{27} dyne-cm. This total moment, however, includes non-source related contributions from beyond the circular source area shown in Figure 2.

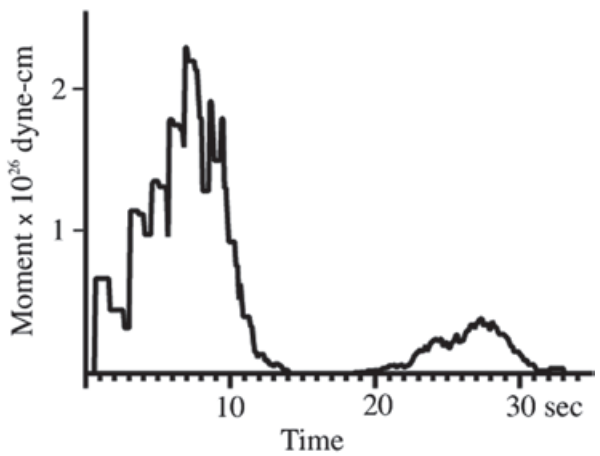

Figure 4. Moment-rate function corresponding to the slip model shown in Figure 2. Moment release in the first 15s is due to coseismic slip within the circular source area of the slip model and corresponds to a seismic moment of 1.3 x 10^{27} dyne-cm. The second small pulse observed beyond 20s is attributed to the mapping of non-source effects onto the fault.

The slip distribution obtained in near-realtime for the 2012 Ometepec-Pinotepa Nacional earthquake is very similar to the finite-fault model derived by the USGS/NEIC (http://earthquake.usgs.gov/earthquakes/eqinthenews/2012/usc0008m6h/) from the analysis of body- and surface-wave data using the method of Ji *et al*. (2002). The USGS/NEIC model shows a single 30-km x 35-km slip area at the hypocenter with a peak slip of ~4.5m and a seismic moment of 1.5 x 10^{27} dyne-cm. A recent study of the event by UNAM Seismology Group (2013), however, suggests that two separate sources may have contributed to the seismic-wave radiation. They use teleseismic body and surface waves and local strong-motion data to identify two areas of slip (up to 4m peak) updip and downdip of the hypocenter. This source detail was obtained assuming an arbitrary 2s time shift in the alignment of the observed body-wave records (UNAM Seismology Group, 2013). Independent of whether this 2s shift is necessary, rapid finite-fault analyses such as the one described in this paper rely on initial

P arrival measurements and would not be able to discern rupture patterns that depend on the identification of weak precursors on the teleseismic records. Nonetheless, it may be possible to derive more source detail than that shown in Figure 2 by using higher-frequency records that could potentially resolve smaller source dimensions.

Analysis using instrumental records

With this in mind, we perform a second finite-fault analysis of the 2012 Ometepec-Pinotepa Nacional earthquake using the instrumental BHZ waveforms recorded at the 26 GSN teleseismic stations with record start times set to the USGS/NEIC P arrival times. These records correspond to velocity and are given in counts/second in the CWB database. In this case, instrument responses are added to the subfault synthetics rather than deconvolved from the observed records, and both observations and synthetics are interpolated to a common time step of 0.25s prior to inversion. The resulting slip model (Figure 5) shows a more elliptical source with slip extending updip and downdip from the hypocenter.

The direction of elongation is consistent with the N-S slip pattern obtained by UNAM Seismology Group (2013). The peak slip is 413 cm, and the total seismic moment is 1.9×10^{27} dyne-cm. This total moment, however, includes contributions from outside the elliptical source area, more than 45 km from the hypocenter. For a rupture velocity of 2.5 km/s, this outer slip would result from an attempt to fit details of the observed records beyond 18s. Record amplitudes beyond this time, however, are relatively small (Figure 6) and correspond either to unmodeled propagation effects or to minor unresolved features of the source. Some of the record start times are again observed to require time shifts, although runs conducted after making these adjustments do not appreciably modify the inferred rupture pattern. The additional detail provided by the instrumental BHZ records is due to the higher

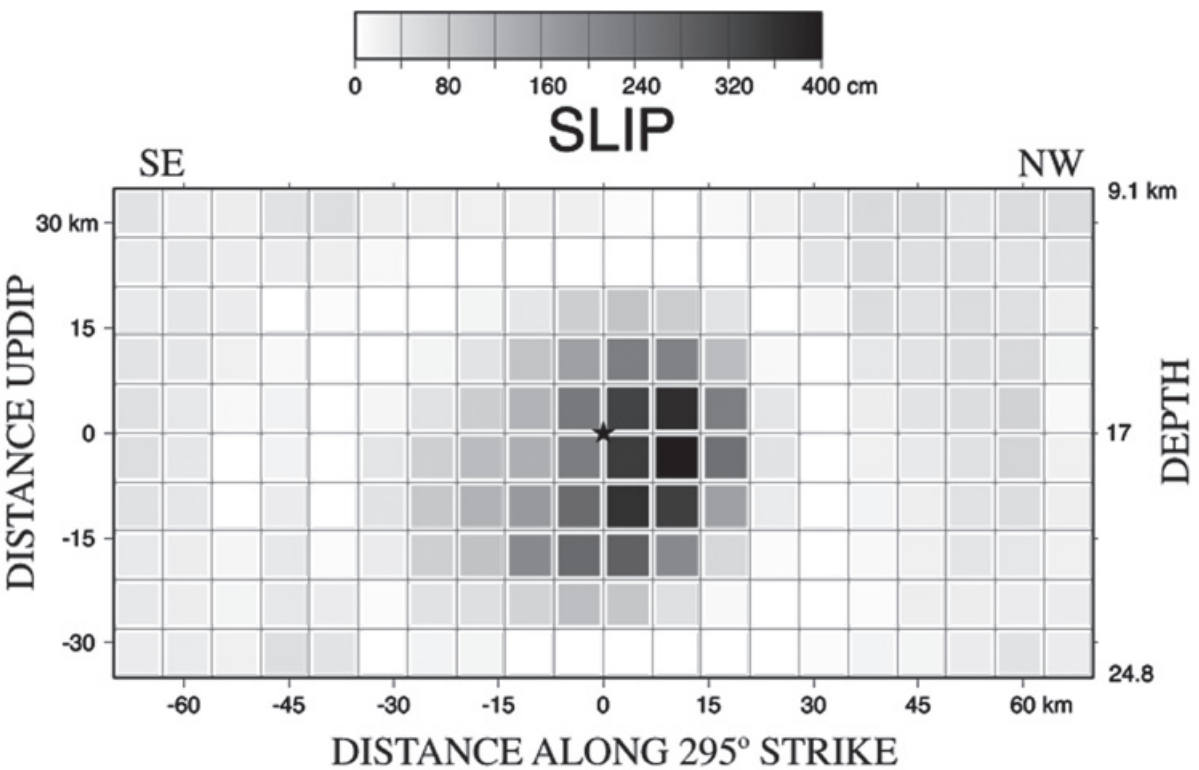

Figure 5. Finite-fault model obtained for the 2012 Ometepec-Pinotepa Nacional from the inversion of the broad-band, teleseismic GSN instrumental P waveforms. Distances and symbols are the same as in Figure 2.

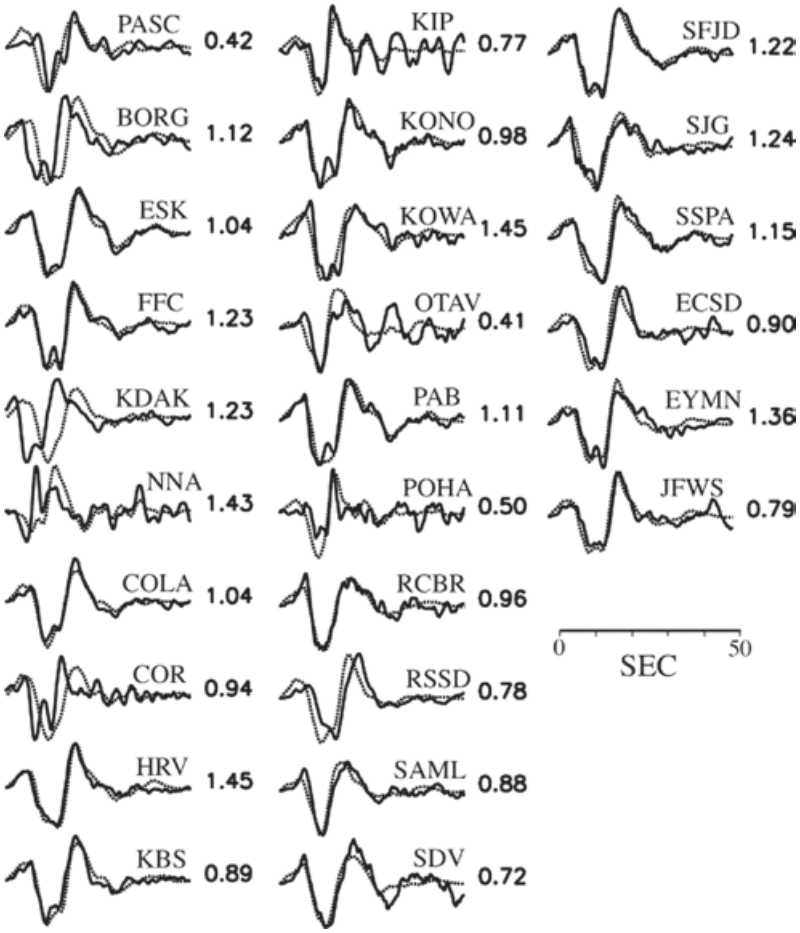

Figure 6. Fits between observed, instrumental teleseismic P waveforms (solid) and those predicted (dashed) for the slip model shown in Figure 5. Records are normalized to their maximum amplitudes, and numbers to the right indicate the ratio of synthetic-to-observed amplitudes corresponding to a total calculated moment of 1.9 x 10^{27} dyne-cm. This total moment, however, includes non-source related contributions due to attempts to fit fine details of the waveforms beyond 18s into the records.

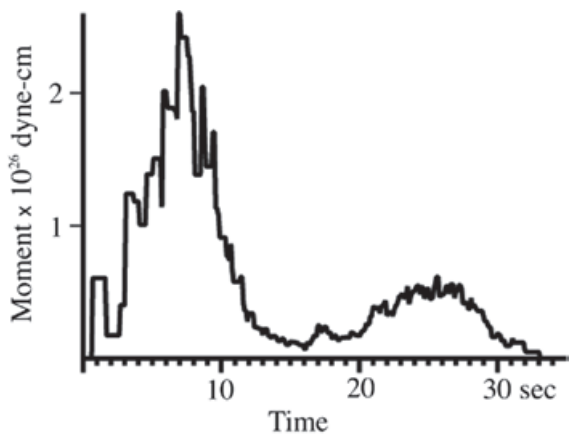

Figure 7. Moment-rate function corresponding to the slip model of Figure 5. The moment release in the first 16s is 1.4 x 10^{27} dyne-cm and corresponds to coseismic slip within the elliptical source region observed in the inferred rupture model. The second pulse observed beyond 16s is attributed to the mapping of non-source effects onto the fault.

frequency content of the velocity waveforms, compared to the ground-displacement records. That is, similar results are obtained using deconvolved, ground-velocity records in the inversion (e.g., records deconvolved within frequency bands of 0.01667-1 Hz and 0.08-1 Hz).

The moment-rate function obtained using the instrumental velocity records (Figure 7) shows a 16s pulse with a seismic moment of 1.4 x 10^{27} dyne-cm that corresponds to the elliptical source area of Figure 5. This source duration and seismic moment are consistent with those identified for the circular slip region in the near-realtime inversion of the deconvolved displacement records. The lower-amplitude pulse observed beyond 16 seconds in the moment-rate function corresponds to slip mapped onto the outer portions of the fault due to the fitting of unmodeled effects in the observed waveforms.

Conclusions and discussion

We derived a first-order rupture model for the 2012 Ometepec-Pinotepa Nacional, Mexico earthquake in near-realtime using 26

broadband, GSN teleseismic P-wave records obtained from the USGS/NEIC Continuous Waveform Buffer (CWB) database. The inversion uses the deconvolved, ground-displacement waveforms to identify a relatively simple, circular 2800-km^2 source near the hypocenter that is comparable in both slip amplitude and rupture extent to the model identified by the USGS/NEIC using body- and surface-wave data. This result indicates that the single-step finite-fault inversion procedure can provide provisional rupture models in near-realtime for large, shallow interplate earthquakes along the Mexico coast using teleseismic P waves. For the Ometepec-Pinotepa Nacional earthquake, the analysis took less than 6 minutes to complete, including the retrieval and processing of the teleseismic P waves and the plotting of the results. For stations located at teleseismic distances, P waveforms would be recorded and stored in the CWB database within 15 minutes following the event, so that a near-realtime inversion could be performed within the first hour provided a source mechanism is available. For large events, moment-tensor mechanisms are generally computed by the USGS/NEIC within this time frame, and these mechanisms could be used in the near-realtime analysis. Alternatively, predetermined fault geometries for subduction events in specific regions could be used to accelerate the process.

We also conducted a second finite-fault analysis of the Ometepec-Pinotepa Nacional earthquake using the instrumental velocity waveforms recorded at the 26 GSN teleseismic stations. The resulting slip pattern shows a more elliptical source that covers an area of about 2500 km^2 and extends updip and downdip from the hypocenter. Slip is oriented SW-NE, consistent with the detailed, dual- source model obtained by UNAM Seismology Group (2013) using local strong-motion data. The velocity records thus provide additional details of the source compared to the ground-displacement waveforms due to their higher frequency content. It would be useful then to include velocity records in near-realtime applications using teleseismic P waves to recover the earthquake rupture history. These could be either deconvolved ground-velocity records or the instrumental waveforms themselves. An advantage of using the instrumental records is that, since the instrument responses are added to the synthetics rather than deconvolved from the observed records, potentially unstable computational steps are avoided in the preparation of the waveforms for inversion. Some long-period filtering, however, may be required for events greater than M_W 8 to adequately account for the finiteness of the source. For example, in their analysis of the 2011 M_W 9.3 Japan and 2012 M_W 8.6 Sumatra earthquakes, Mendoza and Hartzell (2013) low-pass filtered the teleseismic P waveforms at 200s. The number of time windows and the duration of the source-time function would also have to be greater to allow for longer rise times for these larger events. For near-realtime applications, the rise-time parameters used by Mendoza and Hartzell (2013) to model different-size events could probably be adopted. Mendoza and Hartzell (2013) used these parameters to derive distributions of coseismic fault slip that compare well with models derived using more sophisticated techniques and more complete data sets.

Acknowledgments

H. Benz and D. Ketchum facilitated access to the USGS Continuous Waveform Buffer database. The use of broadband instrumental records was prompted following collaborative work conducted with S. Hartzell. Comments provided by two anonymous reviewers greatly improved the manuscript. Partial support for this work was provided by PAPIIT Project IN104013.

References

Ammon C.J., Velasco A.A., Lay T., 2006, Rapid estimation of first-order rupture characteristics for large earthquakes using surface waves: 2004 Sumatra-Andaman earthquake, *Geophys. Res. Lett.,* 33, L14314, doi: 10.1029/2006GL026303.

Dreger D.S., Gee L., Lombard P., Murray M.M., Romanowicz B., 2005, Rapid finite-source analysis and near-fault strong ground motions: Application to the 2003 M_W 6.5 San Simeon and 2004 M_W 6.0 Parkfield earthquakes, *Seism. Res. Lett.,* 76, 40-48.

Hansen P.C., 1998, Rank-Deficient and Discrete Ill-Posed Problems, Numerical Aspects of Linear Inversion, SIAM Monographs on Mathematical Modeling and Computation, Philadelphia, PA.

Hartzell S.H., Heaton T.H., 1983, Inversion of strong ground motion and teleseismic waveform data for the fault rupture history of the 1979 Imperial Valley, California, earthquake, *Bull. Seism. Soc. Am.,* 73, 1553-1583.

Hayes G.P., 2011, Rapid source characterization of the 2011 M_W 9.0 off the Pacific coast of Tohoku earthquake, *Earth Planets Space,* 63, 529-534.

Helmberger D.V., Harkrider D., 1978, Modeling earthquakes with generalized ray theory, in "Modern Problems in Elastic Wave Propagation", J. Miklowitz and J. D. Achenbach (Eds.), John Wiley and Sons, New York.

Ji C., Wald D.J., Helmberger D.V., 2002, Source description of the 1999 Hector Mine, California, earthquake, Part I: Wavelet domain inversion theory and resolution analysis, *Bull. Seism. Soc. Am*., 92, 1192-1207.

Juarez García H., Gómez Bernal A., Rangel Nuñez J.L., Tena-Colunga A., Roldan Islas J., Pelcastre Pérez E., 2012, Learning from earthquakes: The March 20, 2012, Ometepec, Mexcio earthquake, EERI Special Earthquake Report.

Kennett B.L.N., Engdahl E.R., Buland R., 1995, Constraints on seismic velocities in the earth from travel times, *Geophys. J. Int*. 122, 108-124.

Mendoza C., 1996, Rapid derivation of rupture history for large earthquakes, *Seism. Res. Lett.,* 67, 19-26.

Mendoza C., Castro Torres S., Gómez González J.M., 2011, Moment-constrained finite-fault analysis using teleseismic P waves: Mexico subduction zone, *Bull. Seism. Soc. Am.,* 101, 2675-2684.

Mendoza C., Hartzell S., 2013, Finite-fault source inversion using teleseismic P waves: Simple parameterization and rapid analysis, *Bull. Seism. Soc. Am.,* 103, 834-844.

UNAM Seismology Group, 2013, Ometepec-Pinotepa Nacional, Mexico earthquake of 20 March 2012 (M_W 7.5): A Preliminary Report, *Geofísica Internacional,* 52, 2, 173-196.

Somerville P., Irikura K., Graves R., Sawada S., Wald D., Abrahamson N., Iwasaki Y., Kagawa T., Smith N., Kowada A., 1999, Characterizing crustal earthquake slip models for the prediction of strong ground motion, *Seism. Res. Lett.,* 70, 59-80.